



Scientific Technical Report

ISSN 1610-0956

On the relation of stress and deformation fields to natural
and induced seismicity

**Habilitationsschrift
zur Erlangung der *venia legendi*
der Fakultät für Geowissenschaften
der Ruhr-Universität Bochum**

vorgelegt von

Dr. Marco Bohnhoff

aus Hameln

Juni 2005

Contents:

Chapter	Title	Page
1.	Overview	5
2.	Probing the crust to 9 km depth: fluid injection experiments and induced seismicity at the KTB superdeep drilling hole, Germany. <i>Reference: Baisch et al., Bull. Seism. Soc. Am., 92(6), 2369-2380, 2002.</i>	17
3.	Mutual relationship between microseismicity and seismic reflectivity: Case study at the German Continental Deep Drilling Site (KTB). <i>Reference: Rothert et al., GRL, 30(17), 1893, 2003.</i>	37
4.	Fault mechanisms of fluid-injection induced seismicity and their relation to local fault structure and stress field <i>Reference: Bohnhoff et al., J. Geophys. Res., 109, B02309, 2004.</i>	47
5.	Strain Partitioning and Stress Rotation at the North Anatolian Fault Zone from aftershock focal mechanisms of the 1999 Izmit Mw=7.4 Earthquake <i>Reference: Bohnhoff et al., Geophys. J., Int., 2005, submitted.</i>	67
6.	Deformation and Stress regimes in the forearc of the Hellenic subduction zone from inversion of focal mechanisms <i>Reference: Bohnhoff et al., J. Seismol., 2005, accepted.</i>	87
7.	CYCNET: A temporary seismic network on the Cyclades (Aegean Sea, Greece) <i>Reference: Bohnhoff et al., Seismol. Res. Lett., 75(3), 352-357, 2004.</i>	115
8.	Microseismic activity in the Hellenic Volcanic Arc, Greece, with emphasis on the seismotectonic setting of the Santorini-Amorgos zone <i>Reference: Bohnhoff et al., Tectonophysics, 2005, submitted.</i>	127
9.	Indications for a balanced state of the upper plate in the central magmatic arc, Greece, from spatial distribution of microseismic activity <i>Reference: Bohnhoff et al., Geophys. Res. Lett., 2005, to be submitted.</i>	147

1. Overview

Global seismic networks are now in operation for about one century and their recordings contributed significantly to the present understanding of ongoing deformation of the Earth. It was only during the past 2-3 decades that a remarkable step forward was realized through regional network densification and use of advanced data-acquisition technology that permitted to record high-quality digital broadband data on a global scale. Simultaneously, new developments in data evaluation techniques allowed moving from purely kinematical analysis towards sophisticated dynamic interpretations of the acquired data.

The global magnitude detection threshold for earthquakes is in the order of $M=4$. However, today this threshold remains mainly for offshore regions (especially large-scaled Deep-Sea Basins), less developed regions (e.g. most of the African continent) and inaccessible parts of the world (e.g. Polar Regions). An immense densification of seismic stations was achieved in a number of regions such as California, Japan or Western Europe resulting in decreased regional thresholds in the order of $M=2$. In recent years, the subsequently growing data base of high-quality recordings from regional permanent seismic networks permitted to refine earlier initial seismotectonic models pioneered in the 1970s. However, in many cases they still form the backbone for state of the art descriptions.

In order to generate seismotectonic models for selected regions today, both is needed: high-quality recordings from appropriate local seismic networks as well as reliable long-term based information on the regional tectonic setting. In this respect, the World Stress Map Project (WSM, Heidbach et al., 2004; Reinecker et al., 2004) offers a fundamental data base on stress field orientation worldwide. The WSM data base contains more than 13600 quality ranked data sets and data is freely available from their website. To determine the tectonic stress orientation different types of stress indicators are used in the WSM. They are grouped into four categories which are (1) earthquake focal mechanisms, (2) well bore breakouts and drilling induced fractures, (3) in-situ stress measurements and (4) young geologic data. A detailed description of the different methodologies used to derive stress information from these indicators can be found in Sperner et al. (2003), Zoback and Zoback (1991) and Zoback et al. (1989).

As in-situ measurements of stress field orientation and stress magnitude are necessarily associated with the presence of boreholes they are extremely cost-intensive. Furthermore, with regard to the determination of stress field orientation from fault plane solutions it has to be noted that there is an inherent error in all stress orientations derived from single focal mechanism solutions (McKenzie, 1969). Taking into consideration recent developments in seismic data acquisition technology, dense local networks offer the outstanding opportunity to significantly refine the stress maps on local scale. Different methods have been developed to determine the orientations of the three principal stresses, σ_{1-3} , as well as a relative stress magnitude R defined as $R=(\sigma_2-\sigma_3)/(\sigma_1-\sigma_3)$ reflecting the shape of the stress ellipsoid from focal mechanism data. The two most common approaches of stress tensor inversion were introduced by Gephart and Forsyth (1984) and Michael (1987). The methods themselves are described in more detail in the relevant chapters of this work. Here, emphasis should be given on the accuracy of the stress field as determined by the stress tensor inversion. Fault mechanisms serve as input data. Assuming the focal mechanisms were determined from appropriate networks with sufficient station distribution to achieve a good coverage of the focal sphere, their accuracy can realistically be estimated to 5° at best. As a consequence, the accuracy in orientation of the principal stresses can neither be better. Once stress tensor inversion is applied to the data, the results can be related to the regional long-term stress field

(WSM) and used to evaluate the local stress field orientation with respect to possible variations in space and time.

This work describes the results of seismological field campaigns and experiments using combined seismic networks of varying geometries such as a combined seismic downhole and surface network or a combined temporary local and permanent regional network. The networks were deployed in different tectonic environments, i.e. in a stable intraplate surrounding, at a plate boundary along a major transform fault zone and in forearc and backarc settings of a subduction zone to record different types of seismicity (induced earthquakes, aftershocks, subduction-related seismicity). Recording periods are typically several months. The basic ideas behind all the different experiments and studies presented here can be described as follows: In a first step, a state of the art seismic network is designed and deployed in a selected area to record local (micro)seismic activity at low magnitude detection threshold. The acquired data base is then evaluated using standard processing techniques to generate a proper hypocenter catalog for the area of investigation during the observational period. This period might be extended (at higher magnitude detection threshold) through re-evaluating and calibrating earlier hypocenter catalogs gained from records of regional permanent networks. This new catalog for the selected region then forms the base for further evaluation using different approaches one of which is the determination of fault plane solutions in order to determine the local stress field orientation and relate it to the WSM data or information on regional displacement fields determined from GPS recordings.

One option to monitor microseismic activity under low-noise conditions at depth is to operate downhole seismometers in deep boreholes. Such environments generally exhibit low-noise conditions due to their position at depth. In addition, the decreased source-receiver distance results in larger signal to noise ratios at the sensor and thus such an instrument represents an ideal detector for a surface network deployed above the borehole seismometer. Such a network was operated twice at the KTB deep drill site in SE Germany where two boreholes were drilled down to 9 and 4 km depth, respectively. The KTB (Kontinentales TiefBohrprogramm) site is located near the western margin of the Bohemian Massif, at the contact zone of the Saxothuringian and the Moldanubian (Wagner et al., 1997). Drilling was finished in autumn 1994 at a final depth of 9101 m. During the following years, extensive research has been carried out at the KTB, including a 48 h hydro-frac experiment at 8.6-9.1 km depth in 1994 (Zoback and Harjes, 1997; Jost et al., 1998). During this experiment, about 400 microearthquakes were detected at the borehole seismometer that was installed ~4 km depth. One principal result was that the crust is nearly critically stressed at 9 km as microseismicity was caused by extremely small (<1 MPa) pressure perturbations (Zoback and Harjes, 1997). Because no hypocenter was located deeper than 9.1 km, it was concluded that the KTB drilling hole penetrated into the brittle-ductile transition zone of the crust.

Based on the results of the 1994 KTB hydro-frac experiment, a new, long-term fluid-injection experiment was performed at the KTB drilling hole in 2000 (Baisch, Bohnhoff et al., 2002; Rothert, Bohnhoff et al., 2003; Bohnhoff et al., 2004a; chapters 2, 3 and 4). KTB 2000 was designed to enable fluid migration away from the injection interval and to cause pore-pressure increase also at larger distances. Therefore, fluid was injected during a total of 60 days at small injection rates between 10 l/min during the first phase and 70 l/min towards the end of the experiment. A total of 4000 m³ of fresh water were injected into the well head to induce seismicity near the open-hole section at 9 km depth. Because of several leaks in the borehole casing that were unknown before, seismicity occurred at distinct depth levels between 3 km and 9.2 km depth. Two events occurred at 10 km and 15 km depth.

Chapter 2 (Baisch, Bohnhoff et al., 2002) focuses on the location technique applied to the seismic recordings of KTB 2000 and spatiotemporal evolution of hypocenters. The combined

network consisted of a temporary, 40-element, three-component surface network of seismometers and a three-component downhole sonde at 3.8 km depth in the nearby pilot hole. This network enabled to determine absolute hypocenter locations with an accuracy of 26 and 147 m for vertical and horizontal direction, respectively, for the strongest 237 events (out of 2799 induced microearthquakes that were detected at the borehole seismometer). The spatiotemporal distribution of hypocenters at each depth level was found to exhibit complex structures extending several hundred meters from the injection points, with strong spatial and temporal clustering. Regions that were seismically active at a certain time often showed reduced or no activity at later times, indicating local shear-stress relaxation. A similar "memory" effect (Kaiser effect) was observed by comparing hypocenter locations of the KTB 2000 experiment with those obtained for the previous injection experiment at the KTB in 1994. The limitation of hypocentral depths to 9.1 km for events near the borehole suggests changes in rheological properties of the upper crust and thus supports a transition from the regime of brittle failure to ductile deformation at this depth. Large fluid-level changes observed in the nearby pilot hole demonstrated that fluid flow occurred over distances greater than 1.5 km and that major flow zones were not mapped by the induced seismicity. This might also explain the occurrence of isolated events at greater distances and depths that indicated the existence of critically stressed fractures even at temperature over 300°C.

In another study (Rothert, Bohnhoff et al., 2003; chapter 3), the data base acquired during the KTB 2000 injection experiment was further analyzed in terms of its spatiotemporal evolution characteristics. An approach was applied which assumes microseismicity to be triggered by a diffusive process of pore pressure relaxation. The method yields estimates of hydraulic parameters of rocks on large spatial scales. At the KTB site the method enabled to study hydraulic diffusivity at two different depth intervals as induced seismicity occurred dominantly in the depth ranges around 5.4 and 8.8-9.2 km. Estimates of hydraulic diffusivity for shallower parts of the crust seemed to be much smaller than for deeper regions. To understand reasons for this, the spatial relations of hypocenter locations have been analyzed and related to the distribution of intensities of seismic reflections. The results indicate that low values of hydraulic diffusivity correlate with low reflection intensities and high diffusivities with large intensities, respectively. The analysis confirms the hypothesis that the process of pore-pressure relaxation along pre-existing and critically stressed natural fractures is an important triggering factor for induced microseismicity.

Following the above described evaluation of KTB 2000 data, focal mechanisms for events induced during KTB 2000 were determined and analyzed to determine the local stress field orientation (Bohnhoff et al., 2004a; chapter 4). Earlier stress field investigations at the KTB were extensively carried out by Brudy et al. (1997) based on hydraulic fracturing experiments as well as analysis of compressional and tensile failures of the borehole wall. They found a subhorizontal orientation of $N160^{\circ}E \pm 10^{\circ}$ for the maximum principal stress (σ_1) that is nearly uniform with depth down to 8.6 km. A significant change in the stress field orientation was observed below a major fault zone (the so called SE1 reflector at 6.8-7.2 km depth, see Harjes et al., 1997). Interestingly, determination of the local stress field using various data sets and methods such as borehole breakouts, earthquake focal mechanism data, overcoring, hydraulic fracturing and analysis of geological stress indicators (e.g. Müller et al., 1992; Zoback, 1992; Dahlheim et al., 1997) revealed comparatively large variations for the average trend of σ_1 of up to 60° in the vicinity of the KTB. It was of interest whether these variations were due to local stress field heterogeneities (as the different studies might look at different depth levels and/or different scales of the stress field) or whether they reflected uncertainties in the applied methods. Reliable fault plane solutions could be determined for the 125 strongest events out of a total of 2799 induced seismic events of the KTB 2000 experiment. A predominant strike-slip mechanism was observed, partly with components of normal but also reverse faulting.

Adding 54 fault plane solutions of the KTB 1994 injection experiment the local stress field was determined. A subhorizontal NS orientation for the maximum principal stress and a near vertical orientation for the intermediate principal stress were found. The stress field was found to exhibit no temporal or spatial variations within the resolved accuracy of $\pm 15^\circ$. However, the results of the stress tensor inversion pointed to heterogeneities of second order. Based on the hypocentral distribution of the induced microearthquakes and the similarity of fault mechanisms the data was related to the local fault structure at the KTB and it was concluded that the larger faults act as pathways for the injected fluid whereas the brittle failure occurred on fault asperities of the larger mapped faults and nearby smaller faults both in agreement with the local stress field. A thorough error analysis of the individual fault plane solutions was applied. Correlating the diversity of mechanisms with their strength it was found that the strongest events tend to a representative mechanism that is in good correspondence with the local stress field. In contrast, the diversity of fault mechanisms was larger for the smaller events indicating local stress perturbations.

Another important earthquake phenomenon is the occurrence of aftershocks following large earthquakes. It is widely accepted that aftershocks are related to static stress changes along the rupture of a mainshock (see e.g. Stein et al., 1997). However, there are also alternative models focussing on the role of fluids activated during a large earthquake (Miller et al., 2004). A major earthquake of $M_w=7.4$ occurred at the western part of the North Anatolian Fault Zone on Aug 17th, 1999, in NW Turkey starting near the town of Izmit. Analysis of aftershock focal mechanisms along the Izmit rupture are presented in chapter 5 (Bohnhoff et al., 2005a).

The rupture length of the Izmit mainshock was about 140 km between the Sea of Marmara and the Düzce region along a right lateral predominantly EW-trending near vertical fault plane. The direction of slip corresponds well to the overall horizontal GPS derived velocity field of 2-2.5 cm/a westward motion of the Anatolian block with respect to fixed Eurasia (e.g. McClusky et al., 2000). Analysis of surface rupture, teleseismic, strong motion and geodetic data all indicate separation of the mainshock in subevents along distinct fault segments (e.g. Barka et al., 2002; Reilinger et al., 2000; Tibi et al., 2001; Gülen et al., 2002; Delouis et al., 2002; Bos et al., 2004). The western termination of the Izmit rupture was located offshore below the Sea of Marmara possibly extending to the area south of the Prince Islands at about 30 km southeast of Istanbul. At the eastern termination of the rupture near the town of Düzce a $M_w=7.1$ event occurred 87 days after the Izmit mainshock extending the rupture towards the East resulting in a total rupture of both events of about 200 km. The eastward propagation of mainshocks is in contrast to a westward migration of strong earthquakes along the NAFZ observed since the 1939 Erzincan event (e.g. Töksöz et al., 1979; Stein et al., 1997).

Shortly after the Izmit mainshock, the German Task Force for earthquakes installed a 41-station seismic network along the rupture. The network was completed only four days after the event. 254 fault plane solutions were determined from recordings of this network. Almost full spatial coverage allowed rejecting all events for which grid-search results permitted multiple fault-plane solutions. The orientation accuracy of individual fault mechanisms was 5° . In addition, 192 fault plane solutions were collected from published studies. The data were from seismic networks with different geometries covering most of the Izmit rupture area (Polat et al., 2002; Karabulut et al., 2002; Özalaybey et al., 2002). Furthermore, source mechanisms determined by regional moment tensor inversion of the 30 largest Izmit aftershocks (Örgülü and Aktar, 2001) were included. This resulted in a total of 446 focal mechanisms with an average orientation error of the fault plane solutions of $\sim 10^\circ$ in strike, dip and rake.

Cluster of aftershock focal mechanisms were found to define 4 individual fault segments that are in accordance with a segmentation of the coseismic slip. Focal mechanisms surrounding

epicentres of the Izmit and subsequent Düzce mainshock ($M_w=7.1$, Nov 12th, 1999) indicated dominantly strike-slip but also normal faulting. Aftershocks in the area between Izmit and Düzce segments were mainly related to EW-extensional normal faulting indicating a small pull-apart structure. Below the easternmost Sea of Marmara, trains of aftershocks suggest branching of the NAFZ into three or more active segments differing significantly in dominant focal mechanisms. Fault segmentation of the NAFZ in the Izmit-Düzce region obtained from coseismic slip corresponds to spatiotemporal evolution of aftershock focal mechanisms. Areas with high coseismic slip show aftershocks that have dominantly strike-slip mechanisms, but low-slip barriers show mostly normal faulting aftershocks. Stress tensor inversions of the focal mechanisms showed systematic rotations of the local stresses following the Izmit mainshock. In the Izmit Sapanca area, maximum compressive stress was rotated counterclockwise with respect to the coseismic and regional stress field. Towards the eastern end of the rupture (Karadere Düzce area) the local fault trend changes by 25°. There, stresses are rotated clockwise. In both areas this observation coincided with the distribution of aftershock hypocenters. It was concluded that the Izmit earthquake caused significant stress partitioning along the rupture. The direction of stress rotation was related to the orientation of the individual fault segments along the NAFZ.

The third type of earthquakes analyzed here is seismicity related to plate subduction. Seismicity in subduction zones is commonly classified in three categories which are earthquakes within the upper plate, interplate seismicity occurring at the contact zone of overriding and subducting plates and activity within the dipping lithosphere. The south Aegean region is the seismically most active region in Europe and hosts its most prominent subduction zone. At present, incipient collision as well as oblique subduction is observed in the western and eastern forearc, respectively. The south Aegean region is an ideal natural laboratory to study subduction-related processes that can be traced back over the past ca. 35 million years, including an intermittent stage of micro-continent collision between about 30 and 20 Ma, followed by breakoff of the subducting slab, and incipient collision with the passive African margin today in the western Hellenic arc.

In chapter 6 (Bohnhoff et al., 2005b) the deformation and stress regimes in the central Hellenic arc are determined from recordings of a number of temporary networks combined with data from regional and global recordings. In this region, the island of Crete represents a horst structure developed within the last 5 million years in the central forearc and provides excellent onshore access to the internal structure of the forearc at various levels. The convergent plate boundary between the African lithosphere and the Aegean plate as part of Eurasia is located south of Crete in the Libyan Sea and approaches the passive continental margin of northern Africa due to roll back of the Hellenic subduction zone and the convergence between Africa and Eurasia (e.g. McKenzie, 1970; LePichon and Angelier, 1979; Jackson and McKenzie, 1988; LePichon et al., 1995). The overall rate of convergence at the plate boundary is ~4 cm/year (e.g. McClusky et al., 2000). A tectonic reorganization in the entire south Aegean region at 3.4 Ma may mark the onset of continent-continent collision between the Aegean plate and the continental African plate (Lyon-Caen et al., 1988; LePichon et al., 1995; Mascle et al., 1999) at the western Hellenic arc. At the central and eastern part of the forearc indications for remnants of oceanic crust were identified (Bohnhoff et al., 2001; Brönnner, 2003; Meier et al., 2004).

The distribution of hypocenters in the south Aegean region dominantly follows the Hellenic arc with stronger seismic activity observed in the eastern part. The hypocenters form an amphitheatrically shape of the Benioff zone in first order approximation (see e.g. Bath, 1983; Engdahl et al., 1998; Knapmeyer, 1999; Papazachos et al., 2000) and thus the trend of the steepest descent of the dipping slab significantly varies along the Hellenic arc. In contrast, the

GPS horizontal velocities in this region as determined by McClusky et al. (2000) show only minor variation in trend (up to 18°) and magnitude (in the order of mm/a).

Several authors have analyzed the stress field at the Hellenic subduction zone mainly based on fault trends and outcropping faults (e.g. Angelier et al., 1982; Meulenkamp et al., 1988; Ten Veen and Kleinspehn, 2003) or analysis of large earthquakes (Taymaz et al., 1990; Papazachos et al., 2000). In the here presented study (Bohnhoff et al., 2005b, chapter 6) focal mechanism data from various local and regional studies as well as global catalogs were collected to determine the deformation and stress regimes for the first time. In addition, newly determined fault plane solutions for smaller events recorded by a local network in the Messara Plain (Central Crete) were determined and included in the data base. The entire data base consisted of 264 source mechanisms and was examined for types of faulting and spatial clustering of mechanisms. Eight regions with significantly varying characteristic types of faulting were identified of which the upper (Aegean) plate includes four. Three regions contained interplate seismicity along the Hellenic arc from west to east and all events below were identified to occur within the subducting African lithosphere. Stress tensor inversion was applied to each of the subsets in order to determine the stress field orientation. Results indicated a uniform N-NNE direction of relative plate motion between the Ionian Sea and Rhodes resulting in orthogonal convergence in the western forearc and oblique ($40\text{-}50^\circ$) subduction in the eastern forearc. There, the plate boundary migrates towards the SE resulting in left-lateral strike-slip faulting that extends to onshore Eastern Crete. $N110^\circ E$ trending normal faulting in the Aegean plate at this part is in accordance with this model. Along-arc extension was observed on Western Crete. Fault plane solutions for earthquakes within the dipping African lithosphere indicate that slab pull is the dominant force within the subduction process.

Chapters 7 (Bohnhoff et al., 2004b), 8 (Bohnhoff et al., 2005c) and 9 (Bohnhoff et al., 2005d) focus on the magmatic arc of the Hellenic subduction zone. The Hellenic volcanic arc (referred to as HVA in the following) is located about 150 km to the north of the Hellenic arc in the southern Aegean Sea and follows the four main volcanic centres of the Hellenic subduction zone namely Aegina, Milos, Santorini and Nisyros/Kos from West to East. The Cyclades cover the central HVA and are assumed to represent a classical example of a high-pressure belt in a back-arc environment (Trotet et al., 2001). Major zones of extensional detachments were described of which some have been shown to be related to post-orogenic crustal-scale extension (e.g. Lister et al., 1984; Avigad and Garfunkel, 1989; Gautier et al., 1993; Gautier and Brun, 1994). There is general agreement on a two-stage extension of the Aegean domain since Oligocene times (e.g. Tirel et al., 2004 and references therein) and extension was accompanied or possibly alternated with shortening perpendicular to the stretching direction recognized in large-scale NE-SW to NNE-SSW trending folds (Avigad et al., 2001). Seismic activity in the HVA is smaller compared to the forearc region and concentrated at the volcanic centres and along the SW-NE trending Santorini-Amorgos zone of crustal weakness. On average, hypocentral depth increases towards the NNE reflecting the subducting oceanic African lithosphere. The northwestern HVA was interpreted to represent an aseismic region based on earthquake catalogs that were complete down to $M\sim 4$ in the late 1970s (Papanikolaou, 1981). The region has now been monitored for almost 40 years by a permanent regional network operated by the National Observatory of Athens (NOA) and the regional magnitude detection threshold for earthquakes was decreased stepwise to $M\sim 3$. The distribution of hypocenters indicates an increasing activity from West to East and the dominantly active regions around Milos and between Santorini and Amorgos are confirmed. Interestingly, the central part of the metamorphic core complex around the islands of Paros and Naxos appeared aseismic also for this magnitude level and a diffuse distribution of hypocenters was observed for the remaining parts of the central HVA. Most events of the

NOA-catalog are located within the Aegean plate and only a small number is associated with the Benioff zone at 100-150 km depth. The two largest earthquakes in the entire south Aegean region during the last century occurred in 1956 within only 12 minutes and had magnitudes of $M_s=7.4$ and 7.2 , respectively. Both events were located between Santorini and Amorgos and they were followed by at least 20 aftershocks of $M>4$ within five months (Papadopoulos and Pavlides, 1992; Papazachos et al., 2000).

To decrease the magnitude detection threshold in the central HVA a local seismic network (CYCNET) was installed on up to 17 islands of the Cyclades (Bohnhoff et al., 2004b; chapter 7). CYCNET recordings allowed analyzing the level and spatiotemporal evolution of microseismic activity in this region for the first time. The principal objectives to be addressed by CYCNET were: 1. How is the shallow and intermediate-depth seismic activity distributed in the central HVA? 2. What is the interaction between spatiotemporal evolution of hypocenters and upward migrating fluids and magma? 3. Why is the seismicity clustered in space and time over a broad range of magnitudes ($M>4$ seismic sequence in 1956 between Santorini and Amorgos; distinct activity maxima for $M<2$ observed by a local network on Milos)? 4. What is the crustal and uppermost mantle structure along the central volcanic arc? Chapter 7 describes the motivation for CYCNET that was installed in autumn 2002 consisting of up to 22 stations on 17 islands. Its combination of short-period and broad-band sensors aimed at providing data for both seismicity studies and structural investigations. The recording period for CYCNET was initially planned for two years. Selected recordings are presented and the data quality that was found to be unexpectedly high is discussed.

Results of CYCNET recordings from the first 20 months of operation were presented in the paper by Bohnhoff et al. (2005c, chapter 8). In this study, CYCNET recordings were analyzed using statistical methods, cluster analysis and relative relocation techniques and related to the regional tectonic setting. Distinct regions with significantly varying spatiotemporal behaviour of microseismicity were identified. A large portion of the seismic activity within the upper crust was associated with the presence of islands representing horst structures that were generated during the major Oligocene extensional phase. In contrast, the central part of the Cyclades metamorphic core complex remained aseismic considering CYCNET's threshold of magnitude completeness of 1.5 with only one exception between Paros and Naxos where activity occurred swarm-like and with highly similar waveforms. The highest activity in the study area was identified along the SW-NE striking Santorini-Amorgos zone. Within this zone the submarine Columbo volcano exhibited strong temporal variations of seismic activity on a high background level. This activity was interpreted to be directly linked to the magma reservoir and therein the migration of magma and fluids towards the surface. NE of Columbo where no volcanic activity had yet been reported a similar seismicity pattern with small-scaled activity spots was observed that might represent local pathways of upward migrating fluids or even developing volcanic activity within this zone of crustal weakness. In contrast, the Santorini and Milos volcanic complexes did not show significant temporal variations and low to moderate background activity, respectively. Relating the results to the distribution of historical earthquakes and the GPS-derived horizontal velocity field it was concluded that the Santorini-Amorgos zone is in the state of right-lateral transtension reflecting a major structural boundary of the volcanic arc subdividing it into a seismically and volcanically quiet western and an active eastern part.

The last study presented in this work (chapter 9, Bohnhoff et al., 2005d) focuses on seismicity as recorded by CYCNET that is related to the occurrence of islands representing elevated crustal blocks. It is discussed whether this seismicity is triggered by increased shear stress at depth induced by the gravitational load of the islands. There is general agreement that either increased shear stress or reduced effective normal stress caused by increased pore pressure on pre-existing faults is the triggering mechanism responsible for induced earthquakes (see

review by Simpson, 1986). Following Ruff (2002), lateral variations in density, topography, and bathymetry are responsible for most of the shear stress within the Earth. Additional gravitational load e.g. caused by local maxima in topography or man-made water dams adds to the tectonic shear stress by enlarging the radius of the Mohr circle through increasing the maximum principal stress (e.g. Jaeger and Cook, 1971). As a consequence, increased vertical stress has the largest impact in normal faulting regimes where the vertical stress is the maximum (Snow, 1972; Simpson, 1976). Earthquakes then would be triggered once the induced stresses are large enough to produce failure. Examples from various sites in different tectonic environments consistently identified that even minor stress perturbations in the order of 0.1-4 MPa may cause shear failure on pre-existing faults (e.g. Beck, 1976; Zoback and Harjes, 1997; Pandey and Chadha, 2003) indicating that brittle-failure equilibrium of the upper part of the Earth's crust is probably a general phenomenon.

Most of the island-related seismicity observed in the central HVA is located within the uppermost 6 km. Taking into consideration the lateral extension of the associated islands with respect to the median regional elevation this correlates with the depth where maximum shear stress induced by the gravitational load of the islands is expected following Jeffreys (1970) who presented a model describing the pressure at the bottom of a load located on the Earth surface. The peak-magnitude of the load-induced shear stress below the islands was found to be ~3 MPa and thus sufficient to reactivate pre-existing faults. It was concluded that load-induced shear-stress caused by elevated crustal blocks in the HVA is one possible triggering mechanism for microseismic activity indicating that the upper plate might be in a balanced state along the rim of the Cyclades metamorphic core complex.

References:

- Angelier, J., Lyberis, N., LePichon, X. & Barrier, E., 1982, The tectonic development of the Hellenic arc and the sea of Crete: A synthesis, *Tectonophysics*, **86**, 159-196.
- Avigad, D., Garfunkel, Z., 1989, Low-angle faults above and below a blueschist belt-Tinos Island, Cyclades, Greece. *Terra Nova*, **1**, 182-187.
- Avigad, D., Ziv, A. & Garfunkel, Z., 2001, Ductile and brittle shortening, extension-parallel folds and maintenance of crustal thickness in the central Aegean (Cyclades, Greece). *Tectonics*, **20/2**, 277-287.
- Baisch, S., Bohnhoff, M., Ceranna, L., Tu, Y. & Harjes, H.-P., 2002, Probing the crust to 9 km depth: fluid injection experiments and induced seismicity at the KTB superdeep drilling hole, Germany. *Bull. Seismol. Soc. Am.*, **92(6)**, 2369-2380.
- Barka, A. & 21 others, 2002, The Surface Rupture and Slip Distribution of the 17 August 1999 Izmit Earthquake (M 7.4), North Anatolian Fault, *Bull. Seism. Soc. Am.*, **92(1)**, 43-60.
- Bath, M., 1983, The seismology of Greece, *Tectonophysics*, **98**, 165-208.
- Beck, J.L., 1976, Weight-induced stresses and the recent seismicity at Lake Oroville, California, *Bull. Seism. Soc. Am.*, **66 (4)**, 1121-1131.
- Bohnhoff, M., Makris, J., Papanikolaou, D. & Stavrakakis, G., 2001, Crustal investigation of the Hellenic subduction zone using wide aperture seismic data, *Tectonophysics*, **343**, 239-262.
- Bohnhoff, M., Baisch, S. & Harjes, H.-P., 2004a, Fault mechanisms of induced seismicity at the superdeep German Continental Deep Drilling Program (KTB) borehole and their relation to fault structure and stress field. *J. Geophys. Res.*, **109**, B02309, doi:10.1029/2003JB002528.
- Bohnhoff, M., Rische, M., Meier, T., Endrun, B., Becker, D., Harjes, H.-P. & Stavrakakis, G., 2004b, A temporary Seismic Network on the Cyclades (Aegean Sea, Greece), *Seismol. Res., Lett.*, **75/3**, 352-357.
- Bohnhoff, M., Grosser, H. & Dresen, G., 2005a, Strain Partitioning and Stress Rotation at the North Anatolian Fault Zone from aftershock focal mechanisms of the 1999 Mw=7.4 Earthquake. *Geophys. J. Int.* (submitted).
- Bohnhoff, M., Harjes, H.-P. and Meier, T., 2005b, Deformation and Stress regimes in the forearc of the Hellenic subduction zone from inversion of focal mechanisms, *J. Seismology*, accepted.
- Bohnhoff, M., Rische, M., Meier, T. Becker, D. Stavrakakis, G. & Harjes, H.-P., 2005c, Microseismic activity in the Hellenic Volcanic Arc, Greece, with emphasis on the seismotectonic setting of the Santorini-Amorgos zone. *Tectonophysics*, submitted.

- Bohnhoff, M., Rische, M. & Harjes, H.-P., 2005d, Indications for a balanced state of the upper plate in the central magmatic arc, Greece, from spatial distribution of microseismicity, *Geophys. Res. Lett.*, to be submitted.
- Bos, A.G., Usai, S. & Spakman, W., 2004, A joint analysis of GPS motions and InSAR to infer the coseismic surface deformation of the Izmit, Turkey earthquake, *Geophys. J. Int.*, **158**, 849-863.
- Brönnner, M., 2003, Untersuchungen des Krustenaufbaus entlang des Mediterranen Rückens abgeleitet aus geophysikalischen Messungen, *PhD thesis*, Faculty of Geosciences, Hamburg University (in German).
- Brudy, M., M.D. Zoback, K. Fuchs, F. Rummel & J. Baumgärtner, 1997, Estimation of the complete stress tensor to 8 km depth in the KTB scientific drill holes: Implications for crustal strength, *J. Geophys. Res.*, **102**, 18453-18475.
- Dahlheim, H.-A., H. Gebrande, E. Schmedes & H. Soffel, 1997, Seismicity and stress files in the vicinity of the KTB location, *J. Geophys. Res.*, **102**, 18493-18506.
- Delouis, B., Giardini, C., Lundgren, P. & Salichon, J., 2002, Joint inversion of InSAR, GPS, Teleseismic, and Strong-Motion Data for the Spatial and Temporal Distribution of Earthquake slip: Application to the 1999 Izmit Mainshock, *Bull. Seism. Soc. Am.*, **92(1)**, 278-299.
- Engdahl, E.R., van der Hilst, R., & Buland, R., 1998, Global teleseismic earthquake relocation with improved travel times and procedures for depth determination, *Bull. Seis. Soc. Am.*, **88**, 722-743.
- Gautier, P. & Brun, J.P., 1994, Crustal-scale geometry and kinematics of late-orogenic extension in the central Aegean (Cyclades and Evvia Island). *Tectonophysics*, **238**, 399-424.
- Gautier, P., Brun, J.P. & Jolivet, L., 1993, Structure and kinematics of Upper Cenozoic extensional detachment on Naxos and Paros (Cyclades islands, Greece), *Tectonics*, **12**, 1180-1194.
- Gephart, J.W. & Forsyth, D.W., 1984, An improved Method for Determining the Regional Stress Tensor Using Earthquake Focal Mechanism Data: Application to the San Fernando Earthquake Sequence, *J. Geophys. Res.*, **89**, 9305-9320, 1984.
- Gülen, L., Pinar, A., Kalafat, D., Özel, N., Horasan, G., Yilmazer, M. & Isikara, A. M., 2002., Surface breaks. Aftershock Distribution, and Rupture Process of the 17 August 1999 Izmit, Turkey, Earthquake, *Bull. Seismol. Soc. Am.*, **92(1)**, 230-244.
- Harjes, H.-P., K. Bram, H.-J. Dürbaum, H. Gebrande, G. Hirschmann, M. Janik, M. Klöckner, E. Lüschen, W. Rabbel, M. Simon, R. Thomas, J. Tormann & F. Wenzel, 1997, Origin and nature of crustal reflections: Results from integrated seismic measurements at the KTB superdeep drilling site, *J. Geophys. Res.*, **102**, 18267-18288.
- Heidbach, O., Barth, A., Connolly, P., Fuchs, K., Müller, B., Reinecker, J., Sperner, B., Tingay, M. & F. Wenzel, 2004, Stress maps in a minute: The 2004 World Stress Map Release, *EoS Trans.*, **85(49)**, 521-529, 2004.
- Jackson, J. & McKenzie, D.P., 1988, The relationship between plate motion and seismic moment tensors, and the rates of active deformation in the Mediterranean and Middle East, *Geophys. J.*, **93**, 45-73.
- Jaeger, J.C. & N.G.W. Cook, 1971, Fundamental of Rock Mechanics, *London: Chapman & Hall*, 515pp.
- Jeffreys, H., 1970, The Earth, *Cambridge University Press, New York*.
- Jost, M. L., Büsselberg, T., Jost, O. & Harjes, H.-P., 1998, Source parameters of injection-induced microearthquakes at 9 km depth at the KTB deep drilling site, Germany, *Bull. Seism. Soc. Am.* **88**, no. 3, 815-832.
- Karabulut, H., M. P. Bouin, M. Bouchon, M. Dietrich, C. Cornou & M. Aktar, 2002, The Seismicity in the Eastern Marmara Sea after the 17 August 1999 Izmit Earthquake, *Bull. Seism. Soc. Am.*, **92(2)**, 387-393.
- Knapmeyer, M., 1999, Geometry of the Aegean Benioff zone. *Ann. Geofis.*, **42**, 27-38.
- LePichon, X. & Angelier, J., 1979, The Hellenic arc and trench system: a key to the neotectonic evolution of the Eastern Mediterranean area, *Tectonophysics*, **60**, 1-42.
- LePichon, X., Chamot-Rooke, N. & Lallemand, S., 1995, Geodetic determination of the kinematics of central Greece with respect to Europe: Implications for Eastern Mediterranean tectonics, *J. Geophys. Res.*, **100**, 12675-12690.
- Lister, G.S., Banga, G. & Feenstra, A., 1984, Metamorphic core complexes of Cordilleran type in the Cyclades, Aegean Sea, Greece. *Geology*, **12**, 221-225.
- Lyon-Caen, H. et al., 1988, The 1986 Kalamata (south Peloponnesus) earthquake: detailed study of a normal fault, evidences for east-west extension in the Hellenic arc, *J. Geophys. Res.*, **93**, 14967-15000.
- Masce, J. et al., 1999, Images may show start of European-African plate collision, *EoS Transactions*, **80 (37)**, American Geophysical Union, 421-428.
- McClusky, S. & 27 others, 2000, Global positioning system constraints on plate kinematics and dynamics in the eastern Mediterranean and Caucasus, *J. Geophys. Res.*, **105**, 5695-5719.
- McKenzie, D.P., 1969, The relation between fault plane solutions for earthquakes and the directions of the principal stresses, *Bull. Seismol. Soc. Am.*, **59 (2)**, 591-601.
- McKenzie, D.P., 1970, Plate tectonics of the Mediterranean region, *Nature*, **226**, 239-243.

- Meier, T., Dietrich, K., Stöckhert, B. & Harjes, H.-P., 2004, One-dimensional models of shear wave velocity for the eastern Mediterranean obtained from the inversion of Rayleigh wave phase velocities and tectonic implications, *Geophys. J. Int.*, **156**, 45-58.
- Meulenkamp, J.E., Wortel, M.J.R., VanWamel, W.A., Spakman & Hoogerduyn Strating, E., 1988, On the Hellenic subduction zone and the geodynamic evolution of Crete since the late Middle Miocene, *Tectonophysics*, **146**, 203-215.
- Michael, A.J., 1987, Use of focal mechanisms to determine stress: a control study, *J. Geophys. Res.*, **92**, 357-368.
- Miller, S.A., Collettini, C., Chiaraluce, L., Cocco, M., Barchi, M., & Kaus, B.J.P., 2004, *Nature*, **427**, 724-727.
- Müller, B., M.L. Zoback, K. Fuchs, L. Mastin, S. Gregersen, N. Pavoni, O. Stephansson & C. Ljunggren, 1992, Regional Patterns of Tectonic Stress in Europe, *J. Geophys. Res.*, **97**, 11783-11803.
- Örgülü, G. & M. Aktar, 2001, Regional Moment Tensor Inversion for Strong Aftershocks of the August 17, 1999 Izmit Earthquake ($M_w=7.4$), *Geophys. Res. Lett.*, **28(2)**, 371-374.
- Özalaybey, S., M. Ergin, M. Aktar, C. Tapirdamaz, F. Bicman & A. Yörük, 2002, The 1999 Izmit Earthquake Sequence in Turkey: Seismological and Tectonic Aspects, *Bull. Seism. Soc. Am.*, **92(2)**, 376-386.
- Pandey, A.P. & R.K. Chadha, 2003, Surface loading and triggered earthquakes in the Koyna-Warna region, western India, *Phys. Earth. Planet. Int.*, **139**, 207-223.
- Papadopoulos, G.A. & Pavlides, S.B., 1992, The large 1956 earthquake in the South Aegean: Macroseismic field configuration, faulting and neotectonics of Amorgos island, *Earth and Planet. Sci. Lett.*, **113**, 383-396.
- Papanikolaou, D., 1981, Morphotectonics and seismicity in the Cyclades, Aegean Sea, *Z. Geomorphologie*, **40**, 165-174.
- Papazachos, B.C., Karakostas, V.G., Papazachos, C.B. & Scordilis, E.M., 2000, The geometry of the Wadati-Benioff zone and lithospheric kinematics in the Hellenic arc, *Tectonophysics*, **319**, 275-300.
- Polat, O., H. Eyidogan, H. Haessler, A. Cisternas & Philip, H., 2002, Analysis and interpretation of the aftershock sequence of the August 17, 1999, Izmit (Turkey) earthquake, *J. Seismol.*, **6**, 287-306.
- Reilinger, R.E. & 12 others, 2000, Coseismic and Postseismic Fault Slip for the 17 August 1999, $M=7.5$, Izmit, Turkey Earthquake, *Science*, **289**, 1519-1524.
- Reinecker, J., Heidbach, O., Tingay, M., Connolly, P. & Müller, B., 2004, The 2004 release of the World Stress Map (available online at www.world-stress-map.org).
- Rotherth, E., Shapiro, S., Buske, S. & Bohnhoff, M., 2003, Mutual relationship between microseismicity and seismic reflectivity: Case study at the German Continental Deep Drilling Site (KTB). *Geophys. Res. Lett.*, **30(17)**, 1893, doi:10.1029/2003GL017848.
- Ruff, L.J., 2002, State of Stress Within the Earth, *Int. Handbook of Earthquake and Engineering Seismology, vol. 81A*, Int. Assoc. Seismol. and Phys. Earth's Int., Committee on Education, 539-557.
- Simpson, D.W., 1976, Seismicity changes associated with reservoir impounding, *Eng. Geol.*, **10**, 371-385.
- Simpson, D.W., 1986, Triggered Earthquakes, *Ann. Rev. Earth Planet. Sci.*, **14**, 21-42.
- Snow, D.T., 1972, Geodynamics of seismic reservoirs, *Proc. Symp. Percolation Through Fissured Rocks, T2-J*, Stuttgart, Ges. Erd- und Grundbau, 1-19.
- Sperner, B., Müller, B., Heidbach, O., Delvaux, D., Reinecker, J. & Fuchs, K., 2003, Tectonic stress in the Earth's crust: Advances in the World Stress Map Project. In: *New Insights in Structural Interpretation and Modelling*, edited by D.A. Nieuwland, *Geol. Soc. Spec. Publ.*, **212**, 101-116.
- Stein, R., 1999, The role of stress transfer in earthquake occurrence, *Nature*, **402**, 605-609.
- Stein, R.S., Barka, A. & Dieterich, J.H., 1997, Progressive failure of the North Anatolian fault since 1939 by earthquake stress triggering, *Geophys. J. Int.*, **128**, 594-604.
- Taymaz, T., Jackson, J. & Westaway, R., 1990, Earthquake mechanisms in the Hellenic trench near Crete, *Geophys. J. Int.*, **102**, 695-731.
- TenVeen, J.H. & Kleinspehn, K.L., 2003, Incipient continental collision and plate-boundary curvature: Late Pliocene-Holocene transtensional Hellenic forearc, Crete, Greece, *J. Geol. Soc. London*, **160**, 161-181.
- Tibi, R., Bock, G., Xia, Y., Baumbach, M., Grosser, H., Milkereit, C., Karakisa, S., Zünbül, S., Kind, R. & Zschau, J., 2001, Rupture processes of the 1999 August 17 Izmit and November 12 Düzce (Turkey) earthquakes, *Geophys. J. Int.*, **144**, F1-F7.
- Tirel, C., Gueydan, F., Tiberi, C. & Brun, J.P., 2004, Aegean crustal thickness inferred from gravity inversion. Geodynamical implications. *Earth Planet. Sci. Lett.*, **228**, 267-280.
- Töksöz, M.N., Shakal, A.F. & Michael, A.J., 1979, Space-time migration of earthquakes along the North Anatolian Fault and seismic gaps, *PAGEOPH*, **117**, 1258-1270.
- Trotet, F., Jolivet, L., Vidal, O., 2001, Tectono-metamorphic evolution of Syros and Sifnos islands (Cyclades, Greece). *Tectonophysics*, **338**, 179-206.
- Wagner, G. A. & others, 1997, Post-Variscan thermal and tectonic evolution of the KTB site and its surroundings, *J. Geophys. Res.* **102**, no. B8, 18,221-18,232.

-
- Zoback, M.L., 1992, First and second order patterns of stress in the lithosphere: The World Stress Map Project, *J. Geophys. Res.*, **97**, 11703-11728.
- Zoback, M. D. & Harjes, H.-P., 1997, Injection-induced earthquakes and crustal stress at 9 km depth at the KTB deep drilling site, Germany, *J. Geophys. Res.* **102**, no. B8, 18,477-18,491.
- Zoback, M.D. & Zoback, M.L., 1991, Tectonic Stress Field of North America and relative plate motions. In: *Neotectonics of North America*, Slemmons, Engdahl, Zoback, Blackwell (eds.), 339-366.
- Zoback, M.L. & 27 others, 1989, Global patterns of tectonic stress, *Nature*, **341**, 6240, 291-298.

2. Probing the crust to 9 km depth: fluid injection experiments and induced seismicity at the KTB superdeep drilling hole, Germany.

This chapter has been published. The reference is

Baisch, S., Bohnhoff, M., Ceranna, L., Tu, Y., Harjes, H.-P. (2002). Probing the crust to 9 km depth: fluid injection experiments and induced seismicity at the KTB superdeep drilling hole, Germany. *Bull. Seismol. Soc. Am.*, **92(6)**, 2369-2380.

2.1. Abstract

A 60-day, long-term fluid-injection experiment was performed at the 9.1 km deep Kontinentale Tiefbohrung, Germany (KTB), borehole. About 4000 m³ of water were injected into the well head to induce seismicity near the open-hole section at 9 km depth. Because of several leaks in the borehole casing (unknown before), seismicity occurred at distinct depth levels between 3 km and 9 km depth. Two events occurred at 10 km and 15 km depth. The combination of a temporary, 40-element, three-component surface network of seismometers and a three-component downhole sonde at 3.8 km depth in the nearby pilot hole enabled us to determine absolute hypocenter locations by using a velocity model that was calibrated from several downhole shots at depths of 5.4 km and 8.5 km. Of a total of 2799 induced events, hypocenter locations were obtained for 237 events having good signal-to-noise ratio at surface stations. The spatiotemporal distribution of hypocenters at each depth level exhibits complex structures extending several hundred meters from the injection points, with strong spatial and temporal clustering. Regions that were seismically active at a certain time often showed reduced or no activity at later times, indicating local shear-stress relaxation. A similar "memory" effect (Kaiser effect) is observed by comparing hypocenter locations of the present experiment with those obtained for a previous injection experiment at the KTB. The limitation of hypocentral depths to 9.1 km for events near the borehole suggests changes in rheological properties of the upper crust and thus supports a transition from the regime of brittle failure to ductile deformation at this depth. Large fluid-level changes observed in the nearby pilot hole demonstrate that fluid flow occurs over distances greater than 1.5 km and that major flow zones are not mapped by the induced seismicity. This might also explain the occurrence of isolated events at greater distances and depths. Brittle failure at depths greater than 10 km indicates the existence of critically stressed fractures even at temperature over 300°C.

2.2. Introduction

The Kontinentale Tiefbohrung (KTB) drilling site is located in South-eastern Germany (Fig. 1) near the western margin of the Bohemian Massif, at the contact zone of the Saxothuringian and the Moldanubian (Wagner et al., 1997). The drill site itself lies within the zone of Erbdorf-Vohenstrauß, a smaller crustal segment mainly composed of metabasites and gneisses (Pechinig et al., 1997). In 1994, the KTB borehole had reached a final depth of 9101 m and temperatures of about 270°C. During the 7 years after completing drilling activities, extensive research has been carried out at the KTB, including a 48-hr, short-term fluid-injection experiment at 9 km depth (Zoback and Harjes, 1997; Jost et al., 1998), named KTB1994 hereafter. Injecting a volume of 200 m³ of heavy brine induced about 400 detected microearthquakes. These gave a detailed picture of the local stress field at 9 km depth and indicated that the crust is nearly critically stressed at this depth, because microseismicity was caused by extremely small (<1 MPa) pressure perturbations (Zoback and Harjes, 1997). Because no hypocenter was located deeper than 9.1 km, it was concluded that the KTB drilling hole penetrated into the brittle-ductile transition zone of the crust (Emmermann and Lauterjung, 1997; Haak and Jones, 1997). Further support for this hypothesis came from analyses of dislocation microstructures of quartz samples (Dresen et al., 1997). On the other hand, Dahlheim et al. (1997) operated a four-station seismic network to monitor natural seismicity in the KTB region. Although natural seismicity is sparse in this region, they found six events occurring near the KTB drilling site within a monitoring period of 5 years. The

deepest event was located at 13 km depth, indicating that brittle failure can also occur at greater depth.

To further investigate whether the limitation of hypocentral depth to the upper 9.1 km during KTB1994 reflects a rheological boundary or simply the limited range of pore-pressure increase, a new, long-term fluid-injection experiment was performed at the KTB drilling hole. The experiment, hereafter named KTB2000, was designed to enable fluid migration away from the injection interval and to cause pore-pressure increase also at larger distances. Based on theoretical modeling of pressure propagation along a vertical crack, pore-pressure perturbations of the order of 0.5 MPa were expected down to 13 km depth (R. Horne, personal comm.). However, because of several previously unknown leaks in the drill-hole casing, fluid was pressed into the rock at different injection intervals, inducing seismicity at distinct depth levels. The outcome of the experiment gives an excellent opportunity to study the mechanical behaviour, the local stress field, and fluid-migration processes at different depth regions ranging from 3.2 km to 9.1 km. Understanding spatiotemporal characteristics of induced seismicity is of primary importance in mapping fractures and potential flow paths, particularly in light of the increasing need for enhanced recovery in oil and gas reservoirs and renewed interest in geothermal techniques (Niitsuma et al., 1998). The current article describes the KTB2000 injection experiment and focuses on the investigation of spatiotemporal distributions of induced seismicity. Absolute hypocenter locations are computed using a linearized inversion technique in combination with statistical criteria. These locations are used to address questions concerning fluid-migration paths, rheological behaviour, and coseismic shear-stress relaxation within the reservoir.

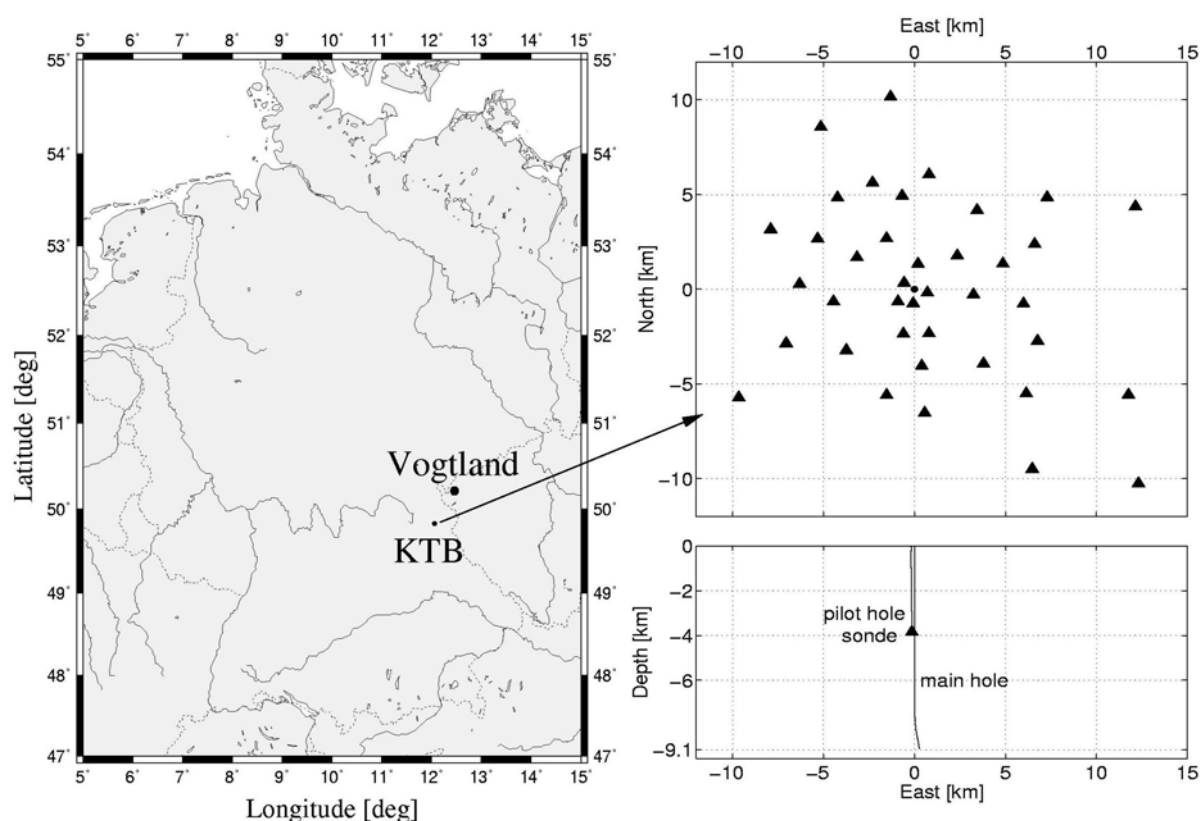


Figure 1: Location of the KTB drilling site (a), seismic network configuration (b), and location of the main hole and pilot hole (c). Origin of local coordinate system is the top of the main hole (49.83°N, 12.12°E). Triangles denote three-component seismometers. Pilot-hole sonde is installed at 3.827 km depth. During the injection experiment, an earthquake swarm occurred in the Vogtland area (indicated as large dot, a).

2.3. Injection Experiment

Starting on 21 August 2000 (Julian day 234; hereafter referred to as day 234), a long-term, fluid-injection experiment (60 days) was performed by injecting a total of 4000 m³ of fresh water into the well head of the 9.1 km deep main hole. Unlike KTB1994, no drilling rig could be used to inject directly into the open-hole section at 9 km depth. Because preceding hydraulic tests did not indicate any leaks in the casing, it was assumed that the main hole was hydraulically closed to at least 6 km depth (J. Kück, internal report, 1998). Fluid was therefore injected directly into the well head, and the entire borehole, which is cased down to 9 km depth, was pressurized. Figure 2 shows the main hydraulic parameters of the experiment. Flow rates were episodically increased from 30 l/min at the beginning to 70 l/min at the end of the experiment, interrupted by several shut-in phases (Fig. 2a). Due to temperature-density and ballooning effects, the well-head pressure (P_{wh}) shows a complex behaviour at the beginning of the injection (until day 240) and then systematically increases to 30 MPa, interrupted only by sharp pressure drops during shut-in phases. Before stopping the injection on 19th October 2000 (day 293), flow rates were increased to >90 l/min for 1.5 h. At this time, P_{wh} reached its maximum value of 31 MPa. After the injection, the well remained closed for about 2 days and P_{wh} quickly decayed. The experiment was terminated with several short periods of opening and closing of the well, during which time fluid flowed back out of the well head (Fig. 2a, dashed curve). Figure 2b also shows rates of induced events detected

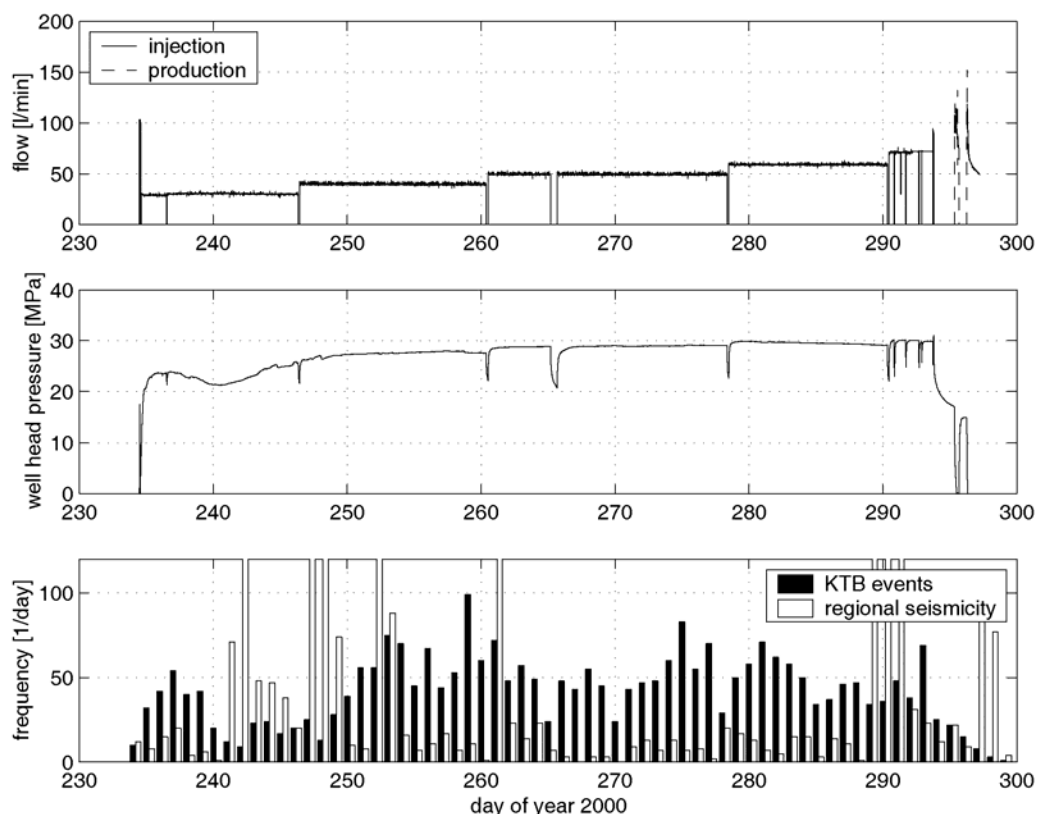


Figure 2: Injection rate (a), well-head pressure (b), and rate of induced events and regional seismicity (c) as a function of Julian day. Injection-induced events (2799) have been detected at the down-hole seismometer. Natural seismicity was dominated by earthquake swarms of the Vogtland area. See text for details.

by the downhole seismometer (see the next section). The temporal evolution of these rates strongly correlates with P_{wh} . Low values of P_{wh} are accompanied by low seismicity rates. This correlation becomes most evident during three shut-in phases between days 260 and 280. At the end of the experiment, the peak value of P_{wh} (day 293) caused a local maximum of the seismicity rate. Thereafter, the seismicity rate quickly subsided, consistent with the decrease of P_{wh} . However, this correlation is perturbed by several "contaminating" effects. For technical reasons, the downhole seismometer had to be exchanged on day 270, resulting in a shorter recording time on this day. Most notably, however, the detection of induced events was complicated by earthquake swarm activities in the Vogtland region, approximately 50 km north-northeast of KTB (see Fig. 1), which started on 28 August (Klinge and Plenefisch, 2001). During periods of swarm activity, the downhole sonde detected a large number of swarm events and may have missed induced KTB events because of their lower signal-to-noise ratio (SNR). Triggered phases from Vogtland swarm events are also marked in Fig. 2b (white boxes). Note that the correlation between decreasing P_{wh} and decreasing rate of induced events during days 237-240 is not an artefact of swarm activity. During the injection experiment, a 40-station surface network and a borehole sonde in the pilot hole (located 200 m to the west of the main hole) were operated to monitor induced seismicity (Fig. 1). All surface stations were equipped with three-component seismometers (Mark L4-3C) recording continuously at a 200 Hz sampling rate on a PDAS-100 data logger. The three-component pilot-hole sonde was operated at a 1 kHz sampling rate. All stations were equipped with Global Positioning System (GPS) modules and the surface and borehole sensors were synchronized at intervals of 1 and 1.5 hr, respectively.

2.4. Monitoring Induced Seismicity at the Pilot-Hole Sonde

Figure 2 shows the temporal evolution of injection-induced event rate determined at the pilot-hole sonde. Information on the spatial hypocenter distribution can be derived by location techniques, which incorporate the station network, or by single-station methods based on wave-field polarization and travel-time differences between S- and P-phase onsets (t_s-t_p times). Hypocenter locations determined from the recordings of the entire station network are presented in the next section. We focus here on the recordings of the pilot-hole sonde only. The main advantage of focusing on these recordings comes from the large number of events with good SNR at the pilot-hole sonde (see Fig. 3 as an example for these events). Of 2799 events recorded at the pilot-hole sonde and validated as injection-induced events, only 261 (<10%) can be identified on more than four stations of the surface network. This was quite different during KTB1994, wherein about 25% of events detected at the pilot-hole sonde were also recorded with the surface network (Jost et al., 1998). The low detection rate at surface stations within KTB2000 results from differences in the event geometry of the two experiments. As will be shown subsequently, the major part of seismicity within KTB2000 is concentrated near the main hole at 5.3 km depth, less than 2 km away from the pilot-hole sonde, but more than 5 km away from the noisier surface stations. Small events can be easily detected at the pilot-hole sonde, but they are undetectable at the surface. Figure 4 shows t_s-t_p times as a function of P-onset time for all 2799 injection-induced events detected at the pilot-hole sonde. These travel-time differences are a measure of the temporal evolution of the (scalar) source-receiver distance. During the entire experiment, seismicity appears to concentrate at several distinct clusterings of t_s-t_p times, which appear as horizontal line structures in Fig. 4. Most pronounced is a broad line at $t_s-t_p \sim 0.2$ sec, which translates to hypocentral distances of ~ 1.6 km. Other lines appear at $t_s-t_p \sim 0.06$ sec, $t_s-t_p \sim 0.34$ sec, $t_s-t_p \sim 0.52$ sec and at $t_p - t_s \sim 0.61$ sec which is the expected time for events located near the open-

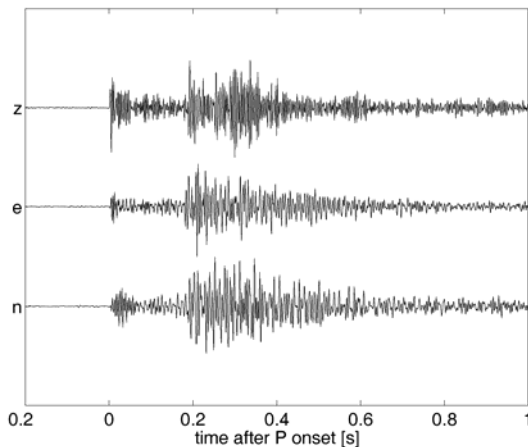


Figure 3: Unfiltered raw waveform example of a weak event recorded at the pilot-hole sonde.

t_p values seems to be slightly larger. The narrow line at $t_s-t_p \sim 0.06$ sec suggests that most of these events occur nearly at the same location. Here, seismicity starts after 19 days of fluid injection and thereafter nearly immediately responds to changes in flow rate. Hardly any event occurs during shut-in phases or after the end of injection. On the other hand, high flow rate and well-head pressure toward the end of the experiment correlate with a broadening of the line structure, indicating a growth of the seismic active volume. Not shown in Fig. 4 are two events with t_s-t_p times of 1.27 sec and 1.77 sec at days 295 and 303, respectively, immediately after termination of the fluid injection. It is not clear whether these are injection-induced events. Seismicity with hypocentral distances of 10-14 km, such as for these events, may be

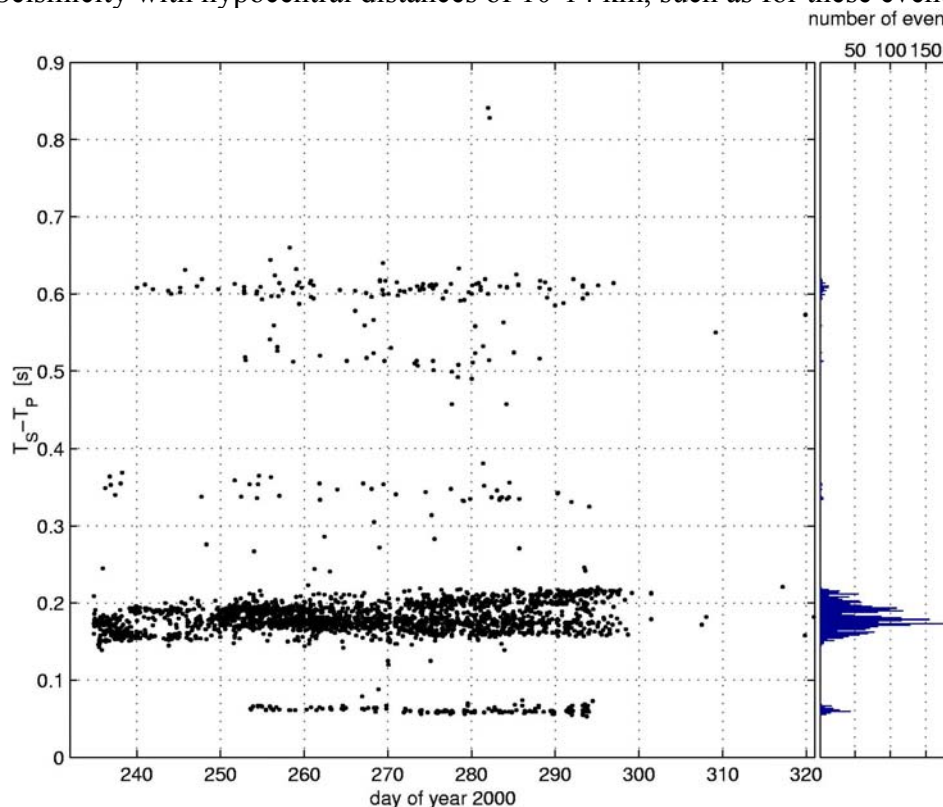


Figure 4: Time differences between S and P onsets for all injection-induced events recorded at the pilot-hole sonde plotted against P-onset time. Two events with $t_s-t_p = 1.27$ sec and $t_s-t_p = 1.77$ sec at days 295 and 303, respectively, were skipped for scaling reasons.

deemed unlikely to be injection induced, particularly when no events (except for two events with $t_s-t_p \sim 0.84$) fill the gap in between. We note, however, that hypocentral distances for the more-distant events ($t_s-t_p > 0.8$) systematically increase with time, consistent with a growing volume of elevated pore pressures. In principle, hypocenter locations can be obtained by combining t_s-t_p times with the P-wave polarization. This, however, would require the exact knowledge of the orientation of the downhole seismometer. Using calibration shots, we were able to determine the instrument orientation (which changed after the instrument was replaced on day 270) with a precision of 10-15° only. This uncertainty would bias hypocenter locations by several hundred meters up to kilometres for the more-distant events. We therefore restrict ourselves to determine hypocenter locations only when recordings of the surface network are available in addition to the borehole sonde data.

2.5. Hypocenter Locations from Surface-Station Recordings

2.5.1. Data Processing

Compared with the pilot-hole sonde, the magnitude threshold is considerably higher for event detection at the surface network. Visual inspection of the strongest events by an experienced analyst provided a subset of 261 events with good SNR at surface stations. For these events, P- and S-onset times were determined manually and assigned weights (ranging from 1 to 4) according to their clarity. The weakest onsets (which normally are assigned the lowest weight) for which phase onsets were read exhibit a SNR of ~ 3 . An average pick precision is estimated to be one sample (=5 msec). Section plots of all surface-station seismograms arranged according to their distance from a synthetic hypocenter at the borehole at 5.4 km depth helped to distinguish between true phase onsets and seismogram contamination, such as so-called bursts or phases of non-KTB events. Furthermore, consistency of picked phase onsets was checked using Wadati diagrams (Wadati, 1933), wherein for each event t_s-t_p determined at surface stations is plotted against t_p . Assuming a constant ratio of P- to S-wave velocity (v_p/v_s ratio), the data of all surface stations should fall on a line. Thus, the quality of the line fit is a measure of the consistency of the data set. We inspected any obvious outliers from the line fit by revisiting and, if necessary, repicking the corresponding seismograms. Data that remained inconsistent during this process because of wrong phase association or, in a few cases, instrument clock drift (caused by receiver problems of the GPS module) were removed. Figure 5 shows typical Wadati diagrams for a strong (a) and a weak (b) event after data revision and demonstrates the high consistency of the data set. From the slope of the straight-line fit, we find a mean v_p/v_s ratio of 1.74 ± 0.09 for the entire data set. Figure 5c also shows the Wadati diagram for the most-distant event. Although data scattering is slightly larger, we note that the line fit is still reasonable ($v_p/v_s = 1.79 \pm 0.1$), and the phase readings are well constrained.

2.5.2. Location Technique

The choice of an optimum location algorithm is crucial for analyzing this data set. One family of location methods is related to a linearized inversion known as Geiger's method (Geiger, 1910). Other techniques are based on relative travel-time differences that can be determined with high precision by waveform cross correlations (e.g., Poupinet et al., 1984; Fremont and Malone, 1987; Deichmann and Garcia Fernandez, 1992; Dodge et al., 1995; Shearer, 1997; Rowe et al., 2002). With use of an already existent well-constrained hypocenter (master event), some of these techniques locate nearby events with similar waveforms relative to the

master event. A main drawback of this approach comes from potential mislocation of the master event, which biases all subsequent hypocenter locations. We experimented with a master-event technique but decided to use an absolute hypocenter-location technique in which results can be compared directly with structural information obtained by in situ logging. In addition to the classic Geiger approach, we incorporated statistical criteria to remove inconsistent data (i.e. mispicked phase onsets) from the event catalog. Jackknife statistics (e.g. Shao and Tu, 1995) reveal the dependence of hypocenter-location results on each individual datum, are used to eliminate inconsistent data, and finally are used to estimate location errors due to insufficient station coverage (e.g. Iversen and Lees, 1996; Lees, 1998). Our location technique is explained as follows: Consider a given hypocenter at location (x_0, y_0, z_0) with source time t_0 . Theoretical phase-onset times T_i (t_0, x_0, y_0, z_0) at station i can be calculated from the known velocity model (which we derived from the calibration shots).

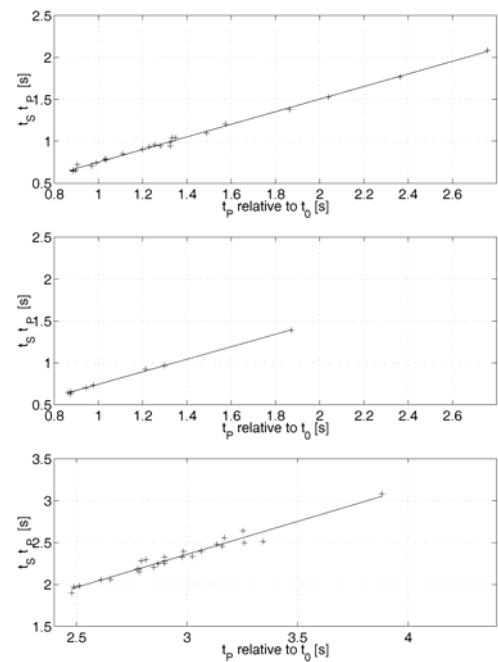


Figure 5: Example of $t_s - t_p$ plotted against t_p (Wadati diagram) for a strong (a) and a weak (b) event within the 5.3 km depth level. The slope of the line fit indicates $v_p/v_s = 1.75 \pm 0.02$ for both events. Bottom panel (c) shows Wadati diagram for a distant event with $t_s - t_p = 1.77$ sec at the pilot-hole sonde, corresponding to a source depth of 15 km.

Let

$$\Delta t_i = w_i [t_i^{\text{obs}} - T_i(t_0, x_0, y_0, z_0)] \quad (1)$$

denote the weighted difference between observed and theoretical onset times; then, a first-order Taylor series expansion leads to (e.g., Lienert et al., 1986)

$$\vec{\Delta t} = \mathbf{J} \vec{\Delta m} \quad (2)$$

where

Δm denotes model differences and Δt data differences, respectively.

Here

$$\mathbf{J} = \begin{bmatrix} w_1 & w_1 \frac{\delta T_1}{\delta x} & w_1 \frac{\delta T_1}{\delta y} & w_1 \frac{\delta T_1}{\delta z} \\ \vdots & \vdots & \vdots & \vdots \\ w_n & w_n \frac{\delta T_n}{\delta x} & w_n \frac{\delta T_n}{\delta y} & w_n \frac{\delta T_n}{\delta z} \end{bmatrix}. \quad (3)$$

and

$$\vec{\Delta m} = (\Delta t_0, \Delta x_0, \Delta y_0, \Delta z_0), \quad (4)$$

with normalized weights such that

$\sum_{i=1}^n w_i = 1$, where n is the number of phase readings. The classic Geiger location procedure (Geiger, 1910) is defined by solving equation (2) and iteratively updating a start model (t_0, x_0, y_0, z_0) by the model difference vector Δm .

2.5.3. Confidence Estimates

For a given hypocenter location (t_f, x_f, y_f, z_f) , the data variance is obtained by

$$\sigma_u^2 = \frac{1}{n - 4} \vec{\Delta t}^T \vec{\Delta t} \quad (5)$$

(e.g. Iversen and Lees, 1996), using the data difference vector (equation 1) for the final hypocenter location. Standard errors of the model vector can be estimated by projecting the data variance into the model space

$$\vec{\sigma}_m = \sigma_d \sqrt{\text{diag}\{(\mathbf{J}^T \mathbf{J})^{-1}\}} \quad (6)$$

2.5.4. Statistical Jackknife Test

Our data processing has provided a consistency check (Wadati diagrams), on the basis of which outliers were removed from the data set. However, this check only works when both P and S onsets were read and does not apply when only one phase (either P or S) could be

identified. In this case, a Jackknife test (e.g., Shao and Tu, 1995) was performed to estimate the influence of each datum (phase reading) on the hypocenter location. The Jackknife test is a statistical method to estimate the bias of an estimator by systematically switching off one datum at a time and recomputing the estimator by using the rest of the data. Let λ denote the hypocenter estimate of an event that was located using a data set with n observations (phase onsets). Further-more, let $\lambda(i)$ denote the hypocenter estimate of the same event by using all observations except for the i -th datum. Using the weighting scheme of equation (1), the bias of the i -th datum is given by (Iversen and Lees, 1996)

$$b_i = n(1 - w_i)(\hat{\lambda} - \hat{\lambda}_{(i)}). \quad (7)$$

This data bias describes the dependence of the solution (hypocenter location) on each datum (phase reading) and can be used as a proxy to find inconsistent phase readings. Within iteration, a threshold test on b_i is applied. At each iteration step, the datum with the strongest bias is removed, and equation (3) is solved with the remaining data until a reduced data set is obtained for which the bias of each datum is below the threshold. The resulting hypocenter location, based on the reduced data set, displays little dependency on each individual datum; that is, hypocenter locations remain approximately constant if further data are removed from the reduced data set.

2.5.5. Location Results

We applied the location technique combined with Jackknife testing to all 261 events recorded at surface network stations. Mean velocities of $v_p=6.08$ km/sec for wave paths to the inner surface stations and $v_p=6.28$ and $v_s=3.63$ km/sec to the pilot-hole sonde were derived from the calibration shots. Because of low SNR, v_s could not be calibrated at surface stations, and we assumed $v_s=(v_p/3)^{1/2}$. In addition, we determined station residuals based on initial hypocenter locations for uncalibrated surface stations and corrected phase onsets at these stations. Because of excellent SNR, we used larger weights for pilot-hole sonde data than we used for surface-station data. We chose weighting factors such that full-weighted P and S picks at the pilot-hole sonde count 10 and 7 times as much, respectively, as full-weighted P and S picks at a surface station. We rejected any location where fewer than five stations passed the Jackknife test. A total of 237 hypocenters that were constrained by an average of 10 P-and 13 S-phase readings remained in our catalog. Figure 6 shows these locations as a function of origin time in different projections.

Seismicity at 5-6 km depth: At the depth level between 5 and 6 km (Fig. 6b-d), where most of the seismicity is concentrated, systematic but complex structures of the spatiotemporal hypocenter distribution evolved. These structures extend several hundred meters and sometimes indicate steeply dipping planes, which appear as lines in Figure 6b,c. For this depth level, average location errors according to equation (6) are 59 m, 48 m, and 23 m for eastern, northern, and vertical directions, respectively. From Jackknife testing, an additional error owing to insufficient station coverage (Lees, 1998) is estimated as 76 m, 58 m, and 14 m, resulting in an overall absolute error (estimated as the quadrature sum of both errors) of 96 m, 75 m, and 27 m for eastern, northern, and vertical directions, respectively. Structures in hypocenter distribution have a much larger extension than location errors, indicating that variability in hypocenter locations does not result entirely from location errors but rather indicates an actual trend of the seismic cloud. The clustering of similar colours in Figure 6b,c indicates that the region of seismic activity changed during the experiment, that is, different crustal volumes were active at different stages of the fluid injection. Seismicity started near the borehole at depths of -5.15 km and -5.32 km (dark blue), thereafter focused between -5.3

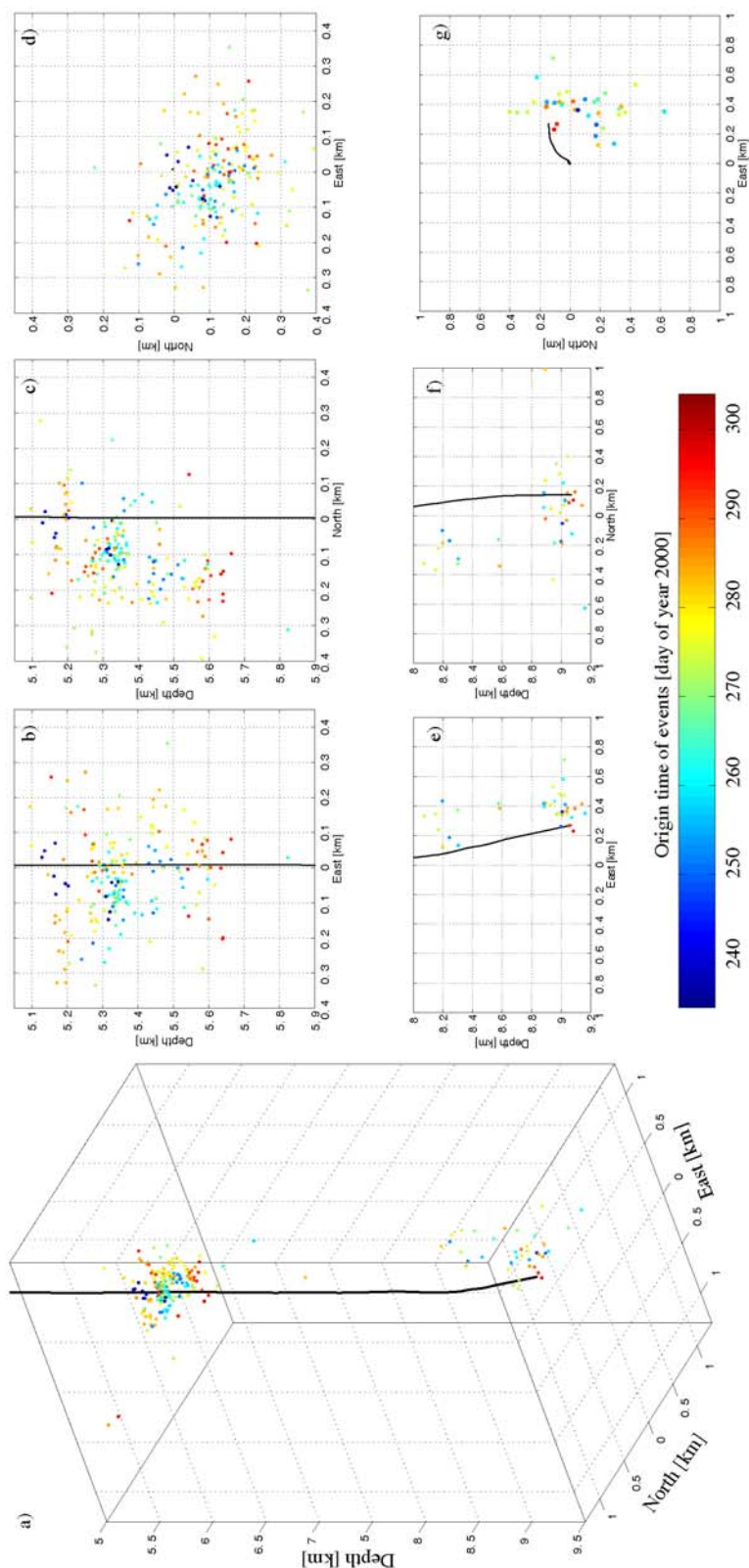


Figure 6: Absolute hypocenter locations of 237 strongest events in perspective view (a). Colour coding denotes origin time. Coordinates are given with respect to the the top of the main hole. Solid line denotes the main-hole trajectory. Enlarged views (b-d) of east depth section, north depth section, and map projection of seismicity between 5 and 6 km depth. Same view angles (e-g) for seismicity between 8 and 9.2 km depth.

and -5.4 km (light blue), and exhibited more scattered structure with larger distances to the borehole at later stages (yellow). Toward the end of the experiment (red), activity was concentrated around 5.6 km depth and above 5.3 km depth (Fig. 6b,c), where it formed a northward-dipping line in Figure 6c. The spatial separation of these two regions causes the observed trend in t_s-t_p , times monitored at the pilot-hole sonde (Fig. 4), where the level of $t_s-t_p \sim 0.2$ sec splits into two branches toward the end of the injection experiment. As can be seen from the map view (Fig. 6d), most of the seismicity occurred south of the borehole, and the entire seismic cloud is elongated approximately southeast-northwest.

Seismicity at 8.0-9.2-km depth: For events between 8.0 and 9.2 km depth (Fig. 6e-g), spatio-temporal structures are less clear. This might result from a smaller number of events and from larger location uncertainties at this depth level. Average location errors (including errors for insufficient station coverage) for these events are estimated to be 149 m, 200 m, and 37 m for eastern, northern, and vertical directions, respectively. Figure 6e,f indicates that fluid injection took place at least at two intervals, near 8.2 km depth and at the open-hole section at 9 km depth. In both intervals, seismic activity started approximately at the same time (blue colours). In contrast to observations between 5 and 6 km depth (Fig. 6d), the map projection of the seismic cloud (Fig. 6g) exhibits a bowed, approximately north-south extending structure. All hypocenters are located east of the borehole, and only two events occurred in the immediate vicinity of the injection interval at a late stage of the experiment (red dots).

Distant Events: Figure 7 focuses on hypocenters of three distant events, the deepest of which (labelled 1) occurred at 15 km depth. For these events, location errors are larger owing to uncertainties in the velocity model, which is not calibrated for these wave paths. However, hypocenter locations are still reasonably well constrained (<400 m in lateral and <200 m in vertical direction), which is also demonstrated in the Wadati diagram of the deepest event (Fig. 5b). Although it is not clear whether these events are injection induced or belong to natural background seismicity, we note that their hypocentral distance from the borehole increases with time.

Comparison with 1994: To compare our location results with those of KTB1994, we reprocessed the 1994 data and applied the same absolute hypocenter-location procedure to these data, including the data processing steps of (visually) reading phase onsets and removing outliers by inspection of Wadati diagrams and application of the Jackknife test. We used mean velocities as determined from the calibration shots of KTB2000 and incorporated station residuals for un-calibrated surface stations. Figure 8 shows the resulting hypocenter distribution. Seismicity is concentrated near the open-hole section and in a second cluster around the borehole at 8.5 km depth, corresponding to a second injection interval. No events

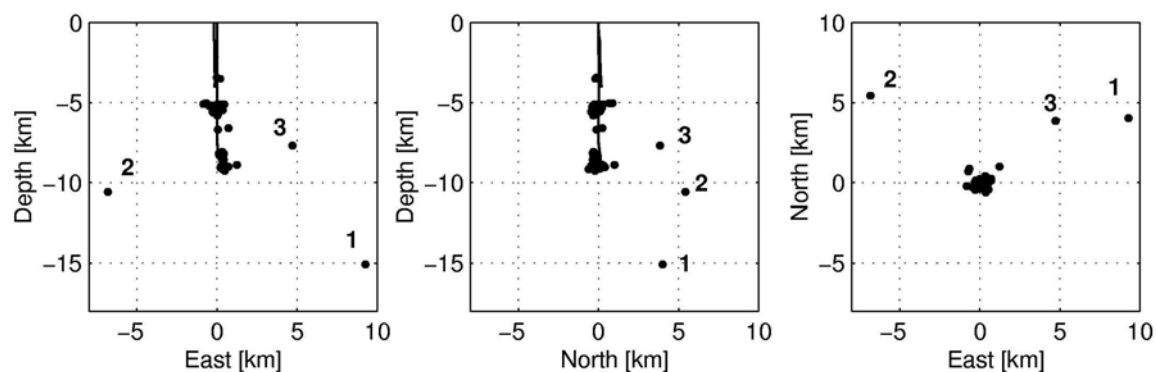


Figure 7: Absolute hypocenter locations of distant events (labeled 1-3). Coordinates are given with respect to the top of the main hole. Solid line denotes the main hole trajectory. Distant events occurred at days 303 (1), 295 (2), and 281 (3).

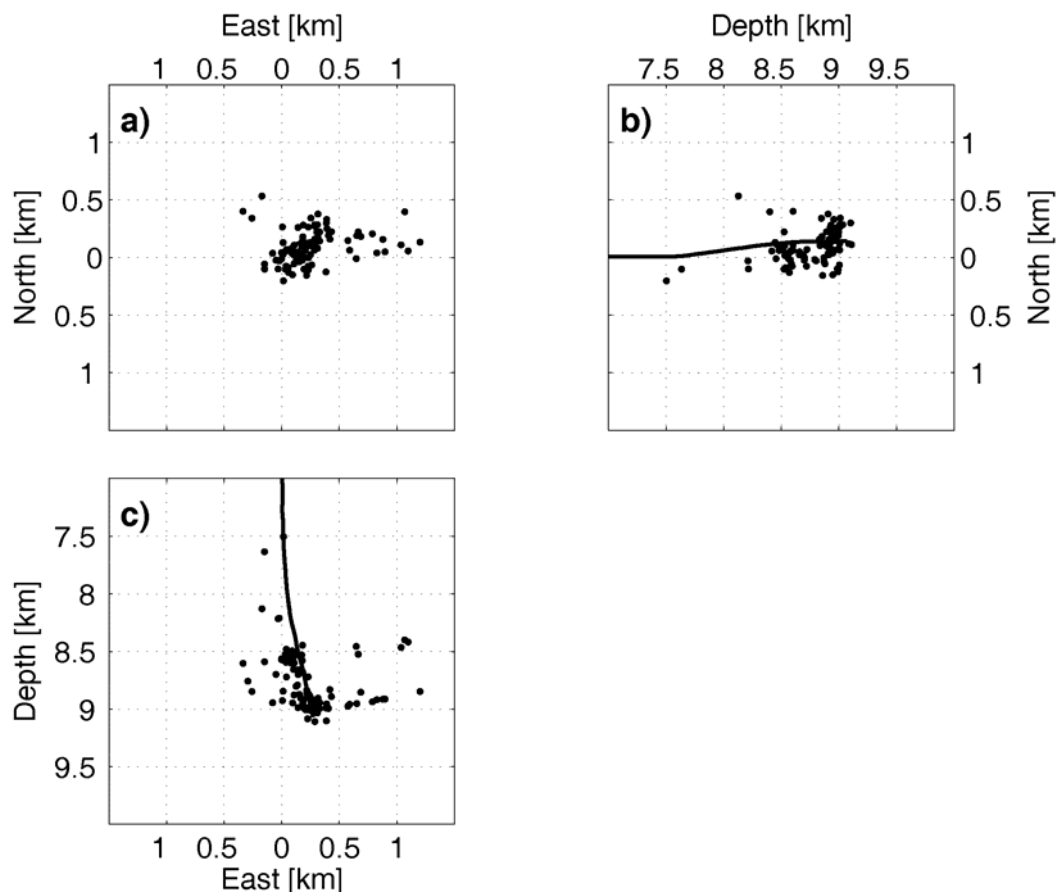


Figure 8: Absolute hypocenter locations for injection-induced events within the 1994 experiment in (a) map view (b) north depth and (c) east-depth section views. Coordinates are given with respect to the top of the main hole.

occurred beneath the bottom of the open-hole section at 9.1 km depth, consistent with master-event location results obtained by Jost et al. (1998; their Figure 4). However, our results differ significantly in lateral hypocenter distribution from those of Jost et al. (1998). Our absolute hypocenters are distributed around the borehole (Fig. 8), whereas their locations relative to a master event showed a systematic offset ~ 200 m southward from the borehole. This discrepancy results from location errors of the master event, which bias all subsequent relative locations. Our average absolute location errors (including errors due to insufficient station coverage) of 147 m, 127 m, and 26 m for eastern, northern, and vertical directions, respectively, are smaller than relative location errors of ~ 200 m and ~ 100 m in horizontal and vertical directions stated in Jost et al. (1998), although the relative location estimates did not include uncertainty estimates of the station-network influence. The larger relative location errors result from the retention of inconsistent data by Jost et al. (1998), whereas our removal of these points reduced the single-event location error estimates. In addition, the velocity model could not be calibrated during KTB1994. These differences notwithstanding, results of the absolute hypocenter technique and master-event technique agree within the error bounds stated in Jost et al. (1998). In map view (Fig. 8a), the majority of hypocenters is grouped around the bottom of the main hole, forming an approximately southwest-northeast-elongated cloud. Compared with Figure 6g, few events of KTB2000 seem to be located in the region where seismic activity occurred in KTB1994. This becomes most evident in Figure 9, in which hypocenters are displayed for both experiments. To avoid possible misinterpretation from hypocenter distribution at different depth levels, only events with hypocentral depths between 8.8 km and 9.1 km are considered in Figure 9. For these, hypocenters of KTB2000

(open circles) are located primarily at the outer rim of the KTB 1994 cloud (filled circles). KTB2000 hypocenters are systematically shifted to the east of the cloud formed by the hypocenters of KTB1994. A possible explanation for this offset is given by shear-stress relaxation during KTB 1994 (this was previously discussed for observations at Soultz-sous-Forets) (Phillips, 2000; Rowe et al., 2002). During fluid injection, effective normal stresses are reduced in proportion to the pore fluid-pressure increase. Seismic failure or frictional sliding occurs on any fracture plane where the ratio of shear to effective normal stress exceeds a critical value (the coefficient of friction). During fracturing, shear stress is lowered, and the ratio of shear to effective normal stress drops below the critical value. To a certain extent, the stress on the fracture plane is released, and the same fracture plane will not fail until either further pore-pressure increase or shear-stress loading causes over-critical conditions again. Consequently, if no shear stress reloading occurs, fractures that already failed at a given pore pressure P_{p1} will not fail at later times so long as $P_{p2} \leq P_{p1}$, (note that $P_{p2} > P_{p1}$ does not necessarily result in an over-critical state, which depends on the shear stress consumed during first failure). For the situation at KTB, our results suggest that the stress in the immediate vicinity of the injection interval at 9 km depth (as outlined by filled circles in Fig. 9) was released during KTB1994, and pore pressures in KTB2000 remained below those of KTB1994. During KTB2000, the experiment duration was greater and injection rates were lower, resulting in greater fluid-migration distances at comparably low overpressures. Thus, pore-pressure increase during the KTB2000 experiment extended over a larger volume than that of KTB1994, producing overcritical conditions only at the outer rim of the relaxed volume, whereas conditions remained subcritical within the relaxed volume. This is consistent with the use of water instead of heavy brine in KTB2000, resulting in lower overpressures at 9 km depth. Furthermore, the pressure supplied at the well head during KTB2000 was reduced via various leaks. Our interpretation is further supported by the fact that the only two events located near the injection interval occurred at the final stage of KTB2000 (compare Fig. 6g and Fig. 9), indicating that pore pressures approached values comparable to those reached during KTB 1994.

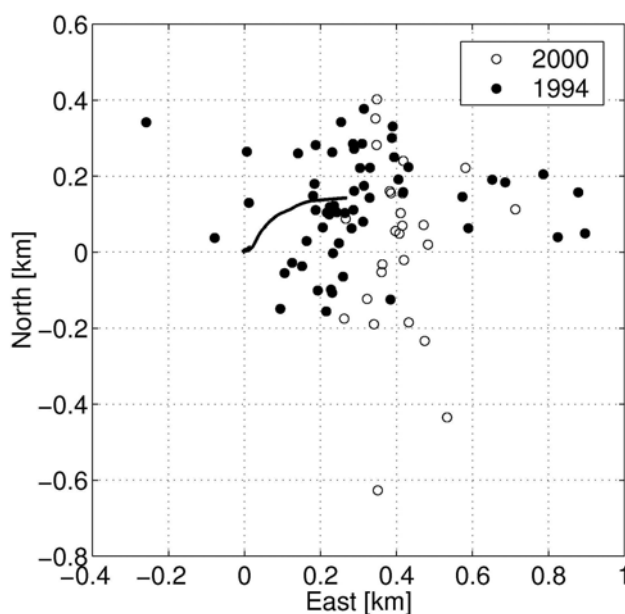


Figure 9: Absolute hypocenter locations for induced events near the open-hole section (hypocentral depth >8.8 km) during KTB2000 (open circles) and KTB 1994 (filled circles) experiments in map view. Coordinates are given with respect to the top of the main hole. Nearly all events of KTB2000 occurred at the edge of the volume, which was seismically active during KTB 1994.

2.6. Discussion and Conclusions

2.6.1. Injection Experiments and Status of the Borehole

We have described a 60-day fluid-injection experiment undertaken in 2000 at the KTB drilling hole and have presented absolute hypocenter locations of induced seismicity, which

we compared with hypocenter locations of a previous injection experiment conducted in 1994. The difference between the two experiments is that KTB2000 lasted 30 times longer than KTB 1994, while the injected volume exceeded the volume of KTB1994 by a factor of 20. In addition, fluid injection during KTB2000 occurred through various leaks in the casing of the borehole, whereas injection in 1994 directly targeted the open-hole section at the bottom of the borehole. However, hypocenter distribution of KTB1994 was not concentrated only near the bottom of the borehole but also formed a second cluster at 8.5 km depth (Fig. 8b,c), indicating a second injection interval, most likely a leak in the casing. During KTB1994, a packer was fixed at 8.5 km depth (Engeser, 1996), such that only the lower 600 m of the borehole was pressurized by the injected brine. Correlation between the packer position and the upper bound of the seismic cloud indicates that a leak in the casing is the most plausible explanation for the shallower activity. A few events of KTB1994 were even shallower (Fig. 8b). For events located at 8.2 km depth, we note that seismicity during KTB2000 (Fig. 6e,f) also occurred at this depth level. This indicates another leak at 8.2 km depth, and we conclude that the lower part of the borehole may not have been entirely sealed by the packer used in KTB1994. After the end of the injection experiment in 2000, several logging tests were undertaken to confirm leaks in the borehole casing. Flow log data obtained for the interval between 5.15 km and 5.65 km clearly indicate two distinct leaks (at 5.35 km and 5.45 km depth), where >75% (possibly more) of the injected fluid entered the surrounding rock. These prominent leaks are also visible in a temperature profile determined by the GeoForschungsZentrum Potsdam (J. Kück, personal comm.), which shows an additional anomaly at 3.25 km depth, consistent with t_s-t_p times monitored at the pilot-hole sonde (Fig. 4) and hypocenter locations. Potential leaks at greater depth (at ~6.8 km, as indicated in Fig. 4 and at 8.2 km depth as discussed previously) could not be confirmed by logging data. Only the temperature profile extended to 7 km depth but did not exhibit an anomaly at 6.8 km; however, a small leak may not be detected by temperature logging.

2.6.2. Hypocenter Location: Requirements and Technique

The location technique we present in this article is based on the classic Geiger approach (Geiger, 1910), combined with statistical criteria to remove inconsistent data from the event catalog. This approach is especially suitable for location problems wherein phase onsets are recorded by a large number of nearby receivers such that hypocenter solutions remain well constrained, even when many phase-arrival times are discarded. If these requirements are met, removing inconsistent data results in a notable reduction of location uncertainties. For KTB2000 data, confidence estimates were reduced by a factor greater than 3 compared with initial solutions obtained without the data selection criteria. The same criteria can also be applied to other location approaches. We combined a master-event technique with the same statistical selection criteria and compared relative with absolute hypocenter-location results. Differences in hypocenter locations are mostly less than 80 m in the horizontal and less than 20 m in the vertical direction. Although location uncertainties are dramatically reduced by incorporating data selection criteria, they are not notably smaller than confidence limits obtained for absolute hypocenter locations.

2.6.3. What Do We Learn from the Shape of Seismic Clouds?

The interpretation of the spatiotemporal hypocenter distribution of KTB2000 data is especially complicated because of several, sometimes closely located, injection intervals. This makes it difficult to unambiguously relate hypocenters to a certain injection point and thus complicates conclusive statements concerning the relation between fluid-transport characteristics and hypocenter distribution. In the depth interval between 5 and 6 km, cross-

sectional views indicate several linear and planar structures in spatial hypocenter distribution (Fig. 6b,c). Some of these dip steeply to the north-east, in good agreement with the trend of major mapped faults near KTB (Harjes et al., 1997; their figure 4 and plates 2 and 3). Other prominent structures in hypocenter distribution are nearly subhorizontal (e.g., events at 5.2 km depth) and do not correlate with major reflectors seen in seismic profiles (Harjes et al., 1997). It is possible, however, that minor faults not resolved in seismic profiles are illuminated by induced seismicity. An intriguing feature of the spatiotemporal distribution of induced seismicity at the KTB is that different crustal volumes were seismically active at different times and were relaxed for given overpressures at later times. In material sciences, such relaxation phenomena are known as the "Kaiser effect" (Kaiser, 1950) and are also used to characterize the state of stress acting in a material (e.g., Wang et al., 2000). Originally, the Kaiser effect was related to acoustic emissions observed during laboratory experiments on deformation. However, the same physical principles may also apply to microearthquake mechanics in reservoir geophysics. When interpreting the distribution of injection-induced hypocenters, a fundamental question is this: To what extent are microearthquake locations related to zones of significant fluid flow? It is commonly accepted that injection of fluid induces microseismic activity because of the related increase in pore pressure (Cornet, 2000). However, the relationship between zones of significant flow and zones of pore pressure increase is not yet clear. Several approaches have been suggested to analyze systematic structures within hypocenter distributions (e.g., Fehler et al., 1987; Jones and Stewart, 1997; Nicholson et al., 2000) and to relate these to lithological or fracture-system characteristics. Another approach assumes that the growth of the seismic cloud can be used to determine crustal permeabilities (Shapiro et al., 1997, 1999; Shapiro, 2000; Tadokoro et al., 2000), but the underlying assumptions on material homogeneity have been criticized by Cornet (2000), who emphasized the role of fracture distribution and hydromechanical coupling. During KTB2000, we note that there has been a continuous increase in fluid level in the pilot hole, reaching a maximum value of -4 m at the end of the experiment. Most likely, this increase was caused by fluid injected at 5.2-5.6 km depth that migrated away from the injection point. However, hypocenters (Fig. 6a) do not exhibit connected structures between injection point and pilot hole. We therefore conclude that zones of significant fluid flow during KTB2000 remained undetected by seismic activity.

2.6.4. Deep Events

Does the KTB hole penetrate into the brittle-ductile transition zone? This was one of the key questions that motivated this long-term injection experiment. From KTB2000, several constraints on rheological behaviour can be gleaned from hypocenter distribution. First, hypocenter distribution near the open-hole section (Fig. 6e,f) is limited in depth, with only two events occurring slightly deeper than the bottom of the borehole. This is consistent with observations during KTB1994 (Fig. 8) and might indicate changes in mechanical rheological properties below 9 km depth. Compared with seismicity at 5 to 6 km depth (Fig. 6b,c), for which the seismic cloud also grows downward, the extension of hypocenter distribution at 9.1 km depth is primarily horizontal and in an upward direction. Two events at hypocentral depths of 10.6 km and 15.1 km (labelled 1 and 2 in Fig. 7), however, demonstrate that brittle failure can also occur at greater depths in this region. Hypocenters for these events are well constrained, and we can exclude the possibility of severe location errors. As discussed before, we can only speculate whether these events belong to the natural background seismicity or are related to the injection experiment. In the latter case, fluid migration during KTB2000 would need to have taken place over considerable distances without inducing microearthquakes. This would require highly permeable fracture systems to enable fluid migration at comparatively low overpressures. Observations of hydrostatic pressure at the bottom of the borehole

(Huenges et al., 1997) indicate the existence of such highly permeable fracture systems for the upper 9.1 km of the local crust. If fracture systems remain highly permeable to greater depths, the events at greater distances may have been caused by KTB2000 injection and might reflect local shear stress concentrations and/or material changes.

2.7. Acknowledgments

We wish to thank the KTB engineers and scientists who provided invaluable assistance in carrying out the injection experiment in 2000, especially J. Kück and L. Wohlgemuth, as well as the RUB field team for installing and maintaining the temporary seismic network. Fritz Rummel and the staff of MESY GmbH are thanked for operating the hydraulic equipment during the experiment and Schlumberger for performing the calibration shots in the borehole. The GFZ instrument pool supplied the portable seismic data-acquisition systems. We thank Mike Jost for discussion and comments, which helped to improve the initial manuscript. We are grateful to Charlotte Rowe for a detailed and constructive review and for comments by Peter Shearer and an anonymous reviewer. DFG provided financial support for this experiment within the SFB 526 collaborative research program "Rheology of the Earth: From Upper Crust to Subduction Zone.

2.8. References

- Cornet, F. (2000). Comment on "Large-scale in situ permeability tensor of rocks from induced microseismicity" by S. Shapiro, P. Audigane, and J.-J. Royer, *Geophys. J. Int.* **140**, 465-469.
- Dahlheim, H.-A., H. Gebrande, E. Schmedes, and H. Soffel (1997). Seismicity and stress field in the vicinity of the KTB location, *J. Geophys. Res.* **102**, 18,493-18,506.
- Deichmann, N., and M. Garcia-Fernandez (1992). Rupture geometry from high-precision relative hypocentre locations of microearthquake clusters, *Geophys. J. Int.* **110**, 501-517.
- Dodge, D. A., G. C. Beroza, and W. L. Ellsworth (1995). Foreshock sequence of the 1992 Landers, California, earthquake and its implications for earthquake nucleation, *J. Geophys. Res.* **100**, no. B7, 9865- 9880.
- Dresen, G., J. Duyster, B. Stöckhert, R. Wirth, and G. Zulauf (1997). Quartz dislocation microstructure between 7000 m and 9100 m depth from the Continental Deep Drilling Program KTB, *J. Geophys. Res.* **102**, no. B8, 18,445-18,452.
- Emmermann, R., and J. Lauterjung (1997). The German Continental Deep Drilling Program KTB: overview and major results, *J. Geophys. Res.* **102**, no. B8, 18,179-18,201.
- Engeser, B. (1996). Das Kontinentale Tiefbohrprogramm der Bundesrepublik Deutschland-Bohrtechnische Dokumentation. KTB report 95-3, Niedersächsisches Landesamt für Bodenforschung, Germany.
- Fehler, M., L. House, and H. Kaieda (1987). Determining planes along which earthquakes occur: method and application to earthquakes accompanying hydraulic fracturing, *J. Geophys. Res.* **92**, no. B9, 9407- 9414.
- Fremont, M.-J., and S. D. Malone (1987). High precision relative locations of earthquakes at Mount St. Helens, Washington, *J. Geophys. Res.* **92**, no. B10, 10,223-10,236.
- Geiger, L. (1910). Herdbestimmung bei Erdbeben aus den Ankunftszeiten, *K. Ges. Wiss. Gott.* **4**, 331-349.
- Haak, V., and A. G. Jones (1997). Introduction to special section: the KTB deep drill hole, *J. Geophys. Res.* **102**, no. B8, 18,175-18,177.
- Harjes, H.-P., K. Bram, H.-J. Dürbaum, H. Gebrande, G. Hirschmann, M. Janik, M. Klockner, E. Luschen, W. Rabbel, M. Simon, R. Thomas, J. Tormann, and F. Wenzel (1997). Origin and nature of crustal reflections: results from integrated seismic measurements at the KTB superdeep drilling site, *J. Geophys. Res.* **102**, no. B8, 18,267-18,288.
- Huenges, E., J. Erzinger, J. Kück, B. Engeser, and W. Kessels (1997). The permeable crust: geohydraulic properties down to 9101 m depth, *J. Geophys. Res.* **102**, no. B8, 18,255-18,265.
- Iversen, E. S., Jr., and J. M. Lees (1996). A statistical technique for validating velocity models, *Bull. Seism. Soc. Am.* **86**, no. 6, 1853-1862.
- Jones, R. H., and R. C. Stewart (1997). A method for determining significant structures in a cloud of earthquakes, *J. Geophys. Res.* **102**, no. B4, 8245-8254.

- Jost, M. L., T. Büsselberg, O. Jost, and H.-P. Harjes (1998). Source parameters of injection-induced microearthquakes at 9 km depth at the KTB deep drilling site, Germany, *Bull. Seism. Soc. Am.* **88**, no. 3, 815-832.
- Kaiser, J. (1950). Untersuchungen über das Auftreten von Geräuschen beim Zugversuch, *Ph.D. thesis*, Fak. f. Maschinenwesen, TH München, Germany (in German).
- Klinge, K., and T. Plenefisch (2001). Der Erdbebenschwarm 2000 in der Region Vogtland-NW-Bohmen, *DGG Mittlg.* **2**, 11-21.
- Lees, J. M. (1998). Multiplet analysis at Coso Geothermal, *Bull. Seism. Soc. Am.* **88**, no. 5, 1127-1243.
- Lienert, B. R., E. Berg, and L. N. Frazer (1986). HYPOCENTER: an earth-quake location method using centered, scaled, and adaptively damped least squares, *Bull. Seism. Soc. Am.* **76**, 771-783.
- Nicholson, T., M. Sambridge, and O. Gudmundsson (2000). On entropy and clustering in earthquake hypocentre distributions, *Geophys. J. Int.* **142**, 37-51.
- Niitsuma, H., R. Baria, M. Fehler, A. Green, K. Hayashi, H. Kaieda, and K. Tezuka (1998). Results and the next step of MTC project: international joint research on new mapping technology for HDR/HWR development, in *Draft Proceedings*, 4th Int. HDR Forum, Strasbourg, France.
- Pechinig, R., S. Haverkamp, J. Wohlenberg, G. Zimmermann, and H. Burkhardt (1997). Integrated log interpretation in the German Continental Deep Drilling Program: lithology, porosity, and fracture zones, *J. Geophys. Res.* **102**, no. B8, 18,363-18,390.
- Phillips, W. S. (2000). Precise microearthquake locations and fluid flow in the geothermal reservoir at Soultz-sous-Fourets, France, *Bull. Seism. Soc. Am.* **90**, no. 1, 212-228.
- Poupinet, G., W. L. Ellsworth, and J. Frechet (1984). Monitoring velocity variations in the crust using earthquake doublets: an application to the Calaveras Fault, California, *J. Geophys. Res.* **89**, no. B7, 5719-5731.
- Rowe, C. A., R. C. Aster, W. S. Phillips, R. H. Jones, B. Borchers, and M. C. Fehler (2002). Using automated, high-precision repicking to improve delineation of microseismic structures at the Soultz geothermal reservoir, *Pageoph* **159**, 536-596.
- Shao, J., and D. Tu (1995). *The Jackknife and Bootstrap*, Springer, New York/Berlin/Heidelberg.
- Shapiro, S. A. (2000). An inversion for fluid transport properties of three-dimensionally heterogeneous rocks using induced microseismicity, *Geophys. J. Int.* **143**, 931-936.
- Shapiro, S. A., P. Audigane, and J.-J. Royer (1999). Large-scale in situ permeability tensor of rocks from induced microseismicity, *Geophys. J. Int.* **137**, 207-213.
- Shapiro, S.A., E. Huenges, and G. Borm (1997). Estimating the crust permeability from fluid-injection-induced seismic emission at the KTB site, *Geophys. J. Int.* **131**, F15-F18.
- Shearer, P. (1997). Improving local earthquake locations using the L1 norm and waveform cross correlation: application to the Whittier Narrows, California, aftershock sequence, *J. Geophys. Res.* **102**, no. B4, 8269-8283.
- Tadokoro, K., M. Ando, and K. Nishigami (2000). Induced earthquakes accompanying the water injection experiment at the Nojima fault zone, Japan: seismicity and its migration. *J. Geophys. Res.* **105**, no. B3, 6089-6104.
- Wadati, K. (1933). On the travel time of earthquake waves 11, *Geophys. Mag.* **7**, 101-111.
- Wagner, G. A., D. A. Coyle, J. Duyster, F. Henjes-Kunst, A. Peterek, B. Schroder, B. Stöckhert, K. Wemmer, G. Zulauf, H. Ahrendt, R. Bischoff, E. Hejl, J. Jacobs, D. Menzel, N. Lal, P. Van Den Haute, C. Vercoutere, and B. Welzel (1997). Post-Variscan thermal and tectonic evolution of the KTB site and its surroundings, *J. Geophys. Res.* **102**, no. B8, 18,221-18,232.
- Wang, H. T., X. F. Xian, G. Z. Yin, and J. Xu (2000). A new method of determining geostresses by the acoustic emission Kaiser effect, *Int. J. Rock Mech. Min. Sci.* **37**, no. 3, 543-547.
- Zoback, M. D., and H.-P. Harjes (1997). Injection-induced earthquakes and crustal stress at 9 km depth at the KTB deep drilling site, Germany, *J. Geophys. Res.* **102**, no. B8, 18,477-18,491.

3. Mutual relationship between microseismicity and seismic reflectivity: Case study at the German Continental Deep Drilling Site (KTB).

This chapter has been published. The reference is

Rothert, E., Shapiro, S., Buske, S., Bohnhoff, M. (2003). Mutual relationship between microseismicity and seismic reflectivity: Case study at the German Continental Deep Drilling Site (KTB). *Geophys. Res. Lett.*, **30(17)**, 1893, doi:10.1029/2003GL017848.

3.1. Abstract

Two fluid injection experiments were conducted at the German Continental Deep Drilling Site (KTB) in 1994 and 2000. Microseismicity occurred at different depth intervals. Hypocenter locations were precisely localized. Here, microseismicity is analyzed in terms of its spatiotemporal evolution characteristics. An approach is applied which assumes microseismicity to be triggered by a diffusive process of pore pressure relaxation. The method yields estimates of hydraulic parameters of rocks on large spatial scales. At the KTB site the method enables us to study hydraulic diffusivity at two different depth intervals. We observe significant variations in the evolution characteristics of the seismic activity at different depths. Estimates of hydraulic diffusivity for shallower parts of the crust seem to be much smaller than for deeper regions. To understand reasons for this, we have analyzed spatial relations of hypocenter locations to the distribution of intensities of seismic reflections. Low values of hydraulic diffusivity correlate with low reflection intensities and high diffusivities with large intensities, respectively. The analysis confirms the hypothesis that the process of pore pressure relaxation along pre-existing and critically stressed natural fractures is an important triggering factor for induced microseismicity.

3.2 Introduction

The German Continental Deep Drilling site (KTB) is located in SE Germany near the western margin of the Bohemian Massif at the contact zone of the Saxothuringian and the Moldanubian (Wagner et al., 1997). Two boreholes were drilled within a crustal segment mainly composed of metabasites and gneisses. The pilot hole reached a maximum depth of 4 km whereas the main hole penetrated down to 9.1 km. During the years after drilling, extensive research was conducted at the KTB. In order to study fluid transport processes at the KTB and to obtain knowledge of crustal stresses, a short-term fluid injection experiment was carried out in 1994 (Zoback and Harjes, 1997; Jost et al., 1998). In 2000, along-term fluid-injection experiment was performed. For details of this experiment we refer to Baisch et al. (2002). During the fluid-injection experiment in 1994 about 200 m³ of KBr/KCl brine were injected at the open hole section within 24 hours. 73 surface seismometers and one 3-component borehole seismometer recorded approximately 400 microearthquakes.

All events were considered to be induced by the injected fluids (Zoback and Harjes, 1997). 94 of these earthquakes could be localized with respect to master events with a relative location accuracy of several 10's of meters (Zoback and Harjes, 1997; Jost et al., 1998). Later, the data was precisely relocated using various hypocenter location improvements (Baisch et al., 2002). The seismically active zone comprises a volume of approximately 0.35 km³ around the bottom of the borehole. Only a small increase in pore pressure (<1MPa) was sufficient to trigger the earthquakes. Surprisingly, only events above 9100 m were observed. Possible explanations were given by Zoback and Harjes (1997): either the occurrence of the brittle-ductile transition zone at this depth (impermeable half-space) and/or a decreased stress level much smaller than the rock's frictional strength. The injection experiment of 2000 was designed to enable fluid migration farther away from the injection interval and to cause pore pressure increase also at larger distances. During this long-term injection experiment, about 4000 m³ of water were injected at the wellhead of the main borehole at injection rates of 30–70 l/min (Baisch et al., 2002). A temporary seismic network consisting of a borehole seismometer in the pilot hole at 3827 m depth and a surface network of 39 stations was instal-

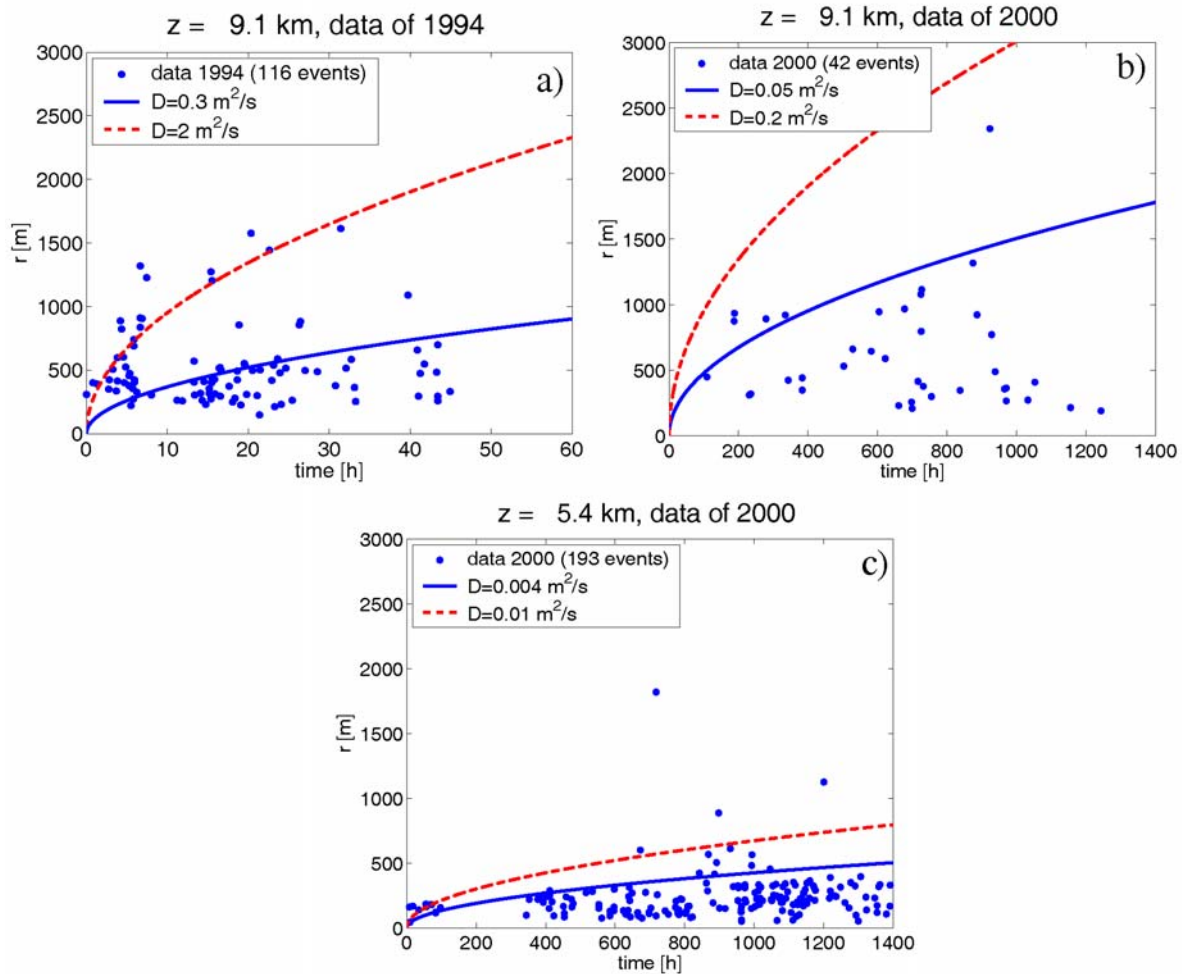


Figure 1: Estimation of scalar hydraulic diffusivity. (a) Depth domain around 9 km for data of 1994 and (b) for 2000 data. (c) Depth domain around 5.4 km. In spite of the small event number, the magnitude of hydraulic diffusivity is found to be much lower in the shallower domain compared with the deeper domain. Note also the different time scale in figures (a) and (b).

led (Baisch et al., 2002). About 2800 microseismic events were detected of which 237 were localized with an accuracy better than 100 m on average. Since preceding hydraulic tests did not indicate any leaks in the casing, it was assumed that the main borehole was hydraulically closed at least down to 6 km depth. However, due to several leakages in the borehole casing which were not known before, about 80% of the fluid was, in fact, injected between 5.35 and 5.4 km depth. Seismic events clustered at two depth levels of 5.0 – 6.0 km (81% of total seismicity) and 8.8 – 9.2 km (11% of total seismicity) (Baisch et al., 2002).

To explain the triggering mechanism of microearthquakes during fluid injection experiments, it was proposed already by Healy et al. (1968) that increasing fluid pressure along pre-existing fractures can cause a reduction of the effective normal stress and initiate the release of tectonic stress. This explanation was further confirmed by Raleigh et al. (1976). If pore pressure perturbations play a dominant role in the triggering mechanism, such a process is directly influenced by the hydraulic properties of the rocks. Therefore, the idea for developing an approach to estimate such properties on large spatial scales using induced microseismicity arises. Such a method was recently proposed. In the following we will explain the fundamentals of this approach.

3.3. The Method

The approach proposed to estimate hydraulic properties of rocks using microseismicity is called “Seismicity Based Reservoir Characterization” (SBRC). It uses a spatiotemporal analysis of fluid-injection induced microseismicity to reconstruct the tensor of hydraulic diffusivity/permeability (see Shapiro et al., 1997; 1999; 2000) and the discussion of the method in Cornet (2000). The approach assumes the following main hypothesis: Fluid injections in boreholes cause perturbations of the pore pressure in rocks. Such perturbations cause a change of the effective stress, which, if large enough, can trigger earthquakes along pre-existing, critically stressed fractures or zones of weakness.

Furthermore, the SBRC method assumes that the spatiotemporal evolution of the hydraulically-induced microseismicity is completely defined by the diffusion-like process of pore-pressure relaxation. The analysis of spatiotemporal features of the microseismicity then provides a possibility to invert for hydraulic diffusivity distributions in fluid-saturated rocks. The approach was successfully numerically verified (Rothert and Shapiro, 2003) and applied to real data several times (Shapiro et al., 2000, 2002).

In the low-frequency limit of the Biot equations of poroelasticity (Biot, 1962) the pore-pressure perturbation p can be approximately described by the differential equation of diffusion. In this equation, the hydraulic diffusivity tensor D_{ij} is the dominant parameter. The tensor of hydraulic diffusivity is directly proportional to the tensor of permeability (see Shapiro et al., 2002).

Let us assume a step-function like point source of pore pressure perturbation. Real injection experiments can be roughly approximated by such a signal in many cases. Shapiro et al. (1997) obtained the following equation describing the spatial position r of the so-called triggering front in an effective isotropic homogeneous poroelastic medium with the scalar hydraulic diffusivity D at time t :

$$r = \sqrt{4\pi Dt}. \quad (1)$$

This front is regarded as a spatial surface which separates the regions of the relaxed and unrelaxed pore pressure perturbation. Given that source location and starting time of pore pressure perturbation are known, equation (1) is able to provide scalar, homogeneous estimates of the hydraulic diffusivity. For this estimate, the scalar distance of each single microseismic event r_i is plotted versus its occurrence time t_i . By fitting the cloud of events by an envelope, the scalar estimate of hydraulic diffusivity is obtained (see Figure 1). Further developments of the method also yield estimates of tensorial properties of hydraulic diffusivity as well as spatial distributions of hydraulic parameters in 3D (Shapiro et al., 2002). In this study we concentrate on the analysis of the fluid-induced microseismicity at two different depth levels: During the 1994 injection experiment, about 100 microseismic occurred around the open hole section at 8.0-9.1 km depth. During the 2000 experiment about 50 events occurred at this depth level. Moreover, a major cloud of approximately 200 events was localized around 5.4 km depth.

3.4. Results of Hydraulic Diffusivity Estimates

The 1994 data set was analyzed in terms of the SBRC method using equation (1) by Shapiro et al. (1997). Reasonable agreement between equation (1) and the data was observed (see

Figure 1a). Estimates of hydraulic diffusivity for the depth interval at the open hole section vary between $0.3 \text{ m}^2/\text{s}$ and $2 \text{ m}^2/\text{s}$. The estimates are in good agreement with independent estimates of hydraulic diffusivity of the crystalline crust (e.g. Scholz, 1990). A tensor of hydraulic diffusivity and permeability was estimated by Rindschwentner (2001). The principal components of this tensor were found to be orientated quasi-parallel to the Franconian Lineament (FL) which continues through the upper crust as a high-reflective zone. This zone (seismic reflector SE1) was crossed by the main borehole at approximately 6.8–7.2 km depth. Moreover, the horizontal projection of the main axes of the tensor were found to be parallel to the maximum horizontal principal stress with an orientation of $\text{N}160^\circ\text{E} \pm 10^\circ$ (Brudy et al., 1997).

Equation (1) was applied to data of the 2000 experiment. For the analysis, the major fluid loss intervals obtained by flow logs (5.35 km, 9.03 km) were used as source locations. As a first result, the estimates of hydraulic diffusivity ranges for the lower depth interval of Shapiro et al. (1997) and Rindschwentner (2001) were confirmed (see Figure 1b). For the 2000 data we find values of hydraulic diffusivity of $0.05 \text{ m}^2/\text{s}$ to $0.2 \text{ m}^2/\text{s}$, which are more or less in the same order of magnitude as before. We think the slight differences are due to the small event number. In contrast, the values of hydraulic diffusivity for the shallower depth interval at 5.4 km were found to be a factor 20 to 100 smaller than at 9.1 km (Figure 1c). In spite of the small event numbers this remarkable difference in diffusivity magnitude is significant. We observe the largest diffusivity at the greatest depth. This observation seems to be in disagreement with the fact that 80% of fluid was lost at the upper borehole interval.

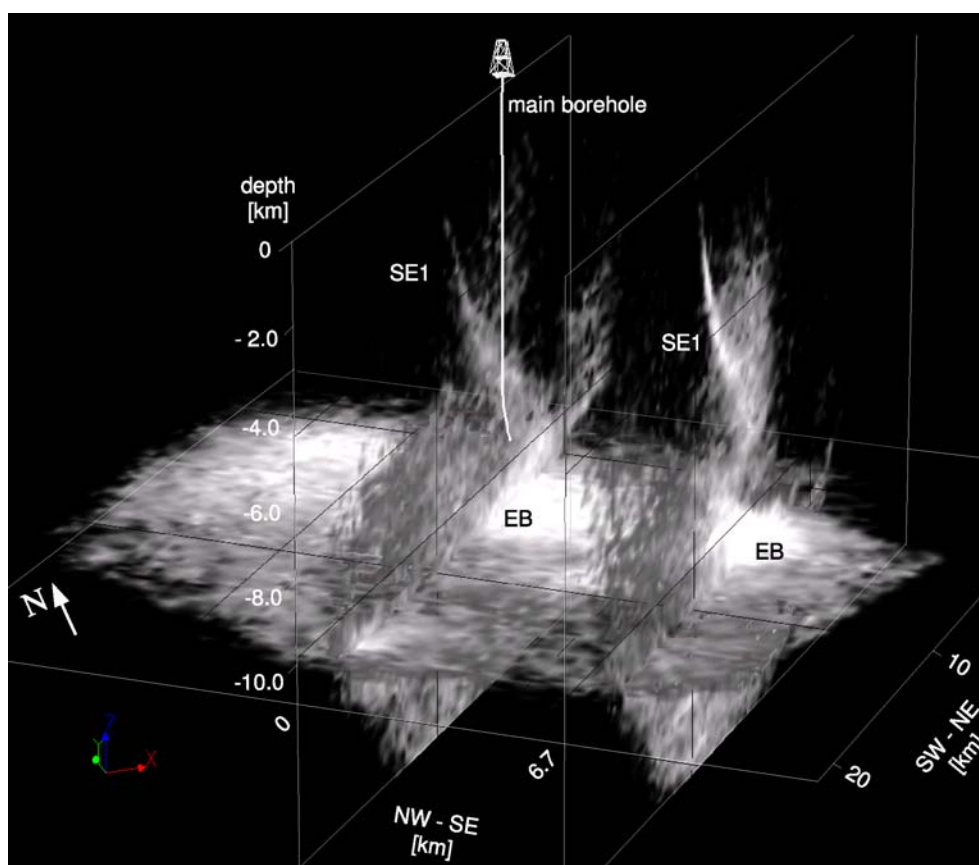


Figure 2: Depth migrated image of profile ISO89-3D. The seismic reflection intensities are shown in grayscale on three slices: one horizontal slice at 11 km depth and two vertical slices with an offset of 6.7 km. The left hand slice is passing through the location of the main borehole. Light colors correspond to large reflection intensities and darker colors with lower ones, respectively. The SE1 reflector is clearly visible as a steeply dipping event. The EB appears with strong reflectivity at a depth of 10–14 km.

This can be explained by a local hydraulic heterogeneity close to the borehole. For example, there can be several small-scale open fractures or even a hydraulic contact to the fluid behind the casing. Such features can cause a large fluid loss without producing any seismicity (Baisch et al., 2002). A local heterogeneity may lead to the effect that only a small part of these 80% was really injected into the seismically active rock volume. The hydraulic diffusivity estimations above have been obtained for the total seismic active zone. Here, we assume that these values are not affected by the properties of the small-scale features causing the large fluid loss.

3.5. 3D Seismic Reflection Intensities

Before and during the drilling phase at the KTB site, intensive seismic studies were carried out. From a 2-D seismic survey (KTB8502), a sharp northeast-dipping seismic reflector zone (SE1) was identified in seismic profiles (Simon et al., 1996; Harjes, 1997; Buske, 1999). This reflector is regarded as the continuation of the FL through the upper crust. A prestack Kirchhoff depth migration of the KTB8502 profile as well as of a 3D seismic reflection survey (ISO89-3D) was presented by Buske (1999). During the ISO89-3D experiment, an area of about 21 km x 21 km with the main borehole located at the center was investigated using reflection seismics. Figure 2 shows the relevant parts of this profile after migration (Buske, 1999). Beneath the SE1 reflector, in the depth range 12 to 14 km, a highly reflective region known as the Erbsdorf body (EB) can be observed. The 3D reflection intensities clearly show the geometry and the lateral extent of the SE1 reflector and of the EB in the subsurface.

3.6. Correlation of Microseismicity and Reflectivity

In order to clarify the results obtained by the SBRC method for data of the KTB injection experiments, we analyze the hypocenter locations in relation to the 3D distribution of seismic reflection intensities. Such a combined analysis may explain the significant differences in depth-dependent magnitudes of hydraulic diffusivity.

The hypocenter locations of microseismicity of 1994 and 2000 together with the migration results are shown in Figure 3. The prominent seismic reflector SE1 is clearly visible as well as the Erbsdorf Body. From Figure 3 it can be observed that the hypocenters of the upper microseismic cloud are sphere-shaped in a first order approximation. This can be explained by more or less isotropic hydraulic properties of rocks at this location. The entire cloud is concentrated within a relatively small region. Note that this part of the rock is characterized by a small hydraulic diffusivity. The seismic clouds which occurred around the open hole section of the main borehole in 1994 and 2000 are characterized by significantly more widespread hypocenter locations (light spheres and dark tetrahedra). The hypocenters are found to be strongly correlated with the dip of the SE1 reflector. The tensor of permeability is also shown in Figure 3. It is characterized by a strong anisotropy. Its principal axes are quasi-parallel to the SE1 fault zone.

The orientations of pre-existing fault structures and fractures affect the hydraulic diffusivity and the spatial distributions of the microseismicity clouds. The migration image (Figure 3) shows that the upper part of the rock is characterized by comparatively lower reflection intensities than the lower part. It can be clearly observed that the upper seismic cloud occurred within a depth domain that shows less reflectivity. The lower cloud occurred in a domain which is characterized by comparatively higher reflectivity. This observation is in

agreement with the previous estimates of hydraulic diffusivity at the KTB: it is smaller in the upper part of the considered rock volume and larger at its lower part.

A model which may explain this correlation is the following: a rock volume characterized by a increased density of pre-existing fractures affects the propagation of seismic waves to a larger extent compared to a region containing less fractures. Here, more seismic energy is reflected or scattered. In a pre-stack depth migration of seismic profiles these parts of the rock will be imaged as zones of increased seismic reflection intensity. Regions of the rock affecting the propagation of seismic waves to a lesser extent will be imaged as low-reflective zones. Therefore it is reasonable to conclude that shallower parts at the KTB site are characterized by less pre-existing natural fractures, correlating with smaller reflection intensities and smaller values of hydraulic diffusivity. Deeper regions show comparatively higher reflection intensities and preferential aligned seismic hypocenters, correlating with large hydraulic diffusivities and more pre-existing, oriented fractures.

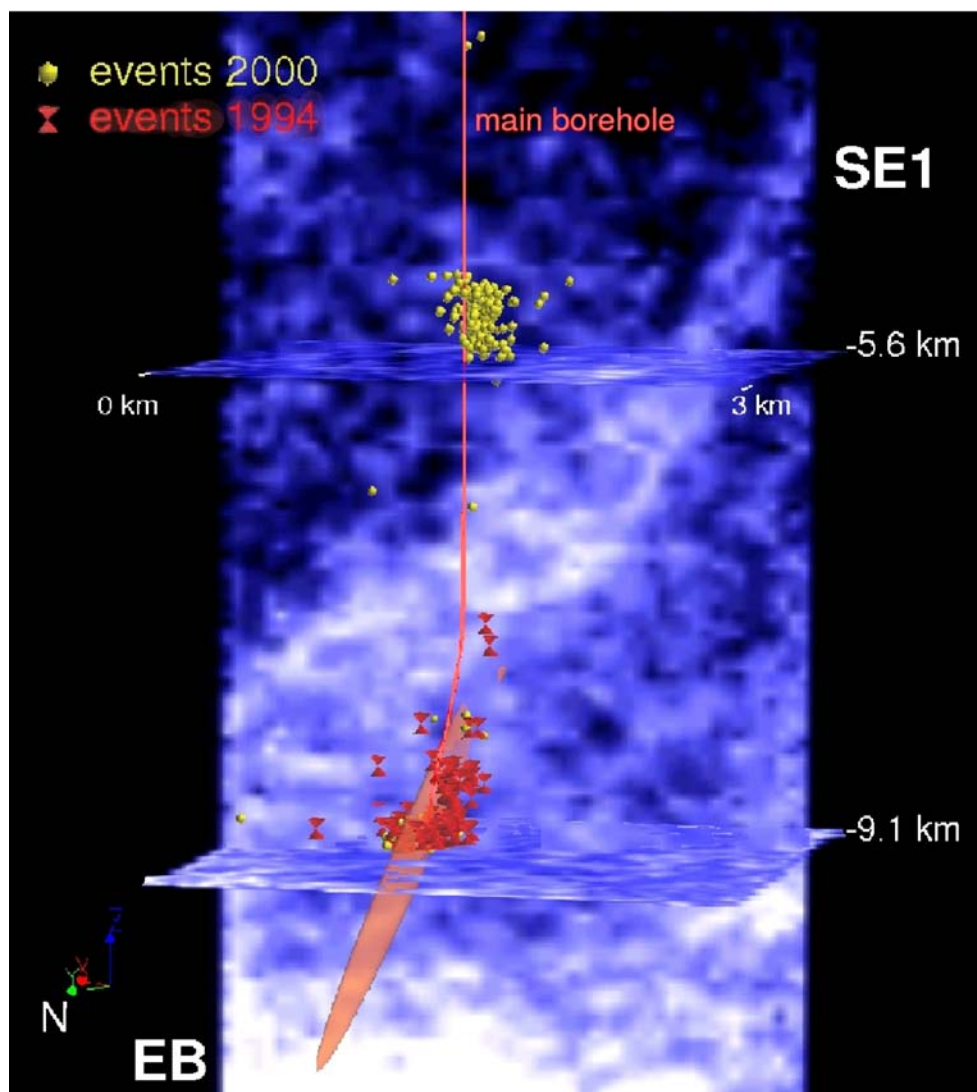


Figure 3: 3D migration together with microseismic hypocenters (1994 = dark tetrahedra, 2000 = light spheres) and the tensor of permeability estimated from the 1994 data set. The volume of rock where the sphere-shaped upper cloud occurred is characterized by comparatively low reflectivity. The lower cloud of events seems to be preferentially orientated along the directions of the high reflective (SE1) zone.

3.7. Conclusion

By analyzing data of two fluid-injection experiments at the KTB it was possible to estimate values of hydraulic diffusivities in situ for two different depth intervals at the same site. The influence of the orientations of pre-existing natural fracture systems on the triggering of microseismicity is obvious. Shallower seismic clouds show more compact shapes. We compared our results with images obtained by 3D Kirchhoff depth migration. The decreased hydraulic diffusivity is correlated with decreased reflectivity. Furthermore, the magnitude of hydraulic diffusivity at the shallower level is significantly smaller than that at the deeper level, where the hypocenters seem to be distributed along preferred orientations of natural fractures. The medium at this depth is characterized by a much higher diffusivity, correlating with larger reflectivity. We would expect this to be observable in different environments as well.

3.8. Acknowledgments

This work was supported by the Deutsche Forschungsgemeinschaft (DFG) through grants SH 55/2-1/2. Seismic data of the injection experiments was provided courtesy of H.-P. Harjes (Bochum). We acknowledge the cooperation with Stefan Baisch (Q-Con GmbH). More detailed images of the migration can be found at <http://www.userpage.fu-berlin.de/seis>. We thank two reviewers for constructive comments improving the manuscript.

3.9. References

- Baisch, S., M. Bohnhoff, L. Ceranna, Y. Tu, and H.-P. Harjes, Probing the crust to 9 km depth: Fluid injection experiments and induced seismicity at the KTB superdeep drilling hole, Germany, *Bull. Seismol. Soc. Am.*, **92**, 2369–2380, 2002.
- Biot, M. A., Mechanics of deformation and acoustic propagation in porous media, *J. Appl. Physics*, **33**, 1482–1498, 1962.
- Brudy, M., M. Zoback, K. Fuchs, F. Rummel, and J. Baumgärtner, Estimation of the complete stress tensor to 8 km depth in the KTB scientific drill holes: Implications for crustal strength, *J. Geophys. Res.*, **102**, (B8), 18,453–18,475, 1997.
- Buske, S., Three-dimensional pre-stack Kirchhoff migration of deep seismic reflection data, *Geophys. J. Int.*, **137**, 243–260, 1999.
- Cornet, F. H., Comment on “Large-scale in situ permeability tensor of rocks from induced microseismicity” by S. A., Shapiro, P. Audigane, and J.-J. Royer, *Geophys. J. Int.*, **140**, 465–469, 2000.
- Harjes, H.-P., et al., Origin and nature of crustal reflections: Results from integrated seismic measurements at the KTB superdeep drill hole, *J. Geophys. Res.*, **102**, 18,267–18,288, 1997.
- Healy, J., W. Rubey, D. Griggs, and C. Raleigh, The Denver earthquakes, *Science*, **161**, 1301–1310, 1968.
- Jost, M. L., T. Büsselberg, O. Jost, and H.-P. Harjes, Source parameters of injection-induced microearthquakes at 9 km depth at the KTB deep drilling site, *Bull. Seismol. Soc. Am.*, **88**, 815–832, 1998.
- Raleigh, C. B., J. Healy, and J. Bredehoeft, An experiment in earthquake control at Rangely, Colorado, *Science*, **191**, 1230–1237, 1976.
- Rindschwentner, J., Estimating the global permeability tensor using hydraulically induced seismicity—implementation of a new algorithm and case studies, *Master thesis*, pp. 101, Freie Universität Berlin, 2001.
- Rothert, E., and S. A. Shapiro, Microseismic monitoring of borehole fluid injections: Data modeling and inversion for hydraulic properties of rocks, *Geophysics*, **68**(2), 685–689, 2003.
- Scholz, C. H., The mechanics of earthquakes and faulting, *Cambridge University Press*, Cambridge, England, 1990.
- Shapiro, S. A., E. Huenges, and G. Borm, Estimating the crust permeability from fluid-injection induced seismic emission at the KTB site, *Geophys. J. Int.*, **131**, F15–F18, 1997.

- Shapiro, S. A., P. Audigane, and J.-J. Royer, Large-scale in situ permeability tensor of rocks from induced microseismicity, *Geophys. J. Int.*, **137**, 207–213, 1999.
- Shapiro, S. A., J.-J. Royer, and P. Audigane, Reply to comment by F. H. Cornet on ‘Large-scale in situ permeability tensor of rocks from induced microseismicity’, *Geophys. J. Int.*, **140**, 470–473, 2000.
- Shapiro, S. A., E. Rothert, V. Rath, and J. Rindschwentner, Characterization of fluid transport properties of reservoirs using induced microseismicity, *Geophysics*, **67**, 212–220, 2002.
- Simon, M., H. Gebrande, and M. Bopp, Pre-stack migration and trueamplitude processing of DEKORP near-normal incidence and wide-angle reflection measurements, *Tectonophysics*, **264**, 381–392, 1996.
- Wagner, G., et al., Post-variscan and thermal and tectonic evolution of the KTB site and its surroundings, *J. Geophys. Res.*, **102**, B8, 18,221–18,232, 1997.
- Zoback, M., and H.-P. Harjes, Injection induced earthquakes and the crustal stress at 9 km depth at the KTB deep drilling site, *J. Geophys. Res.*, **102**, 18, 477–492, 1997.

4. Fault mechanisms of fluid-injection induced seismicity and their relation to local fault structure and stress field

This chapter has been published. The reference is

Bohnhoff, M., Baisch, S., Harjes, H.-P. (2004). Fault mechanisms of induced seismicity at the superdeep German Continental Deep Drilling Program (KTB) borehole and their relation to fault structure and stress field. *J. Geophys. Res.*, **109**, B02309, doi:10.1029/2003JB002528.

4.1. Abstract

125 Fault plane solutions for microearthquakes induced during a long-term fluid-injection experiment at the KTB boreholes (Germany) in 2000 are investigated. A predominant strike-slip mechanism is observed, partly with components of normal but also reverse faulting. Adding 54 fault plane solutions of an earlier injection experiment at the KTB we determine the local stress field and find a subhorizontal NS orientation for the maximum principal stress and a near vertical orientation for the intermediate principal stress. The stress field exhibits no temporal or spatial variations within the resolved accuracy of $\pm 15^\circ$. However, the results of the stress tensor inversion point to heterogeneities of second order.

Based on the hypocentral distribution of the induced microearthquakes and the similarity of fault mechanisms we relate our data to the fault structure at the KTB. We find that the larger faults act as pathways for the injected fluid whereas the brittle failure occurs on fault asperities of the larger mapped faults and nearby smaller faults both in agreement with the local stress field. Applying a thorough error analysis of the individual fault plane solutions we correlate the diversity of mechanisms with their strength and find that the strongest events tend to a representative mechanism that is in good correspondence with the stress field. In contrast, the diversity of fault mechanisms is larger for the smaller events indicating local stress perturbations.

4.2. Introduction

Analysis of fault mechanism data for the state of stress in the Earth's crust is an important and widely used tool when trying to understand the mechanics and dynamics of the lithosphere. Deep drill holes are natural laboratories offering the possibility for well-controlled in-situ experiments to correlate between microseismicity and local fault structure. The German Continental Deep Drilling Program (Kontinentales Tiefbohrprogramm der Bundesrepublik Deutschland - KTB) with its two drill holes of 9101 and 4000 m depths allow this relation to be addressed. The KTB is located in SE Germany close to the border with the Czech Republic at the western margin of the Bohemian Massif and the contact zone of the Saxothuringian with the Moldanubian (Wagner et al., 1997). The deep main and the shallower pilot hole were drilled in a smaller crustal segment: the Erbsdorf-Vohenstrauß Zone consisting mainly of metabasites and gneisses (Pechinig et al., 1997). Major results were summarized by Emmermann and Lauterjung (1997). Since the main hole reached its final depth in October 1994, extensive research has been carried out using both boreholes as a deep crustal laboratory.

Figure 1 shows the location of the KTB deep drill holes as well as selected principal results being of interest for this study. Natural seismicity is sparse in the area. Dahlheim et al. (1997) operated a local network over a period of five years consisting of four stations. About 80 local earthquakes were detected with the majority (73) belonging to earthquake swarms near Marktredwitz at 20 km distance to the KTB site. These events are related to the Vogtland/West Bohemia seismotectonic unit that is well known for its swarm activity. The size of the beachballs in Figure 1 is scaled to the strongest event with a local magnitude (M_l) of 2.8. Six events were detected in the vicinity of the KTB. Two are interpreted as quarry blasts and are not considered here. The strength of the events near KTB does not exceed $M_l=0.5$ and the hypocentral depth is limited to 13 km. In summary, natural seismicity at the KTB is sparse with about 1 event per year.

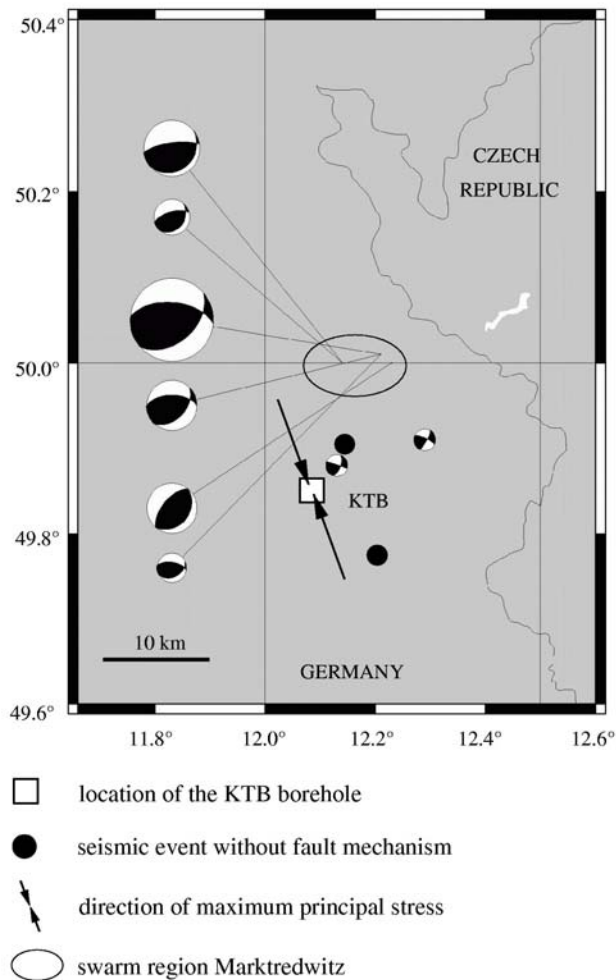


Figure 1: Location map of the KTB superdeep drill hole in SE Germany, fault plane solutions of natural seismicity (Dahlheim et al., 1997) and the local stress field after Brudy et al. (1997). The size of the beachballs is scaled to the largest event of $M_l=2.8$ being recorded during a five-year period by a local network. Black circles indicate seismic events for which no fault mechanism was determined. Black arrows indicate the trend of the maximum principal stress σ_1 being subhorizontal (Brudy et al., 1997).

The regional stress field in Western Europe is oriented NNW-SSE with a 17° clockwise rotation with respect to the direction of absolute plate motion between Africa and Europe (Müller et al., 1992). Stress field investigation at the KTB was extensively carried out by Brudy et al. (1997) based on hydraulic fracturing experiments as well as analysis of compressional and tensile failures of the borehole wall. They found a subhorizontal orientation of $N160^\circ E \pm 10^\circ$ for the maximum principal stress (σ_1) that is nearly uniform with depth down to 8.6 km and the only significant change in the stress field orientation was observed below a major fault zone (the so called SE1 reflector at 6.8-7.2 km depth, see Harjes et al., 1997). In addition, Barton and Zoback (1994) found a stress field heterogeneity at 5.4 km depth that is limited to a vertical extent of only 4 m. Interestingly, determination of the local stress field using various data sets and methods such as borehole breakouts, earthquake focal mechanism data, overcoring, hydraulic fracturing and analysis of geological stress indicators (e.g. Müller et al., 1992; Zoback, 1992; Dahlheim et al., 1997) revealed comparatively large variations for the average trend of σ_1 of up to 60° in the vicinity of the KTB. It is of interest whether these variations are due to local stress field heterogeneities (as

the different studies might look at different depth levels and/or different scales of the stress field) or whether they reflect uncertainties in the applied methods.

In this study, we focus on microearthquakes that were induced during a long-term fluid-injection experiment at the KTB. We determine and analyze highly reliable fault plane solutions due to a network geometry that was optimised for events occurring in direct vicinity of the main hole. The fault mechanisms are analyzed and correlated with the local fault structure that is well known from numerous pre-site surveys and coring results. We invert the data for the stress tensor to analyze the local stress field and determine the level of stress-field heterogeneity at the KTB.

4.3. Injection experiments at the KTB

Such experiments have been carried out twice at the KTB drilling site with slightly different objectives. During a short-term fluid-injection experiment, immediately after drilling was terminated in 1994, microseismicity was induced at mid-crustal depth levels. A total of 200 m³ of heavy brine was injected into the main hole within a period of 48 hours at rates of up to 600 l/min (Zoback and Harjes, 1997; Jost et al., 1998). The seismic activity during the experiment was monitored by a borehole sonde in the pilot hole at nearly 4 km depth and a surface network consisting of 73 short-period seismometers. About 400 microearthquakes were detected by the borehole sonde, the strongest 100 were recorded at the surface stations. The largest induced event with $M_l=1.2$ was seen even by stations of the regional network at 150 km epicentral distance. Magnitudes of all other events were below zero. The hypocentral depth was limited to 9.1 km. The principal conclusion of the experiment was that very small pressure perturbations are able to trigger seismicity, i.e. that Byerlee's law is valid to great crustal depth and that the crust is in brittle-failure equilibrium even at depths and temperatures approaching the brittle-ductile transition.

Fault plane solutions could be determined for 54 microearthquakes with the majority (30) of them being compound solutions for highly similar events (correlation coefficient >0.9, see below).

In 2000, a long-term injection experiment was designed based on the results of KTB1994. For an overview see Baisch et al. (2002). This experiment was motivated by the question whether the limited hypocentral depth observed within KTB1994 reflects a change in rheological behaviour or the limited range of pore pressure increase during short term injection. Therefore, a total of 4000 m³ of fresh water was injected over a period of 60 days at low flow rates between 30 and 70 l/min. A temporary seismic network consisting of a borehole sonde in the pilot hole at 3827 m depth yielding an extremely low threshold of $M_w = -2.5$ and a surface network of 39 stations was installed (Figure 2). All stations were equipped with three-component seismometers. Seismicity was monitored continuously over three months including the injection period. A total of 2799 events was detected at the borehole sonde. The 237 strongest events could be located using the borehole seismometer and the surface station recordings. In average, the location accuracy for these events is

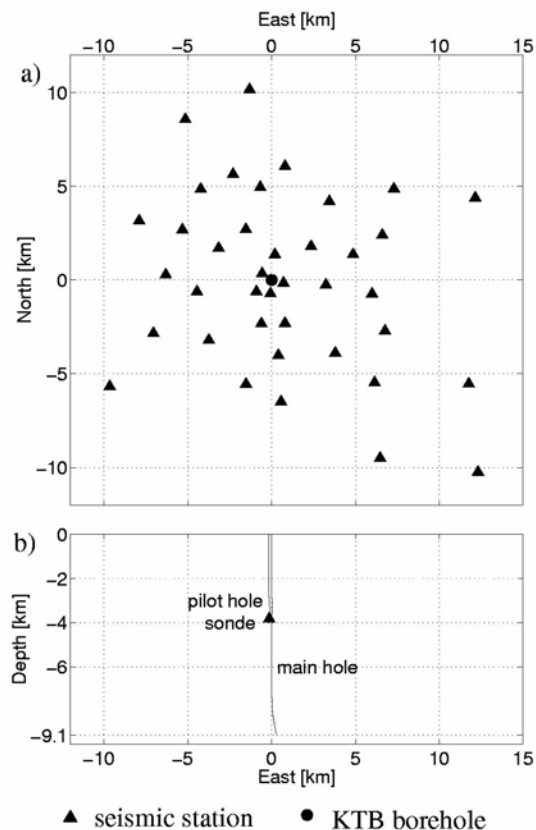


Figure 2: Geometry of the temporary seismic network operating during the long-term injection experiment KTB2000. a) Map view of the 39 stations forming the surface network. Location is given relative to the surface position of the KTB main hole that is indicated by the black dot. The focal coverage clearly stresses the excellent conditions for determining highly confident fault plane solutions for events occurring in direct vicinity of the main hole. b) Position of the borehole seismometer that was operated at 3827 m depth in the pilot hole at about 200 m distance to the main hole (view from South).

± 147 m, (127 m, and (26 m for eastern, northern and vertical directions, respectively (Baisch et al., 2002). The events cluster at two depth levels of 5.0 - 6.0 km (81 %) and 8.8 - 9.2 km (11 %).

4.4. Determination of fault plane solutions

In contrast to the earlier injection experiment in 1994, the KTB2000 surface network was designed to allow an equal-area coverage of the focal hemisphere for microearthquakes occurring in the direct vicinity of the main hole. The aperture of the network was fixed to 30 km with the surface position of the main hole located at its centre (see Figure 2). As all microearthquakes considered here occurred at maximum offsets of 500 m to the main hole this configuration clearly allows us to determine accurate and highly reliable fault plane solutions.

In order to evaluate whether pure shear faulting can be assumed for the induced seismic events we estimated the fluid pressure conditions during injection (see Figure 3). We added the maximum additional pressure caused by fluid injection (30 MPa) to the natural hydrostatic fluid pressure Pfl-nat (Huenges et al., 1997). Comparing the magnitudes of the resulting fluid pressure (Pfl-inj) to the magnitude of the smallest horizontal stress (Sh) that is subhorizontal and therefore equivalent to the smallest principal stress (3 (Brudy et al., 1997) we find that Pfl-inj is at least 17 MPa less than Sh at depth levels where the induced seismicity occurred (deeper than 5.0 km, see Figure 3). As a result no new tensile fractures could be generated by the injection as the additional pressure did not reach the magnitude of the smallest principal stress. Consequently, the microearthquakes represent pure shear failure on existing faults that were re-activated (see also Baisch and Harjes, 2003). To determine fault mechanisms we ap-

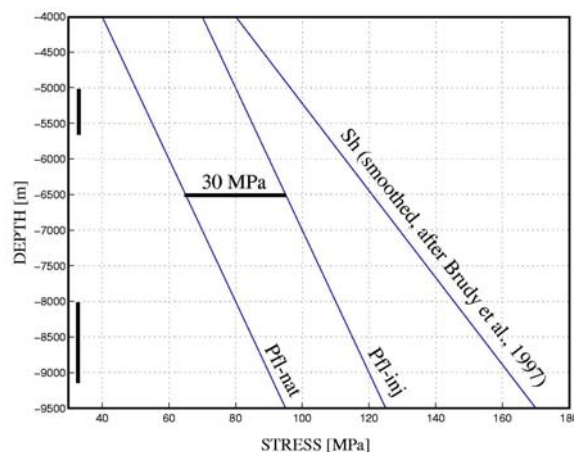
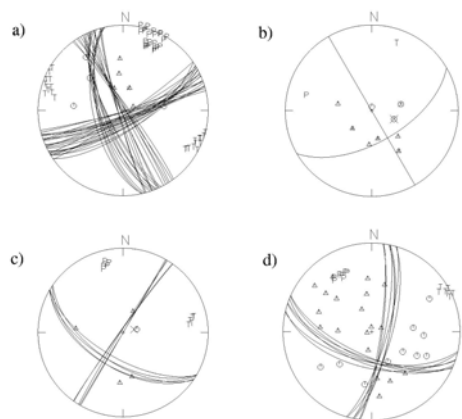


Figure 3: Stress magnitudes at the KTB at 4000-9500 m depth. Plotted are from left to right 1. the natural pore fluid pressure (Pfl-nat) being hydrostatic in the area of investigation as determined by Huenges et al. (1997), 2. The resulting pore fluid pressure during injection (Pfl-inj) estimated from Pfl-nat + 30 MPa that was the maximum additional pressure during injection, 3. the magnitude of the smallest horizontal stress (Sh) being equivalent to σ_3 following Brudy et al. (1997). The vertical lines to the left indicate the hypocentral depth for events considered in this study.

plied the FOCMEC program (Snoke et al., 1984; Snoke, 2003) that performs a grid search over all possible fault plane orientations assuming a pure double-couple model. We proceeded as follows: For each of the microearthquakes considered, the seismograms were converted to true ground motion and rotated into ray co-ordinates. All traces of the 237 microearthquakes (that fulfil the above mentioned accuracy in hypocenter location) were examined for the first-arrival polarity to be applied to the FOCMEC program. From the inversion results, we computed the individual error of each fault plane solution in terms of standard deviation of all P and T axes that are compatible with the polarity data. If this error exceeded 25° or if multiple mechanisms were permitted we refined the results adding SH/P amplitude ratios as additional information for the inversion procedure. All the events that did not pass these criteria were discarded resulting in a total of 98 single-event solutions. In addition

we determined 27 fault mechanisms as compound solutions for groups of earthquakes which are thought to represent repeated slip on particular fracture planes (discussed in detail in Baisch and Harjes, 2003). As these earthquakes exhibit nearly identical waveforms (correlation coefficient >0.9) we assume that the underlying source processes are very similar. We therefore combined the recordings of each group of repeating earthquakes to improve the focal coverage. In summary, 98 events gave stable single-event solutions, 27 events form the compound solutions and 112 events were discarded from further evaluation.

For the entire set of 125 well constrained fault plane solutions the seismic moment (M_0) was calculated from the P, SH and SV onsets, respectively (Kueperkoch et al., 2003). Based on M_0 we derived the moment magnitude M_w following Kanamori and Hanks (1979). The 125 events for which fault plane solutions were determined were found to cover a magnitude range of $-1.2 \leq M_w \leq +1.1$. In Figure 4 we refer to four events that are representative for the entire set of fault mechanisms: The event shown in Figure 4a is one of the weakest microearthquakes for which a fault mechanism could be determined ($M_w = -0.6$). Due to only 9 P polarities and 1 SH/P amplitude ratio, the solution is comparatively poorly constrained (error of 12.4° for P and T axes, respectively). In Figure 4b we show an event for which nine P polarities and five SH/P amplitude ratios were identified resulting in only 1 possible solution while the example in Figure 4c stresses the importance of implementing amplitude ratios when only a few polarities could be determined. For this event multiple solutions are permitted without the amplitude ratio information. One of the strongest events ($M_w = 0.9$) is plotted in Figure 4d. 29 P polarities were identified resulting in a stable solution. On average, 17 polarities were identified per event with a mean of 0.4 polarity errors. The reliability of the entire set of fault mechanisms is shown in Figure 5. The mean error for the individual mechanisms is 7.7° for the P axes and 8.1° for the T axes.



	a)	b)	c)	d)
moment magnitude	-0.6	-0.3	0.1	0.9
P polarities/errors	9/0	9/0	5/0	29/0
SH/P ampl. rat./err.	2/1	5/0	1/0	0/0
standard deviation P	12.4	2.5	5.8	7.6
standard deviation T	12.4	2.5	5.9	5.4

Figure 4: Representative examples for the fault plane solutions of KTB2000. T and P indicate orientations of all tension and pressure axes being allowed by the input data. Triangles (dilatation) and circles (compression) indicate P wave polarity, crosses indicate SH/P amplitude ratios. Great circles on the focal sphere represent possible orientations of the fault and auxiliary planes, respectively.

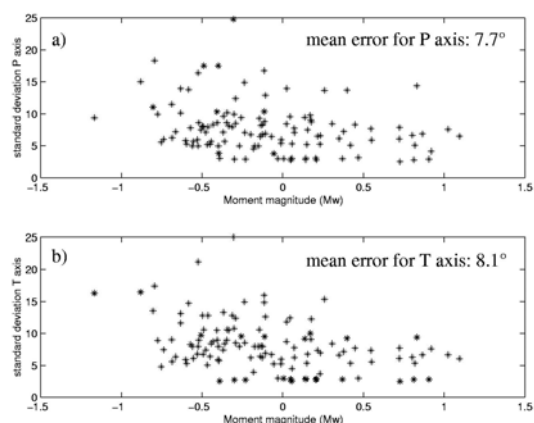


Figure 5: Accuracy of all 125 fault plane solutions in terms of standard deviation of all P (a) and T (b) axes orientations allowed by the polarity and amplitude ratio data. Standard deviations are plotted with M_w (see text for details).

4.5. Stress tensor inversion

Numerous methods have been developed for the determination of the stress field orientation from fault plane data. The most widely used ones are the inversion algorithms of Gephart and Forsyth (Gephart and Forsyth, 1984; Gephart, 1990) and Michael (Michael, 1984). Both methods are based on the assumption that, if various orientations of focal mechanisms exist within a region of uniform stress, one may determine the directions of the principal stresses (σ_{1-3}) and a relative stress magnitude (R) from the condition that slip occurs in the direction of the maximum shear stress (Bott, 1959). The main difference between these methods is the description of the deduced misfit and the way to define the best model. Hardebeck and Hauksson (2001) performed an extensive comparison of both methods based on synthetic focal mechanism data sets. The results revealed no fundamental discrepancy in terms of stress field orientation, but it was found that the method of Gephart and Forsyth usually provides more accurate estimates of stress field orientation, especially for high-quality data sets while its confidence regions are in most cases too large.

As discussed above, the 125 fault plane solutions determined in this study are well constrained (see Figure 5). We therefore decided to apply the Focal Mechanism Stress Inversion (FMSI) method of Gephart and Forsyth. The method is based on the following assumptions: (1) stress is uniform in the area of investigation during the observed time interval, (2) the earthquakes are shear-dislocations on pre-existing faults, and (3) slip occurs in the direction of the resolved shear stress on the fault plane. Four stress parameters are determined: The directions of the three principal compressive stresses (σ_1 = maximum, σ_2 = intermediate and σ_3 =minimum) and a measure of the relative stress magnitude $R=(\sigma_1-\sigma_2)/(\sigma_1-\sigma_3)$ with $0 < R < 1$. These parameters are determined by finding the best fitting stress tensor to the observed focal mechanisms. The FMSI package performs a grid-search over the entire model space. In their algorithm, Gephart and Forsyth offer two methods: an 'approximate method' that searches through the whole parameter space with a wider grid and an 'exact method' to precisely determine the best fitting stress tensor. We started inverting the fault plane solution data with the 'approximate method' and used the result as starting solution for the time-consuming 'exact method' searching through a narrower grid. In addition to the orientation of the three principal stresses and the relative stress magnitude the inversion result includes a parameter termed misfit (F). F is a measure for the level of stress field heterogeneity in the volume of investigation. This misfit describes the average minimum rotation about an arbitrary axis that brings the fault plane geometry in coincidence with the resolved shear stress tensor. In order to determine whether the deduced stress tensor represents a homogeneous stress field as assumed prior to inversion or whether the result reflects stress field heterogeneities one has to further analyze the meaning of F. Different authors (e.g. Wyss et al., 1992; Gillard et al., 1996; Cocina et al., 1997) found that the quality of the fault mechanism data is critical for the interpretation of F. Following the results of Gillard et al. (1996) who tested the relation of F to the error in fault plane solutions for a high quality data set comparable to ours, a misfit smaller than 6° should represent crustal volumes with relatively uniform stress. Misfits larger than 6° are interpreted to indicate heterogeneities in the stress field.

The database used for stress tensor inversion consisted of 125 fault plane solutions as determined in this study. In addition, we included 54 fault mechanisms as determined for the earlier injection experiment at the KTB (Zoback and Harjes, 1997; Jost et al., 1998). Implementing the error analysis for the fault plane solutions we estimate the accuracy of the resulting stress field orientation to be $\pm 15^\circ$. We started to invert the entire data set for the stress tensor followed by independent inversions for various temporary and spatial subsets in order to detect variations of the local stress field in space and time.

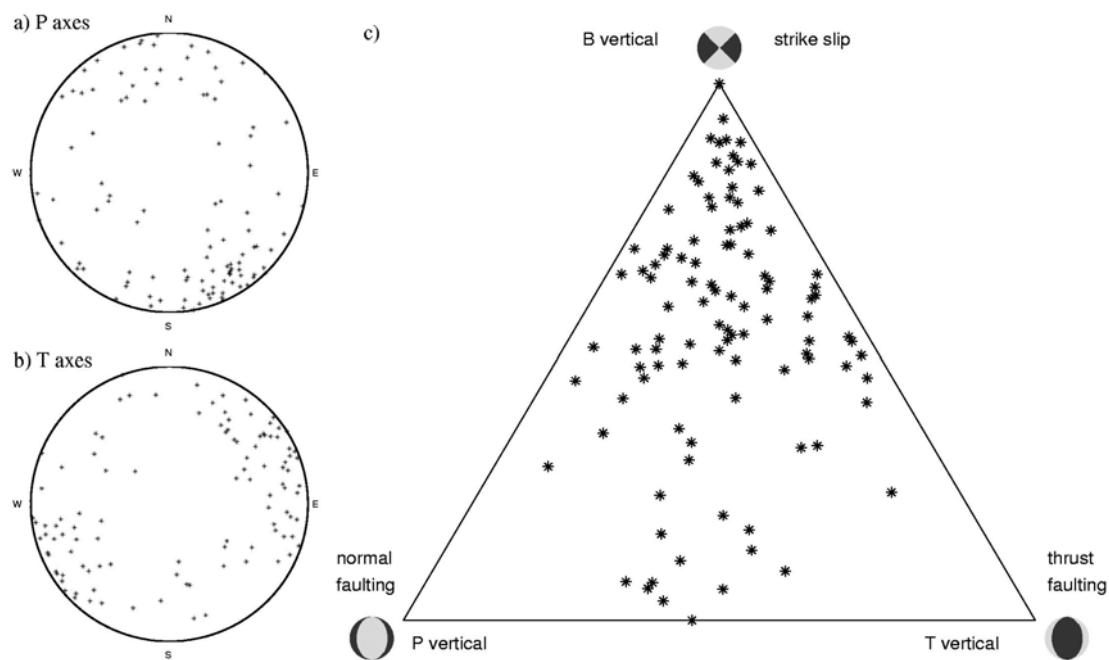


Figure 6: Orientations of P (a) and T (b) axes of all 125 fault plane solutions plotted in a polar scheme (lower hemisphere). c) Dipping angle of the P, T and B axes of all 125 fault plane solutions visualised in a ternary scheme following Frohlich (2001, equation 3). Beachballs in each corner represent pure strike-slip, normal and thrust faulting for vertical B, P and T axis, respectively.

4.6. Results and discussion

4.6.1. Faulting mechanisms and stress field

An established procedure to further analyze fault plane data is to refer to the orientations of their P and T axes indicating the direction of maximum compression and tension, respectively. In addition the B axis, that represents the intersection of the fault and auxiliary planes, allows to further evaluate fault plane solutions. In Figure 6 we show all 125 fault plane solutions in terms of orientation of P, T and B axes. Obviously a large number of events clusters around a trend of N160°-180°E for P (Figure 6a) and N50°-80°E for T (see Figure 6b) whereas the plunge is predominantly subhorizontal in both cases. However, a comparatively high level of diversity in orientation is observed which will be discussed later. For a thorough analysis of the orientation of P, T and B axes we applied the visualisation method of Frohlich (2001, equation 3) and plotted the focal mechanisms in a ternary diagram neglecting their trend in Figure 6c. There, each corner of the triangle represents a plunge of 90° (i.e. vertical) for the specific axis. More than 68% of all mechanisms have a B-axis plunge $\geq 50^\circ$ and thus can be classified as strike-slip events while no pure normal or thrust faulting is observed. This indicates a strike-slip regime at the KTB confirming results of Brudy et al. (1997) who observed a near vertical orientation of the intermediate principal stress (σ_2) over the entire length of the deep drill hole. In order to determine the local stress field at the KTB from the fault mechanism data we started by inverting the entire set of 179 fault mechanisms from both injection experiments. We find a subhorizontal NS orientation for σ_1 (trend N352°E, plunge 18°) and σ_2 to be oriented near vertical. The relative stress magni-

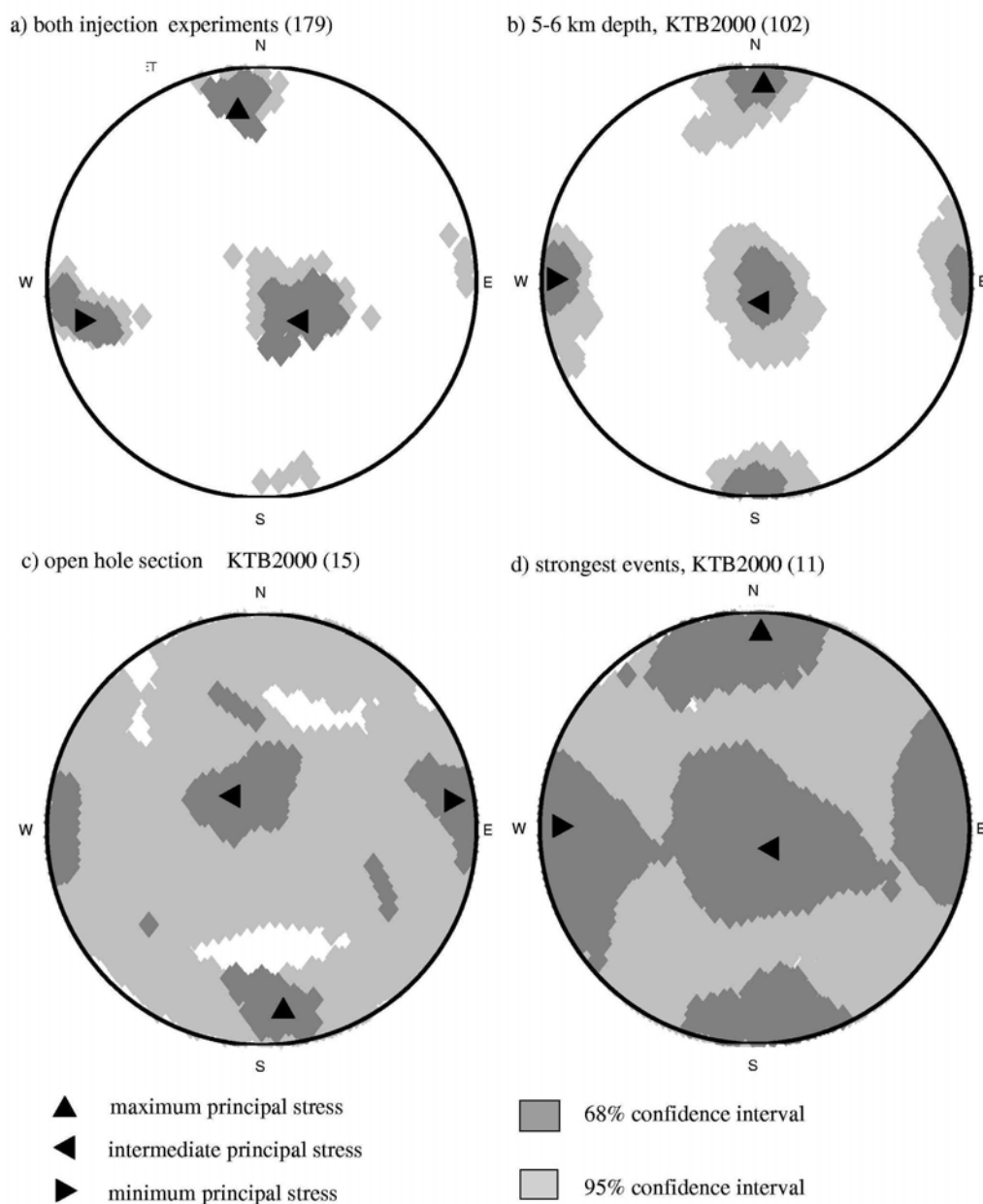


Figure 7: Results of the stress tensor inversion (Gephart and Forsyth, 1984; Gephart, 1990) for different sets of fault plane solution data: a) entire set of fault mechanisms (KTB1994+KTB2000), b) events at 5-6 km depth (KTB2000), c) events at the open hole section at 8.8-9.25 km depth (KTB2000), d) 11 strongest events (KTB2000). Numbers in brackets give the number of fault mechanisms being inverted. Black triangles indicate best-fitting orientations for (1-3, grey shading represents the 68% (dark) and 95% (light) confidence intervals.

tude was found to be 0.4 which means that σ_2 is well described by the mean of σ_1 and σ_3 . This stands in good correspondence to results obtained by Brudy et al. (1997). In their Figure 11 the relative stress magnitude can be calculated directly from the magnitudes of the principal stresses for various depths. In Figure 7a we plotted the inversion result in a polar scheme combining

Inverted data set	mechanisms	misfit	R	σ_1	σ_2	σ_3
KTB2000 and KTB1994	179	8.7	0.4	352/18	134/68	258/13
Temporal subsets:						
KTB1994, all	54	4.2	0.4	351/20	120/60	253/2
KTB1994, prior to main event	23	1.3	0.8	134/24	015/47	241/33
KTB1994, after main event	31	4.5	0.3	166/24	070/13	314/62
KTB2000, all	125	8.8	0.6	002/07	160/82	271/03
KTB2000, prior to main events	48	7.2	0.7	349/08	219/77	080/10
KTB2000, after main events	66	9.3	0.6	002/07	160/82	271/03
Subsets based on hypocentral depth z:						
KTB2000, 5.0 km >z> 6.0 km	102	8.8	0.6	002/07	160/82	271/03
KTB2000, 5.1 km >z> 5.2 km	20	5.3	0.5	312/18	085/65	217/17
KTB2000, 5.1 km >z> 5.3 km	37	7.0	0.6	180/00	187/72	091/02
KTB2000, 5.4 km >z> 5.7 km	34	8.8	0.5	173/14	302/67	079/17
KTB2000, 6.0 km >z> 9.3 km	23	6.4	0.4	181/20	359/70	091/01
KTB2000, 8.8 km >z> 9.3 km	15	7.3	0.6	173/14	322/73	081/08
Subsets based on event strength:						
KTB2000, 11 strongest	11	2.7	0.5	002/07	136/80	271/07
KTB2000, 12 th -35 th strongest	24	5.5	0.6	173/16	309/60	079/15
KTB2000, 36 th - 80 th strongest	45	7.4	0.6	002/07	136/80	271/07
KTB2000, 81 st - 125 th strongest	45	9.9	0.5	115/00	025/74	205/16
KTB2000, 35 strongest	35	6.3	0.6	183/14	005/76	274/00
KTB2000, 80 strongest	80	7.2	0.5	002/07	160/82	271/03
KTB2000, 114 weakest	114	9.8	0.5	001/05	160/81	273/03

Table 1: Results of stress tensor inversion (Gephart and Forsyth, 1984; Gephart, 1990). Mechanisms indicate the number of fault plane solutions forming the inverted data set. R is the relative stress magnitude as described in the text. (1-3 is given in degree for trend/plunge).

the best solutions for the orientations of σ_1 -3 (black triangles) with the 68% (dark grey) and the 95% (light grey) confidence intervals. The confidence intervals were calculated according to Parker and McNutt (1980). The deduced misfit of 8.7 in combination with the high number of input data indicates slight stress field heterogeneities. We therefore decided to form subsets of the fault plane data. In Table 1, an overview on subsets and inversion results is given. As a first step we inverted the fault plane data of the two experiments separately. The insignificant change in stress field orientation (difference for the trend of (1: 11°) suggests that the 1994 injection experiment did not cause stress field perturbations. In addition, this indicates that no natural changes in the stress field orientation occurred between both experiments which is what can be expected for such a comparatively short time interval of 6 years in a tectonically stable environment.

Furthermore, we subdivided the input data defining the strongest events of each injection experiment as indicators for possible stress field changes. For KTB2000, we find that these events did not cause changes in the orientation of the stress field being larger than the resolved accuracy of 15°. This result is further supported by the absence of mainshock-aftershock sequences which would be an indicator of major changes in the stress field (see e.g. Stein, 1999). For the two subsets of KTB1994, however, a significant change in stress field orientation is observed (see Table 1). This is well explained by the large number of

cluster solutions (17/23 before and 13/30 after the main event, respectively) that remarkably decrease the reliability of the inversion due to a small variability of the input data.

Looking for depth-dependent changes we subdivided the data of KTB2000 into different clusters of similar hypocentral depth (see Table 1). Results for the depth ranges 5.0 - 6.0 km (102 fault plane solutions) and 8.8 - 9.2 km (open-hole section, 15 fault plane solutions) are shown in Figure 7b and 7c, respectively. Both inversions agree in the direction for the best-fitting solutions of (1-3 confirming the results of Brudy et al. (1997) who found no significant perturbation of the stress field at the depth intervals covered by our fault plane data. Note, that the remarkable difference for the confidence intervals in Figure 7b and 7c is well explained by the larger diversity and larger number of fault plane solutions at 5.0 - 6.0 km. Discussing changes of the stress field at depth ranges covered by our data, we refer to Barton and Zoback (1994) who identified a stress-field discontinuity at 5.4 km depth at the KTB main hole indicated by changes of breakout orientation. The stress field discontinuity was found to extend over only 4 m in vertical direction which is far below what we can resolve with our database although we are dealing with a comparatively high density of fault mechanisms (125 fault plane solutions within 1 km³). Inversion results for the different depth intervals exhibit a rather uniform stress field orientation except for the depth interval at 5.1 - 5.2 km. We explain this result by the small number of inverted events (20) containing eight compound solutions that further reduce the reliability of the inversion result. Looking for a possible relation between strength of the inverted microearthquakes and the corresponding stress field we for-

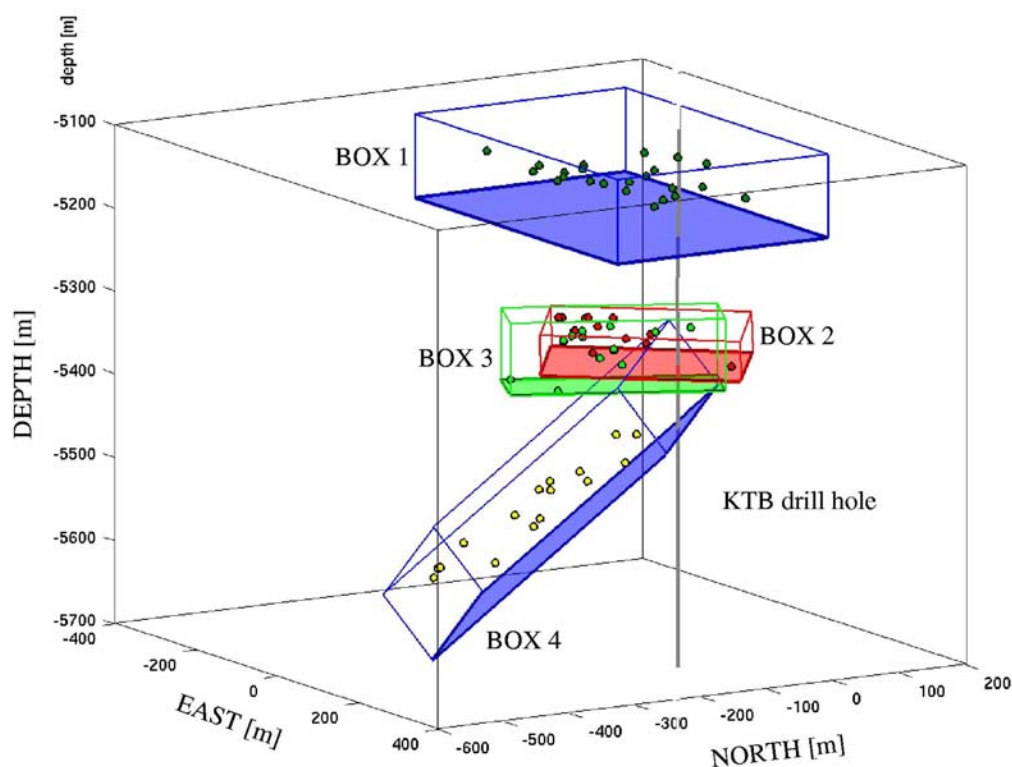


Figure 8: Three-dimensional visualisation of selected hypocenters, seen from ESE. The microearthquakes shown here were identified to form plane structures. Structures are surrounded and encoded structure 1-4. The vertical line indicates the KTB main hole. Scaling of the axes is in m relative to the surface position of the KTB main hole. See text for details.

med subsets based on M_w (see Table 1). Interestingly the orientations of the three principal stresses are stable in most cases (see Figure 7d for the inversion result of the 11 strongest events) and only the weakest events reveal an orientation differing strongly ($\sigma_1=N115^\circ E/0^\circ$) from the average orientation. We explain this by the catalog being incomplete for $M_w < -0.5$ and would expect the same best-fitting orientation for (1-3 from the weaker events if the detection threshold would have been even lower. Note, that the misfit is increasing with decreasing strength of the events stressing that the larger events represent the local stress field more uniformly while the smaller events exhibit a comparatively high level of disorientation. We will refer to this point later in the text.

We conclude that stress tensor inversion based on the 179 fault plane solutions reveals stable results for the orientation of the local stress field at the KTB (see confidence intervals in Figure 7a). We find that although we are dealing with a high spatial density of well-constrained fault plane data we hesitate from quantifying stress field perturbations as indicated by the misfit and limit our conclusions on stress field changes stating that no perturbations larger than 15° were identified between 5.0 - 6.0 and 8.8 - 9.2 km depth for reliable inversions. Thus, the previously stated variations of up to 60° for the trend of (1 in the vicinity of the KTB (e.g. Müller et al., 1992, Zoback, 1992, Dahlheim et al., 1997) most likely reflect the different scale of the stress field analyzed in the studies as well as the different depth levels covered. Furthermore, the accuracy of the different methods needs to be considered when discussing local stress field heterogeneities.

4.6.2. Relation of fault mechanisms to fault structure

The predominant orientation of major faults in the vicinity of the KTB was identified to be NE-ward dipping at about 40° on average whereas the smaller structures exhibit a steep inclination to the SW (see e.g. Hirschmann, 1994; Barton and Zoback, 1994; Harjes et al., 1997; Wagner et al., 1997). The two largest fault zones at the KTB are located at 6.8 - 7.2 km and 4.2 km depth and termed SE1 and SE2 (see Harjes et al., 1997). In principle, these form a good base for relating larger scale structures to hypocentral distribution of (micro)seismicity and its faulting mechanisms. Although at least some injection-induced events occurred at the 7 km depth level, these were not strong enough to allow the determination of their fault mechanisms. Moreover, all induced microearthquakes for which fault mechanisms were determined are located at 5.0 - 6.0 km and 8.0 - 9.2 km depths in correspondence with leaks in the casing and the open-hole interval, respectively (see Baisch et al., 2002). Because of the limited number of events in the open-hole interval we focus our analysis on the shallower events at 5.0-6.0 km depth: There, a major fault was mapped at 5.3 km depth probably related to the SE12 reflector for which orientation and dip remained unresolved (Wagner et al., 1997). Another fault was identified by Barton and Zoback (1994) at 5.4 km depth based on borehole breakouts indicating a strike of $N177^\circ E$ and a dip of 68° .

In order to correlate hypocenters and fault mechanisms of the induced microearthquakes with the local structure in the vicinity of the KTB we analyze the entire set of 192 microearthquakes that were located at 5.0 - 6.0 km depth. We analyze the hypocenter distribution at that depth level to find planar sub-structures in the seismic cloud. This is a widely used approach for analysing induced seismicity in geothermal and hydrocarbon reservoirs (e. g. Fehler et al., 2000; Phillips et al., 2002) based on the assumption that the most effective coupling of hydraulic overpressures (injection pressure) occurs along planar fracture planes. In the current study we combine the geometrical structures derived from the hypocenter distribution with the source mechanisms obtained in the previous section (similar comparisons have previously been done by Sasaki & Kaieda, 2002) i.e. we search for planar structures which exhibit a similar source mechanism. We find that a total of 66 events

including 40 with fault plane solutions are grouped into four planar structures to which we refer as structure 1-4 in the following. The remaining events do not exhibit systematic patterns in structure or mechanism and thus are not considered for further analysis. Figure 8 shows the four structures in a perspective view (seen from ESE). Interestingly, these structures do not exhibit a uniform orientation. Whereas structure 1 at 5.15 - 5.2 km depth is oriented subhorizontal, the remaining three structures are dipping at 40° - 60° to the SW and SSW, respectively. In the following the structures will be discussed in detail.

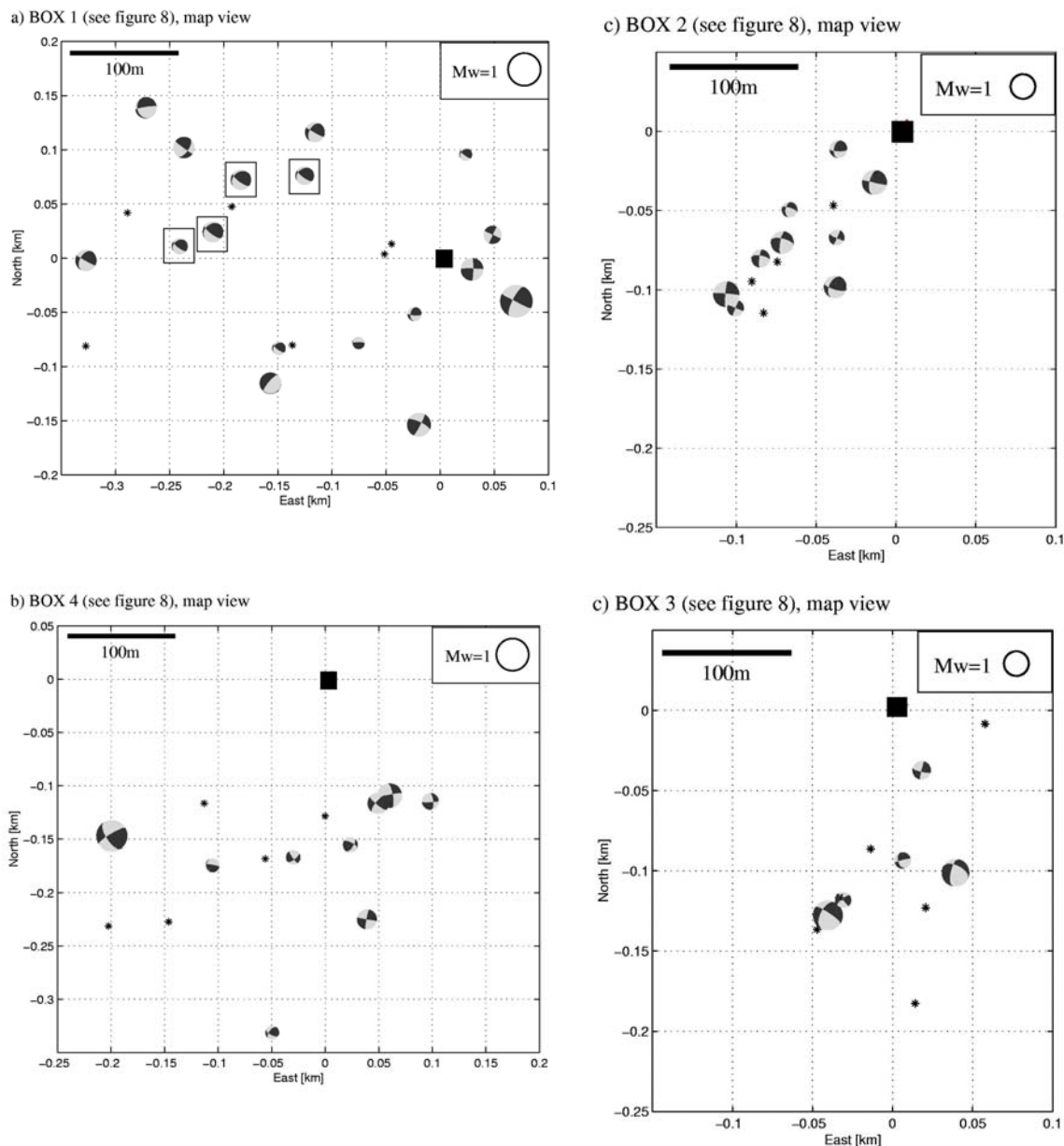


Figure 9: Map view of the four structures shown in figure 8: The size of the beachballs is scaled to M_w . Stars indicate events for which no fault plane solution was determined. The black square marks the position of the borehole at the corresponding depth.

Structure 1: This structure contains 23 events including 17 fault mechanisms (see Figure 9a) forming a subhorizontal plane at 5.15 - 5.2 km depth (see Figure 8). The 3 strike-slip events close to the borehole occurred right after the start of injection whereas the events NW of the borehole

occurred only after a seismic silence of 30 days. These later events exhibit a highly similar mechanism. One of the two fault planes permitted by the fault plane solution is subhorizontal and thus in good correspondence with the horizontal orientation of the plane formed by their hypocenters. However, when analysing the hypocentral distribution the different location accuracy in horizontal (~120 m) and vertical (~30 m) direction has to be considered. Four of these events (surrounded by rectangles in Figure 9a) have the same mechanism as they represent compound solutions for repeating earthquakes (see Baisch and Harjes, 2003). These events are likely to originate from a common hypocenter and differences in source location as displayed in Figure 9a can be explained by the absolute hypocenter location uncertainty. For these repeating earthquakes hypocenter location error-ellipsoids are overlapping. Thus, the subhorizontal plane identified as structure 1 may be an artifact of the difference in location accuracy between the vertical and horizontal direction. This is supported when correlating the subhorizontal orientation with the known fault geometry at the KTB that does not exhibit any horizontal structures. In contrast, the temporal evolution of hypocenters forming this particular structure indicates an increasing distance to the KTB main hole being a possible indicator for a larger subhorizontal fault that has not been mapped by borehole investigations.

Structures 2, 3 and 4: About 80% of the injected fluid entered the rock formation at two distinct depth levels (5.35 and 5.41 km, see Baisch and Harjes, 2003). This was indicated by the distribution of hypocenters and confirmed by a flow-log test performed right after injection was terminated. The majority of events in structures 2, 3 and 4 are grouped according to a predominant SW-NE direction forming plane structures dipping to the SSW (structures 2 and 4, dip of about 40°) and to the SW (structure 3, dip of about 60°) in good agreement with the prevailing orientation of larger scale faults at the KTB. All three structures cross the borehole at the depth intervals 5.3 - 5.4 km. However, the prevailing strike-slip mechanisms do not agree with the orientation of the planes formed by their hypocenters. Unlike horizontally layered structures, these three structures cannot be an artifact of the location accuracy. Consequently, we interpret these three structures to be real due to the significantly smaller location error in vertical direction. The orientation of the dipping planes is not in correspondence with the local stress field but coincides well with the known fault structure at the KTB that developed under different stress field orientations (Wagner et al., 1997). We thus interpret these events as being caused by fluid using the larger structures as pathways without causing brittle failure due to their non-critical orientation to the present stress field. In contrast, microseismic activity might occur on critically orientated small-scaled nearby faults as well as on fault asperities of the larger mapped faults. This might explain the discrepancy between the vertical orientation of fault planes (strike-slip mechanism) and the 40°-60° dipping planes formed by their hypocenters. Our interpretation suggests that larger structures that were formed under different stress field orientations are of major importance for the spatio-temporal evolution of fluid-induced seismicity. Ito and Zoback (2000) examined the relationship between fracture permeability and in situ stress at the KTB. They conclude that critically-stressed faults are also the most permeable faults. At first glance this seems to contradict our findings that some of the most permeable fractures (structures 2-4) were not seismically activated because of their non-critical orientation. The interpretation of Ito & Zoback (2000), however, is a general conclusion drawn from a large data set of fracture orientations covering the range between 3 and 7 km depth. We note that especially in the interval between 5-6 km depth Ito & Zoback (2000) also observe a number of highly permeable but non-critically oriented fractures (their Figure 3c). It might exactly be these fractures that form the structures described in Figure 8.

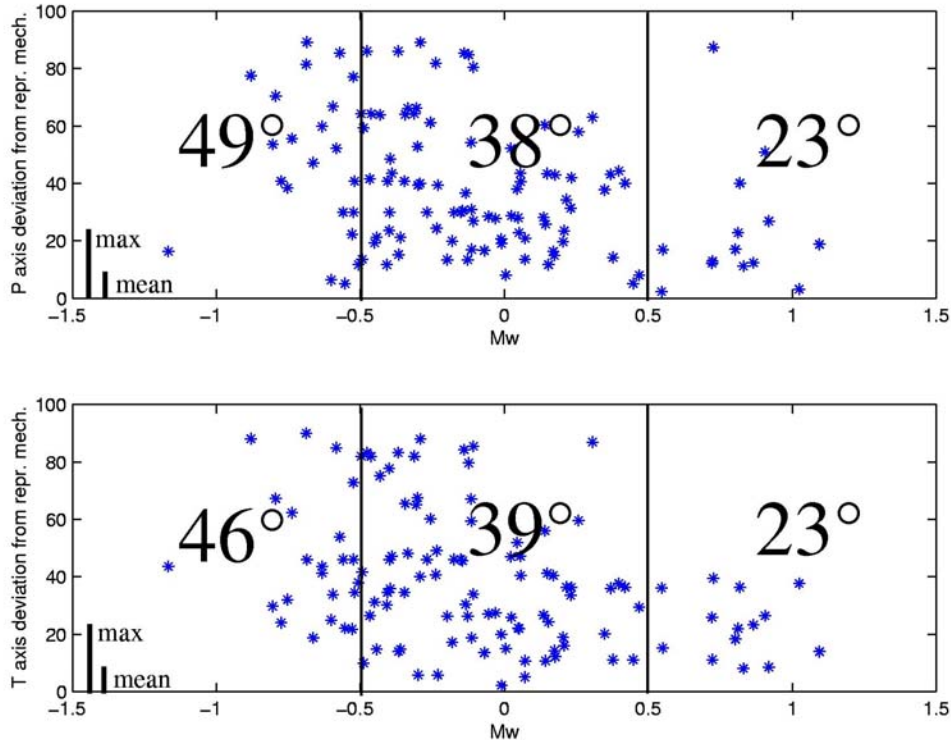


Figure 10: Deviation of all 125 fault mechanisms from the representative mechanism (P axes: N161°E/14°, T axes: N72°E/1°, see text for details) plotted with M_w . Bold numbers indicate the mean deviation within the three intervals of M_w . The small bars indicate the maximum and mean error of the P and T axes of all fault plane solutions, respectively.

4.6.3. Diversity of fault mechanisms

As described above, the results from the stress tensor inversion as well as the analysis of the structure-related distribution of fault mechanisms indicates a relation between fault mechanism and strength for the induced microearthquakes. To analyze this further, we focus on the orientation of the P and T axes and the moment magnitude M_w of the individual events.

Referring to Figure 7 we recall that the entire set of fault plane solutions shows a preferred strike-slip mechanism with a predominant trend of about N160°-180°E for the P axes and N50°-80°E for the T axes. Subsets formed for the stress tensor inversion based on event strength indicated that the stronger events are of a rather uniform mechanism and the weaker ones to be of a higher diversity on average. In order to test and quantify this hypothesis we look for an objective measure and compute the mean fault mechanism of the 11 strongest events. We find an orientation (trend/plunge) of N161°E/14° for the P and N72°E/1° for the T axes, respectively. In the following we will refer to this orientation as the representative mechanism. Note, that this representative mechanism is in good correspondence with the local stress field as deduced from the entire set of fault plane data.

As a second step we calculate the deviation of each fault plane solution from the representative mechanism as the minimum rotation about an arbitrary axis that brings both fault plane geometries in coincidence (similar to the misfit in the stress tensor inversion). We plotted this deviation for all 125 fault plane solutions with M_w for P and T axes, respectively (Figure 10). To further quantify the relation between diversity and strength we formed three subsets ($M_w < -0.5$, $-0.5 \leq M_w \leq 0.5$, $M_w > 0.5$) and calculated the mean deviation from the representative mechanism within each subset for P and T axes (see bold numbers in Figure 10). Obviously, this mean deviation is remarkably decreasing with increasing M_w for the P (49°-38°-23°) as well as for the T axes (46°-39°-23°). This effect is not caused by the individual error of the fault plane solutions. This becomes obvious when combi-

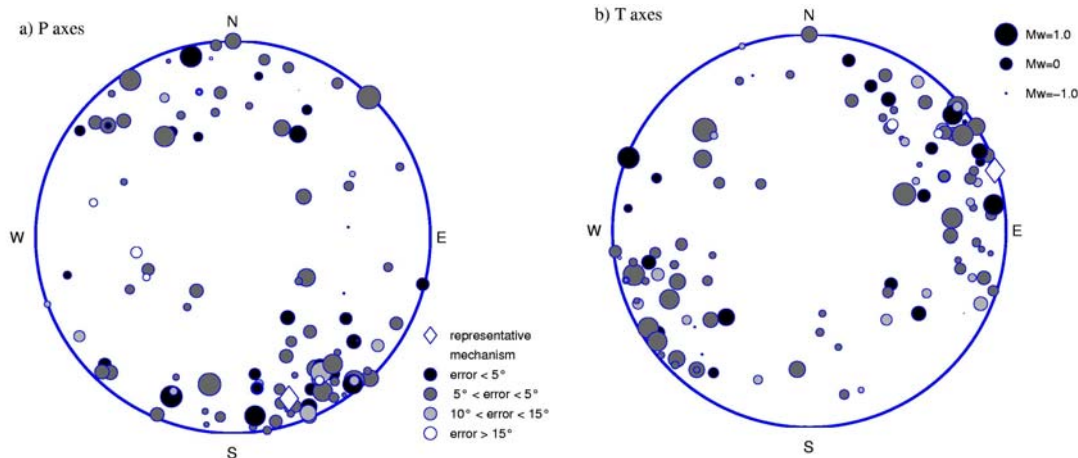


Figure 11: Polar scheme of all 125 fault plane solutions in terms of orientation of P (a) and T (b) axes, respectively. The size of the circles is scaled to M_w and shading is scaled to the error of each fault mechanism. White diamonds indicate the representative mechanism of which the fault plane solution is shown in lower left.

ning error (P, T) and strength of each individual fault plane solution with the orientation of P and T axes in a polar scheme (Figure 11). While the larger events cluster around the representative mechanism, the weaker ones, on average, deviate significantly from its orientation.

4.7. Conclusions

We determined and analyzed 125 highly reliable fault plane solutions from injection-induced microearthquakes with moment magnitudes of $-1.2 < M_w < +1.1$. Based on the fault plane solutions we deduced and interpreted the local stress field at the KTB applying the stress tensor inversion algorithm of Gephart and Forsyth (1984) and Gephart (1990). In terms of direction we find a homogenous stress field within the resolved accuracy of $\pm 15^\circ$. The maximum principal stress is subhorizontal with a NS orientation. The intermediate principal stress is oriented near vertical. Based on error analysis of the fault plane solutions we study the relation between hypocentral distribution, diversity of mechanisms and local fault structure. We conclude that the large mapped faults act as pathways for the injected fluid without being reactivated since they are disoriented to the present stress field. The brittle failure occurs on asperities of these faults as well as on nearby small-scaled faults both favourably oriented to the local stress field. Furthermore, we find that the stronger events exhibit a uniform mechanism in good correspondence with the local stress field. Weaker events show an increasing diversity probably related to local stress field heterogeneities. To our knowledge this effect is unique and has not yet been observed which is due to the extremely low magnitude threshold of the temporary network ($M_w = -2.5$). We think that this effect should also be observable in other environments as long as 1. the conditions permit to reach a low detection threshold and 2. a thorough error analysis is performed.

4.8. Acknowledgements

We thank D.R. Schmitt, M. Zoback and an anonymous reviewer for constructive criticism and comments that helped to improve the manuscript significantly. We benefited from discussions with G. Dresen, J. Renner and L. Ceranna. Furthermore we thank the GFZ Potsdam for their support in carrying out the injection experiments, especially J. Kück and L. Wohlgemuth, and for supplying seismic acquisition systems from the instrument pool. We are grateful to the Deutsche

Forschungsgemeinschaft for funding the project B1 within the collaborative research centre 526 'Rheology of the Earth - from the Upper Crust to the Subduction Zone'.

4.9. References

- Baisch, S. and H.-P. Harjes, A model for fluid injection induced seismicity at KTB, Germany, *Geophys. J. Int.*, **152**, 160-170, 2003.
- Baisch, S., M. Bohnhoff, L. Ceranna, Y. Tu and H.-P. Harjes, Probing the crust to 9 km depth: Fluid injection experiments and induced seismicity at the KTB superdeep drilling hole, Germany, *Bull. Seismol. Soc. Am.*, **92**, 2369-2380, 2002.
- Barton, C.A. and M.D. Zoback, Stress perturbations associated with active faults penetrated by boreholes: Possible evidence for near-complete stress drop and a new technique for stress magnitude measurement, *J. Geophys. Res.*, **99**, 9373-9390, 1994.
- Bott, M.H.P., The mechanics of oblique slip faulting, *Geol. Mag.*, **96**, 109-117, 1959.
- Brudy, M., M.D. Zoback, K. Fuchs, F. Rummel and J. Baumgärtner, Estimation of the complete stress tensor to 8 km depth in the KTB scientific drill holes: Implications for crustal strength, *J. Geophys. Res.*, **102**, 18453-18475, 1997.
- Cocina, O., G. Neri, E. Privitera and S. Spampinato, Stress tensor computations in the Mount Etna area (Southern Italy) and tectonic implications, *J. Geodyn.*, **23**, 109-127, 1997.
- Dahlheim, H.-A., H. Gebrande, E. Schmedes and H. Soffel, Seismicity and stress fields in the vicinity of the KTB location, *J. Geophys. Res.*, **102**, 18493-18506, 1997.
- Emmermann, R. and J. Lauterjung, The German Continental Deep Drilling Program KTB: Overview and major results, *J. Geophys. Res.*, **102**, 18179-18201, 1997.
- Fehler, M., House, L. and H. Kaieda, Determining Planes Along Which Earthquakes Occur: Method and Application to Earthquakes Accompanying Hydraulic Fracturing. *J. Geophys. Res.*, **92(B9)**, 9407-9414, 1987.
- Frohlich, C., Display and quantitative assessment of distributions of earthquake focal mechanisms, *Geophys. J. Int.*, **144**, 300-308, 2001.
- Gephart, J.W., Stress and the direction of slip on fault planes, *Tectonics*, **9**, 845-858, 1990.
- Gephart, J.W. and D.W. Forsyth, An improved Method for Determining the Regional Stress Tensor Using Earthquake Focal Mechanism Data: Application to the San Fernando Earthquake Sequence, *J. Geophys. Res.*, **89**, 9305-9320, 1984.
- Gillard, D., M. Wyss and P. Okubo, Type of faulting and orientation of stress and strain as a function of space and time in Kilauea's south flank, Hawaii, *J. Geophys. Res.*, **101**, 16025-16042, 1996.
- Hardebeck, J.L. and E. Hauksson, Stress Orientations Obtained from Earthquake Focal Mechanisms: What are Appropriate Uncertainty Estimates?, *Bull. Seismol. Soc. Am.*, **91**, 250-262, 2001.
- Harjes, H.-P., K. Bram, H.-J. Dürbaum, H. Gebrande, G. Hirschmann, M. Janik, M. Klöckner, E. Lüschen, W. Rabbel, M. Simon, R. Thomas, J. Tormann and F. Wenzel, Origin and nature of crustal reflections: Results from integrated seismic measurements at the KTB superdeep drilling site, *J. Geophys. Res.*, **102**, 18267-18288, 1997.
- Hirschmann, G., The KTB location and models of the crustal structure, *KTB Report*, **94-2**, A35-A44, 1994.
- Huenges, E., J. Erzinger, J. Kück, B. Engeser and W. Kessels, The permeable crust: Geohydraulic properties down to 9101 m depth, *J. Geophys. Res.*, **102**, 18255-18265, 1997.
- Ito, T. and M.D. Zoback, Fracture permeability and in situ stress to 7 km depth in the KTB Scientific Drillhole, *Geophys. Res. Lett.*, **27**, 1045-1048, 2000.
- Jost, M., T. Büsselberg, Ö. Jost and H.-P. Harjes, Source parameters of Injection-Induced Microearthquakes at 9 km Depth at the KTB Deep Drilling Site, Germany, *Bull. Seismol. Soc. Am.*, **88**, 815-832, 1998.
- Kanamori, H. and T.C. Hanks, A moment magnitude scale, *J. Geophys. Res.*, **84**, 2348-2349, 1979.
- Kueperkoch, L., M. Bohnhoff and H.-P. Harjes, Source Parameters from Fluid Injection Induced Microearthquakes at the KTB, *Ann. Meet. of the German Geophysical Society (DGG)*, Jena, Abstract volume, p. 352, 2003.
- Michael, A.J., Determination of stress from slip data; faults and folds, *J. Geophys. Res.*, **89**, 11517-11526, 1984.
- Müller, B., M.L. Zoback, K. Fuchs, L. Mastin, S. Gregersen, N. Pavoni, O. Stephansson and C. Ljunggren, Regional Patterns of Tectonic Stress in Europe, *J. Geophys. Res.*, **97**, 11783-11803, 1992.
- Parker, R.L. and M.K. McNutt, Statistics for the One-Norm Misfit Measure, *J. Geophys. Res.*, **85**, 4429-4430, 1980.
- Pechinig, R., S. Haverkamp, J. Wohlenberg, G. Zimmermann and H. Burckhardt, Integrated log interpretation in the German Continental Deep Drilling Program, *J. Geophys. Res.*, **102**, 18363-18390, 1997.
- Phillips, W.S., Microearthquake Locations and Fluid Flow in the Geothermal Reservoir at Soultz-sous-Forets, France. *Bull. Seism. Soc. Am.*, **90(1)**, 212-228, 2000.
- Phillips, W.S., Rutledge, J.T., House, L.S. and M.C. Fehler, Induced Microearthquake patterns in Hydrocarbon and Geothermal Reservoirs: Six Case Studies. *PAGEOPH*, **159**, 345-369, 2002.
- Sasaki, S. and H. Kaieda, Determination of stress state from focal mechanisms of microseismic events induced during hydraulic injection at the Hijiori Hot Dry Rock site. *PAGEOPH*, **159**, 489-516, 2002.

- Snoke, J. A., FOCMEC: FOcal MEChanism determinations, International Handbook of Earthquake and Engineering Seismology (W. H. K. Lee, H. Kanamori, P. C. Jennings, and C. Kisslinger, Eds.), Academic Press, San Diego, Chapter 85.12, 2003.
- Snoke, J.A., J.W. Munsay, A.G. Teague and G.A. Bollinger, A program for focal mechanism determination by combined use of polarity and SV-P Amplitude ratio data, *EQ Notes*, **55**, 15, 1984.
- Stein, R.S., The role of stress transfer in earthquake occurrence, *Nature*, **402**, 605-609, 1999.
- Wagner, G.A., D.A. Coyle, J. Duyster, F. Henjes-Kunst, A. Peterek, B. Schröder, B. Stöckhert, K. Wemmer, G. Zulauf, H. Ahrendt, R. Bischoff, E. Heijl, J. Jacobs, D. Menzel, N. Lal, P. Van Den Haute, C. Vercoutere and B. Welzel, Post-Variscan and thermal and tectonic evolution of the KTB site and its surroundings, *J. Geophys. Res.*, **102**, 18221-18232, 1997.
- Wyss, M., B. Liang, W. Tanigawa and W. Xiaoping, Comparison of orientations of stress and strain tensor based on fault plane solutions in Kaoiki, Hawaii, *J. Geophys. Res.*, **97**, 4769-4790, 1992.
- Zoback, M.L., First and second order patterns of stress in the lithosphere: The World Stress Map Project, *J. Geophys. Res.*, **97**, 11703-11728, 1992.
- Zoback, M.D. and H.-P. Harjes, Injection-induced earthquakes and crustal stress at 9 km depth at the KTB deep drilling site, Germany, *J. Geophys. Res.*, **102**, 18477-18491, 1997.

5. Strain Partitioning and Stress Rotation at the North Anatolian Fault Zone from aftershock focal mechanisms of the 1999 Mw=7.4 Earthquake

This chapter has been submitted for publication. The reference is

Bohnhoff, M., Grosser, H., Dresen, G. (2005). Strain Partitioning and Stress Rotation at the North Anatolian Fault Zone from aftershock focal mechanisms of the 1999 Mw=7.4 Earthquake. *Geophys. J. Int.* (submitted).

5.1. Abstract

We investigate aftershock focal mechanisms of the $M_w=7.4$ Izmit earthquake of Aug 17th, 1999 on the western North Anatolian Fault Zone (NAFZ). Spatial clustering and orientation of 446 fault plane solutions are analyzed. The Izmit mainshock results from right-lateral slip on an EW-trending near vertical fault plane. Aftershock clusters define 4 individual fault segments. Focal mechanisms surrounding epicentres of the Izmit and subsequent Düzce mainshock ($M_w=7.1$, Nov 12th, 1999) indicate dominantly strike-slip but also normal faulting. Aftershocks in the area between Izmit and Düzce segments are mainly related to EW-extensional normal faulting indicating a small pull-apart structure. Below the easternmost Sea of Marmara, trains of aftershocks suggest branching of the NAFZ into three or more active segments differing significantly in dominant focal mechanisms. Fault segmentation of the NAFZ in the Izmit-Düzce region obtained from coseismic slip corresponds to spatiotemporal evolution of aftershock focal mechanisms. Areas with high coseismic slip show aftershocks that are dominantly strike-slip, but low-slip barriers show mostly normal faulting aftershocks.

Stress tensor inversions of the focal mechanisms show systematic rotations of the local stresses following the Izmit mainshock. In the Izmit Sapanca area, maximum compressive stress is rotated counterclockwise with respect to the coseismic and regional stress field. Towards the eastern end of the rupture (Karadere Düzce area) the local fault trend changes by 25°. There, stresses are rotated clockwise. In both areas this observation coincides with the distribution of aftershock hypocenters. We conclude that the Izmit earthquake caused significant stress partitioning along the rupture. The direction of stress rotation is related to the orientation of the individual fault segments along the NAFZ.

5.2. Introduction

The Izmit $M_w=7.4$ (Aug 17th, 1999) earthquake occurred on the northern strand of the North Anatolian Fault Zone (NAFZ) in the Gulf of Izmit region. The rupture length was about 140 km between the Sea of Marmara and the Düzce region along a right lateral predominantly EW-trending near vertical fault plane (Figure 1). Calculations of average fault slip of the Izmit mainshock vary between 2.5 m (e.g. Tibi et al., 2001) from inversion of teleseismic data and 2.9 m (Bouchon et al., 2002) from records of near-fault accelerometers. Maximum slip at the surface reached about 5 - 6 m (Barka et al., 2002; Bouchon et al., 2002; Bos et al., 2004 and others). The direction of slip corresponds well to the overall horizontal GPS derived velocity field of 2-2.5 cm/a westward motion of the Anatolian block with respect to fixed Eurasia (e.g. McClusky et al., 2000, Figure 1a). Analysis of surface rupture, teleseismic, strong motion and geodetic data all indicate separation of the mainshock in subevents along distinct fault segments (e.g. Barka et al., 2002; Reilinger et al., 2000; Tibi et al., 2001; Gülen et al., 2002; Delouis et al., 2002; Bos et al., 2004). The western termination of the Izmit rupture is located offshore below the Sea of Marmara (e.g. Wright et al., 2001) possibly extending to the area south of the Prince Islands (Bouchon et al., 2002; Özalaybey et al., 2002) at about 30 km southeast of Istanbul. Rupture propagation towards the East ended near Düzce where a large earthquake occurred 87 days after the Izmit event (Nov 12th 1999, $M_w=7.1$). Nodal planes of focal mechanisms for the Izmit main event, the major subevent (S2, Tibi et al., 2001) and for the Düzce earthquake trend dominantly EW (Figure 1b). The combined rupture length for the Izmit and Düzce earthquakes is estimated to about 200 km. Several authors (Wright et al., 2001; Parsons et al., 2000; Parsons, 2004) estimated Coulomb stress changes and the potential for future earthquakes in the Marmara region including the city of Istanbul with its >10 million inhabitants. These authors suggest that the Izmit earthquake increased seismic hazard for the Mar-

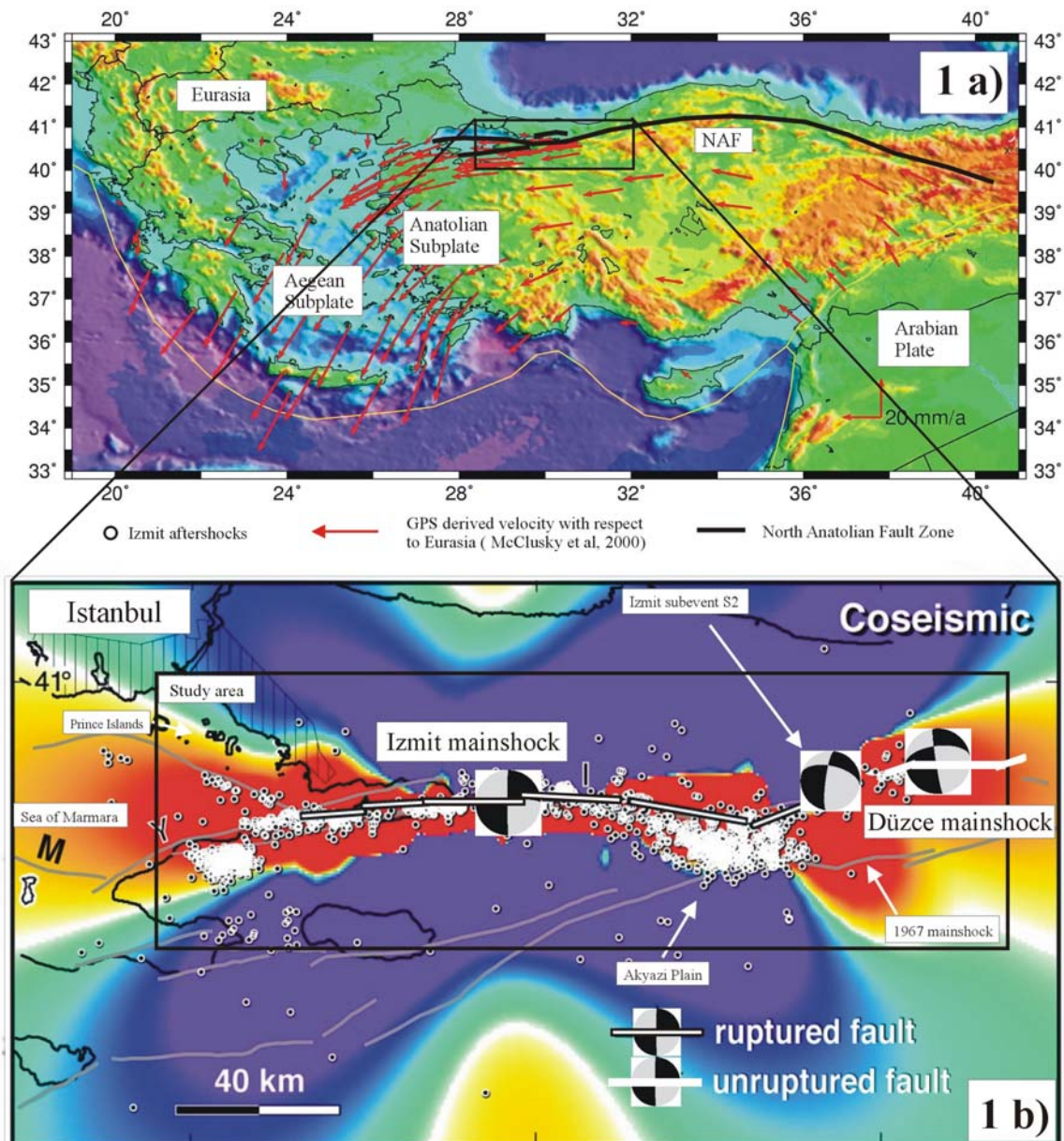


Figure 1: a. Location map of the Aegean-Anatolian region. Red arrows represent the GPS-derived horizontal velocity field (after McClusky et al., 2000). The bold black line is the simplified trace of the North Anatolian Fault Zone (NAFZ). The Izmit segment of the NAFZ is indicated by the black rectangular and enlarged in Figure 1b. b. Coulomb stress map after the Izmit $M_w=7.4$ (17th Aug, 1999) earthquake (after Parsons et al., 2000, their Figure 1). Red and blue colours indicate regions of increased and decreased Coulomb stress, respectively. White dots indicate locations of Izmit aftershocks. Fault mechanisms are shown for the Izmit mainshock, Izmit subevent S2 ($M_w=6.9$, Tibi et al., 2001) and Düzce mainshock ($M_w=7.1$, Nov 12th, 1999) from West to East. The black rectangle indicates the area investigated in this study.

mara region (Figure 1b) that is considered a seismic gap. Increased Coulomb stress was also found for the Düzce region. The eastward propagation of mainshocks is in contrast to a westward migration of strong earthquakes along the NAFZ observed since the 1939 Erzincan event (e.g. Töksöz et al., 1979; Stein et al., 1997). Here, we focus on aftershocks of the Izmit earthquake covering the inter-event time span Aug 17th - Nov 12th, 1999. We analyze the spatiotemporal evolution of aftershock hypocentral distribution and focal mechanisms and perform stress tensor inversion to determine the local stress field. The results are related to coseismic rupture and afterslip of the Izmit earthquake and to the regional tectonic setting.

5.3 Analysis of Aftershock Focal Mechanisms

The data set consists of 446 aftershock fault mechanisms in total. 254 fault plane solutions were determined from recordings of a 41-station seismic network that covers the entire Izmit rupture area. The network was installed only four days after the Izmit mainshock and was operated by the GeoForschungsZentrum Potsdam (Grosser et al., 1998). Fault mechanisms for these events were determined by a grid search over all possible fault plane orientations assuming a double-couple model (FPFIT program, Reasenber and Oppenheimer, 1985). Almost full spatial coverage allowed rejecting all events for which grid-search results permitted multiple fault-plane solutions. The orientation accuracy of individual fault mechanisms is equal to the step-width of the grid search (5°).

In addition, 192 fault plane solutions were collected from published studies. The data are from seismic networks with different geometries covering most of the Izmit rupture area (Polat et al., 2002; Karabulut et al., 2002; Özalaybey et al., 2002). We also include source mechanisms determined by regional moment tensor inversion of the 30 largest Izmit aftershocks (Örgülü and Aktar, 2001). Multiple occurrences of events are excluded from the data set. We estimate the average orientation error of the fault plane solutions contained in our data to be $\sim 10^\circ$ in strike, dip and rake. The events cover an area between 28.95° - 31.4° E and 40.5° - 41.0° N and reach to a maximum depth of 18 km (a single event was located at 23 km depth) (Figure 2a).

Spatial clustering of aftershock locations, fault mechanisms and slip directions are statistically investigated. Temporal distribution and event magnitude are also considered. Orientation distribution of aftershock fault mechanisms is given by the respective P and T axes in lower-hemisphere polar projection plots (Figure 2b). P and T axes bisect the dilatational and compressional quadrants of the focal mechanisms indicating the direction of maximum compression and tension, respectively.

5.4 Segmentation of the Izmit Rupture Zone

Aftershock epicentres are clustered in an E-W direction along the fault between 40.55° N and 41° N. Orientation distribution of P and T axes suggest spatial separation of the 446 fault mechanisms along the rupture zone into 4 major segments (Figure 2a). Between 29.5° E and 30.4° E, aftershock epicentres follow the trend of the rupture trace of the Izmit event. A prominent cluster containing 169 events is located at about 30.6° E in the Akyazi area. Trains of aftershocks indicate activation of secondary fault structures inclined to the E-W trending NAFZ. The magnitude of aftershocks decreases with time after the Izmit event. In general, P-axes are either subvertical or strike subhorizontally between $N90^\circ$ E- $N180^\circ$ E; T axes are dominantly horizontal with a large scatter ($N160^\circ$ E- $N290^\circ$ E). This orientation distribution of focal mechanisms indicates strike-slip and normal faulting regimes dominating the western part of the NAFZ.

Segment 1 (28.95° E- 29.3° E) contains 110 fault plane solutions covering the western termination of the Izmit rupture located below the easternmost Sea of Marmara (Figure 3). Aftershock clusters indicate activation of three different branches of the NAFZ. For each branch, fault mechanisms are very similar and nodal planes often coincide with mapped faults. The northern part (subsegment 11) contains dominantly strike-slip events located on a $\sim N305^\circ$ E striking vertical plane. A series of events indicating normal faulting is aligned along a parallel small fault segment (Figure 3). The southern branch (subsegment 12) contains NNE-SSW-extensional normal fault events and some NW-SW-compressional thrust fault events revealing a complex local fault structure. This area largely coincides with the Yalova cluster that showed swarm activity covering a time period of several years (e.g. Gurbuz et al., 2000).

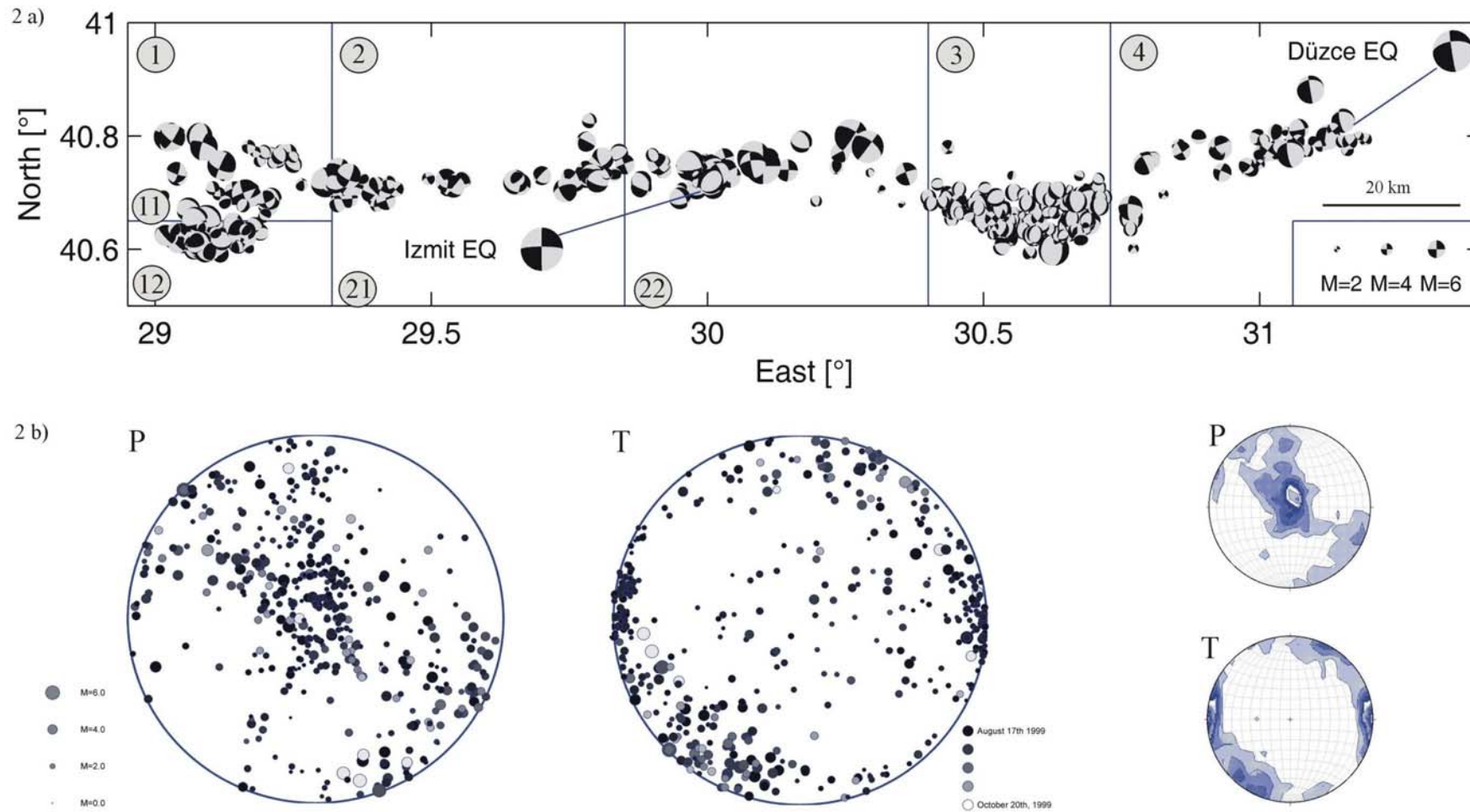


Figure 2: a. Epicentre distribution of the 446 fault plane solutions analyzed in this study in map view of the lower hemisphere. The size of the beachballs scales with magnitude. The Izmit and Düzce mainshocks are indicated by their fault mechanisms. Numbers indicate (sub) segments along the Izmit rupture zone that were identified based on spatial clustering of fault mechanisms as discussed in the text.

b. Distribution of P and T axes for the 446 fault plane solutions in polar projection of the lower hemisphere. The size of circles scales with magnitude and the shading indicates the hypocentral time (lighter colour \approx later occurrence). In addition we plotted the density distribution for the P and T axes of the entire data set. Shading is scaled to maximum for P and T separately.

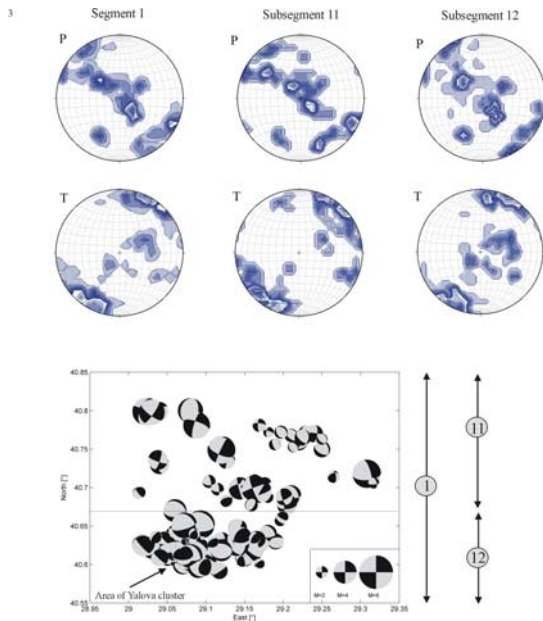


Figure 3: Density distribution of P and T axes and map view of fault plane solutions for all events contained in segment 1 (see Figure 2). The epicentral distribution exhibits trains with highly similar focal mechanisms matching one of the two possible fault planes. This suggests further subdivision into a northern (11) and a southern (12) subsegment (see text for details).

Segment 2 (29.3°E-30.4°E) contains 107 aftershocks and the Izmit mainshock epicentre (Figure 4). It covers the Izmit Sapanca area. In the western part (subsegment 21), aftershock epicentres are aligned with the surface rupture trace trending E-W. P and T axis indicate a wide distribution of focal mechanisms. However, in the eastern part (subsegment 22) aftershock locations trend ~N75°E and are therefore inclined to the rupture trace and slip direction of the Izmit mainshock. Focal mechanisms indicate dominantly right-lateral strike-slip and some normal faulting. Trends of P-axes and nodal planes of individual strike-slip events are rotated counterclockwise by ~15° with respect to the Izmit main shock focal mechanism.

Segment 3 (30.4°E-30.85°E) is located near the town of Akyazi at a triple junction formed by the Izmit Sapanca and Karadere Düzce faults and the ESE striking Mudurnu segment where a major contains 60 aftershock fault plane solutions including the epicentres of Izmit subevent S2 (Tibi et al., 2001) and the Düzce mainshock (Figure 1b). Aftershock locations in-

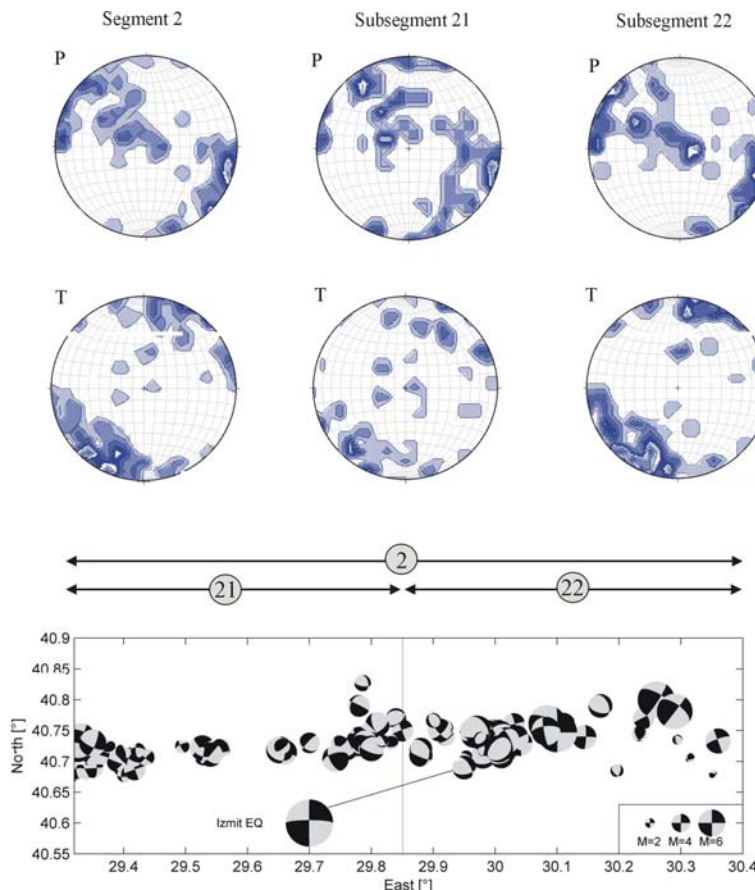


Figure 4: Density distribution of P and T axes and map view of fault plane solutions for all events contained in segment 2 that includes the epicentre of the Izmit mainshock. The eastern subsegment (22) consists dominantly of strike-slip mechanisms in good accordance with the mainshock and contains a number of NNE-SSW extensional normal faulting events; the western subsegment (21) does not exhibit a preferred fault mechanism. In subsegment 22, hypocenters follow a trend that is inclined to the E-W striking fault west of the Izmit epicentre; P axis distribution in this subsegment show several preferred orientations some of which are rotated by up to 20° with respect to the Izmit mainshock.

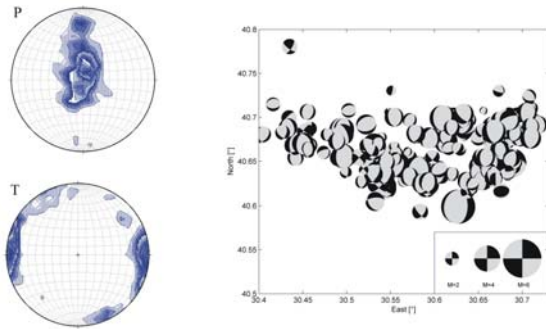


Figure 5: Density distribution of P and T axes and map view of fault plane solutions for all events contained in segment 3. A dominant EW-extensional normal faulting regime is observed along this segment that contains about 40% of the entire set of fault plane solutions analyzed in this study. Different to the three other segments no alignment is observed from the distribution of hypocenters; instead the aftershock activity cover the entire Akyazi plain that is identified as a pull-apart structure.

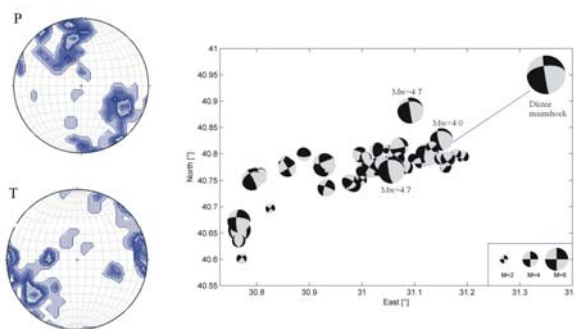


Figure 6: Density distribution of P and T axes and map view of fault plane solutions for all events contained in segment 4 that includes the Düzce mainshock epicentre. A dominant strike-slip mechanism is observed for this easternmost part of the Izmit rupture area. Events with indicated magnitude mark the largest and earliest aftershocks in this segment and are discussed in the text. Most hypocenters are aligned on a $\sim 80^\circ$ -trending structure that is inclined to the local fault trend of $N65^\circ E$ (Karadere segment, see Figure 8).

5.5. Stress tensor inversion

The aftershock fault mechanisms investigated in this study were used for a stress tensor inversion. Stress tensor inversion techniques using focal mechanisms have been discussed repeatedly by various authors (e.g. Gephart and Forsyth, 1984; Gephart, 1990; Michael, 1987a; Michael, 1991; Hardebeck and Hauksson, 2001; Bohnhoff et al., 2004). We use a technique proposed by Michael (1984, 1987a). The statistical analysis allows determining the orientation of the three principal stresses (σ_1 = maximum, σ_2 = intermediate and σ_3 = minimum) and the stress ratio $R = (\sigma_2 - \sigma_3) / (\sigma_1 - \sigma_3)$, $0 < R < 1$. The method involves the assumptions that (1) in the area of investigation stresses remain uniform in time and space, (2) earthquakes represent dislocations on existing faults, and (3) slip occurs in the direction of the resolved maximum shear stress on the fault plane. Heterogeneity

dicates a 20° clockwise earthquake occurred in 1967 (Figure 1b). This segment contains 169 fault plane solutions, i.e. 40% of the entire data set. Focal mechanisms of a dense cluster of events show strongly preferred orientation indicating E-W extensional normal faulting (Figure 5). The high aftershock activity is in striking contrast to the small co-seismic displacement of < 1 m in this area as suggested by surface slip and inversion of strong motion data (Langridge et al., 2002; Barka et al., 2002; Bouchon et al., 2002). The ESE striking southern branch of the NAFZ displayed only very few aftershocks and no surface slip, possibly due to stress relaxation after the 1967 event. Segment 4 ($30.85^\circ E$ - $31.3^\circ E$) rotation against the local trend of the Karadere segment ($N65^\circ E$). P axes of events show a maximum in accordance with activation of an ENE-WSW striking fault segment. In general, a broad orientation distribution of focal mechanisms reflects uniform right-lateral strike-slip with frequently E-W oriented sets of nodal planes (Figure 6).

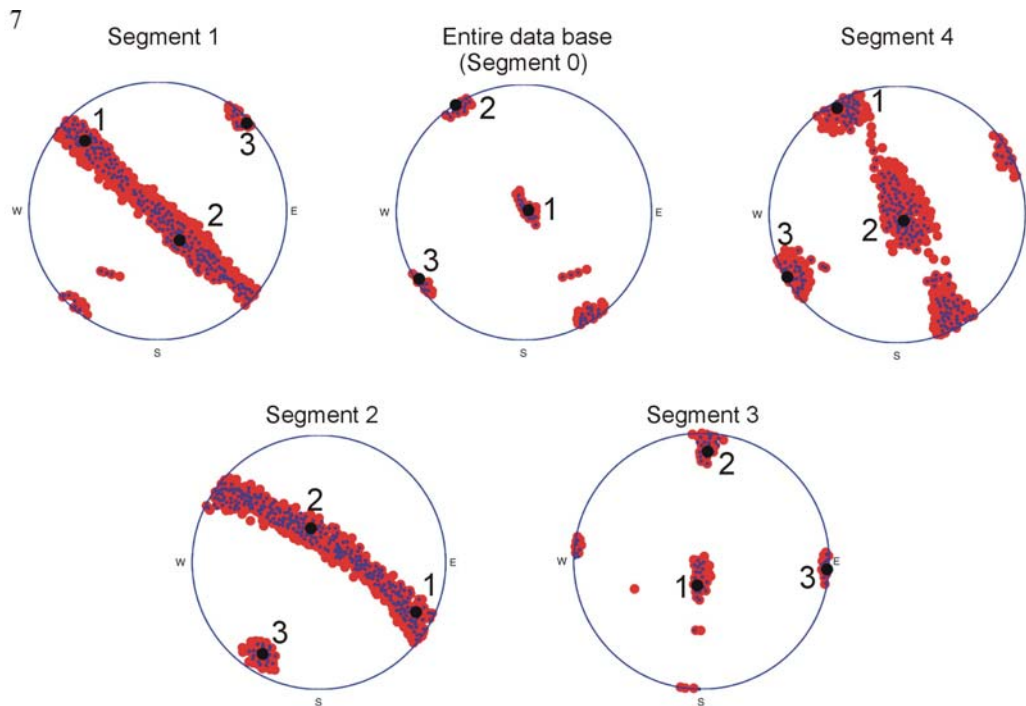


Figure 7 : Results of stress tensor inversion for the entire data base containing 446 fault plane solutions and the four segments (see Figures 3-6 for map view of fault mechanisms contained therein). Bold black dots represent the best fitting orientations for the three principal stresses (σ_1 =maximum, σ_2 =intermediate ; σ_3 =minimum). Small blue dots and large red dots represent the 1σ (68%) and 2σ (95%) confidence intervals.

of the stress field is reflected in misfit level and width of the confidence interval of the inversion (Table 1 and Figure 7). For each stress inversion 2000 bootstrap iterations were performed.

The stress inversion of all focal mechanisms results in a normal faulting regime with clear separation of the principal stresses. The maximum compressive stress σ_1 is almost vertical and σ_3 is horizontal trending N237°E. This result is in contrast to estimates of the regional stress field in NW Turkey that suggest dominantly strike-slip deformation with a \sim N125° striking subhorizontal direction of σ_1 (Kiritzi, 2002; Heidbach et al., 2004; Reinecker et al., 2004) and points towards significant local and temporal stress variations along the NAFZ. Furthermore, the data set as a whole is dominated by the large number of events located in segment 3 where a significantly different faulting regime was observed. To investigate the local variations of dominant stress regimes along the Izmit rupture we subdivided the catalog according to the segmentation as identified from the distribution of P and T axes (segments 1-4). Stress inversion of the four segments reveals a clear variation of local stress field orientation along the Izmit rupture (Figure 7). For the Akyazi area (segment 3) results indicate a clear separation of the principal stresses (black dots) with narrow 1σ (68%, dark grey) and 2σ (95%, light grey) confidence intervals. For the remaining segments, however, confidence intervals for the largest and intermediate principal stresses form a great circle (Figure 7). Stress ratio ($R=0.83$) and confidence intervals for segments 1 and 2 reflect the dominating deformation regimes (strike-slip and normal faulting). Magnitudes of principal stresses σ_1 and σ_2 do not differ significantly and both stress directions trend roughly NW-SE within both segments (N314°E and N117°E, respectively). The minimum stress σ_3 is clearly separated statistically from σ_1 and σ_2 trending subhorizontally NE-SW. The Izmit Sapanca area (segment 2) includes the Izmit mainshock epicenter. Here, the postseismic trend of σ_1 and σ_2 indicates a counterclockwise rotation of about 8° with respect to the regional stress field and the coseismic stress field that was derived from inverting the focal mechanisms of the six Izmit

Area covered	Time covered	focal mech. [no.]	σ_1 (tr/pl) [°]	std [°]	σ_2 (tr/pl) [°]	std [°]	σ_3 (tr/pl) [°]	std [°]	misfit	R	source .
NW Turkey	1943-1999	11	126/ 3	13	269/86	-	35/ 3	13	3.3° (*)	0.5	Kiratzi (2002)
NW Turkey	1943-1999	10 ^(#)	124/ 0	(20)	- /90	-	34/ 0	-	-	-	Reinecker et al. (2004)
E Sea of Marmara	Jan-Sep 1996	37	305/ 1	14	206/86	20	35/ 4	17	0.31	0.5	Ergin et al. (1997)
Izmit rupture	coseismic	6	124/ 3	15	231/79	15	34/11	15	0.31	0.5	Gülen et al. (2002)
Izmit rupture	postseismic	30	316/13	10	81/68	10	222/18	10	0.16	0.74	Örgülü & Aktar (2001)
Izmit rupture (segment 0)	postseismic	446	66/87	6	327/ 0	6	237/ 3	6	0.22	0.64	this study
E Sea of Marmara (segment 1)	postseismic	110	314/23	6	144/57	6	45/ 4	6	0.20	0.83	this study
Izmit Sapanca (segment 2)	postseismic	107	117/15	6	347/67	6	212/17	6	0.22	0.83	this study
Akyazi plain (segment 3)	postseismic	169	190/74	6	3/15	6	94/ 1	6	0.09	0.62	this study
Karadere Düzce (segment 4)	postseismic	60	339/ 6	8	49/74	8	251/15	8	0.19	0.63	this study

standard deviation (std) refers to the trend for s1-3

^(#) and shallow boreholes

^(*) misfit as given by the FMSI routine (Gephardt and Forsyth, 1986)

Table 1: Overview on information available for stress field orientation in NW Turkey and especially along the Izmit rupture in pre-, co- and postseismic times with respect to the Izmit mainshock.

subevents (Gülen et al., 2002) (Table 1). In the Akyazi area (segment 3) directions of principle stresses σ_1 - σ_3 are well constrained and correspond to an E-W extensional normal faulting regime. The relative stress magnitude $R=0.62$, i.e. the magnitude of σ_2 is close to the mean of σ_1 and σ_3 . The easternmost segment 4 covers the N65°E trending Karadere segment pointing towards the Düzce area where a $M_w=7.1$ earthquake occurred 87 days after the Izmit mainshock. Stress orientation and confidence intervals for this area indicate a strike-slip regime with a stress ratio of $R=0.63$ (Figure 7). The maximum principle stress (σ_1) is subhorizontal and trends N159°E indicating a clockwise rotation with respect to the regional stress field of $>30^\circ$.

5.6. Discussion

5.6.1. Segmentation of the Izmit rupture zone

The Izmit earthquake ruptured a 140 km long E-W trending segment of the western NAFZ. Below the easternmost Sea of Marmara the NAFZ splays in different branches producing a complex network with the Izmit-Sapanca, Düzce, Iznik, Geyve and Mudurnu faults (Figure 8). The width of this network is about 30 km and in the order of the thickness of the seismogenic upper crust. Regional tectonics in western Turkey are dominated by right-lateral strike-slip along the ~EW-trending NAFZ and a NE-SW extensional regime associated with a >3 cm SSW-ward migration of the South Aegean domain with respect to stable Eurasia (e.g. McClusky et al., 2000; Flerit et al., 2004). At the NAFZ, GPS data indicates a westward motion of northwestern Anatolia of about 2-2.5 cm/a. In this tectonic regime, the Sea of Marmara formed as a large pull-apart structure (e.g. Armijo et al., 1999) in a transtensional environment. Also, on a smaller scale, fault segments are separated by releasing bends and small scale pull-apart structures such as the Izmit Bay and Lake Sapanca.

Analysis of aftershock focal mechanisms along the Izmit rupture reveals dominantly strike-slip and normal faulting events in combination with few thrust events indicating that strain partitioning and variations in the local stress field plays a dominant role in this region. Thrust faulting is restricted to a small area around Yalova where swarm activity is a well-known phenomenon that was reactivated after the Izmit earthquake (Figure 3). In the Izmit Sapanca and Karadere Düzce areas (our segments 2 and 4), aftershock focal mechanisms dominantly reflect strike-slip and normal faulting. In general, epicenters of individual events form trails delineating fault segments that correspond to one set of aftershock nodal planes (Figure 2 and Figure 8).

E-W extensional normal faulting dominating the Akyazi plain of segment 3 (Figure 5) is in good agreement with the local topography at 30.6°E reflecting >500 m subsidence with respect to the surrounding area (Figure 8). We interpret this plain to represent a small pull-apart basin similar to the Lake Sapanca, the Izmit Bay and the somewhat larger Sea of Marmara. In the following we relate aftershock segmentation along the rupture zone to spatial distribution and temporal evolution of coseismic slip of the Izmit earthquake.

5.6.1.1. Coseismic slip along the Izmit rupture trace

The Izmit earthquake produced an E-W trending rupture trace of about 140 km length between 29.3°E and 31°E. Seismic moment release and coseismic slip along the fault vary significantly from $> 12 \cdot 10^{19}$ Nm and > 5 m in high-slip zones to $< 1 \cdot 10^{19}$ Nm and < 1 m at low-slip barriers, respectively (e.g. Bouchon et al., 2002; Papageorgiou, 2003). Mapped surface ruptures indicate five separate fault segments reaching from West to East separated by releasing (pull-apart) step-overs of about 1-4 km width (Figure 8) (Tibi et al., 2001, Barka et

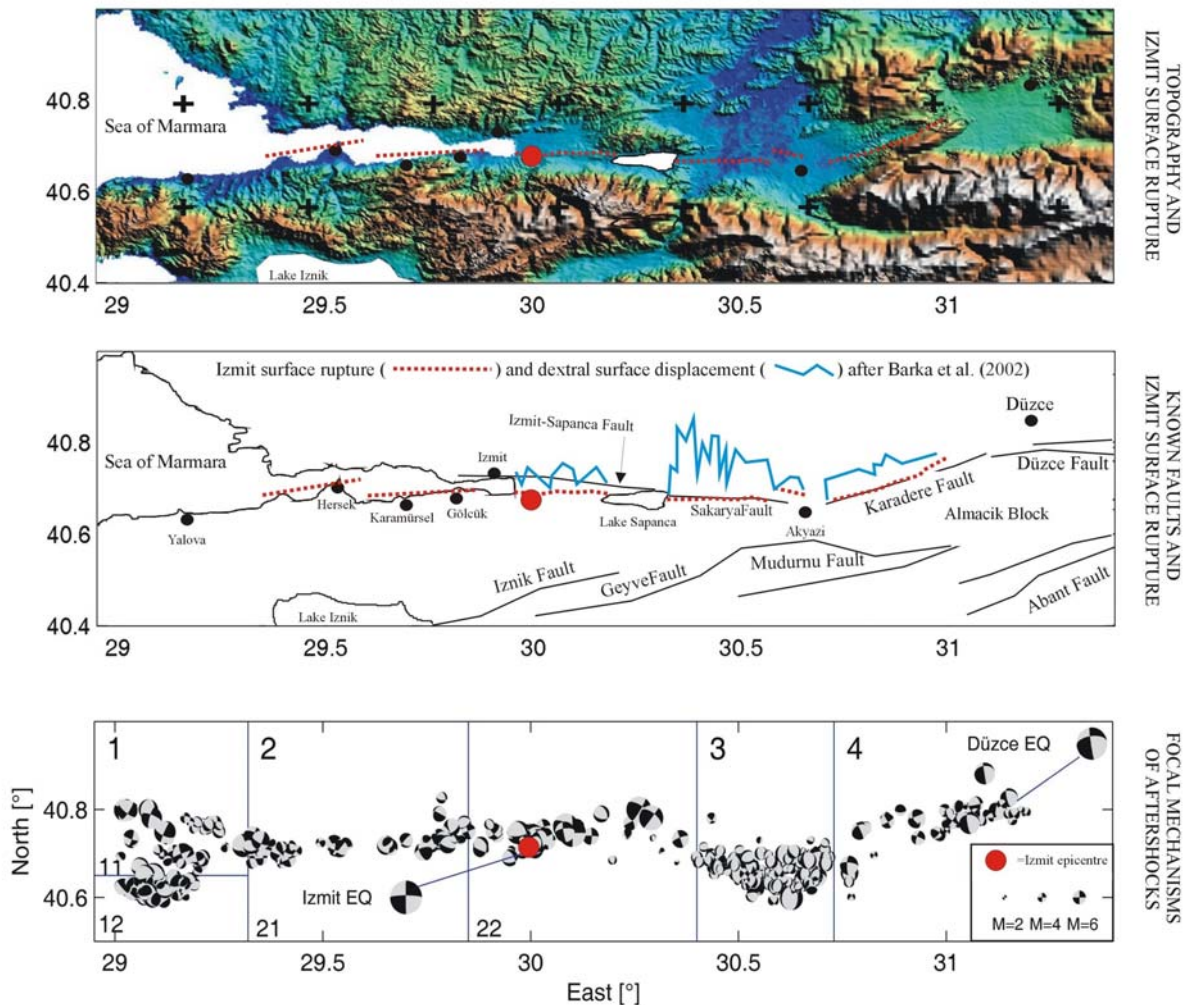


Figure 8: Upper part: Topographic map of the Izmit segment of the North Anatolian Fault Zone (after E. Fielding et al., 1999) and surface rupture of the Izmit event after Barka et al. (2002).

Middle part: Main faults along the Izmit rupture area. Red dotted lines indicate the simplified surface rupture of the Izmit event (after Barka et al., 2002). Blue lines along the three onshore segments represent lateral distribution of surface slip after Barka et al. (2002) scaled to the slip maximum of ~6 m.

Lower part: Distribution of the 446 focal mechanisms analyzed in this study (see also Figure 2).

al., 2002, Langridge et al., 2002, Polat et al., 2002). From West to East the segments are Yalova-Hersek (striking N80°E), Karamürsel-Gölcük (N70°-80°E), Izmit-Sapanca (~N90°E), Sapanca-Akyazi (N75°-85°E) and Karadere (N65°E). Step-overs between segments exhibit vertical offsets of up to 2.4 m indicating a significant portion of normal faulting in agreement with aftershock fault mechanisms at several locations along the rupture trace.

Coseismic rupture started at the main shock epicentre just west of Gölcük and propagated westward along the Karamürsel-Gölcük segment with little moment release (Bos et al., 2004). Eastward propagation was triggered on the Izmit-Sapanca segment with short delay resulting in asymmetric rupture of the main source (Delouis et al., 2002; Li et al., 2002). Rupture propagation was complex involving several subevents possibly triggered on different fault segments. Total source duration, number of subevents and distribution of moment release succeeding the first ~20 s are still controversial (Tibi et al., 2001; Delouis et al., 2002; Gülen et al., 2002; Li et al., 2002; Bos et al., 2004). From source time functions up to 90 seconds, 3-6 subevents have been identified (Tibi et al., 2001; Gülen et al., 2002).

Inversions of teleseismic, ground motion and space geodetic data also indicate distributed slip on separate fault segments with two slip maxima of 5-6 m near Gölcük and Lake Sapanca

(e.g. Bouchon et al., 2002, Reilinger et al., 2000, Gülen et al., 2002, Li et al., 2002). Slip maxima were found between surface and about 12 km depth. Delouis et al. (2002) presented a joint inversion of InSAR, GPS, teleseismic and strong motion data (see also Salichon et al., 2003) delineating four fault segments. Maximum slip is up to 8 m at about 6-12 km depth below Gölcük-Izmit and Lake Sapanca. The Akyazi plain (30.4-30.7°E) is consistently identified as an area of reduced slip < 1 m.

5.6.1.2. Aftershock activity and postseismic slip along the Izmit rupture trace

Postseismic slip estimated from GPS and accumulated over 75 days after the Izmit earthquake was about 0.43 m. The corresponding total geodetic moment is equivalent to $M_w=7.0$ (Reilinger et al., 2000; Bürgmann et al., 2002; Ergintav et al., 2002) and therefore one order of magnitude higher than energy liberated by the >4000 largest aftershocks (see Table 2). This indicates that postseismic deformation was largely aseismic. Modelling of afterslip suggests that maximum creep is expected at depth > 20 km (Reilinger et al., 2000).

Maxima of coseismic and postseismic slip and the aftershock activity are anti-correlated. For example, minima of aftershock activity at 29.5°E - 29.6°E, 30.2°E - 30.3°E in segment 2 and at 30.8°E in segment 4 coincide with the coseismic slip maxima. High coseismic slip in the

	Mw	Mo [10^{20} Nm]	rupture area [km ²]	average slip [m]
Izmit mainshock	7.4	1.4 - 2.0	140 x 20	2.5-2.9
Düzce mainshock	7.1	0.5	60 x 20	0.8-1.0
Cumulative geodetic moment (Izmit-Düzce interevent time)	7.0	0.3	140 x 20	0.43
Izmit-Aftershocks (30 largest)	6.6	0.012	140 x 20	-
Izmit-Aftershocks (4400 largest)	6.8	0.025	140 x 20	-

Table 2: Energy release, rupture area and average slip for the Izmit and Düzce mainshocks (coseismic) and the Izmit postseismic time (after Bouchon et al., 2002; Bürgmann et al., 2002; Ergintav et al., 2002; Örgülü and Aktar, 2001; Reilinger et al., 2000; Tibi et al., 2001; Umutlu et al., 2004).

Izmit-Sapanca (segment 2) and Karadere Düzce (segment 4) areas are correlated with a dominantly strike-slip faulting regime of the aftershocks. In contrast, high aftershock activity and abundant normal faulting events in the Akyazi area and at the western end of the rupture trace coincide with low slip at barriers and step-overs between fault segments.

Significant afterslip occurred at depth along the eastern Karadere segment close to the epicentre of the Düzce mainshock ($M_w=7.1$, Nov 12th, 1999). Interestingly, we observe a relatively high aftershock activity in this region. Focal mechanisms of the three largest aftershocks on this segment ($M \geq 4$, Figure 6) are very similar to the Izmit subevent S2 that occurred about 30 seconds after the mainshock (Tibi et al., 2001) and to the Düzce event, which was about three months after the Izmit earthquake. The three events all occurred within 6 hours after the Izmit mainshock. In contrast, fault plane solutions of small aftershocks show a larger variability, which was not observed on any of the three segments to the west. This observation suggests that small events also reflect small-scale structural complexity of the NAFZ. With increasing magnitude, focal mechanisms increasingly reflect orientation of far-field stresses. This effect was also observed for fluid-injection induced microseismicity (Bohnhoff et al., 2004), but at a lower magnitude level.

5.6.2. Evolution of the stress field at the NAFZ

To perform a thorough analysis of spatial and temporal variations of the stress field along the NAFZ and especially along the Izmit rupture we collected available information on the regional stress field. In addition, we performed stress tensor inversion of focal mechanisms of events prior and during the mainshock. The entire set of information on stress field orientation in the area of investigation is summarized in Table 1. Information on the regional stress field in NW Turkey was taken from the World Stress Map data base (Heidbach et al., 2004; Reinicker et al., 2004) reporting 10 stress orientation measurements for the area of investigation that indicate a mean maximum horizontal stress (S_H) trending N124°E. In addition, Kiratzi (2002) performed stress tensor inversion of the 11 largest earthquakes that occurred in the region since 1943 and revealed a strike-slip faulting regime with NW-SE trending orientation of the maximum principal stress and a near vertical intermediate principal stress. Further information on the preseismic stress field was derived from inverting focal mechanisms obtained by a local network in the easternmost Sea of Marmara during Jan-Sep 1996 (Ergin et al., 1997).

The coseismic stress field during the Izmit event was determined from inverting the focal mechanisms of the six Izmit subevents covering the entire Izmit rupture (Gülen et al.; 2002). Furthermore, the 30 largest aftershocks (Örgülü and Aktar, 2001) served as input to derive the regional postseismic stress field. Interestingly, this data base contains only three EW-extensional normal faulting events from the Akyazi plain and results in a stable stress regime being almost identical to the preseismic regional stress field.

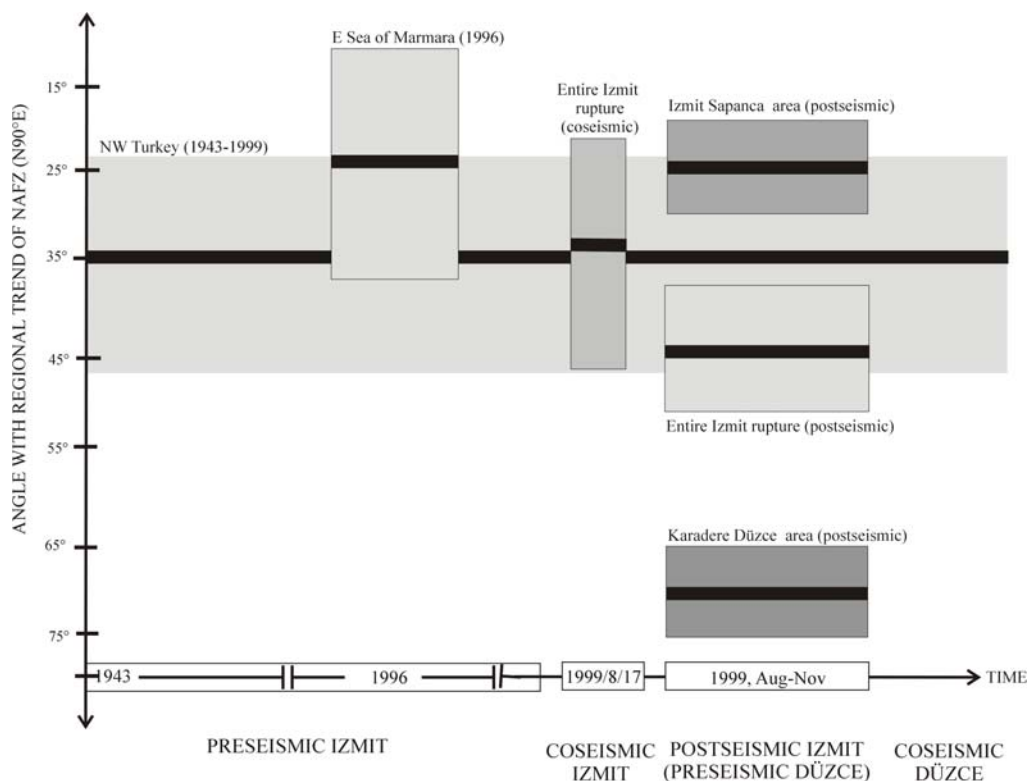


Figure 9: Trend of the maximum principal stress (σ_1) with respect to the average trend of the NAFZ in the Izmit region (EW) plotted with time. Black lines indicate best solution and grey area mark the standard deviation. Shown are results as collected from different published studies and from stress tensor inversion of the here analyzed set of aftershock focal mechanisms (see Text for details).

In Figure 9 the stress field orientations of the data sets as described above is shown in chronological order. The angle between the trend of σ_1 and the regional trend of the NAFZ (N90°E) is indicated by the black lines and the grey-shaded areas represent their standard deviation. The stress field orientations of Kiratzi (2002) and World Stress Map are almost identical with a deviation of $\leq 2^\circ$ and we consider the data to represent the long-term regional stress field in NW Turkey. Noteworthy, the regional stress field is almost identical with the coseismic stress field during the Izmit earthquake while both confidence regions are in the range of 12° . The local stress field within the eastern Sea of Marmara in 1996 differs by $\sim 10^\circ$ to the regional stress field while confidence regions intersect.

The stress field after the Izmit mainshock is spatially heterogeneous along the rupture. Orientations of the principal stresses vary significantly between segments 1-4 reflecting fault complexity. For segments 1, 2 and 4 the maximum compressive stress direction σ_1 is oriented subhorizontal striking N117°E to N159°E. In segment 3, σ_1 is almost vertical (Figure 7, Table 1). Note, that the accuracy for these orientations is in the range of 6-8° for one standard deviation and therefore unprecedentedly small for this region. We interpret the strong partitioning of the postseismic stress field to reflect the local fault structure along the rupture. A striking result of the stress inversion of the aftershock focal mechanisms in the Izmit Sapanca (segment 2) and Karadere Düzce (segment 4) areas is that the local stresses are rotated compared to the regional stress field. It is a widely accepted phenomenon that earthquakes change the state of stress in the vicinity of coseismic slip maxima which results in the reactivation of secondary faults and modification of the local fault structure. In particular, shear failure and the associated drop in shear stress may result in a rotation of the principal stresses acting on the fault. This has been observed for a few earthquakes at strike-slip and reverse faults in California such as the 1992 Landers (Hauksson, 1994; Hardebeck and Hauksson, 1999, 2001), 1989 Loma Prieta (Michael et al., 1990; Zoback and Beroza, 1993), 1983 Coalinga (Michael, 1987b), 1986 Oceanside (Hauksson and Jones, 1988), and 1994 Northridge (Zhao et al., 1997) earthquakes. Stress ratios varied significantly indicating local transtensional faulting ($R = 0.43 - 0.65$, Hauksson, 1994,) and transpression ($R = 0.2 - 0.55$, Michael et al., 1990). Principal stresses were rotated significantly between about 10° - 20° both

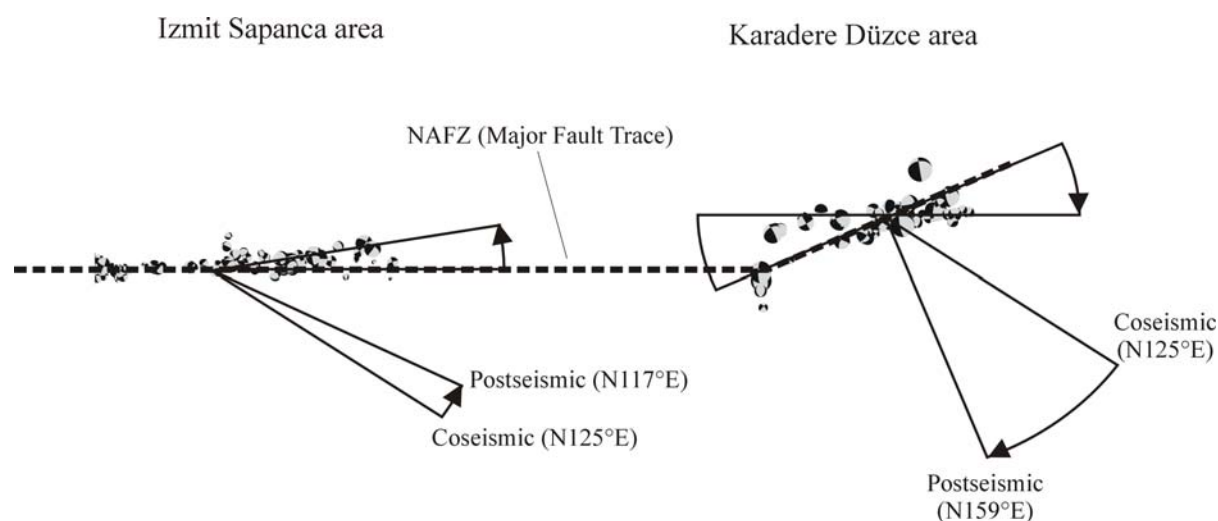


Figure 10: Rotation of the postseismic stress field orientations along the Izmit Sapanca and Karadere Düzce segments, respectively, with respect to the long-term regional stress field. In addition, the distribution of aftershock hypocenters reflects an almost identical rotation in either segment. Rotations are counterclockwise (Izmit Sapanca area) and clockwise (Karadere Düzce area) which is due to the locally varying fault trend that changes by $\sim 25^\circ$.

clockwise and counterclockwise. In some cases (Northridge, Coalinga, Landers) stress rotations reversed with time and varied along the rupture trace. Notwithstanding that stress rotations during the seismic cycle and especially in connection with large earthquakes are in accordance with the present understanding of faulting kinematics, observed stress rotations should be interpreted with care as was shown for the case of Landers by Townend and Zoback (2001).

Assuming stress rotations as discussed above exist, it is generally still a matter of debate whether such rotations are detectable with the present state-of-the-art techniques and data quality. The accuracy of stress field determination is naturally limited to $\sim 5^\circ$ at best, one reason being that the focal mechanisms themselves as input for the stress inversion contain uncertainties. Unfortunately, this accuracy is in the order of or slightly less than the magnitude of the expected rotation itself.

In the Izmit Sapanca area (segment 2) we observe a counterclockwise rotation of the postseismic stress field with respect to the average regional and coseismic stress field in the order of 10° . At this part of the NAFZ a more or less uniform EW-trending fault was activated during the Izmit mainshock. Interestingly, the hypocentral distribution of aftershocks in this area shows the same $\sim 10^\circ$ counterclockwise rotation with respect to the local coseismic fault trend (Figure 10) indicating that the mainshock stress drop induced a local rotation of the stress field that resulted in reactivation of now optimally oriented faults. Stress rotation is also observed at the eastern termination of the Izmit rupture (Karadere Düzce area, segment 4). Here the local fault trend of the NAFZ is $N65^\circ E$ along the Karadere segment where most of the Izmit aftershocks in segment 4 occurred. The postseismic orientations of the three principal stresses in this area are well resolved and separated in their confidence intervals (see Figure 7). Assuming the same regional stress field along the Karadere segment as for the rest of the Izmit rupture we identify a $>30^\circ$ clockwise rotation after the mainshock. Again, as in the Izmit Sapanca area this rotation is consistent with the local distribution of hypocenters that indicate a rotation of $\sim 25^\circ$ (Figure 10). However, at the Karadere segment the stress rotation occurred in opposite direction (clockwise) compared to the Izmit Sapanca segment (counterclockwise). We suggest that the opposing rotations of the postseismic stress field is related to the locally varying trend of the NAFZ segments in relation to the regional stress field that results in different loading states along the fault trace through time. In the central region around the Izmit epicentre, stress drop associated with the Izmit main event reduced the shear stresses acting on the fault segment causing stresses to rotate counterclockwise. However, stress release at the eastern part of the rupture seems to have produced a progressive clockwise rotation of the static stress field, since the Karadere segment is exposed differently to the regional principal stresses by about 25° . As a consequence, the $M_w=7.1$ Düzce mainshock that occurred 87 after the Izmit mainshock and that extended the Izmit rupture by ~ 60 km eastwards occurred not only in a region of positive Coulomb stress (e.g. Parsons et al., 2000) but also in an area of increasingly rotated stress field.

5.7. Conclusions

We have investigated aftershock focal mechanisms of the $M_w=7.4$ Izmit earthquake of Aug 17th, 1999 on the western North Anatolian Fault Zone (NAFZ). Aftershock clusters define 4 individual fault segments. Focal mechanisms surrounding epicentres of the Izmit and subsequent Düzce mainshock ($M_w=7.1$, 12.11.99) indicate dominantly strike-slip but also normal faulting. Aftershocks in the area between Izmit and Düzce segments are mainly related to EW-extensional normal faulting indicating a small pull-apart structure. West of the Izmit mainshock, trains of aftershocks suggest branching of the North Anatolian Fault into three or more active segments differing significantly in dominant focal mechanisms. Areas

with high coseismic slip show aftershocks that are dominantly strike-slip, but low-slip barriers show mostly normal faulting aftershocks.

Stress tensor inversions of the focal mechanisms show systematic rotations of the local stress field following the Izmit mainshock. In the Izmit region the direction of the maximum compressive stress is rotated counterclockwise with respect to the regional stress field. Towards the eastern end of the rupture, stresses are rotated clockwise. We suggest that the opposing rotations of the postseismic stress field is related to the locally varying trend of the NAFZ segments in relation to the regional stress field that results in different loading states along the fault trace through time. The observed temporal variations in orientation of the principal stresses are significant, but can only be detected by dense local networks with a low magnitude threshold permitting the determination of highly confident focal mechanisms as basis for stress inversion. We expect that the observed spatiotemporal changes of the stress field should effect modelling of Coulomb stress changes and local estimates of seismic hazard.

5.8. Acknowledgments

We thank the German Task Force and especially E. Guenther and C. Milkereit for providing the seismic data and for excellent maintenance of the network. We acknowledge contributions by M. Messar and benefited from discussions with C. Janssen and E. Rybacki. We gratefully acknowledge comments by T. Plenefisch and an anonymous reviewer that helped to improve the manuscript.

5.9. References

- Armijo, R., B. Meyer, A. Hubert & A. Barka, 1999. Westward propagation of the North Anatolian Fault into the northern Aegean: timing and kinematics, *Geology*, **27**, 267-270.
- Barka, A. & 21 others, 2002. The Surface Rupture and Slip Distribution of the 17 August 1999 Izmit Earthquake (M 7.4), North Anatolian Fault, *Bull. Seism. Soc. Am.*, **92(1)**, 43-60.
- Bohnhoff, M., S. Baisch & H.-P. Harjes, 2004. Fault mechanisms of induced seismicity at the superdeep German Continental Deep Drilling Program (KTB) borehole and their relation to fault structure and stress field, *J. Geophys. Res.*, **109**, B02309, doi: 10.1029/2003JB002528.
- Bos, A.G., Usai, S. & Spakman, W., 2004. A joint analysis of GPS motions and InSAR to infer the coseismic surface deformation of the Izmit, Turkey earthquake, *Geophys. J. Int.*, **158**, 849-863.
- Bouchon, M., M. N. Töksöz, H. Karabulut, M.-P. Bouin, M. Dietrich, M. Aktar & M. Edie, 2002. Space and Time Evolution of Rupture and Faulting during the 1999 Izmit (Turkey) Earthquake, *Bull. Seism. Soc. Am.*, **92(1)**, 256-266.
- Bürgmann, R., Ergintav, S., Segall, P., Hearn, E.H., McClusky, S., Reilinger, R.E., Woith, H. & Zschau, J., 2002. Time-dependent Distributed Afterslip on and Deep below the Izmit Earthquake Rupture, *Bull. Seism. Soc. Am.*, **92(1)**, 126-137.
- Delouis, B., Giardini, C., Lundgren, P. & Salichon, J., 2002. Joint inversion of InSAR, GPS, Teleseismic, and Strong-Motion Data for the Spatial and Temporal Distribution of Earthquake slip: Application to the 1999 Izmit Mainshock, *Bull. Seism. Soc. Am.*, **92(1)**, 278-299.
- Ergin, M., Aktar, M., Bicmen, F., Yörüük, A., Yalcin, M.N. & Kuleli, S., 1997. Detailed microearthquake monitoring of the Izmit Bay, Aktif Tektonik Arastirma Grubu Birinci Toplantisi, ITÜ, Istanbul.
- Ergintav, S., Bürgmann, R., McClusky, S., Cakmak, R., Reilinger, R.E., Lenk, O., Barka, A. & Özener, H., 2002. Postseismic Deformation near the Izmit Earthquake (17 August 1999, M 7.5) Rupture Zone, *Bull. Seism. Soc. Am.*, **92(1)**, 194-207.
- Fielding, E.J., Wright, T.J., Parsons, B.E., England, P.C., Rosen, P.A., Hensley, S. & Bilham, R., 1999. Topography of northwest Turkey from SAR interferometry: applications to the 1999 Izmit earthquake geomorphology and co-seismic strain, *EoS Trans., Am. Geophys. Union*, **80**, 46, F762.
- Flerit, F., Armijo, R., King, G. & Meyer, B., 2004. The mechanical interaction between the propagating North Anatolian Fault and the back-arc extension in the Aegean, *EPSL*, **224**, 347-362.

- Gephart, J.W. & Forsyth, D.W., 1984. An improved Method for Determining the Regional Stress Tensor Using Earthquake Focal Mechanism Data: Application to the San Fernando Earthquake Sequence, *J. Geophys. Res.*, **89**, 9305-9320, 1984.
- Gephart, J.W., 1990. Stress and the direction of slip on fault planes, *Tectonics*, **9**, 845-858, 1990.
- Grosser, H. & 11 others, 1998. The Erzincan (Turkey) Earthquake (M_s 6.8) of March 13, 1992 and its aftershock sequence, *PAGEOPH*, **152**, 465-505.
- Gülen, L., Pinar, A., Kalafat, D., Özel, N., Horasan, G., Yilmazer, M. & Isikara, A. M., 2002., Surface breaks. Aftershock Distribution, and Rupture Process of the 17 August 1999 Izmit, Turkey, Earthquake, *Bull. Seismol. Soc. Am.*, **92(1)**, 230-244.
- Gurbuz, C. & 16 others, 2000. The seismotectonics of the Marmara region (Turkey): results from a microseismic experiment, *Tectonophysics*, **316**, 1-17.
- Hardebeck, J.L. & Hauksson, E., 1999. Role of fluids in faulting inferred from stress field signatures, *Science*, **285**, 236-239.
- Hardebeck, J.L. & Hauksson, E., 2001. Crustal stress field in southern California and its implications for fault mechanics, *J. Geophys. Res.*, **106**, 21,859-21,882.
- Harris, R.A., 1998. Introduction to a special section; stress triggers, stress shadows, and implications for seismic hazard, *J. Geophys. Res.*, **103**, 24347-24358.
- Hauksson, E., 1994. State of stress from focal mechanisms before and after the 1992 Landers earthquake sequence, *Bull. Seism. Soc. Am.*, **84**, 917-934.
- Hauksson, E. & Jones, L.M., 1988. The July 1986 Oceanside ($M_f=5.3$) earthquake sequence in the continental borderland, southern California, *Bull. Seism. Soc. Am.*, **78(6)**, 1885-1906.
- Heidbach, O., Barth, A., Connolly, P., Fuchs, K., Müller, B., Reinecker, J., Sperner, B., Tingay, M. & F. Wenzel, 2004. Stress maps in a minute: The 2004 World Stress Map Release, *EoS Trans.*, **85(49)**, 521-529, 2004.
- Karabulut, H., M. P. Bouin, M. Bouchon, M. Dietrich, C. Cornou & M. Aktar, 2002. The Seismicity in the Eastern Marmara Sea after the 17 August 1999 Izmit Earthquake, *Bull. Seism. Soc. Am.*, **92(2)**, 387-393.
- King, G.C.P., Stein, R.S. & Lin, J., 1994. Static stress changes and the triggering of earthquakes, *Bull. Seism. Soc. Am.*, **84(3)**, 935-9530.
- Kiratzi, A., 2002. Stress tensor inversions along the westernmost North Anatolian Fault Zone and its continuation into the North Aegean Sea, *Geophys. J. Int.*, **151**, 360-376.
- Kiratzi, A. & Louvari, E., 2001. Source parameters of the Izmit-Bolu 1999 (Turkey) earthquake sequences from teleseismic data, *Ann. Geophysics*, **44**, N.1.
- Langridge, R.M., Stenner, H.D., Fumal, T.E., Christofferson, S.A., Rockwell, T.K., Hartleb, R.D., Bachhuber, J. & Barka, A.A., 2002. Geometry, Slip Distribution, and Kinematics of Surface Rupture on the Sakarya Fault Segment during the 17 August 1999 Izmit, Turkey, Earthquake, *Bull. Seism. Soc. Am.*, **92(1)**, 107-125.
- Li, X., Cormier, V.F. & Töksöz, M.N., 2002. Complex Source Process of the 17 Aug 1999 Izmit, Turkey, Earthquake, *Bull. Seismol. Soc. Am.*, **92(1)**, 267-277.
- McClusky, S. & 27 others, 2000. Global positioning system constraints on plate kinematics and dynamics in the eastern Mediterranean and Caucasus, *J. Geophys. Res.*, **105**, 5695-5719.
- Michael, A.J., 1984. Determination of stress from slip data; faults and folds, *J. Geophys. Res.*, **89**, 11517-11526.
- Michael, A.J., 1987a. Use of focal mechanisms to determine stress: a control study, *J. Geophys. Res.*, **92**, 357-368.
- Michael, A., 1987b. Stress rotation During the Coalinga Aftershock Sequence, *J. Geophys. Res.*, **92**, 7963-7979.
- Michael, A.J., Ellsworth, W.L. & Oppenheimer, D.H., 1990. Coseismic stress changes induced by the 1989 Loma Prieta, California earthquake, *Geophys. Res. Lett.*, **17(9)**, 1441-1444.
- Michael, A.J., 1991. Spatial variations in stress within the 1987 Whittier Narrows, California, aftershock sequence: New techniques and results, *J. Geophys. Res.*, **96**, 6303-6319.
- Michael, A. & Jones, L.M., 1986. Stress fluctuations due to the North Palm Springs earthquake, *Trans. Am., Geophys. U.*, **67**, p.1090.
- Öncel, A. & Wyss, M., 2000. The major asperities of the 1999 $M_w=7.4$ Izmit earthquake defined by the microseismicity of the two decades before it, *Geophys. J. Int.*, **143**, 501-506.
- Örgülü, G. & M. Aktar, 2001. Regional Moment Tensor Inversion for Strong Aftershocks of the August 17, 1999 Izmit Earthquake ($M_w=7.4$), *Geophys. Res. Lett.*, **28(2)**, 371-374.
- Özalaybey, S., M. Ergin, M. Aktar, C. Tapirdamaz, F. Bicman & A. Yörük, 2002. The 1999 Izmit Earthquake Sequence in Turkey: Seismological and Tectonic Aspects, *Bull. Seism. Soc. Am.*, **92(2)**, 376-386.
- Papageorgiou, A.S., 2003. The Barrier Model and Strong Ground Motion, *PAGEOPH*, **160**, 603-634.
- Parsons, T., 2002. Global Omori law decay of triggered earthquakes: Large aftershocks outside the classical aftershock zone, *J. Geophys. Res.*, **107**, 2199, doi: 10.1029/2001JB000646.
- Parsons, T., 2004. Recalculated probability of $M \geq 7$ earthquakes beneath the Sea of Marmara, Turkey, *J. Geophys. Res.*, **109**, doi:10.1029/2003JB002667.
- Parsons, T., Toda, S., Stein, R.S., Barka, A. & Dieterich, J.H., 2000. Heightened Odds of Large Earthquakes Near Istanbul: An interaction-Based Probability Calculation, *Science*, **288**, 661-664.

- Polat, O., H. Eyidogan, H. Haessler, A. Cisternas & Philip, H., 2002. Analysis and interpretation of the aftershock sequence of the August 17, 1999, Izmit (Turkey) earthquake, *J. Seismol.*, **6**, 287-306.
- Reasenber, P.A. & Oppenheimer, D., 1985. FPFIT, FPLOT, and FPPAGE: Fortran computer programs for calculating and displaying earthquake fault-plane solutions. Dept. of Interior, *US Geological Survey, Open-file report*, **85-739**, 109pp.
- Reilinger, R.E. & 12 others, 2000. Coseismic and Postseismic Fault Slip for the 17 August 1999, M=7.5, Izmit, Turkey Earthquake, *Science*, **289**, 1519-1524.
- Reinecker, J., Heidbach, O., Tingay, M., Connolly, P. & Müller, B., 2004. The 2004 release of the World Stress Map (available online at www.world-stress-map.org).
- Salichon, J., Delouis, B., Lundgren, P., Giardini, D., Constantini, M. & Rosen, P., 2003. Joint inversion of broadband teleseismic and interferometric synthetic aperture radar (InSAR) data for the slip history of the Mw=7.7, Nazca ridge (Peru) earthquake of 12 November 1996, *J. Geophys. Res.*, **108**, 2085, doi:10.1029/2001JB000912.
- Stein, R., 1999. The role of stress transfer in earthquake occurrence, *Nature*, **402**, 605-609.
- Stein, R.S., Barka, A. & Dieterich, J.H., 1997. Progressive failure of the North Anatolian fault since 1939 by earthquake stress triggering, *Geophys. J. Int.*, **128**, 594-604.
- Tibi, R., Bock, G., Xia, Y., Baumbach, M., Grosser, H., Milkereit, C., Karakisa, S., Zünbül, S., Kind, R. & Zschau, J., 2001. Rupture processes of the 1999 August 17 Izmit and November 12 Düzce (Turkey) earthquakes, *Geophys. J. Int.*, **144**, F1-F7.
- Töksöz, M.N., Shakal, A.F. & Michael, A.J., 1979. Space-time migration of earthquakes along the North Anatolian Fault and seismic gaps, *PAGEOPH*, **117**, 1258-1270.
- Townend, J. and Zoback, M.D., 2001. Implications of earthquake focal mechanisms for the frictional strength of the San Andreas fault system. *Geol. Soc. Spec. Publ.*, **186**, p. 13-21.
- Umutlu, N., Koketsu, K. & Milkereit, C., 2004. The rupture process during the 1999 Düzce, Turkey, earthquake from joint inversion of teleseismic and strong-motion data, *Tectonophysics*, **391**, 315-324.
- Wright, T., Fielding, E. & Parsons, B., 2001. Triggered slip: observations of the 17 August 1999 Izmit (Turkey) earthquake using radar interferometry, *Geophys. Res. Lett.*, **28(6)**, 1079-1082.
- Yagi, Y. & Kikuchi, M., 2000. Source rupture process of the Kocaeli, Turkey, earthquake of August 17, 1999, obtained by joint inversion of near-field data and teleseismic data, *Geophys. Res. Lett.*, **27(13)**, 1969-1972.
- Yin, Z.M. & Rogers, G.C., 1995. Rotation of the Principal Directions Due to Earthquake Faulting and Its Seismological Implications, *Bull. Seismol. Soc. Am.*, **85(5)**, 1513-1517.
- Zhao, D., Kanamori, H. & Wiens, D., 1997. State of stress before and after the 1994 Northridge earthquake, *Geophys. Res. Lett.*, **24(5)**, 519-522.
- Zoback, M.D. & Beroza, G.C., 1993. Evidence for near-frictionless faulting in the 1989 (M 6.9) Loma Prieta, California, earthquake and its aftershocks. *Geology*, **21(2)**, 181-185.

6. Deformation and Stress regimes in the forearc of the Hellenic subduction zone from inversion of focal mechanisms

This chapter has been submitted for publication. The reference is

Bohnhoff, M., Harjes, H.-P., Meier, T. (2005). Deformation and Stress regimes in the forearc of the Hellenic subduction zone from inversion of focal mechanisms. *J. Seismology* (accepted).

6.1. Abstract

Fault plane solutions for earthquakes in the central Hellenic arc are analyzed to determine the deformation and stress regimes in the Hellenic subduction zone in the vicinity of Crete. Fault mechanisms for earthquakes recorded by various networks or contained in global catalogs are collected. In addition, 34 fault plane solutions are determined for events recorded by our own local temporary network on central Crete in 2000-2001. The entire data set of 264 source mechanisms is examined for types of faulting and spatial clustering of mechanisms. Eight regions with significantly varying characteristic types of faulting are identified of which the upper (Aegean) plate includes four. Three regions contain interplate seismicity along the Hellenic arc from west to east and all events below are identified to occur within the subducting African lithosphere. We perform stress tensor inversion to each of the subsets in order to determine the stress field orientation. Results indicate a uniform N-NNE direction of relative plate motion between the Ionian Sea and Rhodes resulting in orthogonal convergence in the western forearc and oblique (40-50°) subduction in the eastern forearc. There, the plate boundary migrates towards the SE resulting in left-lateral strike-slip faulting that extends to onshore Eastern Crete. N110°E trending normal faulting in the Aegean plate at this part is in accordance with this model. Along-arc extension is observed on Western Crete. Fault plane solutions for earthquakes within the dipping African lithosphere indicate that slab pull is the dominant force within the subduction process and interpreted to be responsible for the roll-back of the Hellenic subduction zone.

6.2. Introduction

The Hellenic subduction zone is the seismically most active region in Europe. There, the convergent plate boundary between the African lithosphere and the Aegean plate as part of Eurasia is located south of Crete in the Libyan Sea. It approaches the passive continental margin of northern Africa due to roll back of the Hellenic subduction zone and the convergence between Africa and Eurasia (e.g. McKenzie, 1970; LePichon and Angelier, 1979; Jackson and McKenzie, 1988; LePichon et al., 1995). The overall rate of convergence is ~4 cm/year (e.g. McClusky et al., 2000). A well-developed Benioff zone was identified by seismicity to a depth of 150-180 km below the central Aegean (e.g. Papazachos, 1973; Makropoulos and Burton, 1981; Papadopoulos et al., 1986; Knapmeyer, 1999; Papazachos et al., 2000) and the subducting lithosphere can be followed down to about 1200 km by seismic tomography (e.g. Spakman et al., 1988; Bijwaard and Spakman, 1998). A tectonic reorganization in the entire south Aegean region at 3.4 Ma may mark the onset of continent-continent collision between the Aegean plate and the continental African plate (Lyon-Caen et al., 1988; LePichon et al., 1995; Mascle et al., 1999) at the western Hellenic arc. This resulted in a complex tectonic frame with a number of details such as the rapid uplift of western Crete (e.g. Lambeck, 1995) that are not yet fully understood. At the central and eastern part of the forearc indications for remnants of oceanic crust were identified (Bohnhoff et al., 2001; Brönnner, 2003; Meier et al., 2004a).

Figure 1 gives an overview on the tectonic setting of the Aegean-Anatolian region with the Hellenic subduction zone. The island of Crete forms the central part of the Hellenic arc. Below the Libyan Sea an accretionary wedge with a sedimentary cover of up to 15 km is located between the active and passive continental margins. Recent microseismicity and surface wave studies (Meier et al., 2004b) as well as active seismic lines (Truffert et al., 1993; Bohnhoff et al., 2001; Brönnner, 2003) allowed to refine the structural model along the Helle-

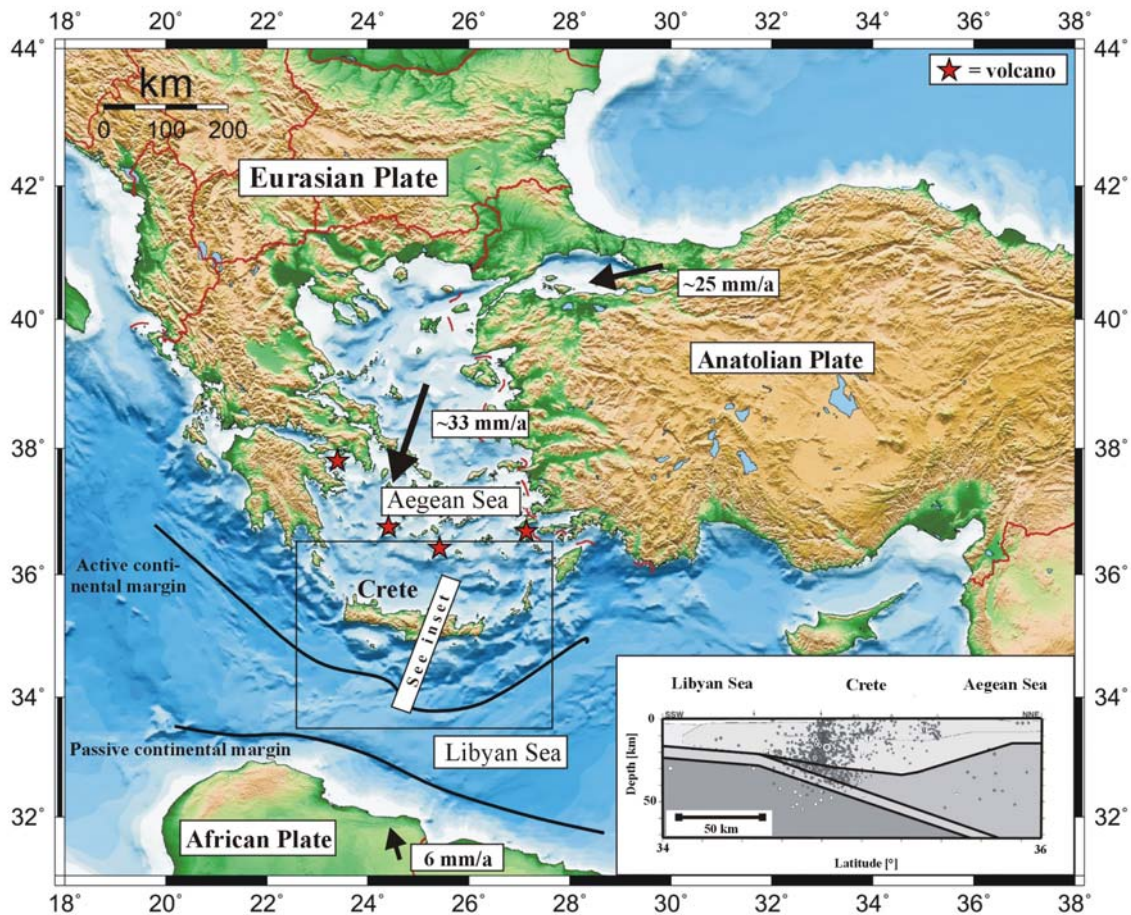


Figure 1: Location map of the Aegean-Anatolian region and its main tectonic elements. The Hellenic Arc is part of the forearc and consists of a number of islands of which Crete is the largest. Stars indicate active volcanic centers along the Hellenic volcanic arc ~ 150 km north of the Hellenic Arc. Bold arrows indicate surface displacement rates with respect to stable Eurasia that are representative for each region (simplified after McClusky et al., 2000). The transect A-B is parallel to the dipping direction of the African lithosphere and shown as a depth section in the lower right. It combines results from microseismicity and surface wave studies in the Hellenic subduction zone (after Meier et al., 2004b). The rectangle marks the area investigated in this study.

nic subduction zone (see inset in Figure 1) exemplifying the complex geometry along a strongly curved plate boundary. The overall seismic activity of the Hellenic subduction zone is small compared to other subduction zones as can be observed from global earthquake catalogs. The distribution of hypocenters in the south Aegean region dominantly follows the Hellenic arc with stronger seismic activity observed in the eastern part. The hypocenters form an amphitheatrically shape of the Benioff zone in first order approximation (see e.g. Bath, 1983; Engdahl et al., 1998; Knapmeyer, 1999; Papazachos et al., 2000) and thus the trend of the steepest descent of the dipping slab significantly varies along the Hellenic arc

In contrast, the GPS horizontal velocities in this region as determined by McClusky et al. (2000) show only minor variation in trend (up to 18°) and magnitude (in the order of mm/a). Several authors have analyzed the stress field at the Hellenic subduction zone mainly based on fault trends and outcropping faults (e.g. Angelier et al., 1982; Meulenkamp et al., 1988; Ten Veen and Kleinspehn, 2003) or analysis of large earthquakes (Taymaz et al., 1990; Papazachos et al., 2000). In this study, we analyze fault mechanisms for earthquakes covering a broad magnitude range along the Hellenic arc in the vicinity of Crete. The area of investigation is indicated by the rectangle in Figure 1. We attempt to determine the deformation and stress regimes based on fault plane solutions that were collected from various

local and regional studies as well as global catalogs. Furthermore, we newly determined fault plane solutions for smaller events recorded by our own local network in the Messara plain (Central Crete).

6.3. Data base and procedure applied

To compile a complete data base of fault mechanisms available we collected data from various published studies as well as from global catalogs available through the World Wide Web. We restricted the data base to events within 22.5-27.5°E and 33.5-36.5°N with no depth limitation. This resulted in a total of 352 events (including multiple occurrences) that cover a magnitude range between 0 and 6.5. Table 1 (see Appendix) gives an overview on all events with occurrence time, hypocentral coordinates, magnitude, fault mechanisms and information on the relevant source. The sources that contributed to the data base and number of fault plane solutions taken are: Becker, 2000 [37 fault plane solutions]; Benetatos et al., 2004 [11], DeChabalier et al., 1992 [16]; Delibasis et al., 1999 [29]; Hatzfeld et al., 1993a and 1993b [37]; Jost et al., 2002 [12]; Kiratzi and Louvari, 2003 [8]; McKenzie, 1972 and 1978 [7]; Papadimitriou, 1993 [3]; Papadopoulos et al., 1986 [21]; Papazachos, 1973, Papazachos and Papazachou, 1997, Papazachos et al., 1991 and 2000 [24]; Taymaz et al., 1990 [14]; Harvard CMT, <http://www.seismology.harvard.edu/CMTsearch.html>, 1977-2004 [42]; MEDNET INGV, <http://mednet.ingv.it/events/QRCMT/Welcome.html>, 2001-2004 [10]; SED ETH Zürich, <http://www.seismo.ethz.ch/mt>, 2000-2004 [43]; USGS (except CMT solutions), <http://neic.usgs.gov/neis/sopar>, 1982-2002 [4]. Clearly, this catalog is heterogeneous as it contains recordings from local, regional and global networks covering different time intervals as well as some relocations and redeterminations. Furthermore, non-uniform methods were

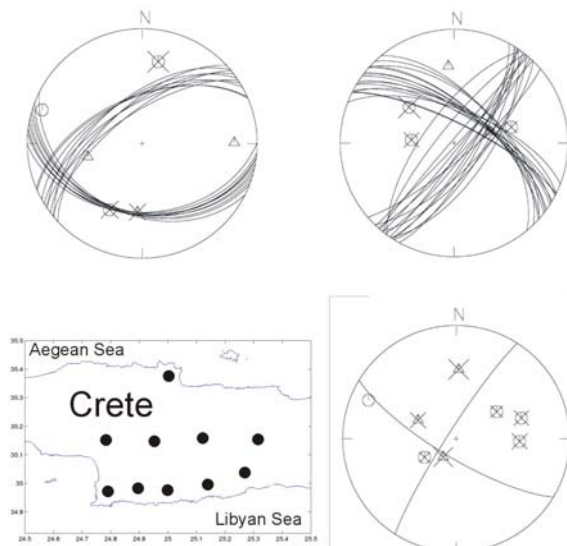


Figure 2: Selected fault plane solutions for earthquakes recorded by the temporal network on southern central Crete. Projection is lower hemisphere. Circles and diamonds represent compressional and dilatational first motions of the P wave, respectively. Crosses indicate stations for which SH/P amplitude ratios were determined. In the lower left the station distribution of our seismic network and two permanent stations of the GEOFON network are shown.

used to determine the fault plane solutions (for description of methods used to determine the fault plane solutions in the individual studies we refer to the relevant article or webpage). Only some authors (Taymaz et al., 1990; Benetatos et al., 2004) give information on the accuracy of their fault mechanisms which was considered when skipping multiple-occurring events (see below). However, we assume having good control on the error bounds as we can compare the solutions from different sources for the same event in a number of cases. We thus estimate the overall errors for strike, dip and rake to be 15°. This value needs to be considered when discussing the significance of our results later in the text. Some earthquakes occur plurally in Table 1 as they are listed in more than one study or catalog and in some cases non-uniform fault mechanisms were given to the same event. We therefore carefully studied the entire catalog and skipped multiple occurrences of individual earthquakes by eliminating all but the most reliable

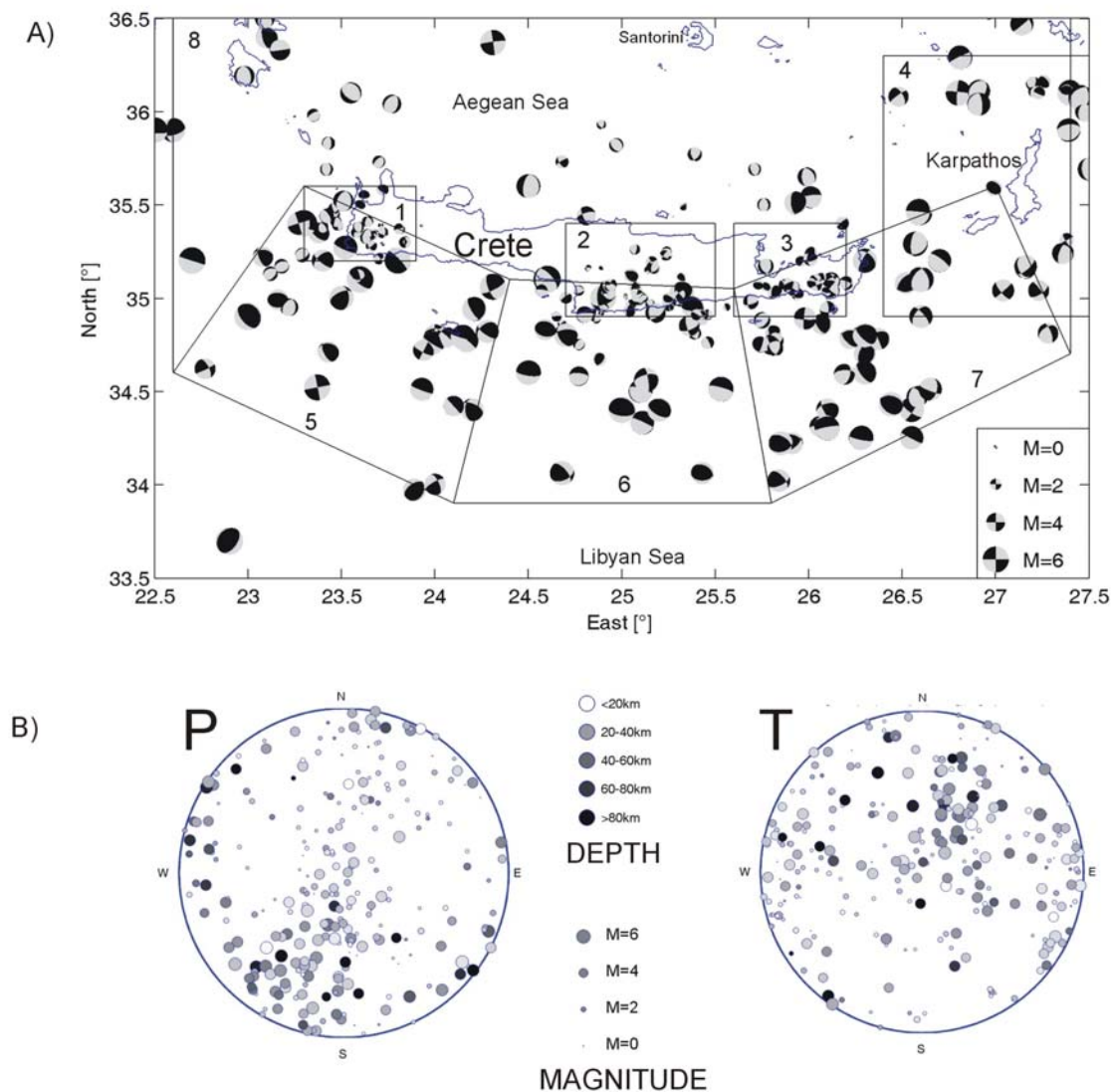


Figure 3: a) Data set analyzed in this study. Shown is the lower hemisphere projection of all 264 fault plane solutions that were collected or determined, respectively (see text for details). The size of the beachballs is scaled to event magnitude. The polygons show the surface boundaries of the subvolumes 1-8 that were identified based on types of faulting (seismicity within the Aegean plate, interplate seismicity and seismicity within the dipping African lithosphere) and spatial clustering of faulting mechanisms (for seismicity within the Aegean plate): 1=Aegean plate, Western Crete; 2=Aegean plate, Central Crete; 3= Aegean plate, Eastern Crete; 4= Aegean plate, Karpathos area; 5= interplate seismicity, Western Hellenic arc; 6= interplate seismicity, Central Hellenic arc; 7=interplate seismicity, Eastern Hellenic arc; 8=seismicity within the dipping African lithosphere. b) Distribution of P (left) and T (right) axes for all 264 fault plane solutions in equal area lower hemisphere projection. Size of circles is scaled with magnitude and shading indicates hypocentral depth.

solution. We define the most reliable solution as the one determined with the best station configuration and most advanced method (which was usually that based on regional waveform modelling). This procedure reduced the catalog to 232 fault mechanisms.

In addition to the collected fault plane solutions we determined source mechanisms for selected microearthquakes that were recorded by our own local network in southern central Crete in 2000/2001 (see Meier et al., 2004b). The network consisted of eight stations surrounding the Messara plain (see Figure 2, lower left). All stations were equipped with

MARK 3C-L4 seismometers and operated at a 50 Hz sampling rate. Recordings from nearby permanent stations of the GEOFON network (Hanka and Kind, 1994) were added to improve the focal coverage for local events. To determine the source mechanisms we applied the FOCMEC program (Snoke et al., 1984; Snoke, 2003) that performs a grid-search assuming a pure double-couple mechanism. P wave polarities as well as SH/P amplitude ratios served as input data. To allow confident fault plane solutions we selected only events that occurred within or near the network and skipped those with errors $>15^\circ$. This resulted in a total of 34 fault plane solutions covering a magnitude range from 0.3-3.5. Three examples of fault plane solutions and the station distribution of the seismic network in central Crete are shown in Figure 2.

Finally, the entire data set of fault mechanisms for earthquakes along the central Hellenic arc consists of 264 fault plane solutions that form the base for further analysis. Figure 3a shows the entire catalog of fault plane solutions in a map view of the lower hemispheres. To further analyze the data base we focus on the orientations of maximum compression (P) and tension (T) in the following. In Figure 3b we plotted the P and T axes of the entire catalog in an equal-area projection of the lower hemisphere and scaled the size and shading of circles with magnitude and hypocentral depth, respectively. The distribution of P and T axes indicates that the stronger and deeper events show preferred orientations whereas the smaller and shallower events indicate a comparatively high diversity of mechanisms. The magnitude frequency of all earthquakes is shown in Figure 4. The catalog is complete for magnitudes ≥ 5 . The large number of smaller ($M < 3$) events documents the contributions from local networks on Crete that were operated for several (3-18) months. A remarkable decrease of number of events is observed within the range $3 < M < 5$. We explain this by the fact that such events are not recorded by the permanent global network (which allows completeness of $M=4$ only since the middle 1990s) due to their size nor by local networks due to their short recording period. To analyze the data set for spatial clustering of faulting mechanisms we proceeded as follows: As a first step we defined a northward dipping layer of ~ 25 km thickness representing the contact zone between upper Aegean and lower African plate. In fact this zone is supposed to be thinner. However, we have to take into consideration the location error of the globally recorded events for the hypocentral depth which is supposed to be in the order of ± 10 km. Furthermore, the complex geometry of the Hellenic subduction zone requires some simplification when trying to analyze the seismic activity at the plate contact zone as a whole. We refer to all events located within this layer as interplate earthquakes in the following. In a second step, this layer was subdivided into three segments along the Hellenic arc from West to East. The dip of each segment was adjusted following structural models of the forearc region that were derived from wide angle seismics (Bohnhoff et al., 2001; Brönnner, 2003), surface wave and receiver function analysis (Li et al., 2003; Meier et al., 2004a; Endrun et al., 2004) and moving source profiles (Truffert et al., 1993). Furthermore, we implement data from a Moho map of the Eastern Mediterranean (Marone et al., 2003). We defined all events above the contact zone as brittle failure within the upper Aegean plate and all events below as earthquakes within the dipping

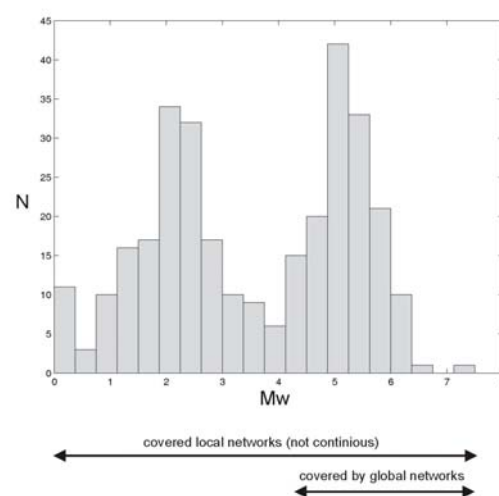


Figure 4: Magnitude frequency for the entire set of fault mechanisms investigated in this study. The catalog covers the time interval 1959-2004 and is complete for $M \geq 5$. A large number of events with small magnitudes were recorded by local networks in distinct regions during several months. Therefore this catalog is somewhat heterogeneous (see text).

African lithosphere. In a third step we scanned all events within the Aegean plate for spatial clustering of P and T axes. We identified four distinct subvolumes with significantly varying clustering of fault mechanisms. This resulted in a total of eight subvolumes (1-4 within the Aegean plate, 5-7 interplate seismicity, 8 within the dipping African lithosphere) that are described in the following.

6.4. Results

6.4.1. Fault mechanisms within the Aegean plate

Most of the fault mechanisms within the Aegean plate group into four subvolumes with significantly different types of characteristic faulting and level of clustering. Figure 5 combines these four subvolumes in a map view of their fault plane solutions and distributions of P and T axes within each subvolume. The westernmost region combines 28 events on and offshore western Crete at a maximum hypocentral depth of 17 km (subvolume 1). The events cover a magnitude range between 0.0 and 4.5. The majority of T axes trends EW at shallow plunge whereas the P axes have a dominant steep plunge and some being shallow with an average NS trend. This reflects a normal faulting regime for western Crete that is currently in

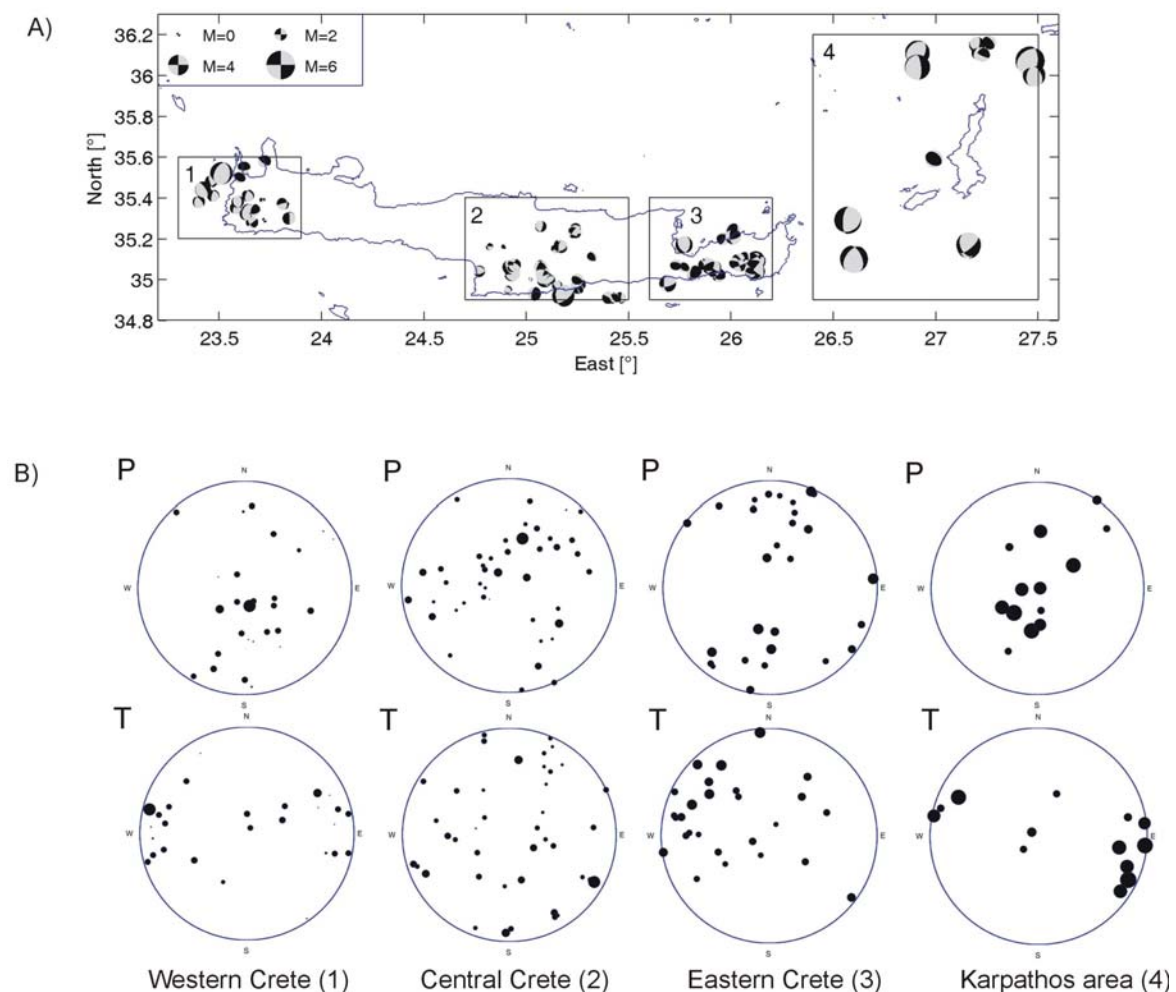


Figure 5 : a) Map view of all fault plane solutions for earthquakes within the Aegean plate that are contained in subvolumes 1-4 (see Figure 3a). b) Distributions of P (top) and T (bottom) axes for each of the four subvolumes. Size of circles scales with magnitude and is enlarged by a factor of two compared to Figure 3b.

the state of EW extension. In contrast, no preferred orientation of the P and T axes was identified in central Crete (subvolume 2). A total of 43 events are contained in this subvolume most of which occurred below the Messara plain in southern central Crete down to 20 km depth. Magnitudes do not exceed $M=4.4$. Whereas most P axes exhibit dominant trends at $N20^{\circ}$ - 70° E subsets based on hypocentral distribution following the main tectonic features of the Messara plain does not result in a more uniform distribution of P and T axes. The distribution of P and T axes can thus not be the result of a locally varying deformation regime, at least not at the scale resolved by the detection threshold of the local networks operated in this region. One possible explanation for such a heterogeneous distribution could be a non-uniform stress field within this subvolume. We refer to this point later in the text.

Further to the East a total of 28 events were investigated that all occurred at depth levels between 10 and 25 km below Eastern Crete (subvolume 3). The depth distribution is different to Western and Central Crete where most events occur at shallower depth. The distribution of P and T axes indicates a predominant strike-slip mechanism with components of mainly reverse but also normal faulting. Interestingly, the P axes tend to the N as well as to the S at a plunge of 20 - 45° . In contrast, the T axes are concentrated to $N270^{\circ}$ - 320° E with a similar plunge. Thus, the fault planes are left lateral, SW/NE oriented and steeply dipping to the SE or right lateral, NW/SE oriented and steeply dipping the NE.

The easternmost subvolume 4 covers the area around the island of Karpathos and contains 13 events. These occurred at depths between 5 and 20 km and are –on average- of greater magnitude compared to the three subvolumes to the West. Although they are distributed over a much wider area than the subsets on Crete, their faulting mechanisms show a stronger clustering of P and T axes indicating an ~EW-extensional deformation within the Aegean plate between Crete and Rhodos. Comparing the four subvolumes within the upper crust with respect to their magnitude contents suggests that stronger shallow events occur more frequently in the east than in the west. This correlates with the observation that the eastern part of the Hellenic subduction zone has higher seismic activity in general (see e.g. ISC catalog by Engdahl et al., 1998). Shallow seismic events are leaking in the Karpathos region as no local network was operated there.

6.4.2. Fault mechanisms of interplate seismicity:

A total of 30 events were classified as interplate earthquakes as they occurred within the three northward dipping layers of ~25 km thickness as described above. In Figure 6 the three subvolumes are plotted in a map view as well as in a depth section where upper and lower boundaries of the contact zone are indicated. The three subvolumes contain 15, 7 and 8 events for the western, central and eastern part, respectively, and cover a magnitude range from 4.0 - 6.5 (smaller magnitudes were excluded as they may have larger location errors due to insufficient station coverage for regional networks on Greek territory). The P and T axes of interplate events in all three subvolumes have a preferred orientation of their deformation axes indicating shallowly N-NNE dipping thrust faulting. From the overall tectonic setting we can conclude that the steep plane does not represent the fault plane. Thus, the interplate events indicate a N-NNE trending direction of relative plate motion between the Aegean and African plates. This direction corresponds with measurements of the recent surface deformation in the south Aegean region (McClusky et al., 2000; see also black arrows in Figure 1). From west (subvolume 5) to east (subvolume 7) we observe a decreasing level of clustering of P and T axes in combination with small number of events contained in the subvolumes.

Furthermore, two of the subvolumes (5 and 7) contain a smaller number of strike-slip events that are among the best-constrained ones. The latest of these occurred in March 2004 south of

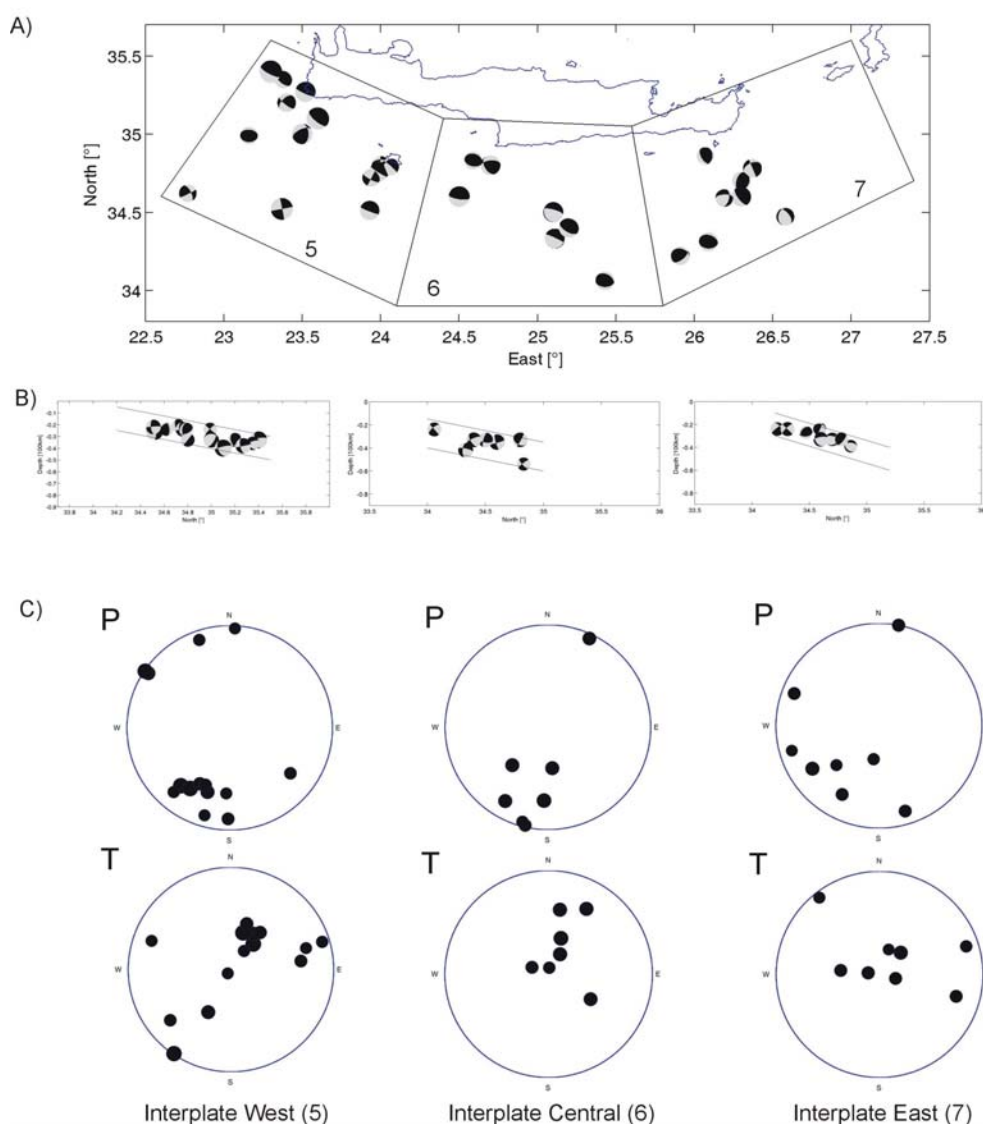


Figure 6: a) Map view of all fault plane solutions for earthquakes within the contact zone between upper (Aegean) and lower (African) plate subdivided into three segments along the Hellenic Arc from West to East (subvolumes 5-7, see Figure 3a). b) Depth sections for the three subvolumes shown in 6a). Upper and lower boundaries for the contact zone were fixed based on existing structural models of the Hellenic subduction zone taking into consideration the depth error for events located with global networks (~ 10 km). Note that the beachballs are rotated according to the viewers' perspective, i.e. lower hemisphere projection, seen from the East. c) Distributions of P (top) and T (bottom) axes for each of the three subvolumes. Size of circles scales with magnitude and is enlarged by a factor of two compared to Figure 3b.

Western Crete near the island of Gavdos (see Figure 6). Such events might reflect brittle failure along pre-existing faults within the upper crust although their hypocentral depth was uniformly set to 33 km as standard depth in the global catalogs. However, the overall set of interplate events indicates a N-NNE trending direction of relative motion between the Aegean and African plates that is uniform along the Hellenic arc.

6.4.3. Fault mechanisms of seismicity within the African lithosphere:

All hypocenters below the contact zone were identified as seismicity within the subducting African lithosphere (subvolume 8, 28 events). In Figure 7 the fault plane solutions of these events are plotted in a map view and as NS-depth section, respectively. The distribution of P

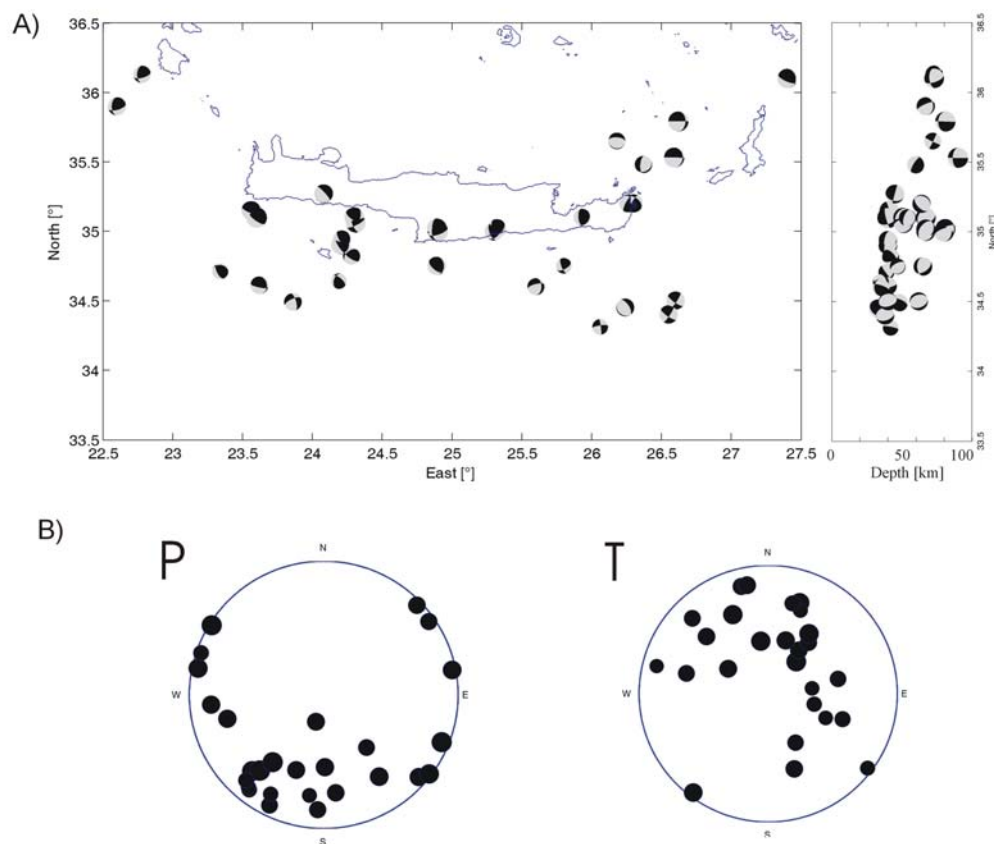


Figure 7: a) Map view and depth section of all fault plane solutions for earthquakes within the subducting African lithosphere (subvolume 8, see Figure 3a). In the depth section the beachballs are rotated according to the viewers direction, i.e. lower hemisphere projection seen from the East.

b) Distribution of P (left) and T (right) axes within subvolume 8. Size of circles scales with magnitude and is enlarged by a factor of two compared to Figure 3b.

and T axes differs from all other subvolumes. Whereas the compressional axes cover a wide azimuthally range (N110-270°E) at shallow plunge, the tensional axes cluster at azimuths between N300°E and N30°E at an average plunge of 45°. Thus, a relevant part of the fault mechanisms within the subducting lithosphere is similar to those observed for the interplate seismicity (shallow thrust faulting; see Figure 6) whereas the majority of fault mechanisms have T axes parallel to the dipping direction of the slab and shallow P axes with considerable scatter of their azimuth. We interpret this distribution to reflect two different types of faulting: A group of about five events reflects a nearly identical deformation mechanism as the interplate seismicity. We classify these events as interplate events which did not match the (simplified) geometry of the contact zone assumed here due to 1. Their error in hypocenter location and 2. Local uncertainties in the existing structural models of the south Aegean region (that do not contain all local structural variations along the strike of the Hellenic arc). Thus, it is a difficult task to relate every single event to a certain type of seismicity (interplate versus in slab). Eliminating these five interplate events results in a sharper image of slab-related faulting mechanisms. The majority of events within the African lithosphere reflect slab-pull as dominant deformation mechanisms with both P and T axes being in plane with the dipping slab. The T axes point towards the dipping direction (N-NNE) whereas the P axes are dominantly trending EW.

6.5. Stress tensor inversion

A stress tensor inversion using the technique of Michael (1984, 1987) was applied to the catalog as a whole as well as individually to the eight subvolumes. The algorithm uses the statistical method of bootstrap resampling and allows determining the orientation of the three principal stresses (σ_1 = maximum, σ_2 = intermediate and σ_3 =minimum) as well as a relative stress magnitude $R=(\sigma_2-\sigma_3)/(\sigma_1-\sigma_3)$, $0<R<1$. These parameters are determined by finding the best fitting stress tensor to the observed focal mechanisms. Assumptions that need to be fulfilled by the input data are: (1) stress is uniform in the area of investigation during the observed time interval, (2) the earthquakes are shear-dislocations on pre-existing faults, and (3) slip occurs in the direction of the resolved shear stress on the fault plane.

The reliability of the deduced stress field orientation (given as the so-called misfit) reflects the level of stress field heterogeneity. We do not discuss the stress tensor inversion techniques here in detail but refer to the relevant articles where the methods themselves and their applications are entirely discussed (e.g. Gephart and Forsyth, 1984; Gephart, 1990; Michael, 1987; Michael, 1991; Hardebeck and Hauksson, 2001; Bohnhoff et al., 2004). The inversion result for the entire catalog reveals a well-constrained NS orientation for the maximum principal stress (σ_1) at shallow dipping angle. In contrast, no clear separation between the intermediate (σ_2) and smallest (σ_3) principal stresses could be identified when considering the 95% (2σ) confidence intervals (Figure 8). This, however, is not surprising considering the varying deformation regimes within the eight subvolumes as discussed in the previous section that are all compatible with \sim NS trending shallow orientation of σ_1 but indicating different directions for σ_2 and σ_3 .

Inversion results for the individual subvolumes reveal the following principal results (see Figure 9 for polar projection of the principal stress axes within each subset and Table 2 for exact values of trend and plunge of σ_{1-3} , misfit and R). Western Crete has a well-defined horizontal EW-trending direction of σ_3 whereas σ_1 and σ_2 overlap in their confidence intervals

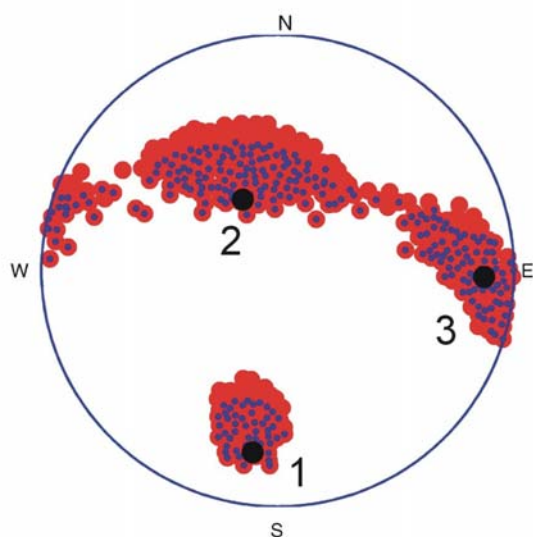


Figure 8: Result of stress tensor inversion for the entire catalog containing 264 fault plane solutions (see Figure 3a). Bold black dots represent the best fitting orientations for the three principal stresses (1=maximum, 2=intermediate ; 3=minimum). Small black dots and large gray dots represent the 1σ (68%) and 2σ (95%) confidence intervals.

For Central Crete no preferred orientation of the stress tensor was found which was expected due to the highly heterogeneous deformation axes contained in this subvolume. Eastern Crete reveals a well-defined orientation for σ_3 that trends EW (which is similar to Western Crete) but at 50° dipping angle. This is compatible with a left-lateral strike-slip regime with components of reverse faulting. σ_1 and σ_2 are not clearly separated in their 95% confidence intervals. However, their 68% confidence intervals do not overlap indicating a $N30^\circ E$ trending subhorizontal orientation for σ_1 . The stress field around Karpathos is very similar to that on Western Crete but rotated clockwise by $\sim 20^\circ$. Inversion results for interplate seismicity should be interpreted carefully due to the comparatively small number of fault mechanisms contained in the subvolumes 5-7 (15, 8 and 7 events, see discussion in Bohnhoff et al., 2004). The best solutions for σ_{1-3} are not as well con-

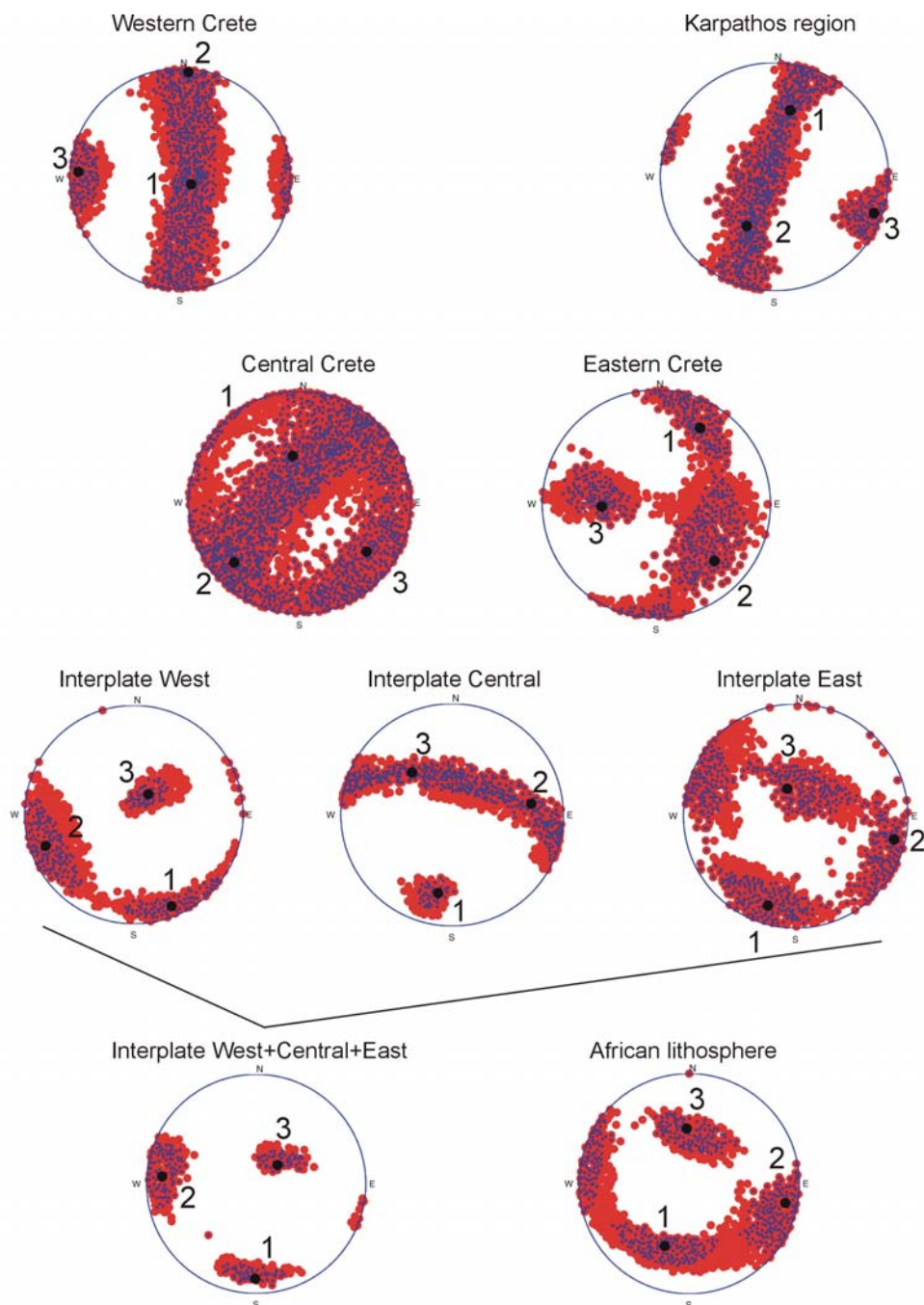


Figure 9 : Results of stress tensor inversion for the eight subvolumes and for the entire set of interplate events as combination of subvolumes 5-7. For explanation of symbols see Figure 8.

Set.	no fps	σ_1 (tr/pl)	σ_2 (tr/pl)	σ_3 (tr/pl)	misfit	R
0	264	188/23	334/63	92/14	0.30	0.48
1	28	115/81	4/3	274/8	0.24	0.70
2	43	351/55	228/21	126/26	0.33	0.59
3	28	30/24	135/30	267/50	0.24	0.60
4	13	14/40	210/49	110/8	0.16	0.83
5	15	157/10	250/15	35/71	0.12	0.54
6	7	180/29	82/29	316/46	0.05	0.27
7	8	193/17	104/11	343/69	0.15	0.50
8	28	201/39	101/12	357/48	0.22	0.63
567	30	181/15	274/15	49/69	0.12	0.50

Table 2 : Results of stress tensor inversion for the entire data base as a whole (termed subvolume 0), for the eight subvolumes (termed subvolume 1-8) and for the sum of interplate events (termed subvolume 567). Results contain number of fault plane solutions within the relevant subvolume, directions for the three principal stresses (σ_{1-3}) in terms of trend and plunge, misfit and relative stress magnitude (R).

straint as for the subvolumes 1-4 discussed above. We therefore combined all fault mechanisms contained in the subvolumes 5-7 (i.e. all interplate events) to one subset. The inversion result gives clear indication for a uniform stress field along the entire part of the Hellenic arc observed here indicating a thrust faulting regime with a subhorizontal and N-NNE trending direction of σ_1 . σ_3 dips at $\sim 70^\circ$ with a trend of about N50°E and σ_2 is almost horizontal trending EW. The stress field within the African lithosphere exhibits a well defined direction for σ_3 that is trending NS at $\sim 50^\circ$ plunge. Different than for the interplate seismicity, σ_1 and σ_2 are not clearly separated but isolated at 68% confidence intervals which is well explained by the five interplate events contained in this subvolume as discussed above. The stress field is compatible with slab pull as dominant force within the dipping slab.

6.6. Discussion

Western Crete reflects a clear normal faulting regime with dominant extension towards EW. Similar results were found earlier for this region based on fault plane data (Lyon-Caen, 1988; Hatzfeld et al., 1993a and 1993b; Jost et al., 2002; their data are contained in the here compiled catalog) and from major fault trends, aerial photographs and outcropping faults (Angelier et al., 1982). Doutsos and Kokkalas (2001) identified normal faulting on Western Crete but with no preferred orientation for σ_3 . Their data, however, cover also earlier stress regimes of different orientation, whereas the data base analyzed in this study reflects the present (last ~ 50 years) tectonic setting. We interpret the present regime on Western Crete to reflect arc-parallel extension. The Karpathos area reflects a similar regime but rotated clockwise by $\sim 20^\circ$. The orientation of the smallest principal stress is thus significantly oblique with respect to the strike of the Hellenic arc at this part (see Figure 1). This is incompatible with the interpretation given by Benetatos et al. (2004) who analyzed focal mechanisms of the Aegean region. They found EW-extension for the eastern Hellenic arc and interpret this as along-arc extension (their Figures 5+6).

Obviously, the extensional domains on Western Crete and around Karpathos are decoupled from the sinistral transtensional fault zone that is located south of Central and Eastern Crete. This fault zone consists of three branches misleadingly called Ptolemeus, Pliny and Strabo 'trenches' (indicated by dotted arrows in Figure 10). The term 'trench' is misleading as these structures do not represent subduction trenches as observed at various forearcs of subduction zones worldwide but, in contrast were identified as deep-sea depressions with wedge-shaped sedimentary basins of up to 4 km thickness (Bohnhoff et al., 2001). Furthermore, these branches have a dominant sinistral strike-slip faulting (LePichon and Angelier, 1979; Huchon et al., 1982; Huguen et al., 2001). Fault mechanisms for Eastern Crete reflect a subhorizontal NE trending direction for σ_1 and a 40-50° dipping EW-trending direction for σ_3 . This correlates with the main fault trend of the three deep-sea depressions which is NE to ENE (Angelier et al., 1982). Surprisingly, the fault mechanisms indicate sinistral transpression rather than transtension. The Eastern part of Crete might thus reflect a continuation of the Ptolemeus branch at slightly modified trend (ENE versus NE). This and the fact that Eastern Crete underwent significantly less stretching compared to the crust below the Libyan Sea (see Bohnhoff et al., 2001) might be responsible for the change from transtension to transpression. Furthermore this might be related to the laterally varying vertical deformation on Crete that is higher on Western and Eastern Crete compared to the central part of the island (Lambeck, 1995; their figure 14). This might also be a possible explanation of the heterogeneous stress field in Central Crete as observed here and for the high scatter of fault trends along this part of Hellenic arc in general (Angelier et al., 1982). Note, that this is different to western Crete where incipient collision is responsible for a blocked state which is probably one reason for the rapid uplift of this part of the island. The uplift seems to occur along steep normal faults as

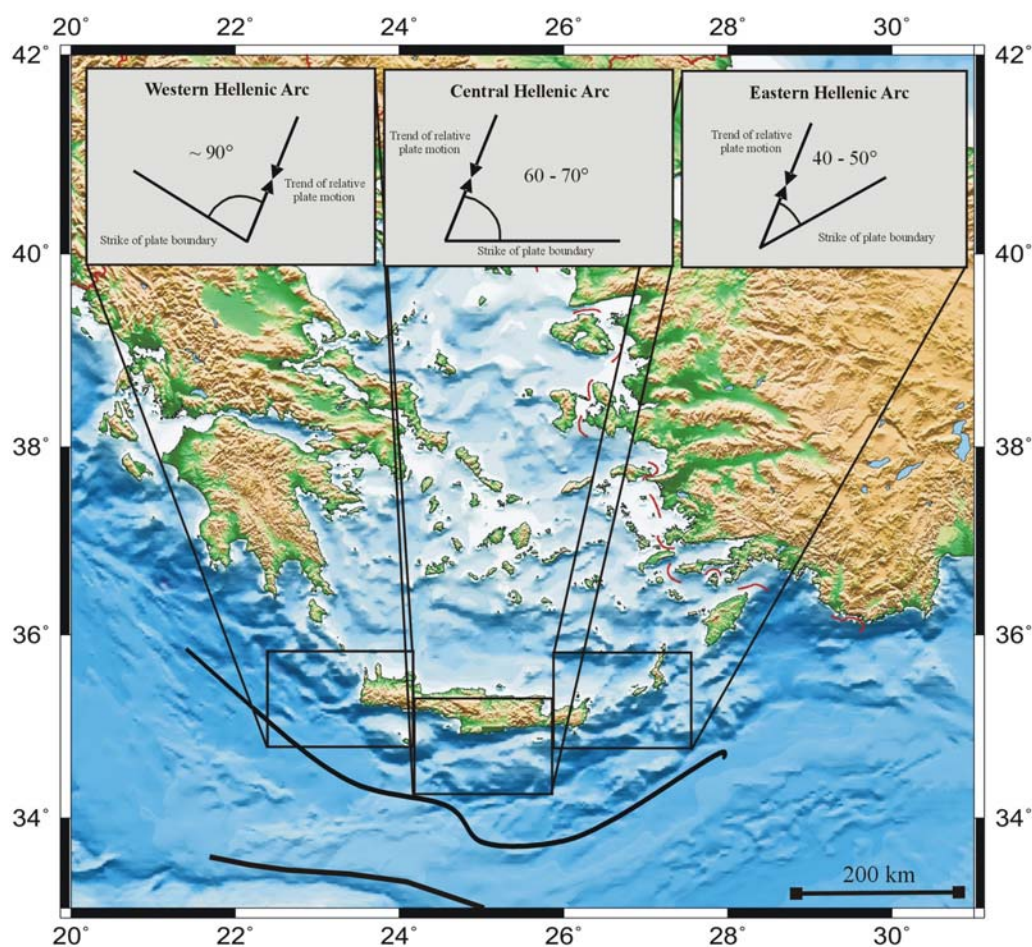


Figure 10: Angle between the direction of relative plate motion (that was identified to be uniform along the Hellenic arc) and the strike of the plate boundary for the Western, Central and Eastern Hellenic arc. Arrows indicate the deformation regime within the upper Aegean plate along the Hellenic arc as determined in this study. Dotted arrows mark the sinistral transensional fault zone at the Ptolemy, Pliny and Strabo deep sea depressions. Black lines indicate the active and passive continental margin, respectively.

suggested by a number of events contained in subvolume 1 (see Figure 5). Ten Veen and Kleinspehn (2003) report on N70°E sinistral faults on southern central Crete to play a major role within the tectonic reorganisation of the Hellenic subduction zone at about 3.4 Ma. These faults are also included in our data and could be interpreted as presently reactivated remnants of the Plio-Pleistocene deformation.

Fault mechanisms of interplate seismicity indicate a uniform N-NNE trending direction of relative plate motion between the Aegean and African plates along the Hellenic arc between the Ionian Sea and Rhodes. This confirms earlier results that partly focussed on smaller portions of the Hellenic subduction zone. McKenzie (1978) proposed N31°E and LePichon and Angelier (1979) argued for N45°E as main trend for the relative motion between Africa and Crete. Taymaz et al. (1990) analyzed events at ~40 km depth and found slip vectors trending N25°E. Our data base covers the entire Hellenic arc between the Ionian Sea and Rhodes and shows that N12°E is the representative orientation of relative plate motion for this part of the Hellenic subduction zone with an accuracy of $\pm 15^\circ$ (see Figures 6 and 9). This result correlates with the GPS horizontal velocities in a Eurasia fixed reference frame (McClusky et al., 2000; see Figure 1) within the accuracy resolved here. The amphitheatrically shape of the Benioff zone as derived from the spatial distribution of hypocenters (e.g. Knapmeyer, 1999), however, is not easily explained by a uniform direction of convergence. We interpret the shape of the Benioff zone to reflect the mechanical response of the subducting plate to the curved geometry of the plate boundary. Slab pull results in roll-

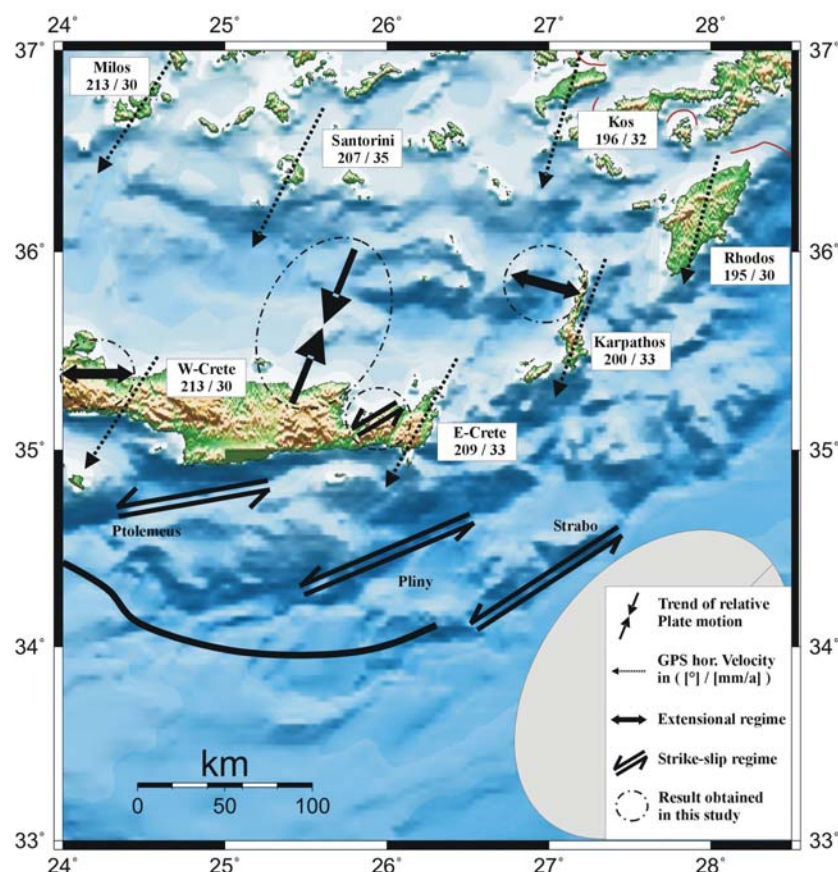


Figure 11 : Summary of results focussing on the eastern Hellenic arc. Dotted arrows indicate strike (direction) and magnitude of the GPS-derived velocity field at the surface (after McClusky et al., 2000) that shows second order variations in the south-east Aegean region. Convergent black arrows indicate the direction of relative plate motion (uniform along the Hellenic arc) and divergent black arrows indicate the trend of extension on Western Crete and in the Karpathos area. Remnants of oceanic crust southeast of the Hellenic arc (indicated by the gray ellipse) form space for retreatment of the plate boundary at this part of the Hellenic as which correlates with the counterclock wise rotation of GPS-derived trend of surface deformation while proceeding from West to East.

back and forces Crete to become the leading edge of the plate boundary. This rollback and the curved earth's surface force the plate boundary to become concave with the consequence that the slab cannot descend in a simple planar shape.

A second major consequence of the uniform direction of relative plate motion along the Hellenic arc is the significantly varying angle of its trend to the strike of the plate boundary along the arc (see Figure 10). Both directions are approximately orthogonal in the western Hellenic arc. There, an incipient collision is likely to occur at present as was also proposed by Mascle et al. (1999) and TenVeen and Kleinspehn (2003). This might also be one principal reason for the rapid uplift of this part of the island. At Central Crete both directions form an angle of 60-70° indicating a state of oblique subduction. The obliqueness increases further to the East towards Karpathos/Rhodos where it reaches a deviating angle of 40-50°.

At the central and eastern forearc, indications for remnants of oceanic lithosphere were identified by wide aperture seismic profiles (Bohnhoff et al., 2001; Brönnner, 2003) that do not exceed 50 km in NS-direction as observed from surface wave studies (Meier et al., 2004a). A combined interpretation of the deformation and stress regimes within the upper plate and at the contact zone incorporating structural information suggests that the south-easternmost part of the Aegean plate advances towards the SE. This is also indicated by the GPS horizontal velocities in this region that show a small but systematically varying trend and increasing magnitudes while proceeding from west to east (Figure 11). We explain this velocity field to be initiated by the overall compressional regime due to the convergence between Aegean-

Anatolia and Africa in combination with remnants of oceanic lithosphere below the eastern Libyan Sea. These remnants form the required space for plate boundary retreat and result in a counter clockwise rotation of the Eastern Hellenic arc towards the SE (see Figure 11) as indicated by the surface-velocity field and by the present deformation at depth. This regime also explains the development of the sinistral transtensional regime consisting of the Ptolemeus, Pliny and Strabo deep-sea depressions SE of Crete. Furthermore, our model requires an ESE-trending normal faulting regime between Crete and Rhodes perpendicular to the direction of present velocity field at the surface which is exactly what we observe around Karpathos. This ESE-trending extension is thus not along-arc but in direction of the retreat of the plate boundary.

Doutsos and Kokkalas (2001) argue that the transtensional regime in the eastern forearc has been established since Late Miocene then comprising NNE- to NNW-tension associated to arc-normal pull of the Aegean plate. In a second state this system then changed to ENE- and N-trending strike slip faulting as well as to NNE-trending oblique-normal faulting representing the result of strain partitioning during oblique convergence. Thus, the setup of the counter clockwise rotation of the eastern Hellenic arc might correlate with the commencing collision in the western Hellenic arc at 3.4 Ma and probably even expanded towards SE Turkey in the following (TenVeen, 2004).

Inversion of fault mechanisms for earthquakes within the dipping African lithosphere reveals a down-dip orientation for σ_3 at a plunge of 48° trending to the North. σ_1 was found to be oriented dominantly orthogonal to the strike of the plate boundary and vary with strike of the Hellenic arc at a plunge of 39° . This indicates that slab pull is the dominant force within the dipping African lithosphere causing gravitational instability at the southern edge of the Aegean domain and resulting in rollback of the slab especially in the East (see also LePichon and Angelier, 1979; Jackson and McKenzie, 1988). Hatzfeld et al. (1993b, based on data from a regional network) and Taymaz et al. (1990, from teleseismic recordings) observed a similar deformation regime within the slab dipping below the South Aegean. Meijer and Wortel (1996) performed forward modeling to derive the stress field in the Aegean region. They conclude that the westward Anatolian push contributes to the stress field while the existence of tension appears to be due to subduction-related forces. Both observations are in agreement with our results. Analysis of stress fields in subduction zones worldwide and its tectonic implications was pioneered by Isacks and Molnar (1971). Since then a number of papers focused on subduction-related stress fields. McGinty et al. (2000) studied the Hikurangi subduction zone (New Zealand) by inversion of focal mechanisms and identified the least compressive stress to be closely aligned with the dip of the subducting plate. Similar results were obtained for the Copiapo (northern Chile) part of the Andean subduction zone (Comte et al., 2002) and for the Alaska subduction zone by Lu et al. (1997) who also found σ_1 to be parallel along strike of the plate boundary. Christova et al. (2004) observed a down dip direction for σ_3 in the Vanuatu (New Hebrides) Wadati-Benioff zone but limited to the upper 60 km. With two exceptions our set of in-slab fault plane solutions covers the uppermost 100 km. As a consequence we can not argue on the stress regime at greater depth levels but find that the stress field in the subducting lithosphere of the Hellenic subduction zone as observed for the uppermost 100 km is compatible with other subduction zones. However, this might be not the case for all subduction zones worldwide.

For the upper plate of the Alaska subduction zone, Lu et al. (1997) observe a non-uniform stress field reflecting strike-slip and thrusting regimes. They observe a direct relation between the size of earthquakes inverted ($M > 3$) and homogeneity of the stress field determined. This phenomenon was also observed for fluid-injection induced seismicity at lower ($-2 < M < 1$) magnitude range (Bohnhoff et al., 2004). However, the data base of fault mechanisms from

the Hellenic subduction zone give no indication for a similar relation which might be due to the smaller number of intermediate-sized ($M \sim 3$) events which is explained by low seismic activity compared to other subduction zones. To perform such an investigation a long-term monitoring for the entire forearc of the Hellenic Subduction Zone at low threshold is required.

6.7. Conclusions

We compiled a data base of focal mechanisms for the Hellenic subduction zone in the vicinity of Crete consisting of 264 fault plane solutions that cover a magnitude range between 0 and 6.5. Eight regions (subvolumes) were identified based on 1. Faulting regimes (upper plate, interplate, in-slab) and 2. Spatial clustering of deformation axes. Where as EW-extensional normal faulting on Western Crete was interpreted as along-arc extension, the $N110^\circ E$ striking direction of σ_3 in the eastern Hellenic arc reflects the SE-directed retreat of the plate boundary at this part resulting in sinistral deformation of the outer forearc. This regime extends to onshore Eastern Crete. Interplate seismicity indicates a uniform N-NNE trending direction of relative plate motion along the Hellenic arc between the Ionian Sea and Rhodes. This corresponds with the GPS-derived horizontal velocity field for this region. Rollback of the subduction zone induced by slab pull as driving mechanism forces the Benioff towards an amphitheatrically shape as observed from the distribution of hypocenters.

6.8. Acknowledgements

We acknowledge the comments by two anonymous reviewers that helped to improve an earlier version of the manuscript. We benefited from discussions with J. Jackson. A. Kiratzi is thanked for helpful comments and making available her manuscript prior to publication. Furthermore, we acknowledge the focal-mechanism catalog for eastern Crete as courtesy of J. Makris and D. Becker and contributions by O. Knabenbauer and M. Messar. We are grateful to the Deutsche Forschungsgemeinschaft (DFG) for partly funding within the Collaborative Research Centre 526 ‘Rheology of the Earth’.

6.9. References

- Angelier, J., Lyberis, N., LePichon, X. and Barrier, E., 1982, The tectonic development of the Hellenic arc and the sea of Crete: A synthesis, *Tectonophysics*, **86**, 159-196.
- Bath, M., 1983, The seismology of Greece, *Tectonophysics*, **98**, 165-208.
- Becker, D., 2000, Mikroseismizität und Deformation der Kruste Ostkretas, Germany, *Master thesis*, Faculty of Geosciences, Hamburg University (in German).
- Benetatos, C., Kiratzi, A., Papazachos, C. Karakaisis, G., 2004, Focal mechanisms of shallow and intermediate depth earthquakes along the Hellenic Arc, *J. of Geodyn.*, **37**, 253-296.
- Bijwaard, H. and Spakman, W., 1998, Closing the gap regional and global travel time tomography, *J. Geophys. Res.*, **103**, 30055-30078.
- Bohnhoff, M., Baisch, S., Harjes, H.-P., 2004, Focal mechanisms of induced seismicity at the superdeep German Continental Deep Drilling Program (KTB) borehole and their relation to fault structure and stress field, *J. Geophys. Res.*, **109**, B02309, doi:10.1029/2003JB002528.
- Bohnhoff, M., Makris, J., Papanikolaou, D. and Stavrakakis, G., 2001, Crustal investigation of the Hellenic subduction zone using wide aperture seismic data, *Tectonophysics*, **343**, 239-262.
- Brönnner, M., 2003, Untersuchungen des Krustenaufbaus entlang des Mittelerranen Rückens abgeleitet aus geophysikalischen Messungen, *PhD thesis*, Faculty of Geosciences, Hamburg University (in German).
- Christova, C., Scholz, C.H. and Kao, H., 2004, Stress field in the Vanuatu (New Hebrides) Wadati-Benioff zone inferred by inversion of earthquake focal mechanisms: evidence for systematic lateral and vertical variations of principal stresses, *J. Geodyn.*, **37**, 125-137.

- Comte, D., Haessler, H., Dorbath, L., Pardo, M., Monfred, T., Lavenn, A., Pontoise, B., Hello, Y., 2002, Seismicity and stress distribution in the Copiapo, northern Chile, subduction zone using combined on- and offshore seismic observations, *Phys. Earth Planet. Sci. Int.*, **132**, 197-217.
- DeChabalier, J.B., Lyon-Caen, H., Zollo, A., Deschamps, A., Bernard, P. and Hatzfeld, D., 2002, A detailed analysis of microearthquakes in western Crete from digital three-component seismograms, *Geophys. J. Int.*, **110**, 347-360.
- Delibasis, N., Ziazia, M., Voulgaris, N., Papadopoulos, T., Stavrakakis, G., Papanastassiou, D. and Drakatos, G., 1999, Microseismic activity and seismotectonics of Heraklion Area (central Crete Island, Greece), *Tectonophysics*, **308**, 237-248.
- Doutsos, T. and Kokkalas, S., 2001, Stress and deformation patterns in the Aegean region, *J. Struct. Geol.*, **23**, 455-472.
- Endrun, B., Meier, T., Bischoff, M. and Harjes, H.-P., 2004, Lithospheric structure in the area of Crete constrained by receiver functions and dispersion analysis of Rayleigh phase velocities, *Geophys. J. Int.*, **158**, 592-608.
- Engdahl, E.R., van der Hilst, R., and Buland, R., 1998, Global teleseismic earthquake relocation with improved travel times and procedures for depth determination, *Bull. Seis. Soc. Am.*, **88**, 722-743.
- Gephart, J.W., 1990, Stress and the direction of slip on fault planes, *Tectonics*, **9**, 845-858.
- Gephart, J.W. and D.W. Forsyth, 1984, An improved Method for Determining the Regional Stress Tensor Using Earthquake Focal Mechanism Data: Application to the San Fernando Earthquake Sequence, *J. Geophys. Res.*, **89**, 9305-9320.
- Hanka, W. and Kind, R., 1994, The GEOFON Program, *Ann. Geofis.*, **37**, 1060-1065.
- Hatzfeld, D., Besnard, M., Makropoulos, K. and Hatzidimitriou, P., 1993a, Microearthquake seismicity and fault-plane solutions in the southern Aegean and its geodynamic implications, *Geophys. J. Int.*, **115**, 799-818.
- Hatzfeld, D. et al., 1993b, Subcrustal Microearthquake Seismicity and Fault Plane Solutions Beneath the Hellenic Arc, *J. Geophys. Res.*, **98**(B6), 9861-9870.
- Huchon, P., Lyberis, N., Angelier, J., LePichon, X and Renard, V., 1982, Tectonic of the Hellenic Trench: a synthesis of Sea-Beam and submersible observations, *Tectonophysics*, **86**, 69-211.
- Huguen, C., Mascle, J., Chaumillon, E., Woodside, J.M., Benkhelil, J., Kopf, A. and Volksonkaia, A., 2001, Deformation styles of the eastern Mediterranean Ridge and surroundings from combined swath mapping and seismic reflection profiling, *Tectonophysics*, **343**, 21-47.
- Isacks, B. and Molnar, P., 1971, Distribution of stresses in the descending lithosphere from a global survey of focal-mechanism solutions of mantle earthquakes, *Rev. Geophys. Space Phys.*, **9**, 1, 103-174.
- Jackson, J. and McKenzie, D.P., 1988, The relationship between plate motion and seismic moment tensors, and the rates of active deformation in the Mediterranean and Middle East, *Geophys. J.*, **93**, 45-73.
- Jost, M.L., O. Knabenbauer, J. Cheng and Harjes, H.-P., 2002, Fault plane solutions of microearthquakes and small events in the Hellenic arc, *Tectonophysics*, **356**, 87-114.
- Kiratzi, A. and Louvari, E., 2003, Focal mechanisms of shallow earthquakes in the Aegean Sea and the surrounding lands determined by waveform modelling: a new database, *J. Geod.*, **36**, 251-274.
- Knapmeyer, M., 1999, Geometry of the Aegean Benioff zone. *Ann. Geofis.*, **42**, 27-38.
- Lambeck, K., 1995, Late Pleistocene and Holocene sea-level change in Greece and southwestern Turkey: a separation of eustatic, isostatic and tectonic contributions, *Geophys. J. Int.*, **122**, 1022-1044.
- LePichon, X. and Angelier, J., 1979, The Hellenic arc and trench system: a key to the neotectonic evolution of the Eastern Mediterranean area, *Tectonophysics*, **60**, 1-42.
- LePichon, X., Chamot-Rooke, N. and Lallemand, S., 1995, Geodetic determination of the kinematics of central Greece with respect to Europe: Implications for Eastern Mediterranean tectonics, *J. Geophys. Res.*, **100**, 12675-12690.
- Li, X., Bock, G. Vafidis, A., Kind, R., Harjes, H.-P., Hanka, W., Wylegalla, K., Meijde, M.v.d. and Yuan, X., 2003, Receiver function study of the Hellenic subduction zone: imaging crustal thickness variations and the oceanic Moho of the descending African lithosphere, *Geophys. J. Int.*, **155**, 733-748.
- Lu, Z., Wyss, M. and Pulpan, H., 1997, Details of stress directions in the Alaska subduction zone from fault plane solutions, *J. Geophys. Res.*, **102** (B3), 5385-5402.
- Lyon-Caen, H. et al., 1988, The 1986 Kalamata (south Peloponnesus) earthquake: detailed study of a normal fault, evidences for east-west extension in the Hellenic arc, *J. Geophys. Res.*, **93**, 14967-15000.
- Makropoulos, K.C. and Burton, P.W., 1981, A catalogue of seismicity in Greece and adjacent areas, *Geophys. J. R. astron. Soc.*, **65**, 741-762.
- Marone, F., Meijde, M.v.d., Lee, S.v.d. and Giardini, D., 2003, Joint inversion of local, regional and teleseismic data for crustal thickness in the Eurasia-Africa plate boundary region, *Geophys. J. Int.*, **154**, 499-514.
- Mascle, J. et al., 1999, Images may show start of European-African plate collision, *EoS Transactions*, **80** (37), American Geophysical Union, 421-428.
- McClusky, S. et al., 2000, Global Positioning System constraints on plate kinematics and dynamics in the eastern Mediterranean and Caucasus, *J. Geophys. Res.*, **105**, 5695-5719.

- McGinty, P., Reyners, M. and Robinson, R., 2000, Stress directions in the shallow part of the Hikurangi subduction zone, New Zealand, from the inversion of earthquake first motions, *Geophys. J. Int.*, **142**, 339-350.
- McKenzie, D.P., 1970, Plate tectonics of the Mediterranean region, *Nature*, **226**, 239-243.
- McKenzie, D.P., 1972, Active Tectonics of the Mediterranean Region, *Geophys. J. R. astr. Soc.*, **30**, 109-185.
- McKenzie, D.P., 1978, Active Tectonics of the Alpine-Himalayan belt: the Aegean Sea and surrounding regions, *Geophys. J. R. astron. Soc.*, **55**, 217-254.
- Meier, T., Dietrich, K., Stöckhert, B. and Harjes, H.-P., 2004a, One-dimensional models of shear wave velocity for the eastern Mediterranean obtained from the inversion of Rayleigh wave phase velocities and tectonic implications, *Geophys. J. Int.*, **156**, 45-58.
- Meier, T., Rische, M., Endrun, B., Vafidis, A. and Harjes, H.-P., 2004b, Seismicity of the Hellenic subduction zone in the area of western and central Crete observed by temporary local seismic networks, *Tectonophysics*, **383**, 149-169.
- Meijer, P.Th. and Wortel, M.J.R., 1996, Temporal variation in the stress field of the Aegean region, *Geophys. Res. Lett.*, **23** (5), 439-442.
- Meulenkamp, J.E., Wortel, M.J.R., VanWamel, W.A., Spakman and Hoogerduyn Strating, E., 1988, On the Hellenic subduction zone and the geodynamic evolution of Crete since the late Middle Miocene, *Tectonophysics*, **146**, 203-215.
- Michael, A.J., 1984, Determination of stress from slip data; faults and folds, *J. Geophys. Res.*, **89**, 11517-11526.
- Michael, A.J., 1987, Use of focal mechanisms to determine stress: a control study, *J. Geophys. Res.*, **92** (B1), 357-368.
- Michael, A.J., 1991, Spatial variations in stress within the 1987 Whittier Narrows, California, aftershock sequence: New techniques and results, *J. Geophys. Res.*, **96**, 6303-6319.
- Papadimitriou, E., 1993, Focal mechanisms along the convex side of the Hellenic arc. *Bollettino de Geofisica Teorica et Applicata*, **XXXV**, 401-426.
- Papadopoulos, G.A., Kondopoulou, D., Leventakis, G.-A. and Pavlides, S., 1986, Seismotectonics of the Aegean region, *Tectonophysics*, **124**, 67-84.
- Papazachos, B.C., 1973, Distribution of seismic foci in the Mediterranean and surrounding area and its tectonic implications, *Geophys. J.R. astron. Soc.*, **33**, 421-430.
- Papazachos, B.C. and Papazachou, C.B., 1997, The earthquakes of Greece, Ziti (ed.), Technical books editions, Thessaloniki, 304pp.
- Papazachos, B.C., Kiratzi, A. and Papadimitriou, E., 1991, Regional Focal Mechanisms for Earthquakes in the Aegean Area, *PAGEOPH*, **126** (4), 405-420.
- Papazachos, B.C., Karakostas, V.G., Papazachos, C.B. and Scordilis, E.M., 2000, The geometry of the Wadati-Benioff zone and lithospheric kinematics in the Hellenic arc, *Tectonophysics*, **319**, 275-300.
- Snoke, J.A., 2003, FOCMEC: FOCal MECHANISM determinations, *International Handbook of Earthquake and Engineering Seismology*, W.H.K. Lee, H. Kanamori, P.C. Jennings and Kisslinger, C. (eds.), Academic Press, San Diego, Chapter 85.12.
- Snoke, J.A., Munsay, J.W., Teague, A.G. and Bollinger, G.A., 1984, A program for focal mechanism determination by combined use of polarity and SV-P amplitude ratio data, *EQ Notes*, **55** (3), 15.
- Spakman, W., Wortel, M.J.R. and Vlaar, N.J., 1988, The Hellenic subduction zone: a tomographic image and its geodynamic implication, *Geophys. Res. Lett.*, **15**, 60-63.
- Taymaz, T., Jackson, J. and Westaway, R., 1990, Earthquake mechanisms in the Hellenic trench near Crete, *Geophys. J. Int.*, **102**, 695-731.
- TenVeen, J.H., 2004, Extension of Hellenic forearc shear zones in SW Turkey: the Pliocene-Quaternary deformation of the Esen Cay Basin, *J. Geodyn.*, **37**, 181-204.
- TenVeen, J.H. and Kleinspehn, K.L., 2003, Incipient continental collision and plate-boundary curvature: Late Pliocene-Holocene transtensional Hellenic forearc, Crete, Greece, *J. Geol. Soc. London*, **160**, 161-181.
- Truffert, C., Chamot-Rouke, N., Lallemand, S., DeVoogd, B., Huchon, P. and LePichon, X., 1993, The crust of the western Mediterranean Ridge from deep seismic data and gravity modelling, *Geophys. J. Int.*, **114**, 360-372.

Appendix : Table 1

year	month	day	hour	min	lat[°N]	lon[°E]	dep [km]	mag	strike	dip	rake	reference
1959	05	14	06	36	35.10	24.60	43	6.3	319	67	-110	PDO
1962	01	26	08	17	35.20	22.70	33	6.2	108	90	90	PDO
1962	04	28	11	18	36.10	26.80	33	5.8	275	85	-174	PDO
1965	04	09	23	57	35.10	24.30	67	6.1	23	56	158	PPA-
1965	04	09	23	57	35.10	24.30	51	6.0	280	77	-134	PDO-
1965	04	09	23	57	35.06	24.31	51	6.0	63	76	157	TAY*
1965	04	27	14	09	35.70	23.50	50	5.5	140	59	-77	MCK-
1965	04	27	14	09	35.60	24.50	13	5.4	191	65	-79	KIR*
1965	04	27	14	09	35.60	23.50	5	5.7	22	27	-81	PPA-
1965	11	28	05	26	36.30	27.50	89	5.8	246	21	349	MCK
1965	11	28	05	26	36.10	27.40	73	6.0	350	30	142	PPA*
1966	03	11	20	01	34.40	24.20	33	5.1	296	59	47	PDO
1966	05	09	00	42	34.40	26.40	20	5.8	295	40	90	MCK(*)
1966	05	09	00	42	34.40	26.40	33	5.8	115	50	89	PDO(*)
1966	05	09	00	42	34.40	26.40	10	5.8	295	40	90	PPA(*)
1966	05	09	00	42	34.43	26.44	16	5.5	132	46	110	TAY*
1966	11	19	07	12	35.00	23.50	33	5.5	245	61	136	PDO
1968	07	08	17	41	34.50	25.10	33	5.4	286	75	-107	PDO
1968	08	15	02	29	35.20	26.70	33	5.2	306	78	-90	PDO
1968	10	19	15	34	35.20	23.40	33	4.9	128	77	147	PDO
1969	04	16	23	21	35.34	27.47	45	5.2	309	32	98	MCK(*)
1969	06	12	15	13	34.40	25.00	19	6.1	294	29	105	PPA*
1969	06	12	15	13	34.40	25.06	25	5.8	294	29	105	MCK(*)
1969	06	12	15	13	34.40	25.00	33	6.1	95	62	90	PDO(*)
1969	06	12	15	13	34.43	25.04	19	5.8	163	50	44	TAY-
1971	01	03	23	18	34.90	26.30	2	5.4	144	70	86	MCK(*)
1971	01	03	23	18	34.60	26.30	33	5.4	143	69	85	PDO*
1972	04	29	18	29	34.80	24.70	33	5.3	264	61	44	PDO
1972	05	04	21	3	35.10	23.60	40	6.2	309	18	89	KIR*
1972	05	04	21	39	35.10	23.60	33	6.5	106	86	90	PDO(*)
1972	05	04	21	39	35.10	23.60	40	6.5	308	18	90	PPA(*)
1972	05	04	21	39	35.15	23.56	41	5.9	112	74	98	TAY(*)
1973	04	06	14	13	34.40	25.20	33	5.4	120	63	90	PDO
1973	06	26	19	05	34.40	26.10	33	5.0	151	70	144	PDO
1973	10	14	18	07	34.70	26.30	33	4.9	200	58	88	PDO
1973	11	29	00	00	35.20	23.80	1	6.0	316	10	90	MCK*
1973	11	29	10	57	35.20	23.80	18	5.7	283	38	97	PDI(*)
1973	11	29	10	57	35.20	23.80	33	6.0	139	82	90	PDO(*)
1973	11	29	10	57	35.20	23.80	1	6.0	316	10	90	PPA(*)
1973	11	29	10	57	35.18	23.81	18	5.7	224	67	10	TAY-
1975	01	09	18	53	34.80	24.00	33	4.8	178	88	-38	PDO
1975	09	17	23	04	36.40	23.10	33	5.1	167	67	117	PDO
1975	09	22	00	44	35.20	26.30	64	5.5	310	50	17	PPA*
1975	09	22	00	44	35.20	26.26	64	5.4	209	75	131	TAY(*)
1977	08	18	09	27	35.27	24.08	45	5.7	85	15	-142	CMT(*)
1977	08	18	09	27	35.30	23.50	38	5.6	270	12	114	PPA(*)
1977	08	18	09	27	35.27	23.52	38	5.5	114	79	96	TAY*
1977	09	11	23	19	34.90	23.00	19	6.3	320	30	90	PPA*
1977	09	11	23	19	34.51	22.99	37	5.8	74	28	100	CMT-
1977	09	11	23	19	34.90	23.00	16	5.8	295	40	95	PDI(*)
1977	09	11	23	19	34.90	23.00	33	6.3	165	76	124	PDO(*)
1977	09	11	23	19	34.95	23.05	19	5.8	276	47	89	TAY(*)
1978	03	07	22	33	34.19	25.45	34	5.5	225	14	40	CMT(*)

Table 1 (cont.)

year	month	day	hour	min	lat[°N]	lon[°E]	dep [km]	mag	strike	dip	rake	reference
1978	03	07	22	33	34.33	25.11	42	5.4	42	18	-162	BEN*
1979	05	15	06	59	34.60	24.50	35	5.7	253	17	65	PPA*
1979	05	15	06	59	34.38	24.80	15	6.1	172	4	-20	CMT(*)
1979	05	15	06	59	34.58	24.45	35	5.5	253	17	65	TAY(*)
1979	06	15	11	34	34.82	24.42	33	5.4	216	11	10	CMT(*)
1979	06	15	11	34	34.94	24.21	40	5.5	150	75	70	TAY*
1979	06	15	11	34	34.90	24.20	40	5.6	21	23	141	PPA(*)
1979	07	23	11	41	35.29	26.57	15	5.6	61	35	-40	CMT*
1979	07	23	11	41	35.50	26.40	11	5.5	61	35	-40	PPA(*)
1979	08	22	20	12	35.90	27.39	68	5.3	64	31	-106	BEN
1981	09	13	23	25	34.56	25.13	15	5.5	256	65	-11	CMT
1982	08	17	22	22	33.70	22.90	23	6.3	219	34	70	CMT(*)
1982	08	17	22	22	33.70	22.90	9	6.4	219	34	93	PPA*
1982	08	17	22	22	33.71	22.94	39	6.0	230	45	109	TAY(*)
1982	08	17	22	22	33.77	22.96	10	6.4	196	28	69	USG(*)
1983	01	03	00	12	33.97	23.89	102	5.1	30	36	70	CMT
1983	03	19	21	41	34.75	24.89	65	5.6	358	39	131	CMT-
1983	03	19	21	41	35.00	25.30	67	5.7	43	51	139	PPA(*)
1983	03	19	21	41	35.02	25.32	67	5.7	44	51	139	TAY*
1984	05	22	13	57	36.13	22.78	73	5.1	182	55	29	CMT(*)
1984	05	22	13	57	35.90	22.60	67	5.5	182	55	29	PPA*
1984	05	22	13	57	35.90	22.60	63	5.1	188	44	32	BEN(*)
1984	06	21	10	43	35.74	23.80	34	6.2	79	7	-128	CMT(*)
1984	06	21	00	00	35.40	23.30	33	6.2	322	16	114	PDI*
1984	06	21	10	43	35.40	23.30	39	6.2	322	16	114	PPA(*)
1984	06	21	10	43	35.31	23.28	39	5.8	110	72	83	TAY(*)
1985	09	27	16	39	34.05	26.94	44	5.6	135	76	13	CMT(*)
1985	09	27	16	39	34.50	26.60	40	5.5	125	77	9	PPA(*)
1985	09	27	16	39	34.40	26.55	38	5.6	125	77	9	TAY*
1986	05	22	19	52	34.12	26.72	33	5.5	227	37	24	CMT(*)
1986	05	22	19	52	34.25	26.55	27	5.3	118	86	99	BEN*
1986	07	16	02	55	36.04	23.77	21	4.0	14	50	-108	HAT
1987	04	12	02	47	35.40	23.27	15	5.1	252	90	180	CMT
1988	07	11	15	54	35.07	25.73	8	1.8	280	60	95	HAT
1988	07	13	11	22	35.06	25.77	13	1.6	125	55	89	HAT
1988	07	15	19	25	35.02	25.31	28	1.9	319	90	18	HAT
1988	07	15	22	55	35.69	25.71	9	2.4	157	50	-107	HAT
1988	07	20	02	09	35.82	24.97	24	2.8	140	50	-90	HAT
1988	07	25	11	11	34.88	25.75	8	3.4	40	50	-90	HAT
1988	07	25	14	45	35.40	26.18	18	2.6	230	77	105	HAT
1988	07	26	21	56	36.11	27.21	14	2.6	209	54	-71	HAT
1988	07	26	23	40	36.15	27.20	15	2.8	14	70	-54	HAT
1988	07	27	05	00	35.44	24.81	29	4.1	253	70	-158	HAT
1988	07	27	10	55	35.50	25.76	24	2.6	350	50	-104	HAT
1988	07	31	21	39	36.11	27.38	23	2.5	94	55	85	HAT
1988	08	01	16	45	35.73	23.70	17	2.4	230	60	-67	HAT
1988	08	02	11	25	35.50	23.61	12	99	230	70	-40	DEC-
1988	08	02	11	25	35.50	23.60	13	1.9	120	50	90	HAT*
1988	08	03	08	09	35.73	24.68	19	2.5	240	80	25	HAT
1988	08	04	05	26	35.45	23.45	27	3.1	270	50	-61	HAT
1988	08	04	06	00	36.16	27.26	19	2.5	319	60	90	HAT
1988	08	04	11	43	35.34	23.67	1	2.0	199	59	47	HAT
1988	08	04	18	43	35.23	23.29	29	2.9	59	60	-92	HAT

Table 1 (cont.)

year	month	day	hour	min	lat[°N]	lon[°E]	dep [km]	mag	strike	dip	rake	reference
1988	08	05	05	21	35.17	23.18	21	2.9	250	50	-90	HAT
1988	08	05	12	53	35.65	25.99	25	4.0	179	56	-67	HAT
1988	08	05	22	37	36.10	27.23	12	2.4	114	80	89	HAT
1988	08	06	04	21	35.31	27.38	26	2.8	60	90	170	HAT
1988	08	10	01	06	35.13	23.12	20	2.9	40	50	-110	HAT
1988	08	13	22	29	35.59	26.99	13	3.3	118	45	82	HAT
1988	08	14	02	30	35.44	23.42	4	2.9	327	70	-94	HAT
1988	08	14	13	28	35.58	23.72	11	2.2	127	68	111	HAT
1988	08	14	16	13	35.55	23.62	11	2.1	90	60	90	HAT
1988	08	15	05	37	35.35	23.58	8	1.9	199	69	-90	HAT*
1988	08	15	05	37	35.36	23.58	9	99	170	70	-75	DEC(*)
1988	08	15	20	08	35.12	25.05	20	2.8	140	50	119	HAT
1988	08	18	13	10	34.95	23.22	23	3.8	214	51	-67	HAT
1988	08	18	18	07	35.12	23.59	22	2.4	345	78	137	HAT*
1988	08	18	18	07	35.15	23.61	23	99	225	75	35	DEC-
1988	08	19	17	12	35.98	23.35	19	2.5	239	69	-90	HAT
1988	08	20	12	16	35.39	23.48	24	99	170	85	-110	DEC
1988	08	20	14	29	35.69	23.42	13	2.5	7	51	-78	HAT
1988	08	20	15	32	35.77	25.39	16	2.8	159	59	-137	HAT
1988	08	22	11	05	35.83	23.43	27	2.5	359	63	-104	HAT
1988	08	27	04	50	35.34	23.64	4	99	0	50	-105	DEC
1988	08	27	15	12	35.32	23.63	3	99	175	50	-75	DEC
1988	08	29	21	07	35.37	23.81	4	99	255	85	-45	DEC
1988	09	02	22	09	35.28	23.66	5	99	145	60	-175	DEC
1988	09	03	15	29	35.38	23.59	3	99	360	50	-75	DEC
1988	09	05	20	03	34.51	26.65	15	5.2	15	55	-11	CMT
1988	09	07	03	22	35.41	23.64	5	99	195	65	-50	DEC
1988	09	12	07	36	35.49	23.48	12	99	195	70	-80	DEC
1988	09	12	14	56	35.41	23.47	8	99	195	75	-55	DEC
1988	09	12	22	18	35.21	23.70	29	99	60	75	-165	DEC
1988	09	13	08	06	35.38	23.40	8	99	320	65	-125	DEC
1988	09	13	10	01	35.48	23.46	10	99	160	75	-135	DEC
1988	09	16	03	42	35.35	23.72	76	99	110	70	-150	DEC
1989	03	17	05	42	34.51	25.53	17	5.7	77	10	-118	CMT
1989	03	28	13	29	34.06	24.68	56	5.5	67	53	29	CMT
1989	06	14	18	06	34.30	26.10	15	5.5	102	8	-68	CMT
1989	08	27	01	21	34.25	26.28	15	5.6	223	19	33	CMT
1990	07	09	11	22	34.45	26.24	33	5.4	129	27	-106	CMT-
1990	07	09	11	22	34.90	26.60	9	5.2	217	56	-21	KIR*
1990	07	09	11	22	34.90	26.60	19	5.5	327	64	-82	PPA-
1991	03	19	12	09	34.60	26.13	15	5.5	245	36	-33	CMT-
1991	03	19	12	09	34.80	26.30	12	5.5	261	30	40	KIR*
1991	03	19	12	09	34.80	26.30	7	5.8	2	71	-122	PPA
1992	04	30	11	44	35.04	26.20	33	5.7	172	38	-106	CMT(*)
1992	04	30	11	44	35.10	26.60	7	5.8	214	52	-47	KIR*
1992	04	30	11	44	35.10	26.60	20	6.1	172	38	-106	PPA(*)
1992	11	21	05	07	35.72	22.80	70	5.9	196	50	16	CMT(*)
1992	11	21	05	07	35.90	22.50	65	6.3	96	78	139	PPA(*)
1992	11	21	05	07	35.90	22.50	52	5.9	97	77	141	BEN*
1994	05	23	06	46	35.02	24.89	81	6.1	177	63	22	CMT(*)
1994	05	23	06	46	35.00	24.90	80	6.1	70	70	137	PPA(*)
1994	05	23	06	46	35.00	24.90	71	6.0	69	59	148	BEN*
1995	09	03	17	03	35.03	24.93	12	2.9	150	35	-11	DEL

Table 1 (cont.)

year	month	day	hour	min	lat[°N]	lon[°E]	dep [km]	mag	strike	dip	rake	reference
1995	09	07	06	29	35.03	25.08	9	2.5	20	85	-150	DEL
1995	09	07	16	03	35.06	25.07	10	2.4	320	50	41	DEL
1995	09	08	00	37	35.04	25.08	9	1.8	290	90	180	DEL
1995	09	11	21	32	35.00	25.02	5	0.0	15	55	-109	DEL
1995	09	12	13	48	35.00	25.12	4	1.1	45	60	-110	DEL
1995	09	15	13	33	34.81	25.39	23	2.4	140	50	-119	DEL
1995	09	25	14	08	35.17	25.16	6	1.5	65	35	-10	DEL
1995	10	07	05	37	34.96	25.05	29	2.1	150	85	40	DEL
1995	10	08	02	53	35.25	25.24	6	1.6	55	45	-120	DEL
1995	10	14	18	30	34.89	24.86	37	1.8	190	75	-139	DEL
1995	10	15	19	23	35.26	25.07	9	1.8	140	30	-139	DEL
1995	10	20	14	09	35.16	25.17	8	2.2	70	20	0	DEL
1995	10	26	18	55	35.23	25.24	5	1.8	100	80	-30	DEL
1995	10	27	00	45	34.75	24.77	24	2.1	55	35	-70	DEL
1995	10	27	19	46	34.67	24.88	24	2.5	180	40	60	DEL
1995	10	28	19	20	35.49	25.33	18	1.1	350	45	31	DEL
1995	10	29	19	01	35.06	24.92	8	2.7	335	30	-90	DEL
1995	10	29	19	04	35.06	24.93	4	1.4	260	60	-140	DEL
1995	10	29	20	15	35.06	24.94	5	1.6	50	60	40	DEL
1995	10	31	11	29	35.15	25.14	12	1.0	60	85	90	DEL
1995	11	02	14	11	35.19	25.16	27	2.3	60	90	-180	DEL
1995	11	05	08	03	35.23	25.23	4	1.8	120	65	-11	DEL
1995	11	09	15	39	35.16	25.17	3	1.8	65	50	-40	DEL
1995	11	13	07	38	35.00	25.09	9	2.9	85	55	-100	DEL
1995	11	20	06	13	35.04	24.77	4	1.8	75	60	-110	DEL
1995	11	21	01	23	34.76	25.46	7	2.3	185	15	-60	DEL
1995	11	26	01	18	35.07	24.94	5	2.3	205	80	-20	DEL
1995	12	07	18	01	34.79	24.15	15	5.6	319	6	123	CMT
1995	12	07	20	04	35.00	25.25	5	1.9	75	30	50	DEL
1995	12	10	03	27	34.37	23.37	21	5.3	289	22	75	CMT(*)
1995	12	10	03	27	34.76	23.99	24	5.2	266	09	54	KIR*
1995	12	10	03	27	34.80	24.10	25	5.5	289	22	75	PPA(*)
1996	04	12	15	39	36.47	27.14	151	5.2	315	44	173	CMT
1996	07	20	00	00	36.07	26.92	15	6.2	196	38	-102	CMT(*)
1996	07	20	00	00	36.07	27.46	12	6.1	232	42	-52	KIR*
1996	07	20	00	00	36.15	27.10	14	6.0	195	44	-85	USG(*)
1996	07	22	01	44	36.11	26.91	15	5.0	223	36	-78	CMT
1997	09	26	08	56	35.30	23.65	13	0.2	214	67	-46	JOS
1997	09	29	18	24	35.31	23.66	14	0.0	201	83	-45	JOS
1997	10	21	05	47	35.32	23.63	15	0.0	106	76	6	JOS
1997	10	21	07	34	35.29	23.72	15	0.2	099	85	-9	JOS
1997	10	22	01	02	35.30	23.84	3	2.2	358	85	65	JOS
1997	10	28	12	44	35.34	23.68	3	0.0	194	42	-31	JOS
1997	11	05	03	18	35.39	23.71	3	0.4	42	86	15	JOS
1997	11	05	07	24	35.34	23.64	4	1.3	312	85	75	JOS
1997	11	05	12	22	34.61	23.62	40	5.4	350	34	154	CMT(*)
1997	11	05	12	22	34.51	23.93	22	5.2	309	06	108	KIR
1997	11	12	16	20	35.33	23.63	5	0.0	209	69	22	JOS
1997	11	13	01	49	35.32	23.62	4	0.6	51	87	-40	JOS
1997	11	25	13	03	35.34	23.62	4	0.0	2	65	-79	JOS
1997	11	27	15	41	35.39	23.93	12	0.0	136	71	-111	JOS
1998	10	07	18	47	34.02	25.84	22	5.1	318	60	150	CMT
1999	01	09	23	29	35.03	25.82	17	2.8	186	58	42	BEC

Table 1 (cont.)

year	month	day	hour	min	lat[°N]	lon[°E]	dep [km]	mag	strike	dip	rake	reference
1999	01	11	11	19	35.02	25.94	19	2.3	205	70	40	BEC
1999	01	13	04	41	35.04	25.92	18	2.3	50	45	-10	BEC
1999	01	14	04	46	35.07	25.89	14	2.4	242	74	70	BEC
1999	01	15	07	50	35.08	26.02	18	1.9	40	40	30	BEC
1999	01	15	10	16	34.86	26.07	39	4.5	5	35	120	BEC
1999	01	19	00	37	35.07	25.87	15	2.1	55	50	0	BEC
1999	01	19	01	12	35.06	25.89	15	2.2	40	40	-50	BEC
1999	01	25	14	40	34.75	25.80	47	4.6	159	72	26	BEC
1999	01	25	14	47	34.76	25.81	44	3.5	35	50	150	BEC
1999	01	26	20	09	35.06	25.92	15	2.1	5	30	-40	BEC
1999	01	27	00	33	35.07	26.04	18	2.3	70	85	0	BEC
1999	01	28	19	00	34.81	25.81	50	3.3	40	50	140	BEC
1999	01	28	19	16	34.77	25.82	45	3.5	54	58	-42	BEC
1999	01	30	20	25	35.08	25.88	15	1.8	58	51	13	BEC
1999	01	31	05	48	35.21	26.01	16	2.8	75	70	150	BEC
1999	02	05	01	59	34.98	25.69	17	3.1	75	70	-30	BEC
1999	02	08	04	52	35.20	25.96	20	2.1	25	70	50	BEC
1999	02	10	01	08	35.07	26.11	22	2.3	85	80	60	BEC
1999	02	10	12	01	35.09	26.11	22	3.1	238	74	-70	BEC
1999	02	10	14	04	35.09	26.12	24	3.8	254	71	-66	BEC
1999	02	14	20	13	35.09	26.04	20	2.8	58	80	15	BEC
1999	02	15	11	21	35.10	26.12	22	2.2	230	80	-30	BEC
1999	02	17	00	16	35.08	26.20	29	2.7	292	75	-42	BEC
1999	02	17	17	09	34.73	25.82	41	3.3	24	58	-42	BEC
1999	02	18	16	49	34.75	25.74	42	3.4	18	76	117	BEC
1999	02	21	03	30	35.17	25.77	13	3.2	12	48	-59	BEC
1999	02	22	12	36	35.09	26.07	22	3.4	267	81	-20	BEC
1999	02	25	02	30	35.24	26.01	18	2.6	15	55	80	BEC
1999	02	26	08	41	34.94	26.12	38	2.3	36	33	-28	BEC
1999	02	26	18	10	34.95	26.10	39	2.4	340	55	-30	BEC
1999	02	27	23	50	35.05	26.11	19	3.9	40	90	175	BEC
1999	02	28	00	19	35.04	26.10	18	2.4	50	45	30	BEC
1999	03	01	03	02	35.05	26.11	22	3.6	70	71	16	BEC
1999	03	01	03	11	35.04	26.10	17	2.2	100	65	50	BEC
1999	03	01	03	28	35.04	26.12	22	3.5	240	85	-60	BEC
1999	03	01	12	18	34.94	26.10	35	3.2	90	65	-170	BEC
2000	01	27	06	51	35.52	23.51	9	4.5	205	53	-75	SED
2000	01	31	07	34	35.24	27.36	27	4.8	200	69	-54	SED
2000	02	22	11	55	34.58	25.51	12	5.2	130	79	90	SED(*)
2000	02	22	11	55	34.15	25.35	33	5.3	347	34	157	CMT(*)
2000	02	22	11	55	34.95	25.38	20	5.0	92	71	68	BEN*
2000	03	10	22	01	34.31	26.09	24	5.1	289	46	102	SED*
2000	03	10	22	01	34.13	25.98	15	5.2	256	22	72	CMT(*)
2000	03	13	14	18	35.35	23.38	36	4.7	130	63	88	SED
2000	04	05	04	36	34.22	25.85	15	5.4	301	55	120	SED*
2000	04	05	04	36	34.08	25.83	15	5.5	276	43	80	CMT(*)
2000	04	05	04	36	34.22	25.69	30	5.6	298	44	-107	USG(*)
2000	04	17	23	55	34.22	25.91	24	4.9	51	64	59	SED
2000	04	30	13	19	34.99	25.10	7	1.4	147	35	-42	MES
2000	04	30	21	15	35.00	24.70	16	2.3	233	76	69	MES
2000	05	02	18	31	34.89	24.79	32	1.2	169	55	-30	MES
2000	05	05	03	42	34.91	25.43	1	1.3	280	85	85	MES
2000	05	23	14	14	34.86	24.68	38	1.3	223	80	24	MES

Table 1 (cont.)

year	month	day	hour	min	lat[°N]	lon[°E]	dep [km]	mag	strike	dip	rake	reference
2000	06	01	17	07	34.90	24.65	13	1.7	265	85	75	MES
2000	06	04	18	38	34.95	25.25	10	1.6	221	55	64	MES
2000	06	05	01	53	35.16	24.82	12	0.8	173	50	-14	MES
2000	06	11	16	27	34.99	25.10	7	1.4	315	42	-54	MES
2000	06	13	01	43	35.15	27.13	24	5.2	141	73	-162	SED(*)
2000	06	13	01	43	35.16	26.74	15	5.4	147	45	-166	CMT(*)
2000	06	13	01	43	35.17	27.16	16	5.0	49	71	-46	BEN*
2000	06	15	13	51	34.95	25.26	9	0.9	160	75	80	MES
2000	06	15	16	10	35.16	27.16	18	4.7	190	47	-91	SED
2000	06	28	08	08	34.97	25.25	10	1.4	38	68	-79	MES
2000	07	13	23	20	34.97	25.24	11	1.5	331	84	-55	MES
2000	07	17	12	12	34.47	26.58	27	4.7	323	62	-116	SED
2000	08	04	11	24	34.98	25.27	11	1.0	314	77	-69	MES
2000	08	15	16	18	34.97	25.27	10	0.9	320	88	-75	MES
2000	09	03	12	33	34.97	25.25	10	1.4	38	68	-79	MES
2000	10	04	10	51	35.04	24.57	4	2.2	143	14	-45	MES
2000	10	13	01	46	34.91	25.43	1	1.4	280	35	48	MES
2000	10	13	22	49	35.04	27.23	24	4.6	323	81	157	SED
2000	10	14	15	23	34.96	25.25	11	2.0	46	62	-66	MES
2000	10	29	19	35	34.92	24.89	32	0.6	55	78	-21	MES
2000	11	10	22	57	34.95	24.91	10	0.9	309	56	-72	MES
2000	12	03	15	44	34.95	25.56	9	1.1	160	75	80	MES
2000	12	15	05	17	34.93	24.84	35	1.4	41	83	-20	MES
2001	03	10	11	20	34.89	25.98	12	5.0	93	84	-6	SED
2001	04	01	16	16	35.01	25.02	22	0.3	129	34	-58	MES
2001	04	10	14	00	34.31	26.06	42	4.6	353	85	-169	SED
2001	04	11	08	25	34.99	23.16	24	4.6	275	48	93	SED
2001	04	27	23	31	34.91	24.80	20	3.5	142	22	-35	MES
2001	04	28	00	06	35.22	23.08	51	4.5	157	67	131	SED
2001	05	01	06	00	35.69	27.50	15	5.1	174	50	-96	SED*
2001	05	01	06	00	35.33	27.17	33	5.2	176	25	-105	CMT(*)
2001	05	04	19	51	34.62	22.77	24	4.6	64	85	22	SED
2001	06	05	15	57	34.93	25.04	15	2.4	359	26	76	MES
2001	06	09	01	28	36.19	22.98	15	4.5	349	51	-99	SED
2001	06	13	00	36	35.93	24.89	24	1.5	18	55	-37	MES
2001	06	14	17	42	35.01	24.94	26	0.8	33	84	14	MES
2001	07	14	22	14	34.97	25.15	11	1.5	14	45	-40	MES
2001	07	31	11	08	34.88	25.43	7	1.6	127	18	-56	MES
2001	07	31	23	56	34.58	24.77	15	4.2	275	71	-80	SED
2001	08	03	09	03	35.11	25.32	15	1.5	111	46	57	MES
2001	08	25	14	37	34.91	25.40	4	2.0	75	7	45	MES
2001	08	27	07	42	34.91	25.42	9	1.8	14	10	90	MES
2001	09	13	05	55	35.16	24.89	11	0.3	101	38	52	MES
2001	09	13	15	42	35.51	25.93	54	5.1	175	65	70	SED
2001	09	23	11	41	34.91	25.46	9	1.8	100	40	5	MES
2001	09	26	04	19	35.04	27.04	27	4.9	49	87	-14	SED
2001	11	04	17	23	34.06	25.43	24	5.0	90	49	71	SED
2001	11	26	04	18	34.42	24.10	15	4.5	228	4	0	MED
2001	11	26	04	21	34.79	24.06	24	4.6	311	83	-134	SED
2001	11	26	05	00	34.77	24.17	15	5.2	194	9	-27	MED
2001	11	26	05	03	34.82	24.28	42	5.1	124	72	135	SED*
2001	11	26	05	03	34.49	23.86	48	5.2	343	32	-178	CMT(*)
2001	12	21	14	25	36.00	27.48	9	4.5	328	53	-126	SED

Table 1 (cont.)

year	month	day	hour	min	lat[°N]	lon[°E]	dep [km]	mag	strike	dip	rake	reference
2002	01	22	04	52	35.30	26.67	99	6.1	23	14	-161	MED(*)
2002	01	22	04	53	35.79	26.62	81	6.2	270	88	-45	SED(*)
2002	01	22	04	53	35.53	26.59	90	6.2	3	32	-178	CMT(*)
2002	01	22	04	53	35.79	26.62	84	6.2	355	30	171	USG(*)
2002	01	22	04	53	35.46	26.59	93	6.1	9	36	-176	BEN*
2002	02	24	05	32	34.81	27.28	15	4.5	340	72	-140	SED
2002	04	03	12	00	35.80	23.71	12	4.5	344	47	-96	SED(*)
2002	04	03	12	00	36.10	23.55	17	4.7	321	34	-79	MED*
2002	02	04	08	10	34.83	24.59	54	4.7	104	50	89	SED
2002	05	09	01	49	36.47	23.33	24	4.3	267	86	21	SED-
2002	05	09	01	49	36.33	23.17	17	4.6	176	21	-176	MED(*)
2002	05	21	20	53	36.34	24.41	100	5.9	260	81	179	CMT(*)
2002	05	21	20	52	36.31	24.58	125	5.8	349	74	12	MED(*)
2002	05	21	20	53	36.37	24.31	105	5.8	352	89	4	BEN*
2002	06	06	22	35	35.65	26.18	72	5.0	274	64	-91	SED(*)
2002	06	06	22	35	35.56	26.26	110	5.2	143	26	-32	CMT(*)
2002	06	06	22	35	35.30	26.56	110	5.1	140	30	-43	MED(*)
2002	06	06	22	35	35.54	26.01	94	4.9	153	31	-22	BEN*
2002	09	02	09	23	35.08	26.52	30	4.9	222	60	68	SED
2002	09	08	16	14	34.71	23.43	39	4.7	152	65	118	SED
2002	09	22	09	46	34.85	25.36	12	4.5	165	75	-156	SED
2002	10	12	05	58	34.78	26.37	33	5.0	337	89	-144	SED*
2002	10	12	05	58	34.61	25.99	15	5.4	250	29	2	CMT(*)
2003	03	01	04	06	34.72	23.94	21	4.7	27	89	-13	SED
2003	05	30	10	47	34.78	26.22	45	4.5	135	65	114	SED
2003	07	16	06	56	34.00	24.00	26	4.7	336	67	15	MED
2003	09	05	23	30	34.59	26.19	24	4.6	267	66	-37	SED
2003	10	16	22	44	36.50	23.09	24	4.3	330	54	-121	SED
2003	11	27	14	49	34.92	25.18	12	4.4	57	64	-49	SED
2004	02	07	21	17	36.04	26.91	9	5.2	355	73	-107	SED
2004	03	17	05	20	34.52	23.37	26	6.0	349	88	0	MED*
2004	03	17	05	21	34.59	23.33	24	6.1	351	88	-3	SED(*)
2004	03	18	15	14	36.08	26.48	90	4.4	234	81	-27	SED
2004	10	07	01	05	36.29	26.81	161	5.5	346	25	-167	MED

Table 1: Overview on the entire set of fault plane solutions analyzed in this study. For each event the relevant reference is given: BEC=Becker, 2000; BEN=Benetatos et al., 2004; DEC=DeChaballier et al., 1992; DEL=Delibasis et al., 1999; HAT=Hatzfeld et al., 1993a and 1993b; JOS=Jost et al., 2002; KIR=Kiratzi and Louvari, 2003; MCK=McKenzie, 1972 and 1978; PDI=Papadimitriou et al., 1993; PDO=Papadopoulos et al., 1986; PPA=Papazachos, 1973, Papazachos and Papazachou, 1997, Papazachos et al., 1991 and 2000; TAY=Taymaz et al., 1990; CMT=Harvard Centroid Moment Tensors (1977-2004); MED=INGV MEDNET (2001-2004); SED=Schweizer Erdbeben Dienst, ETH Zürich (2000-2004); USG=US Geological Survey (except CMT solutions, 1982-2002).

In case of multiple occurrences of events we selected the most reliable fault plane solution (see text); in the table ‘*’ indicates the most reliable fault mechanism for the relevant event, ‘(*)’ indicates ‘similar to most reliable solution but not considered’ and ‘-’ indicates rejected fault plane solutions (those that highly deviate from the most reliable solution). No symbol is given for events that occur only once.

Note 1: In the paper by DeChaballier et al. (1992) no information is given on the event magnitude. All events from this study are shallow and were recorded by a local network on western Crete. Furthermore, none of these events was recorded by a regional network. We thus set the magnitude of these events (99 in the table) to $M=2$.

Note 2: The list in the paper by Papadopoulos et al. (1986) contains no information on the hypocentral depth; instead a subdivision into shallower ($z < 60$ km) and deeper ($z > 60$ km) is given. We have set the depth of the shallower category to $z=33$ km similar to the procedure applied for the global catalogues. This was also done for two events from Papazachos et al. (1991).

7. **CYCNET: A temporary seismic network on the Cyclades (Aegean Sea, Greece)**

This chapter has been published. The reference is

Bohnhoff, M., Rische, M., Meier, T., Endrun, B., Becker, D., Harjes, H.-P., Stavrakakis, G. (2004). A temporary Seismic Network on the Cyclades (Aegean Sea, Greece). *Seismol. Res., Lett.*, **75/3**, 352-357.

7.1. Introduction

Densely spaced digital recording temporary seismic networks are a fundamental and widely used tool to monitor microseismic activity at a low magnitude detection threshold. Such networks provide data for various types of investigations such as the evaluation of the seismic hazard potential, structural analysis and determination of stress field orientation. Here, we focus on monitoring in the south Aegean region, which has the highest seismic activity in Europe. In this region, such networks have been operated previously on the island of Crete (see e.g. Delibasis et al., 1999; Harjes et al., 1997; Becker, 2000; Jost et al., 2002; Meier et al., 2004), in western Greece (e.g. Leydecker et al., 1978; Hatzfeld et al., 1989; Sachpazi et al., 2000), and at the volcanic centers of Milos (Ochmann et al., 1989), Santorini (Panagiotopoulos et al., 1996), and Nisyros (Makris and Chonia, 1999). Furthermore, Hatzfeld et al. (1993a, 1993b) analyzed a seismic network covering the whole Aegean region. The present knowledge on seismotectonics of the volcanic arc of the Hellenic subduction zone poses a number of questions that can best be addressed via an investigation of the spatio-temporal distribution of hypocenters. The principal open questions in the area of investigation are: 1. How is the shallow and intermediate-depth seismic activity distributed in the central Hellenic volcanic arc? 2. What is the interaction between spatiotemporal evolution of hypocenters and upward migrating fluids and magma? 3. Why is the seismicity clustered in space and time over a broad range of magnitudes? 4. What is the crustal and uppermost mantle structure along the central volcanic arc? To address these questions, it is desirable to obtain hypocenters with small location errors and at a low magnitude detection threshold.

In this paper we describe a seismic network that was installed in autumn 2002 on the Cyclades island group that cover the central Hellenic volcanic arc, referred to as HVA in the following. The CYClades seismic NETwork (CYC-NET) consists of 22 stations that are distributed on 17 islands. Its combination of short-period and broad-band sensors provides data for both seismicity studies and structural investigations. The recording period for CYC-NET is two years. We highlight the scientific background of CYC-NET and describe the field campaign. Furthermore, selected CYC-NET recordings are shown that quantify the seismic data. Data recorded by CYC-NET are available upon request, preferably linked to a cooperation focussing on specific scientific targets.

7.2. Tectonic setting

The convergent plate boundary between the African lithosphere and the Aegean plate as part of Eurasia is located south of Crete in the Libyan Sea (see Figure 1a). There, the plate boundary approaches the passive continental margin of northern Africa due to roll back of the Hellenic subduction zone and the convergence between Africa and Eurasia (LePichon and Angelier, 1979; Jackson and McKenzie, 1988; LePichon et al., 1995; Stöckhert, 1999). The overall rate of convergence is about 4 cm/year (e.g. McKenzie, 1970; Jackson, 1994; LePichon et al., 1995; McClusky et al., 2000). A well-developed Benioff Zone was identified by seismological observations to a depth of 150-180 km below the central Aegean (Galanopoulos, 1963; Papazachos, 1973; Makropoulos and Burton, 1981; Papadopoulos et al., 1986; Papazachos et al., 2000). Subducting lithosphere can be followed down to about 1200 km by seismic tomography (e.g. Spakman et al., 1988; Wortel et al., 1990; Papazachos and Nolet, 1997; Bijwaard and Spakman, 1998; Karason and van der Hilst, 2000). A tectonic reorganization in the entire south Aegean region about 5 Ma ago may mark the onset of continent-continent collision between the Aegean plate and Northern Africa (LePichon et al.,

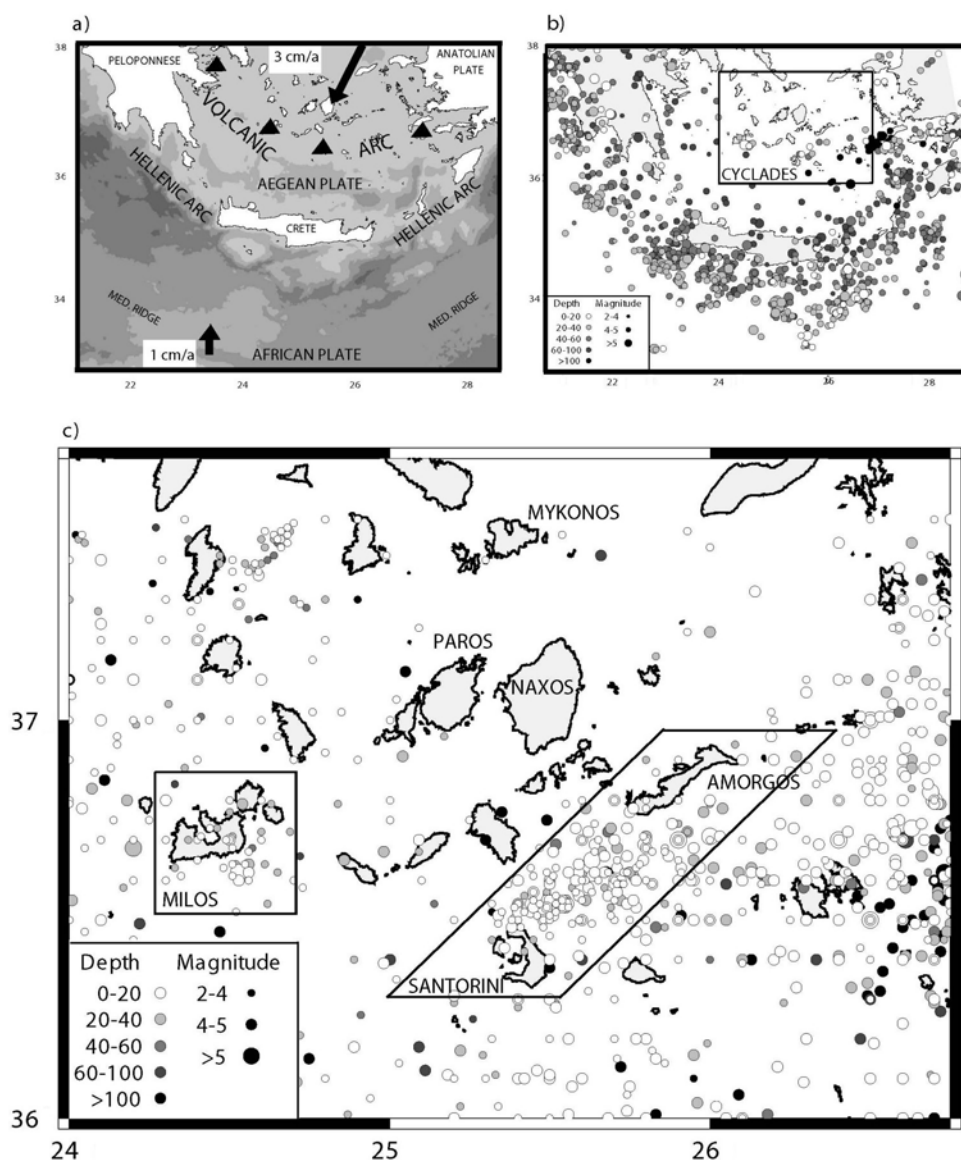


Figure 1: a) Main tectonic elements of the south Aegean region. Grey shades indicate 1000 m steps in water bathymetry. Arrows show present directions and rates of surface deformation (after McClusky et al., 2000). Black triangles represent the volcanic centers of Aegina, Milos, Santorini and Nisyros (from west to east). b) Distribution of hypocenters in the south Aegean region based on the relocated ISC catalog (Engdahl et al., 1998) for the time interval 1965-1998 (complete for $M > 4$). The Cyclades region is marked by the rectangle and enlarged in Figure 1c). c) Distribution of hypocenters in the central Hellenic volcanic arc (HVA) during the period 1965-2001 as recorded by the permanent Greek network that is operated by the National Observatory of Athens (NOA). The catalog is complete for $M > 2.7$. Rectangles mark the seismically active regions at Milos and Santorini-Amorgos (see text for details).

1995, Mascle et al., 1999). It resulted in a complex tectonic frame with a number of details, such as the rapid uplift of western Crete (e.g. Meulenkaamp et al., 1994; Lambeck, 1995), that are not yet fully understood.

The Hellenic volcanic arc (HVA) is located about 150 km to the north of the Hellenic (non-volcanic) arc in the southern Aegean Sea (see Figure 1a). The subducting slab was identified at 100-120 km depth by distribution of hypocenters (see e.g. Knapmeyer, 1999). Upward movement of magmas and fluids causes internal deformations of the Aegean plate. Surface expressions of this magma flow are the active volcanic centers at Aegina, Milos, Santorini and Nisyros.

7.3. Seismic activity at the Hellenic Volcanic Arc (HVA)

Seismicity in the south Aegean region predominantly follows the Hellenic (non-volcanic) arc as identified in the relocated ISC catalog by Engdahl et al. (1998). The catalog, which is complete to $M=4$, is plotted in Figure 1b. More details of the hypocentral distribution in the HVA can be resolved by analysing seismic activity at a lower magnitude threshold. The permanent Greek network, operated by the National Observatory of Athens (NOA), provides a completeness threshold of $M_I=2.7$ (see Figure 1c). The earthquakes in the HVA occur at distinct depth levels: a comparatively small number of events can be related with the Benioff zone at >100 km depth. The predominant activity below the Cyclades occurs at rather shallow depth levels ranging from the surface down to about 50 km depth and is concentrated around the volcanic centers of Milos and Santorini. The seismic activity at Milos is concentrated below the volcano. In contrast, in the Santorini-Amorgos region epicenters align in a SW-NE oriented zone northeast of the active volcanic center at Santorini.

Local temporary networks were operated on Santorini (Panagiotopoulos et al., 1996) and on Milos (Ochmann et al., 1989) for several months. Data from these deployments allowed to identify a strong spatiotemporal clustering below Milos. Time intervals with average seismic activity of about 3-5 events per day were interrupted by single days with up to 600 events. The events were weak ($M<2$) and occurred within the uppermost 10 km. In contrast, the Santorini volcano is characterized by low seismic activity.

Referring to larger earthquakes in the HVA within the last century a remarkable sequence of 21 earthquakes with M_s ranging from 7.5 (main shock) to 4.1 is of note (Papadopoulos and Pavlides, 1992). The main shock was followed by a second strong earthquake of $M_s = 7.2$ after only 12 minutes, at a distance of 100 km. These earthquakes are not included in the cata-

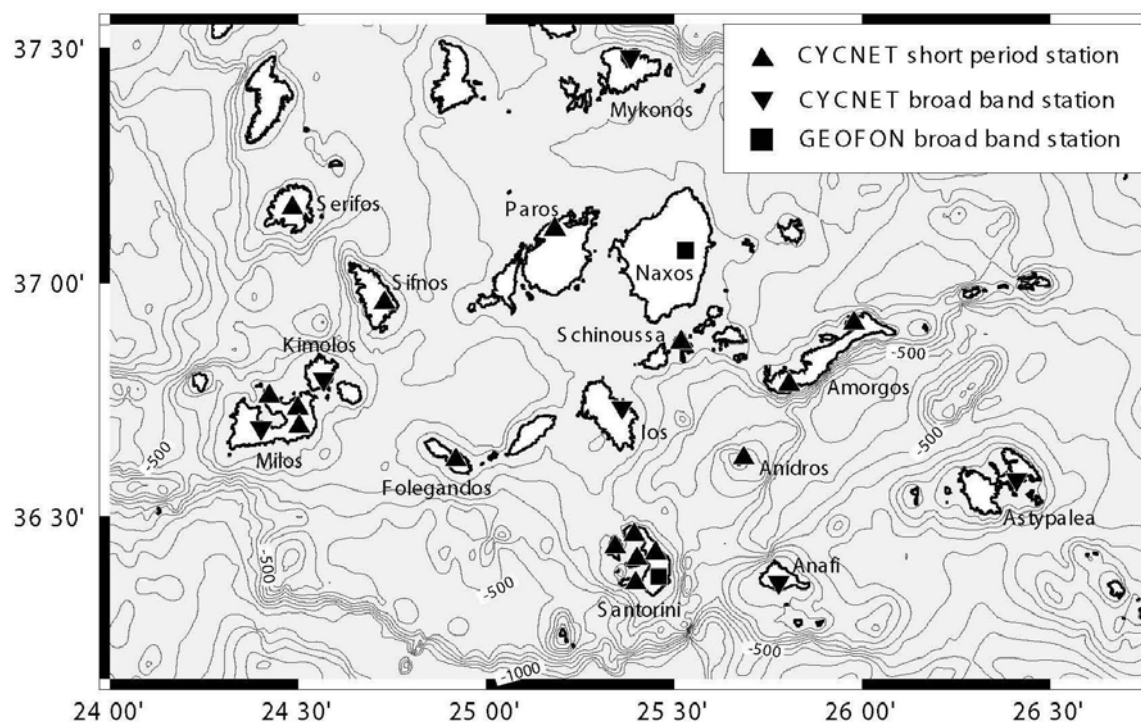


Figure 2: Station distribution of the CYClnades seismic NETwork (CYC-NET). Triangles mark stations that are equipped with a short-period sensor. Broad-band stations are indicated by reversed triangles (CYC-NET) and squares (GEOFON network), respectively. See text for details. Water depth is given by 100 m isolines.

logues discussed above. They occurred during a single five month interval starting on July 8th 1956. Interestingly the events cluster around a SW-NE trend between Santorini and Amorgos - the same trend that was observed for instrumental seismicity from the ISC and NOA catalogs. In summary, the HVA exhibits strong temporal clustering of seismic activity along the entire depth range down to the Benioff zone over a broad range of magnitudes. Hypocentral depths are concentrated in the uppermost 50 km and slab-related events are sparse.

7.4. Site selection and installation of stations

To perform accurate hypocenter determinations for events occurring at shallow depths a local network is needed to provide sufficient spatial and azimuthal coverage. For common onshore networks the distribution of stations is restricted mainly by the level of civilian noise, ground coupling and station access. In contrast, the selection of recording sites for a network at the central HVA is primarily restricted by the distribution of adequately located islands of sufficient size. Building up a seismic network on the Cyclades is a major logistic challenge due to difficult access to the smaller islands. This becomes even more evident in winter when the inter-island traffic is limited. For surveying potential station sites on selected islands, the following quality criteria needed to be combined and optimized:

- (1.) A solid rock foundation. Most of the islands consist of gneiss covered by soft-sediments. We thus selected locations with outcropping gneiss that provides good ground coupling.
- (2.) Low microseismic and cultural noise, the first of which is generated primarily by the sea. Due to the small size of most islands, the level of microseismic noise is high compared to larger islands and mainland. On the Cyclades cultural noise varies seasonally. During summer intense tourism causes a higher background noise than during winter.
- (3.) Acceptable weather conditions. A main task was to find sites that are protected from the well-known Meltemi, a strong wind on the Cyclades occurring throughout the year.

Our final deployment includes 22 stations on 17 islands that cover the entire central HVA (Figure 2 and Table 1, see Appendix). Most islands are equipped with a single seismic station. At the volcanic centers of Milos and Santorini station spacing is more dense to further decrease the magnitude detection threshold (see Figure 2). In addition, two stations of the GEOFON network (Hanka and Kind, 1994) enlarge the CYC-NET. Whereas the station on Santorini further improves the local monitoring conditions, the overall azimuthal coverage of the CYC-NET benefits from the station on Naxos.

Our particular note among the CYC-NET is the station on Anidros, a small (2 km²) uninhabited island between Santorini and Amorgos that cannot be reached by regular traffic. Because of the comparatively strong seismic activity in this region (see Figure 1c) this station improves location accuracy significantly.

Shallow earthquakes occurring within the CYC-NET that are strong enough to produce reliable P and S onsets can be located to an accuracy of a few kilometers. For intermediate depth earthquakes we include recordings from the permanent Greek network operated by the National Observatory of Athens (NOA) and the regional GEOFON network (Hanka and Kind, 1994). Selected stations of both networks together with stations of the CYC-NET are shown in Figure 3. This procedure provides sufficient azimuthal coverage for slab-related events. For larger events, locations from different regional and global networks will be compared to locations from CYC-NET data alone. This allows us to estimate location errors also for events that occurred in the past. Thus, we will be able to refine existing hypocenter maps for this region.

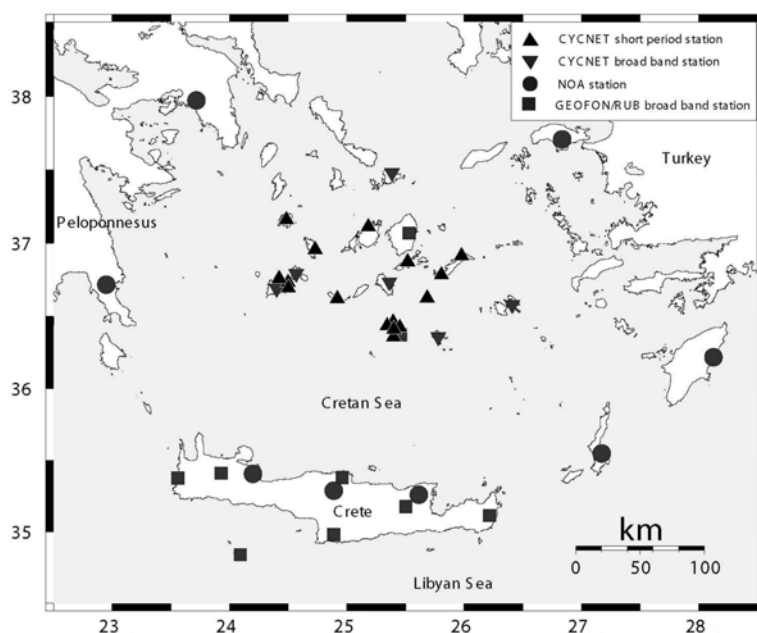


Figure 3: Station distribution used to locate intermediate depth earthquakes. Large black circles and squares mark selected stations of the permanent networks of NOA and GEOFON, respectively, which improve the azimuthal coverage. Triangles mark stations of the CYC-NET as shown in Figure 2.

7.5. Instrumentation and station maintenance

All stations are equipped with the same 24-bit data-logger (Earth Data PR6-24-3AA portable field recorder; Earth-Data Ltd., 2002). An internal GPS receiver is integrated in each of the units. As a frequency content of up to 40 Hz is expected for local events, we fixed the sampling frequency to 100 samples per second. In this recording mode the data-logger provides a signal-to-noise ratio of 140 dB. Seismic data as well as additional information such as timing and position is stored on a removable disk running a LINUX operating system. This system is powered at distinct times to transfer data from the buffer; average power consumption is less than 10 W. To reduce vulnerability to power instabilities two different systems were installed to supply the station with electricity. In most cases we operate the entire recording unit independent of the power-net using solar panels (80 W) in combination with strong (138 Ah) rechargeable batteries. This combination allows to supply the stations with power throughout the year. Some stations are connected to the main power supply. At these stations we implemented specific precautions such as power buffer and lightning protection to guarantee continuous recording.

16 of the 22 stations are equipped with short-period sensors (type MARK 4L-3C, eigenfrequency 1 Hz). The remaining six stations are equipped with broad-band seismometers (STS-2), which allows to evaluate long-period recordings for structural studies based on receiver functions and surface wave recordings. The six broad-band stations are deployed in a North-South and East-West orientation, respectively (see Figure 2). The aim is to observe variations of the crustal and uppermost mantle structures inline and normal to the direction of subduction that was identified to be NNE at the central part of the Hellenic arc (see e.g. Spakman et al., 1988; Granet and Trampert, 1989; Knapmeyer, 1999; Bohnhoff et al., 2001). The stations of the CYC-NET are maintained on a three or six-monthly basis according to storage capacity of the hard discs included in the recording units (6 and 10 GB). Moreover, stations on islands with difficult access, such as Anidros or Folegandros (see Figure 2), are equipped with 20 GB hard discs allowing longer recording periods. We installed online access based on standard or mobile modems at 3 stations. These stations can be monitored remotely to minimize down-time, which is an important step towards a continuous seismic monitoring.

7.6. Data quality and first results

A first quality check of the recordings is performed in the field. This allows us to identify and fix problems directly at the station, an important capability considering the difficult station access. Later, amplitude spectra are calculated to evaluate the noise conditions at each station by averaging recording intervals of 120 minutes. Frequencies are analyzed from 0.1 to 40 Hz (short-period sensors) and 0.005 to 40 Hz (broad-band sensors). To classify the data quality of the CYC-NET recordings, we compare the spectra to the new global low-noise model (NLNM) and the new global high-noise model (NHNM) as given by Peterson (1993). Figure 4 combines the spectra of CYC-NET stations that have been in operation since September 2002. Considering that the stations are temporarily installed on rather small islands (2-200 km²) the quality is unexpectedly high. Based on the noise conditions we estimate the detection threshold to be $M_l=0$ for shallow earthquakes that occur within the network. In Figure 5 we show an earthquake that occurred while the installation of stations was still in progress (20th September 2002, 13:59:03.23 GMT, 25.843°E/36.695°N, depth: 6 km), at which time data from 11 sites were already available. The vertical components of the respective stations are plotted against hypocentral distance (Figure 5a). Each seismogram was filtered between 2 and 15 Hz with a Butterworth bandpass and individually normalized to maximum amplitude. The seismic traces exhibit a high signal-to-noise ratio. Only the station SANN, located on the northern crater rim of the Santorini volcano, is an exception. In general, the stations on Santorini have a slightly higher noise level which is explained by the station underground (quaternary volcanic rock and tuff) and the high civilian and tourist activity on the island. This becomes obvious when comparing SANN with IOSI, both of which are at the same hypocentral distance and located close to the shore (see Figure 2). Figure 5b shows the three-component seismogram of the same event recorded on the island of Paros at 76 km hypocentral distance. The high signal-to-noise ratio allows precise determination of the P and S phase onsets.

The event shown in Figure 5 occurred at about 6 km depth in the Santorini-Amorgos region, where the highest rate of seismicity within the network was expected. Inspection of the first data (September 15th -31st in 2002) revealed the following results: 1. The seismic activity in the central part of the HVA is moderate, with about ten events per day with $M_l \geq 0$. During the same time period only 1 event was detected by the NOA network. Thus, the CYC-NET recordings exemplify the high data quality achievable in recordings of micro-events using a dense local network even on small (2-200 km²) islands. 2. Location results for events that occurred within this recording period show an unexpected distribution of the hypocenters. About 70% of the events occurred in the Paros-Naxos region, which appears to be seismically inactive when events from the ISC and NOA catalogs are considered (see Figure 1b+c). All of

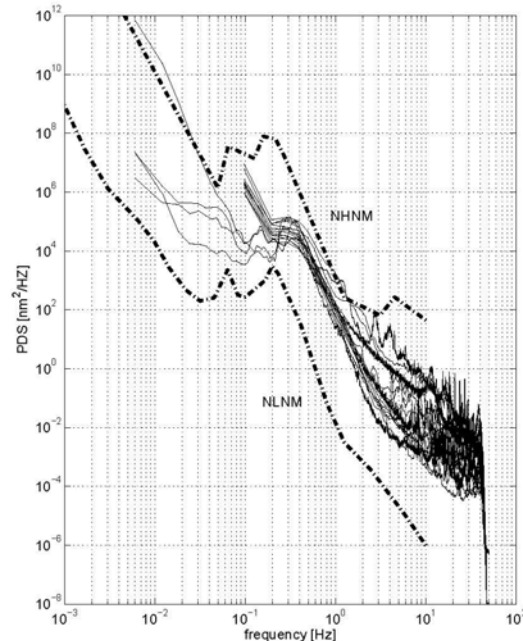


Figure 4: Mean power density spectrum for short-period and broad-band stations of the CYC-NET. Each spectrum was calculated by averaging recording windows of 120 min. To estimate the noise conditions at the CYC-NET stations the new global low-noise model (NLNM) and the new global high-noise model (NHNM) as given by Peterson (1993) are plotted.

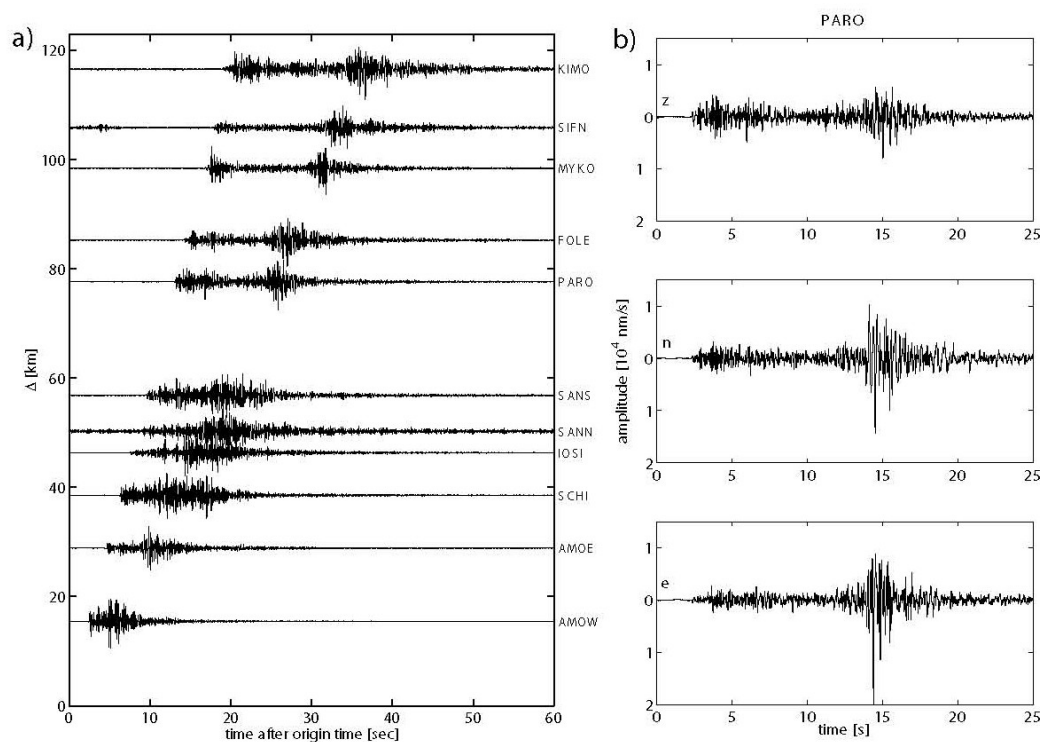


Figure 5: a) Recording example of a local event that occurred within the Santorini-Amorgos region on September, 20th 2002 (see text) at which time data from 11 sites were already available. The vertical components of the respective stations are plotted against hypocentral distance. Each seismogram was filtered between 2 and 15 Hz with a Butterworth bandpass and individually normalized to maximum amplitude. Hypocentral distances vary between 15 and 120 km. Station codes are given on the right hand side. b) 3-component seismogram for the same event as in Figure 5a) recorded at the station on Paros.

the recorded events occurred within the upper 8 km and were of rather small magnitude ($M_1 \leq 1$). Clearly, these initial results may not reflect a characteristic distribution of microseismic activity in the central HVA due to the short time interval. However, our results suggest that the strong temporal clustering observed for larger and moderate magnitudes is present also for weaker events.

7.7. Discussion and summary

A 22-station digital broad-band/short-period seismic network (CYC-NET) was installed at the central volcanic arc of the Hellenic subduction zone in autumn 2002. Maintenance of the CYC-NET is a difficult task as the stations are distributed on 17 islands. The azimuthal coverage allows precise hypocenter determinations for earthquakes that occur within the network at shallow depth levels. Recordings from regional networks will be used to locate intermediate depth earthquakes. The CYC-NET offers the opportunity to study the interaction between local seismicity from the surface down to the Benioff zone as well as the interplay between seismicity and magma and fluid flow. Furthermore, the combination of short-period and broad-band sensors provides the opportunity to perform structural investigations from crustal down to uppermost mantle depths. Although the stations are installed on rather small islands, the data quality is high and provides state-of-the-art recordings with which we can investigate one of the scientifically most interesting and seismically most active volcanic regions in Europe. Our preliminary results highlight the important role of local networks for monitoring of weak micro-earthquakes. Interested readers are welcome on our website

(www.geophysik.rub.de/seismology.html) where additional information and updates on the results can be found.

7.8. Acknowledgements

We are grateful to B. Klotz, L. Kühne and G. Michaletos for their support during installation of the seismic stations on the islands under difficult conditions. This program was funded by the German Research Foundation (DFG) within the collaborative research center 526 'Rheology of the Earth – from the Upper Crust to the Subduction Zone'. We thank the GeoForschungsZentrum Potsdam for supplying acquisition systems from the Geophysical Instrument Pool. We gratefully acknowledge comments by S.E. Hough, E. Rybacki and C. Janssen.

7.9. References

- Becker, D. (2000). Mikroseismizität und Deformation der Kruste Ostkretas, Diploma thesis, University of Hamburg (in German).
- Bijwaard, H. and W. Spakman (1998). Closing the gap between regional and global travel time tomography, *J. Geophys. Res.*, **103**, 30055-30078.
- Bohnhoff, M., J. Makris, G. Stavrakakis, D. Papanikolaou (2001). Crustal investigation of the Hellenic subduction zone using wide aperture seismic data, *Tectonophysics*, **343**, 239-262.
- Delibasis, N., M. Ziaza, N. Voulgaris, T. Papadopoulos, G. Stavrakakis, D. Papanastassiou and G. Drakatos (1999). Microseismic activity and seismotectonics of Heraklion Area (central Crete Island, Greece), *Tectonophysics*, **308**, 237-248.
- Earth Data Ltd. (2002). Instruction manual for PR6-24 seismic data-logger, EDM021 (2), Southampton/U.K., 53 pages.
- Engdahl, E.R., R. Van Der Hilst and R. Buland (1998). Global teleseismic earthquake relocation with improved travel times and procedures for depth determination, *Bull. Seismol. Soc. Am.*, **88**, 722-743.
- Galanopoulos, A.G. (1963). On mapping of seismic activity in Greece, *Ann. Geofis.*, **16**, 37-100.
- Granet, M. and J. Trampert (1989): Large-scale P-velocity structure in the Euro-Mediterranean area, *Geophys. J. Int.*, **99**, 583-594.
- Hanka, W. and R. Kind (1994): The GEOFON Program, *Ann. Geofis.*, **37**, 1060-1065.
- Harjes, H.-P., M. Janik, T. Büsselberg, M. Knapmeyer, H. Schmidt, J. Schweitzer, A. Vafides (1997). Structure and dynamics of the Hellenic subduction zone under Crete from seismic array measurements, *Abstract IASPEI 97*, 18, Thessaloniki.
- Hatzfeld, D., M. Besnard, K. Makropoulos and P. Hatzidimitriou (1993a). Microearthquake seismicity and fault-plane solutions in the southern Aegean and its geodynamic implications, *Geophys. J. Int.*, **115**, 799-818.
- Hatzfeld, D., M. Besnard, K. Makropoulos, N. Voulgaris, V. Kouskouna, P. Hatzidimitriou, D. Panagiopoulos, G. Karakaisis, A. Deshamps and H. Lyon-Caen (1993b). Subcrustal microearthquake seismicity and fault plane solutions beneath the Hellenic arc, *J. Geophys. Res.*, **98**, 9861-9870.
- Hatzfeld, D., G. Pedotti, P. Hatzidimitriou, D. Panagiotopoulos, M. Scorditis, I. Drakopoulos, K. Makropoulos, N. Delibasis, I. Latonsakis, J. Baskoutas and M. Frogneux (1989). The Hellenic subduction beneath the Peloponnesus: first results of a microearthquake study, *Earth and Planet. Sci. Lett.*, **93**, 283-291.
- Jackson, J. (1994). Active tectonics of the Aegean region, *Annu. Rev. Earth Planet. Sci.*, **22**, 239-271.
- Jackson, J. and McKenzie, D.P. (1988). The relationship between plate motion and seismic moment tensors, and the rates of active deformation in the Mediterranean and Middle East, *Geophys. J.*, **93**, 45-73.
- Jost, M.L., O. Knabenbauer, J. Cheng, H.-P. Harjes (2002). Fault plane solutions of microearthquakes and small events in the Hellenic arc. *Tectonophysics*, **356**, 87-114.
- Karason, H. and R. Van Der Hilst (2000). Constraints on mantle convection from seismic tomography, in: Richards, M.A., Gordon, R.G. and v.d. Hilst, R. (eds.), *The history and dynamics of global plate motions*, 277-288.
- Knapmeyer, M. (1999). Geometry of the Aegean Benioff zones, *Ann. Geofis.*, **42**, 27-38.
- Lambeck, K. (1995). Late Pleistocene and Holocene sea-level change in Greece and south-western Turkey: a separation of eustatic, isostatic and tectonic contributions, *Geophys. J. Int.*, **122**, 1022-1044.
- Le Pichon, X. and J. Angelier (1979). The Hellenic arc and trench system: a key to the neotectonic evolution of the Eastern Mediterranean area, *Tectonophysics*, **60**, 1-42.

- Le Pichon, X., N. Chamot-Rooke and S. Lallemand (1995). Geodetic determination of the kinematics of central Greece with respect to Europe: Implications for eastern Mediterranean tectonics, *J. Geophys. Res.*, **100**, 12675-12690.
- Leydecker, G., H. Berckhemer and N. Delibasis (1978). A study of seismicity in the Peloponnesus region by precise hypocenter determinations, Alps, Apennines, Hellenides, Inter-Union Commission on Geodynamics, *Scientific Report*, **38**, 406-410.
- Makris, J. and T. Chonia (1999). Active and passive seismic studies of Nisyros Volcano – East Aegean Sea, Proceedings of the 1999 CCSS Workshop, Communications of the Dublin Institute for advanced studies, A.W.B. Jacob, C.J. Bean, S.T.F. Jacob (eds.), Series D, *Geophysical Bulletin*, **49**, 9-12.
- Makropoulos, K.C. and P.W. Burton (1981). A catalogue of seismicity in Greece and adjacent areas, *Geophys. J.R. astron. Soc.*, **65**, 741-762.
- Masce, J., C. Huguen, J. Benkhelil, N. Chamot-Rooke, E. Chaumillon, J.P. Foucher, R. Griboulard, A. Kopf, G. Lamarche, A. Volkonskaia, J. Woodside, T. Zitter (1999). Images may show start of European-African Plate collision, *Eos. Trans.*, **80(37)**, 421, 425,428.
- Mc Kenzie, D.P. (1970). Plate tectonics of the Mediterranean region, *Nature*, **226**, 239-243.
- McClusky, S. et al. (2000). Global Positioning System constraints on plate kinematics and dynamics in the eastern Mediterranean and Caucasus, *J. Geophys. Res.*, **105**, 5695-5719.
- Meier, T., M. Rische, B. Endrun, A. Vafidis, H.-P. Harjes (2004). Seismicity of the Hellenic Subduction Zone in the area of western and central Crete observed by temporary local seismic networks, *Tectonophysics*, **383**, 149-169.
- Meulenkamp, J.E., Van Der Zwaan, G.J. and W.A. Van Wamel (1994). On late Miocene to recent vertical motions in the Cretan segment of the Hellenic arc, *Tectonophysics*, **234**, 53-72.
- Ochmann, N., Hollnack, D. and J. Wohlenberg (1989). Seismological exploration of the Milos geothermal reservoir, Greece, *Geothermics*, **18(4)**, 563-577.
- Panagiotopoulos, D.G., G. Stavrakakis, K. Makropoulos, D. Papanastasiou, C. Papazachos, A. Savvidis and A. Karagianni (1996). Seismic monitoring at the Santorini volcano, The European laboratory volcanoes, *Proceedings of the second workshop Santorini, Greece*, 311-324.
- Papadopoulos, G.A. and S.B. Pavlides (1992). The large 1956 earthquake in the South Aegean: Macroseismic field configuration, faulting and neotectonics of Amorgos island, *Earth and Planet. Sci. Lett.*, **113**, 383-396.
- Papadopoulos, G.A., D.P. Kondopoulou, G.A. Leventakis and S.B. Pavlides (1986). Seismotectonics of the Aegean region, *Tectonophysics*, **124**, 67-84.
- Papazachos, B.C. (1973). Distribution of seismic foci in the Mediterranean and surrounding area and its tectonic implications, *Geophys. J.R. astron. Soc.*, **33**, 421-430.
- Papazachos, B.C., V.G. Karakostas, C.B. Papazachos and E.M. Scordilis (2000). The geometry of the Wadati-Benioff zone and lithospheric kinematics in the Hellenic arc, *Tectonophysics*, **319**, 275-300.
- Papazachos, C.B. and G. Nolet (1997). P and S deep velocity structure of the Hellenic area obtained by robust nonlinear inversion of travel times. *J. Geophys. Res.*, **102(B4)**, 8349-8367.
- Peterson, J. (1993). Observations and modeling of seismic background noise, *U.S.Geol. Survey Open-File Report*, **93-322**, 95pp.
- Sachpazi, M., A. Hirn, C. Clement, F. Haslinger, M. Laigle, E. Kissling, P. Charvis, Y. Hello, J.-C. Lepine, M. Sapin, J. Ansorge (2000). Western Hellenic subduction and Cephalonia transform: local earthquakes and plate transport and strain, *Tectonophysics*, **319**, 301-319.
- Spakman, W., M.J.R. Wortel and N.J. Vlaar (1988). The Hellenic subduction zone: a tomographic image and its geodynamic implication, *Geophys. Res. Lett.*, **15**, 60-63.
- Stöckhert, B. (1999). The Hellenic Subduction Zone, a world site to study the mechanics of roll back, *Workshop on Mediterranean scientific drilling perspectives*, Proceedings, Granada, 103-108.
- Wortel, M.J.L., S.D.B. Goes, W. Spakman (1990). Structure and seismicity of the Aegean subduction zone, *Terra Nova*, **2**, 554-562.

Appendix : Table 1

Station-ID	Island / Location	LAT [°N]	LON [°E]	Sensor	in operation since
AMOE	Amorgos East	36.92	25.98	MARK L-4C-3D	09/2002
AMOW	Amorgos West	36.78	25.81	MARK L-4C-3D	09/2002
ANAF	Anafi	36.36	25.78	STS-2	09/2002
ANID	Anidros	36.62	25.68	MARK L-4C-3D	09/2002
APE	Naxos (GEOFON)	37.07	25.53	STS-2	09/2000
ASTY	Astypalea	36.58	26.41	STS-2	09/2002
FOLE	Folegandros	36.62	24.92	MARK L-4C-3D	09/2002
IOSI	Ios	36.73	25.36	STS-2	09/2002
KIMO	Kimolos	36.79	25.57	STS-2	09/2002
MILE	Milos East	36.73	24.50	MARK L-4C-3D	11/2002
MILN	Milos North	36.76	24.42	MARK L-4C-3D	11/2002
MILO	Milos	36.69	24.40	STS-2	09/2002
MILS	Milos South	36.69	24.50	MARK L-4C-3D	11/2002
MYKO	Mykonos	37.48	25.38	STS-2	09/2002
NEAK	Nea Kameni, Santorini	36.41	25.40	MARK L-4C-3D	11/2002
PARO	Paros Island	37.12	25.18	MARK L-4C-3D	09/2002
SANC	Thira Center, Santorini	36.42	25.45	MARK L-4C-3D	11/2002
SANN	Thira North, Santorini	36.46	25.39	MARK L-4C-3D	09/2002
SANS	Thira South, Santorini	36.36	25.40	MARK L-4C-3D	09/2002
SANT	Thira, Sant. (GEOFON)	36.37	25.46	STS-2	08/1996
SCHI	Schinoussa	36.87	25.52	MARK L-4C-3D	09/2002
SERI	Serifos	37.16	24.49	MARK L-4C-3D	11/2002
SIFN	Sifnos	36.96	24.73	MARK L-4C-3D	09/2002
THIR	Thirasia, Santorini	36.43	25.34	MARK L-4C-3D	11/2002

Table 1: Station overview of the CYClades seismic NETWORK.

8. Microseismic activity in the Hellenic Volcanic Arc, Greece, with emphasis on the seismotectonic setting of the Santorini-Amorgos zone

This chapter has been submitted for publication. The reference is

Bohnhoff, M., Rische, M., Meier, T. Becker, D. Stavrakakis, G., Harjes, H.-P. (2005). Microseismic activity in the Hellenic Volcanic Arc, Greece, with emphasis on the seismotectonic setting of the Santorini-Amorgos zone. *Tectonophysics*, (submitted).

8.1. Abstract

The volcanic arc of the Hellenic subduction zone with its four volcanic centres is of major relevance when evaluating the seismovolcanic hazard for the Aegean region. We present results from a 22-station temporary seismic network (CYCNET) in the central Hellenic volcanic arc (HVA). CYCNET recordings allow analyzing the level and spatiotemporal evolution of microseismic activity in this region for the first time. A total of 2175 events recorded between September 2002 and July 2004 are analyzed using statistical methods, cluster analysis and relative relocation techniques. We identify distinct regions with significantly varying spatiotemporal behaviour of microseismicity. A large portion of the seismic activity within the upper crust is associated with the presence of islands representing horst structures that were generated during the major Oligocene extensional phase. In contrast, the central part of the Cyclades metamorphic core complex remains aseismic considering our magnitude threshold of 1.5 except one spot where events occur swarm-like and with highly similar waveforms.

The highest activity in the study area was identified along the SW-NE striking Santorini-Amorgos zone. Within this zone the submarine Columbo volcano exhibits strong temporal variations of seismic activity on a high background level. This activity is interpreted to be directly linked to the magma reservoir and therein the migration of magma and fluids towards the surface. NE of Columbo where no volcanic activity has yet been reported we observe a similar seismicity pattern with small-scaled activity spots that might represent local pathways of upward migrating fluids or even developing volcanic activity within this zone of crustal weakness. In contrast, the Santorini and Milos volcanic complexes do not show significant temporal variations and low to moderate background activity, respectively. Relating our results to the distribution of historical earthquakes and the GPS-derived horizontal velocity field we conclude that the Santorini-Amorgos zone is presently in the state of right-lateral transtension reflecting a major structural boundary of the volcanic arc subdividing it into a seismically and volcanically quiet western and an active eastern part.

8.2. Tectonic setting

The Hellenic subduction zone represents the seismically most active region in Europe with predominant activity along the Hellenic arc as part of the Aegean plate. The convergent plate boundary between the African lithosphere and the Aegean plate is located 100-150 km south of the Hellenic arc in the Libyan Sea and approaches the passive continental margin of northern Africa due to roll back of the Hellenic subduction zone and the convergence between Africa and Eurasia (e.g. LePichon and Angelier, 1979; Jackson and McKenzie, 1988; LePichon et al., 1995; Meier et al., 2004). The overall rate of convergence is about 4 cm/a (e.g. McKenzie, 1970; Jackson, 1994; LePichon et al., 1995; McClusky et al., 2000) with a major contribution from the >3cm/a SW-ward migration of the southern Aegean plate. A well-developed Benioff zone was identified by seismological observations to a depth of 150-180 km below the central Aegean (Galanopoulos, 1963; Papazachos, 1973; Makropoulos and Burton, 1981; Papadopoulos et al., 1986; Papazachos et al., 2000). The volcanic arc of the Hellenic subduction zone (Hellenic volcanic arc, referred to as HVA in the following) is located about 150 km to the north of the Hellenic arc in the southern Aegean Sea. The HVA follows the four main volcanic centres of the Hellenic subduction zone namely Aegina, Milos, Santorini and Nisyros/Kos from West to East (see Figure 1a). In this paper, we focus on the central HVA represented by the Cyclades island group. The Cyclades are assumed to

represent a classical example of a high-pressure belt in a back-arc environment (Trotet et al., 2001). Major zones of extensional detachments were described of which some have been shown to be related to post-orogenic crustal-scale extension (e.g. Lister et al., 1984; Avigad and Garfunkel, 1989; Gautier et al., 1993; Gautier and Brun, 1994). There is general agreement on a two-stage extension of the Aegean domain since Oligocene times (e.g. Tirel et al., 2004 and references therein). The first phase of extension occurred during Oligocene to middle Miocene and was initiated by the southward migration of the subducting African lithosphere. This dominantly NS-stretching period was marked by the formation of core complexes in the Cyclades that today form the central HVA (see also LePichon and Angelier, 1979; Lister et al., 1984). However, extension was accompanied or possibly alternated with shortening perpendicular to the stretching direction recognized in large-scale NE-SW to NNE-SSW trending folds (Avigad et al., 2001) one of which is the Santorini-Amorgos zone of crustal weakness (see Figure 1b). The second phase of extension which occurred in Late Miocene is related either to the westward extrusion of Anatolia or to gravity spreading of the Aegean lithosphere (see discussion in Gautier et al., 1999). During this phase, the Cyclades block remained rather inactive and stretching was concentrated in the North Aegean and in the Cretan Sea (see also Walcott and White, 1998).

Volcanic activity in the HVA began approximately 3-4 Ma ago and the area is considered as a region of extensive Quaternary volcanism (e.g. Keller et al., 1990). The main explosive centers of the Upper Quaternary are Milos, Santorini and Nisyros/Kos. The volcanic island of Milos has been the site of explosive rhyolitic volcanism during Plio-Quaternary times (Rinaldi and Campos Venuti, 2003) and no volcanic activity was reported for the last 40ka. A comprehensive summary on the eruption history of the Santorini volcano complex was given by Druitt et al. (1999) and Friedrich (2000). Activity of the Santorini complex started ~600ka b.p. (Perissoratis, 1995) and the volcano is well known for its Late Bronze Age eruption of 1640 BC that was classified as very large (Volcanic Explosivity Index 6.9 or 7.0; Dominey-Howes, 2004). This eruption also formed the general shape of the present caldera. Historic activity has resulted in the present-day islands of Palea and Nea Kameni. Approximately 7 km NE of the main island of Santorini, a new volcanic centre broke the water surface in 1650 AD (e.g. Vougioukalakis et al., 1994; Perissoratis, 1995). This volcanic field is referred to as the Columbo volcanic reef and is considered to be active today (Dominey-Howes and Minos-Minopoulos, 2004).

8.3. Seismicity in the HVA

Seismicity in the south Aegean region predominantly follows the Hellenic arc as identified in the relocated ISC catalog by Engdahl et al. (1998) that covers the time period 1965-1998 and is complete to $M=4$ (Figure 1a). In general, activity at the HVA is smaller compared to the forearc region and concentrated at the volcanic centres and along the SW-NE trending Santorini-Amorgos zone of crustal weakness. On average, hypocentral depth increases towards the NNE reflecting the subducting oceanic African lithosphere. The catalog for the central HVA based on recordings from the permanent Greek seismic network that is operated by the National Observatory of Athens (NOA) is complete to $M=3$ and covers the time span 1965-2001 (Figure 1b). There, the distribution of hypocenters indicates an increasing activity from West to East and the dominantly active regions around Milos and between Santorini and Amorgos are confirmed. Interestingly, the central part of the metamorphic core complex around the islands of Paros and Naxos appears aseismic also for this magnitude level and a diffuse distribution of hypocenters is observed for the remaining parts of the central HVA. Most events of the NOA-catalog are located within the Aegean plate and only a small number is associated with the Benioff zone at 100-150 km depth.

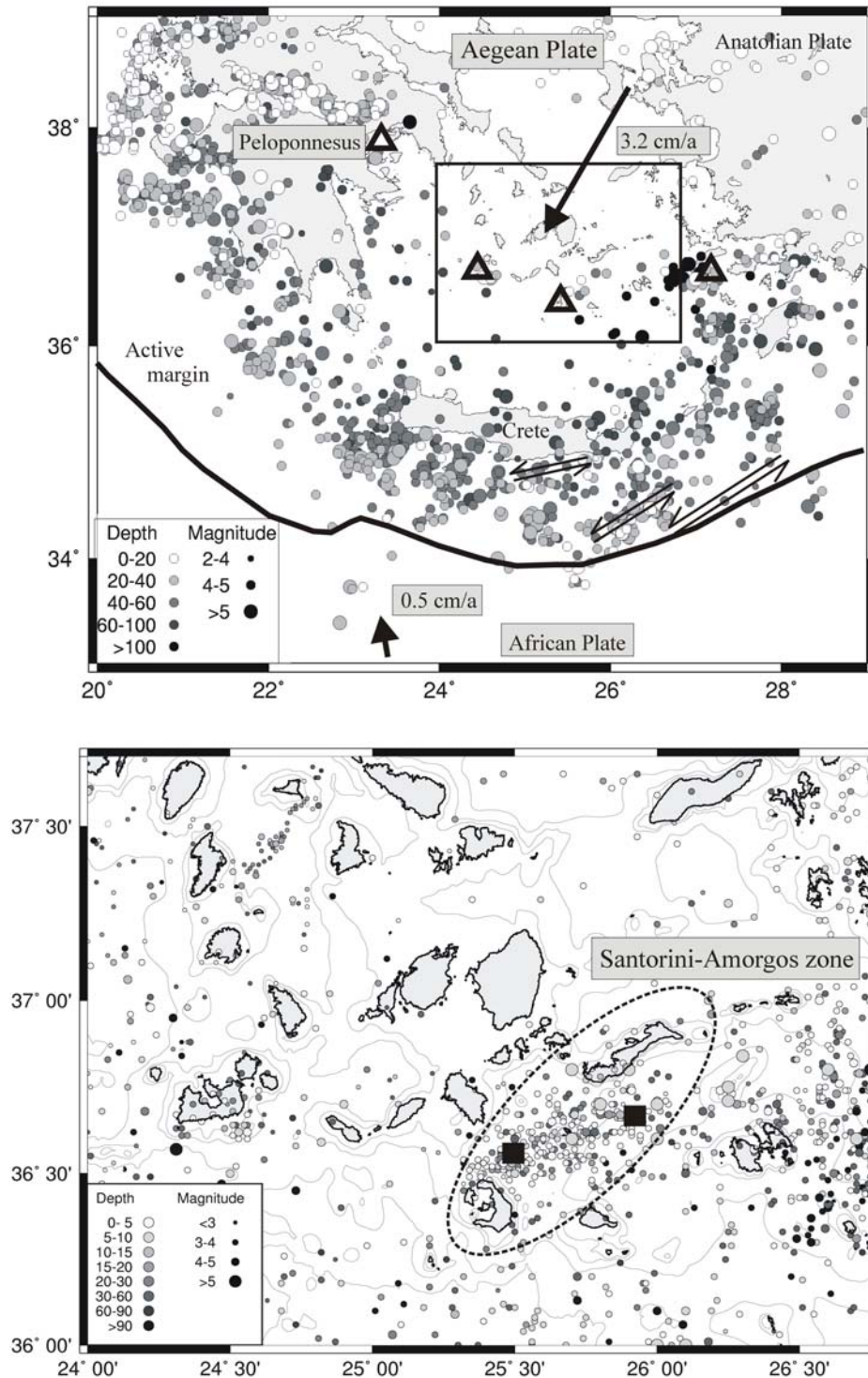


Figure 1: a) Main tectonic elements of the south Aegean region and GPS-derived horizontal velocity field (simplified, after McClusky et al., 2000). Triangles represent the volcanic centres of Aegina, Milos, Santorini and Nisyros (from west to east). Circles are hypocenters from the relocated ISC catalog (Engdahl et al., 1998) for the time interval 1965-1998 (complete for $M > 4$). The Cyclades region is marked by the rectangle and enlarged in Figure 1b). Hypocentral depth scales with shading and magnitude scales with size of circles. b) Distribution of hypocenters in the central Hellenic volcanic arc (HVA) during the period 1950-2004 as recorded by the permanent Greek network that is operated by the National Observatory of Athens (NOA). The catalog is complete for $M > 3$. Hypocentral depth scales with shading and magnitude scales with size of circles (encoding different than in 1a). The ellipse marks the Santorini-Amorgos zone of crustal weakness and the black squares mark the two $M > 7$ events of 1956.

The two largest earthquakes in the entire south Aegean region during the last century occurred in 1956 within only 12 minutes and had magnitudes of $M_s=7.4$ and 7.2 , respectively. Both events were located between Santorini and Amorgos (indicated by rectangles in Figure 1b) and they were followed by at least 20 aftershocks of $M>4$ within five months (Papadopoulos and Pavlides, 1992; Papazachos et al., 2000). Interestingly, the hypocenters of this seismic sequence form the same SW-NE trend between Santorini and Amorgos that is observed from instrumental seismicity from the ISC and NOA catalogs. Based on the presently available data, the most challenging objective towards a better understanding of the present seismotectonic setting of the HVA is to lower the magnitude threshold for local seismic activity in this region. Local temporary networks were operated on Santorini (Panagiotopoulos et al., 1996) and on Milos (Ochmann et al., 1989) for several months. Data from these deployments allowed identifying a strong spatiotemporal clustering below Milos where time intervals with average seismic activity of 3-5 events per day were interrupted by single days with up to 600 events. The events were weak ($M<2$) and occurred within the uppermost 10 km. No such temporal clustering was observed at the Santorini volcano where seismic activity was low and concentrated to the NE of the caldera.

In this paper we focus on microseismic activity in the central HVA based on recordings from a temporal seismic network in the Cyclades island group (CYCNET). CYCNET allows to simultaneously monitor the entire central HVA at low magnitude detection threshold for the first time. We analyze the spatiotemporal behaviour of seismic activity using statistical methods as well as cluster analysis and relative relocation techniques and focus on the role of the Santorini-Amorgos zone for the seismotectonic setting of this region.

8.4. Data Base

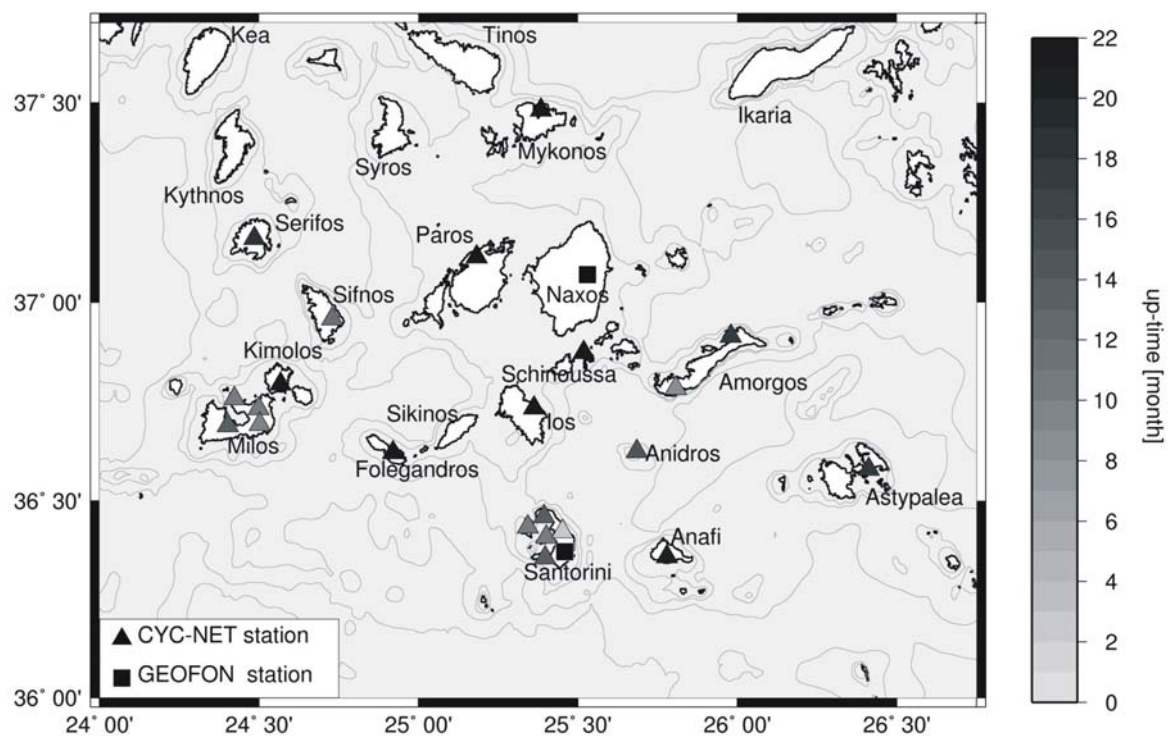


Figure 2: Station distribution of the Cyclades temporary seismological network (CYCNET) that is operated in the central Hellenic Volcanic Arc since autumn 2002. Triangles mark newly deployed stations of CYCNET and their shading represents individual uptime (scaled to the maximum of 22 months (September 2002- July 2004)). Black squares represent stations of the permanent global GEOFON network (Hanka and Kind, 1994). Thin lines mark the 100 m, 200 m and 500 m isolines of water depth, respectively.

With the aim to simultaneously monitor the microseismic activity in the central HVA we installed a seismic network on the Cyclades island group (CYCNET) in autumn 2002 (Bohnhoff et al., 2004). For common onshore networks the distribution of stations is restricted mainly by the level of civilian noise, ground coupling and station access. In contrast, the selection of recording sites for a seismic network in the area of consideration is primarily restricted by the distribution of adequately located islands of sufficient size. Our final deployment included 22 stations on 17 islands covering the entire central HVA. Figure 2 shows the distribution of CYCNET stations where the uptime of each recording unit is indicated by the shading of the station symbol. Most islands are equipped with a single seismic station. At the volcanic centres of Milos and Santorini station spacing is denser to further decrease the magnitude detection threshold. In addition, two stations of the GEOFON network (Hanka and Kind, 1994) enlarge the CYC-NET. Our particular note among the CYC-NET is the station on Anidros, a small (2 km²) uninhabited island between Santorini and Amorgos that cannot be reached by regular traffic. Because of the strong seismic activity in this region (see Figure 1b) this station improves location accuracy significantly. Considering the two arrays on Milos and Santorini as one station results in mean station-spacing of 40 km for CYCNET. Data are continuously sampled at 100 samples per second and the quality of recordings achieved by CYCNET is comparable to those from larger islands such as Crete and thus unexpectedly high (see Bohnhoff et al., 2004, for details).

In this study we consider the time interval September 2002 - July 2004. To evaluate the data, we ran a STA/LTA trigger on the vertical component of each station as a first step. Events were selected if passing a coincidence trigger (>3 stations) combined with an algorithm neglecting events far outside CYCNET. This was done to exclude the strong seismic activity in the forearc and in the Nisyros/Kos region from further consideration. Onsets of P and S phases were picked manually. A total of 45885 (P) and 39646 (S) onsets were identified, respectively, and served as input together with S-P times if available. To determine the hypocenters we applied the HYPO71 routine (Lee and Lahr, 1972; 1975) that includes a linearized hypocenter inversion. We used a 1D-velocity model (Table 1) that was derived from a wide-aperture seismic profile in the eastern HVA (Makris and Chonia, 1999) combined with information on Moho depth achieved from CYCNET recordings using receiver function analysis techniques (Endrun et al., pers.comm.) and gravity modeling (Tirel et al., 2004). As the hypocentral depth is sensitive to the start location we iteratively varied

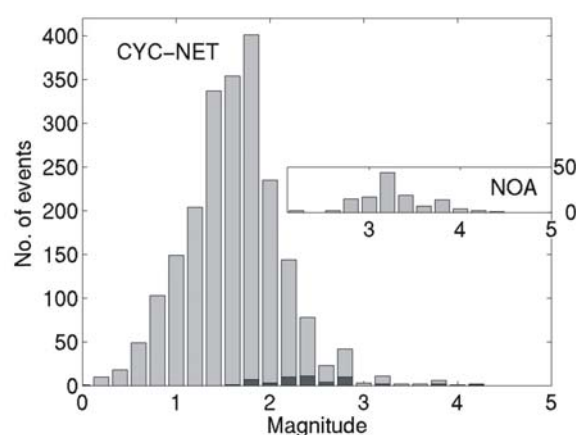


Figure 3: Magnitude frequency distribution for the CYCNET catalog containing all 2175 events within 24-26.75°E and 36-37.7°N with no depth limitation covering the time interval September 2002 – July 2004. Dark gray bars indicate the 51 events located at >60 km depth. The inset shows the magnitude frequency distribution of the NOA catalog for the same area and time interval (127 events).

Vp [km/s]	z [km]
5.00	0.00
5.50	2.00
5.80	5.00
6.70	12.00
7.90	24.00

Table 1: Velocity model for the central HVA used for hypocenter determination (see text for details).

this parameter between 5 and 40 km and proceeded with the solution resulting in the lowest root mean square (RMS) value. With this we were able to locate a total of 3438 events. The hypocenter catalog was then restricted to the range 24.0°-26.75°E and 36.0°-37.7°N with no depth limitation and only events based on at least eight (including at least two S) picks and a RMS value <0.7 s were considered for further analysis. This resulted in a final hypocenter catalog containing 2175 events. Figure 3 shows the magnitude-frequency distribution for this catalog. The threshold of completeness is $M \sim 1.5$ and the largest event had a magnitude of 4.2. Events located at depths >60 km are separately indicated by the dark grey bars. For reference we also plotted the NOA catalog for the same time interval in Figure 3. The significant difference between both catalogs exemplifies the benefit of densely spaced temporary seismic networks to evaluate the small-scale brittle deformation in regions classified as aseismic based on existing hypocenter catalogs. The distribution of hypocentres recorded by CYCNET is plotted in Figure 4 in map view. The hypocentral depth is colour-encoded and grey-shading in the background indicates water depth. More than 80% of the events occur within the uppermost 15 km, i.e. within the Aegean plate that has an average crustal thickness of ~ 24 km in this region (Tirel et al., 2004). Furthermore, a significant number of events is located at intermediate depth levels and can thus be associated with the Benioff zone at 100-150 km depth. These events were located incorporating recordings from surrounding permanent NOA stations to enlarge CYCNET's aperture which significantly im-

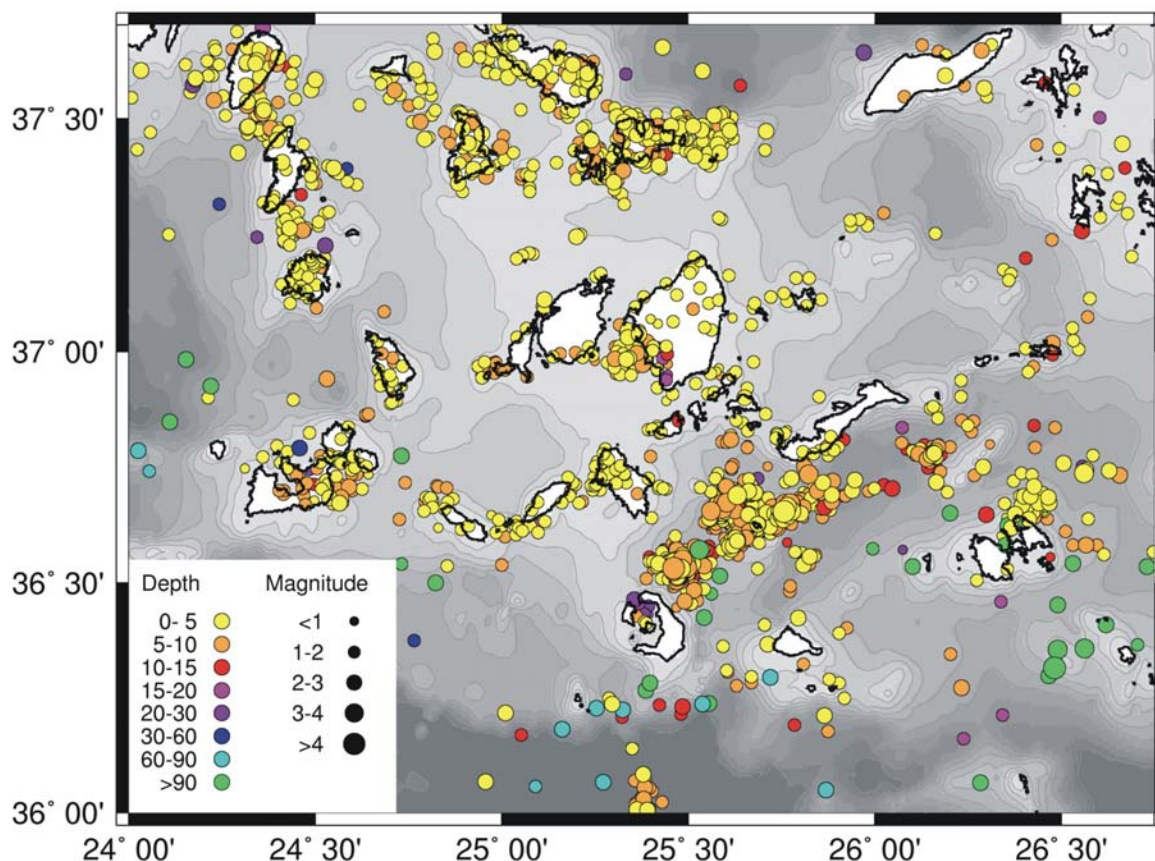


Figure 4: Hypocenter catalog for the central Hellenic Volcanic Arc determined by CYCNET during the time interval September 2002 - July 2004. Hypocentral depth is color encoded and size of circles scales with magnitude. Gray shading indicates water depth in 100 m steps for the first 500 m; dark gray areas in the south reach water depth of more than 1000 m. Shallow seismicity in the central HVA does not occur randomly distributed but shows a number of systematic spatiotemporal patterns. A large portion of the seismic events is related to the occurrence of islands and adjacent offshore areas of <100 m water depth. This effect is not an artefact of CYCNET's station distribution as it is observed also on islands where no seismic station was operated and even on islands outside the network. In contrast, most offshore regions exhibit a significantly lower level of seismic activity

proved the accuracy of hypocenter determination. Apart from crustal and intermediate-depth seismicity, a small number of earthquakes are observed at 24-60 km depth. These events might be associated with rising fluids and magma below the volcanic centres of the central HVA. In this study we focus on the seismic activity within the upper plate and thus do not further consider earthquakes below the Moho.

8.5. Discussion

8.5.1. Spatiotemporal microseismic pattern in the central HVA

Shallow seismicity in the central HVA does not occur randomly distributed but, in contrast, shows a number of systematic spatiotemporal patterns. A clear spatial clustering is observed from the distribution of hypocenters in Figure 4. A large portion of the seismic events is related to the occurrence of islands and adjacent offshore areas of <100m water depth. This effect is not an artefact of CYCNET's station distribution as it is observed also on islands where no seismic station was operated (e.g. islands of Sikinos and Syros) and even on islands outside the network (e.g. Kythnos, Kia, Tinos and Ikaria) (see Figures 2, 4). In contrast, most offshore regions exhibit a significantly lower level of seismic activity, e.g. between Paros and Mykonos, or do not contain a single event at all like the region between Paros and Folegandros. The region surrounded by the chain of islands consisting of Ios-Folegandros-Milos-Serifos-Syros-Mykonos is seismically almost inactive except for the spot between Paros and Naxos that will be discussed in more detail later in the text. Interestingly, the area of low activity coincides with the centre of the metamorphic core complex that formed during the major extensional phase during Oligocene (e.g. Lister et al., 1984; Trotet et al., 2001) and that today represents a major part of the Cyclades island group. Apart from the relation between seismic activity and the occurrence of islands a large number of events align along the SW-NE trending Santorini-Amorgos zone. Here, we observe also the highest density of earthquakes in the entire study area clustering at two spots ~5-10 km NE of Santorini and around Anidros. This zone was also identified as the most active region within the central HVA from the ISC and NOA catalogs (Figure 1). Note, that the here presented catalog contains magnitudes <3 with a few exceptions only and thus a different scale of brittle failure. To further analyze the occurrence of microseismic activity and to elucidate its spatiotemporal evolution we subdivided the central HVA into 48 segments with an equal size of $0.3^{\circ} \times 0.3^{\circ}$ restricted to the uppermost 24 km (see Figure 5). Within each of the 48 segments we compute the temporal evolution of seismic activity in terms of monthly event rate. The results allow identifying four different types of spatiotemporal behaviour in the area of investigation referred to as type A-D in the following. Type A is characterized by little or almost no seismic activity during the entire observation period. This type is observed in a total of 30 segments and thus represents almost 65% of the central HVA. To a large extend, these segments are located at the outer part of CYCNET. However, this is not only an artefact of the network geometry as a number of aseismic segments are located also within the network (e.g. 19-22, 27). Type B seismicity represents a low background level interrupted by short-term peaks of high activity. Such behaviour is observed in segments 3, 26, 28, 31, 35, 36 and 40. Type B seismicity is a possible indicator for swarm activity and may contain earthquake cluster, i.e. events with highly similar waveforms. However, we cannot exclude that segments considered as type A might host type-B activity with periods of silence being at least as long as our observation period. Type-C activity reflects segments with considerable background activity without significant variations during the recording period. This is observed along a west-east trend in segments 9-13 following the occurrence of islands in this part. In addition, type-C activity is identified in segments 18, 29, 30 and 34. Finally, activity of type D is described by

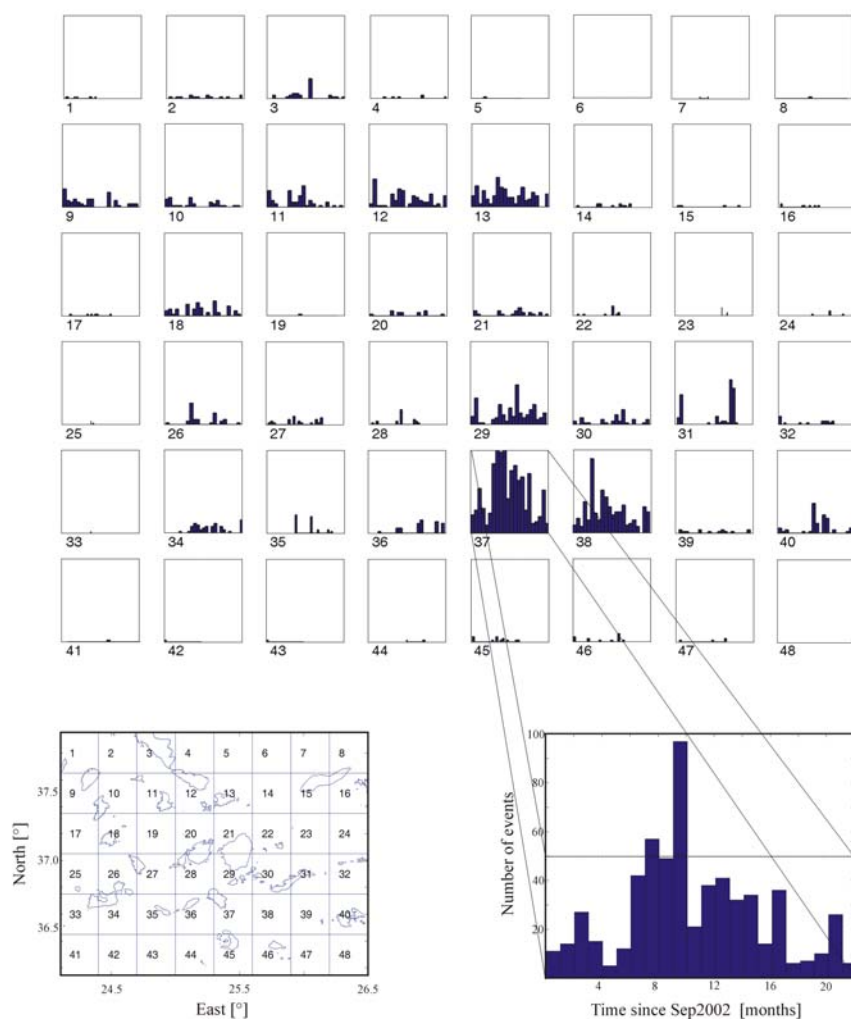


Figure 5: Spatiotemporal evolution of seismicity within a total of 48 segments (size: $\Delta\text{lat}=0.3^\circ$ and $\Delta\text{lon}=0.3^\circ$ limited to a hypocentral depth of 24 km) covering the central Hellenic Volcanic Arc. The event rate is scaled to 50 to visualize the locally varying activity pattern. Four different types of activity pattern are identified and discussed in the text. In segment 37, activity exceeds the monthly event rate of 50 during two months; it is therefore enlarged scaled to the overall maximum of 100 exemplifying the overall highest seismic activity that is directly linked to the here located submarine Columbo volcano. In the lower left we plotted a map view of all 48 segments.

an overall strong seismic activity with significant temporal variations. This is observed in segments 37 and 38, i.e. between Santorini and Amorgos around the submarine Colombo volcano and the island of Anidros. The monthly event rate in Figure 5 is uniformly scaled to 50 for all 48 segments for visualisation reasons. Only activity in segment 37 (area around Columbo) exceeds this rate during two months and is therefore shown enlarged and complete in the lower right of Figure 5.

In the following we discuss representative examples for the different types of activity in more detail which are segments 31 (type B), 13 (type C) and 37+38 (type D). Figure 6 shows the temporal evolution of event magnitudes for these segments. Seismicity SE of Amorgos (segment 31, Figure 6a) shows strong temporal clustering at a single location that covers two orders of magnitude (see also hypocentral distribution in Figure 4). Two main and one weaker peaks of activity are identified of which the latest is also the strongest and active for ~ 7 days. In between, we observe a >1 year long period of seismic quiescence. This pattern indicates seismic swarm activity and occurs in a similar way in segments 3 and 35; it may thus be one typical feature of microseismic activity in the area of investigation caused by fluids. The tem-

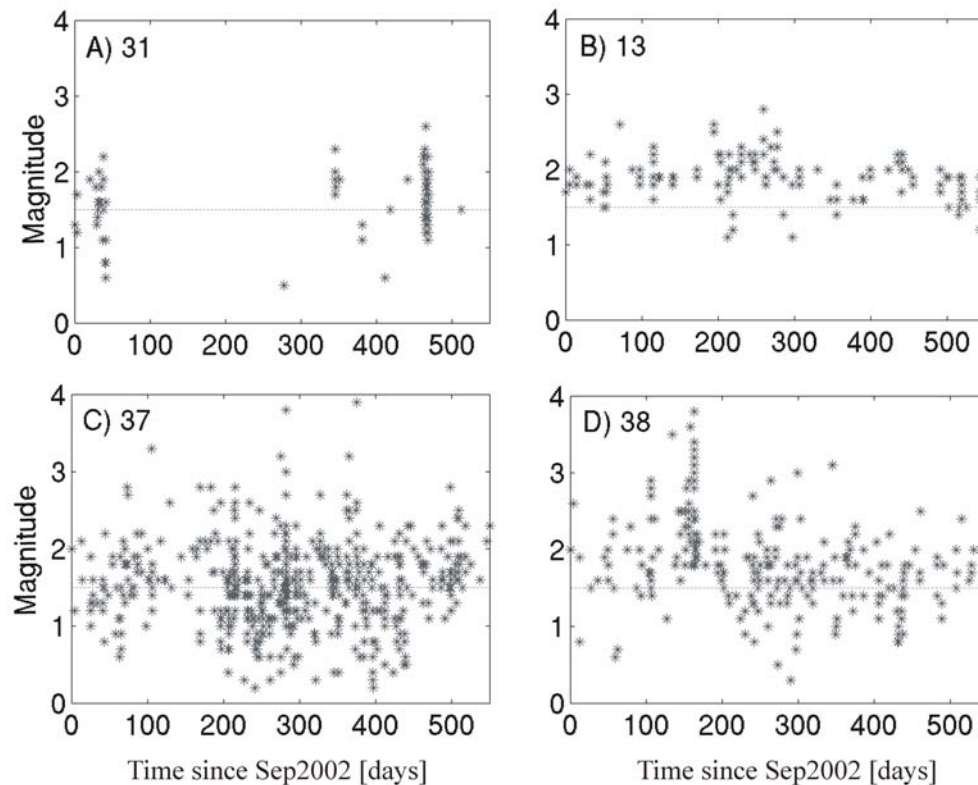


Figure 6: Temporal distribution of magnitudes within four segments that are representative for the different types of spatiotemporal seismicity pattern observed in the central Hellenic Volcanic Arc. The dotted line indicates the overall magnitude threshold for CYCNET.

porally uniform activity on and around Mykonos (segment 13, Figure 6b) is restricted to magnitudes 2 ± 0.5 to a large extent. This indicates a constant release of shear stress in this area. The dominant magnitude of 2 may reflect characteristic event strength for this area. However, we cannot exclude that this is an artefact of our magnitude threshold of $M=1.5$ and $M=2$ reflects the upper boundary of earthquake activity around the island of Mykonos while we do not observe a large portion of $M < 1.5$ events.

8.5.2. Volcano-related seismicity and cluster activity in the Santorini-Amorgos fault zone

Activity within segments 37 and 38 is the highest in the area of investigation (Figure 6 c+d and Figure 5). The distribution of magnitudes reflects the long-period change of activity within both segments and clearly indicates the absence of mainshock-aftershock behaviour although the magnitude range is high especially in segment 37 (not an artefact of station distribution). As described earlier, the activity spot ~ 5 - 10 km NE of Santorini (segment 37) represents the today-active Columbo volcanic reef (Dominey-Howes and Minos-Minopoulos, 2004). In fact, segments 37 and 38 reflect similar long-period changes in seismic activity with maxima lasting 9-12 months overprinted on an overall high background activity. Our data suggest a similar activity pattern in both regions, i.e. Columbo and the area around Anidros. However, no volcanic activity has yet been reported for the area around Anidros. To further constrain the distribution of activity along the Santorini-Amorgos zone, we selected all events along its trend of $\sim 50^\circ$ within a 40 km wide band resulting in a total of 1038 events which is almost half of the entire CYCNET data base. These events are plotted in a depth section in Figure 7a. The distribution of events along the profile clearly suggests that the activity just NE of Santorini is related to the volcanic activity of Mt. Columbo. A bulk of events clusters at

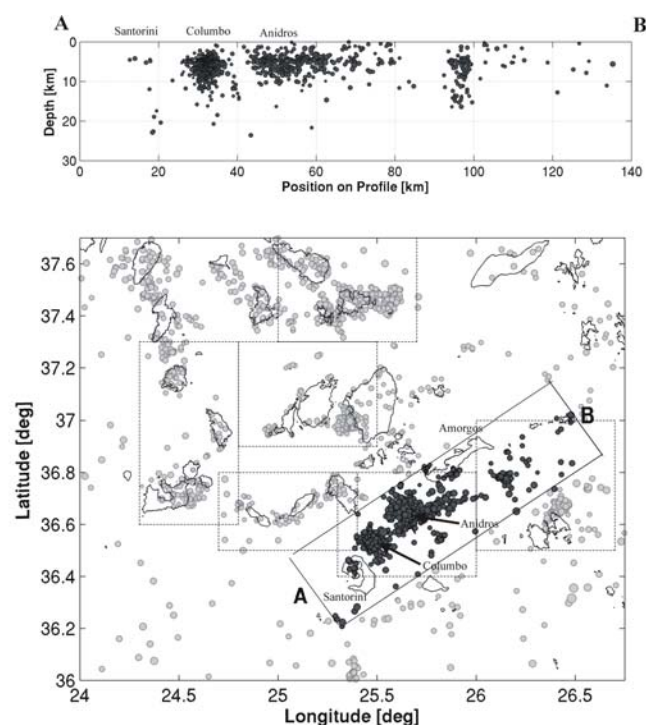


Figure 7: Seismic activity in the Santorini-Amorgos zone observed by CYCNET. The upper part shows a depth section that includes all events within a 40 km wide SW-NE trending profile that is indicated in the lower part by the $\sim 50^\circ$ trending rectangle. A total of 1038 events are included in this profile which is almost half of the entire CYCNET data base. The distribution of events along the profile suggests that the activity just NE of Santorini is related to the volcanic activity of Mt. Columbo. A bulk of events clusters at 3-10 km depth possibly imaging the location of Columbo's magma reservoir and therein the migration of magma and fluids towards the surface. This stresses the active character of this volcano with all its implications for possible future eruptions. The second area with high density of microearthquakes is located NE of Columbo around the island of Anidros possibly consisting of several distinct centres of seismic activity. The activity SE of Amorgos reflects a vertical structure extending between 5 and 15 km depth. The rectangles in the lower part indicate areas investigated by cluster analysis (see text for details).

3-10 km depth possibly imaging the location of Columbo's magma reservoir and therein the migration of magma and fluids towards the surface. This stresses the active character of this volcano with all its implications for possible future eruptions. The second area with high density of microearthquakes is located NE of Columbo around the island of Anidros possibly consisting of several distinct centres of seismic activity. Furthermore, we want to put emphasis on the dike-like structure SE of Amorgos extending between 5 and 15 km depth. For further analysis we have to consider that the hypocenters shown in Figure 7 are absolute locations. The spatiotemporal pattern of seismicity suggests that some areas contain swarm-like activity, possibly with nearly identical waveform which is a commonly observed feature in volcanic regions as shown e.g. for Mt. Etna/Italy (Brancato and Gresta, 2003), Mt. Kilauea/Hawaii (Got et al., 1994) and Volcan de Colima/Mexico (Zobin et al., 2002). Usually such pattern is interpreted as the passive brittle response of the volcanic basement to the intrusion of the eruptive dyke. However, a number of studies (e.g. Hayashi and Morita, 2003; Ukawa and Tsukahara, 1996; Spicak and Horalek, 2001) point out that this might be related to the magma transport in dykes as well. To further investigate this objective for the central HVA and especially for the area NE of Santorini we performed a cluster analysis for distinct regions that are indicated by rectangles in Figure 7b. Within each selected area and for each station we calculated a similarity matrix using a standard waveform cross-correlation technique considering all events contained therein. An adaptive time window starting 1 sec before the P wave onset and including both the P wave and S wave onset was used for the cal-

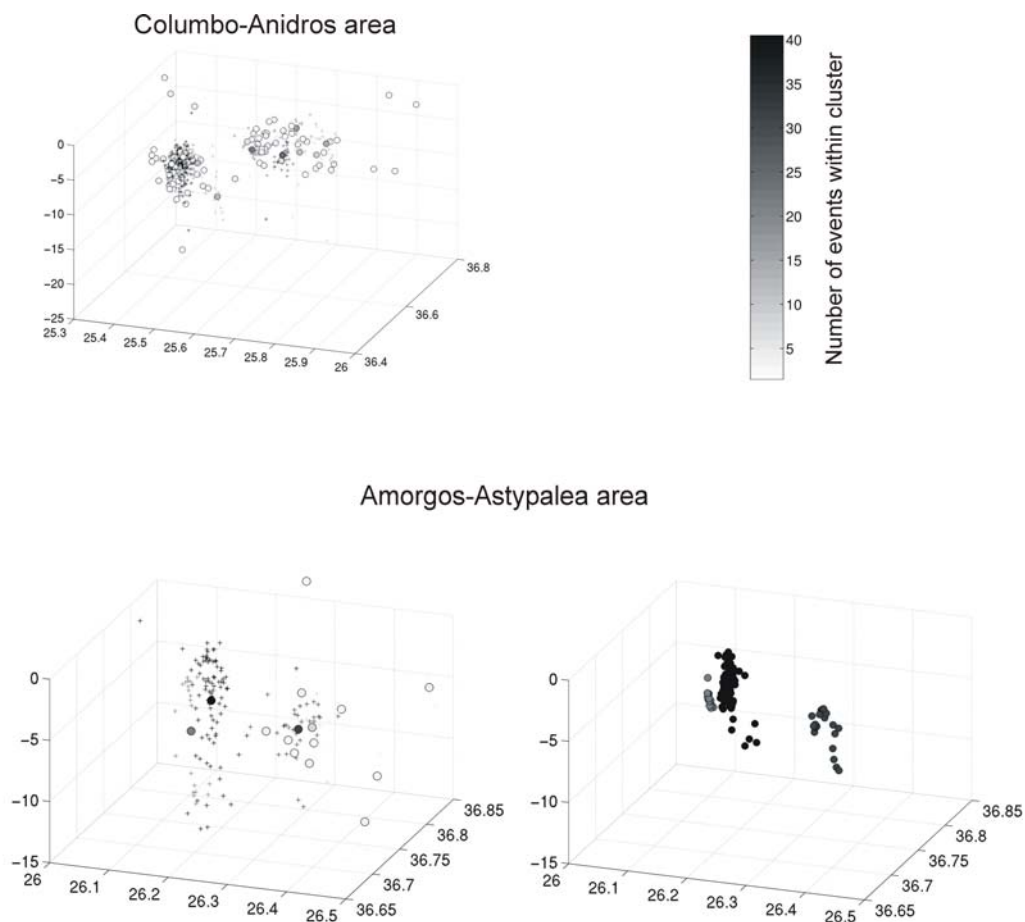


Figure 8: Results of cluster analysis for the Columbo-Anidros (upper left) and Amorgos-Astypalea (lower left) areas. Areas are indicated by rectangles in Figure 7b. Plotted are the median locations of all events belonging to one cluster indicated by circles (one per cluster). The shading of the circles reflects the number of events contained therein. Crosses indicate single events that are not associated with cluster activity. Cluster activity in either area concentrates in two spots forming sphere-shaped structures below Columbo and Anidros but a more dike-like pattern between Amorgos and Astypalea. In addition, we plotted the results of relative relocation for the Amorgos-Astypalea area (lower right) that consists of three main clusters (indicated by the dark grey circles in the lower left). Still the distribution of hypocenters indicates a vertical structure possibly related to the migration of fluids or degassing processes SE of Amorgos.

culuation of the cross correlation coefficient. The data was bandpass filtered between 2 and 15 Hz using a Butterworth filter of 3rd order and the time series were normalized to yield a cross correlation coefficient of 1 at zero lag. The subdivision of events into different clusters was achieved by a single linkage algorithm (see Becker et al., Tectonophysics, subm., for details). In our analysis a cross correlation coefficient of 0.7 was used as threshold value. A minimum of two stations above this value was required to link an event to an already existing cluster. This correlation value is not high enough to identify repeating event series or internal structures of clusters but permits us to perform a relative relocation of individual clusters to investigate e.g. small-scale migration of hypocenters within distinct clusters. We identified a total of 264 clusters containing more than 1170 events. The level of clustering is highly variable within the different regions ranging from very low cluster activity in the Ios-Folegandros region to the area between Amorgos and Astypalea in which almost every single event can be associated with a larger cluster. The activity between Paros and Naxos is of special relevance as it occurs in the otherwise aseismic central part of the metamorphic core complex as mentioned earlier. There, 92 out of 132 events can be associated with clusters, mainly duplets and triplets, which separates this activity spot from the generally island-related

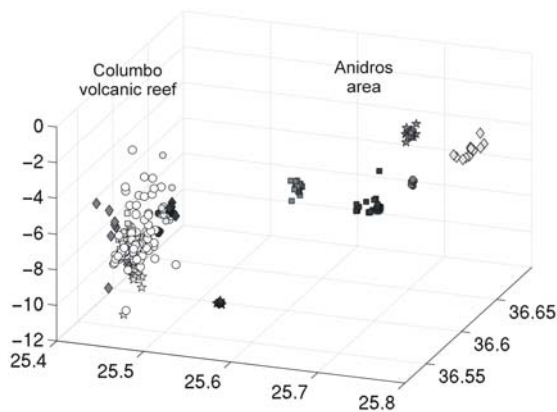


Figure 9: Results of relative relocation for events contained in the clusters shown in figure 8 in the Columbo-Anidros area (perspective view). Individual cluster are marked by different symbols. The largest identified cluster contains 162 events and is located below Mt. Columbo (white circles). The spatial distribution of relocated hypocenters shows a locally varying pattern. Whereas microearthquakes below Mt. Columbo concentrate within one ellipsoidal structure extending between 5 and 8 km depth we identify distinctly separated spots of activity around Anidros. This supports our hypothesis that the Columbo activity might be related to magmatic processes below the volcano possibly representing its magma chamber. In contrast, the activity around Anidros reflects small-scaled activity spots that might represent local pathways of upward migrating fluids within the overall zone of crustal weakness between Santorini and Amorgos or even developing volcanic activity.

seismicity that exhibits only minor cluster activity. In Figure 8 we plotted the results of cluster analysis for the Columbo-Anidros and Amorgos-Astypalea areas. There, the circles represent the median locations of all events belonging to one cluster and their shading indicates the number of members. Crosses mark single events that are not associated with cluster activity. The Columbo-Anidros area hosts the overall largest cluster activity (118 clusters). Between Amorgos and Astypalea we identified the largest cluster containing 87 events following a 21-member cluster in the same region after 14 months of silence (see also segment 31 in figure 5). In either of the two regions clusters concentrate in two spots forming sphere-shaped structures below Columbo and Anidros but a more dike-like pattern between Amorgos and Astypalea. To further resolve the hypocentral distribution within the larger clusters we applied a relative relocation technique using the hypoDD code by Waldhauser and Ellsworth (2000) to all clusters with >10 members within the Santorini-Amorgos fault zone. Apart from the catalog times which were available from the routine data processing a precise waveform cross correlation was performed to obtain highly accurate relative

travel times as input for the relocation scheme. This was done for the P and S onsets separately after resampling the data to 1000 Hz. The differential times obtained from cross correlation were weighted according to their cross correlation coefficients. In Figure 8 (lower right) we plotted the results of relative relocation for the Amorgos-Astypalea area. Still the distribution of hypocenters indicates a vertical structure possibly related to the migration of fluids or degassing processes SE of Amorgos. However, considering the location error for the vertical direction (up to 3 km) might significantly reduce the vertical extension of this pattern. We thus may only speculate whether these features are related to fluid-extrusion or degassing processes at the seafloor which we suggest to be investigated for this entire region between Santorini and Amorgos in the future. Results for relative relocation of the Columbo-Anidros area are shown in Figure 9. Different cluster in the Columbo-Anidros area are marked by symbols. The largest identified cluster contains 162 events and is located below Mt. Columbo (white circles). The spatial distribution of clusters shows a locally varying pattern. Whereas clusters below Mt. Columbo concentrate within one ellipsoidal structure extending between 5 and 8 km depth we identify distinctly separated spots of activity around Anidros. This supports our hypothesis that the Columbo activity might be related to magmatic processes below the volcano possibly representing its magma chamber whereas the activity around Anidros reflects small-scaled activity spots that might represent local pathways of upward migrating fluids within the overall zone of crustal weakness between Santorini and Amorgos or even developing volcanic activity.

8.5.3. Implications for the regional seismotectonic setting

The distribution of hypocenters contained in the ISC, NOAA and also CYCNET catalogs revealed a consistent image of seismicity along the HVA emphasizing that activity is generally higher in the eastern than in the western part. This is of importance as the catalogs cover different magnitude ranges as discussed above. Furthermore, the dominant activity along the Santorini-Amorgos zone is highlighted by either catalog. A similar subdivision along the HVA is observed when considering volcanic activity. In the eastern section, Mt. Columbo is presently the most prominent example being located close to the Santorini complex with its devastating eruptions in historic times. Apart, also the Nisyros/Kos area shows increasing activity (Papadopoulos et al., 1998; Sachpazi et al., 2002), contrary to the decreasing volcanic activity in the western HVA (e.g. Rinaldi and Campos Venuti, 2003). Both observations require a transitional zone or even a sharp structural boundary in between. In Figure 10 we plotted the catalog of historic seismicity that was compiled by Papazachos et al. (2000) for the central HVA. The distribution of hypocenters covers ~2000 years for the larger magnitudes and supports our hypothesis of a subdivided volcanic arc giving further evidence that the boundary in between both segments is represented by the Santorini-Amorgos zone of crustal weakness. Interestingly, the area between Santorini and Amorgos also faced the two largest earthquakes in the entire Aegean region during the last century.

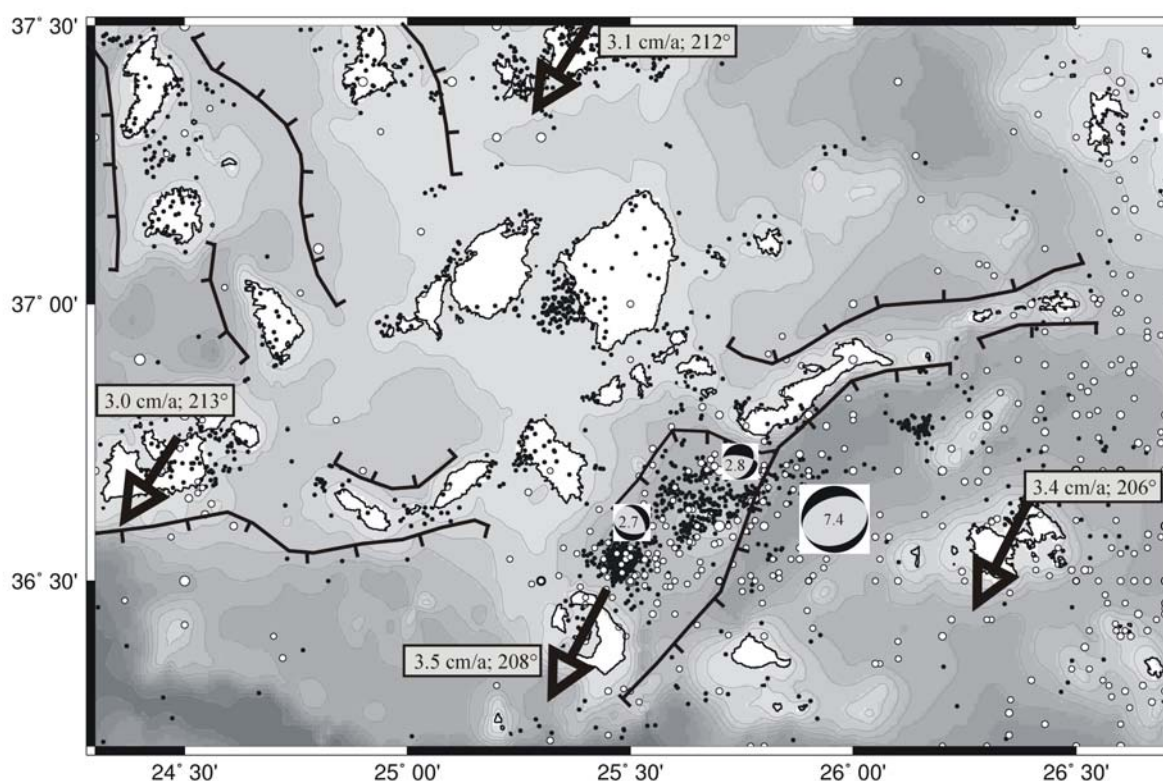


Figure 10: Present seismotectonic setting for the central Hellenic Volcanic Arc. Small black dots are hypocenters recorded by CYCNET and large white dots are hypocenters of the historical seismicity catalog (Papazachos et al., 2000). Black lines indicate major fault structures of the area (simplified after Gautier and Brun, 1994; Tsapanos et al., 1994). Arrows show the GPS-derived horizontal velocity field (after McClusky et al, 2000). Fault plane solutions are taken from Hatzfeld et al., 1993, ($M=2.7/2.8$ of 1988) and from Papadopoulos and Pavlides, 1992, ($M_s=7.4$ which is the mainshock of the 1956 seismic sequence). Results uniformly stress that the Santorini-Amorgos zone marks a major structural boundary in a right-lateral transtensional regime that subdivides the Hellenic Volcanic Arc into a seismically and volcanically quiet western and an active eastern part.

Both events occurred within only 12 minutes in July 1956 ($M_s=7.4$ and 7.2) and were followed by at least 20 aftershocks of $M>4$. Furthermore, the two mainshocks caused a tsunami with regional impact (Ambraseys, 1960; Perissoratis and Papadopoulos, 1999). Papadopoulos and Pavlides (1992) analyzed this seismic sequence including field mapping from Amorgos and concluded on a NW-SE-trending main extensional stress for the Santorini-Amorgos fault region which is supported by the fault mechanism of the 1956 mainshock (see discussion in their paper). The extensional character of this area is confirmed by Hatzfeld et al. (1993) who propose a normal faulting regime with roughly NS trending T axes based on two focal mechanisms that are plotted in Figure 10.

CYCNET earthquake hypocenters are also plotted in Figure 10 (black dots). Although both catalogs cover widely different time and magnitude intervals, the Santorini-Amorgos zone is a common prominent feature in either one indicating that this region represents the major structural boundary between the eastern and western parts of the HVA. To further evaluate the present setting of this zone we implement information on the GPS-derived horizontal velocity field of this region. The most comprehensive study for the Aegean-Anatolian region was presented by McClusky et al. (2000) refining earlier observations of relative plate motion for this region. They report on an average 3.2 cm/a SW-ward movement of the Aegean plate in a Eurasian reference frame with little deformation within the plate itself. However, considering the central HVA, data from four sites were presented that are also plotted in our Figure 10. Putting these into a south-Aegean reference frame allows identifying a NW-SE extensional regime between Mykonos/Milos and Santorini-Astypalea (their Figure 8) which confirms results obtained for the regional seismotectonic setting as described above. In summary, differences of 0.5 cm/a and 7° are found throughout the Santorini-Amorgos zone indicating a right-lateral transtensional character of this area. To further evaluate timing consistency of our hypothesis we relate our findings to structural maps of the south Aegean region (see e.g. Tsapanos et al., 1994; Gautier and Brun, 1994, and references therein). These allow discriminating two types of major faulting directions. Earlier E-W trending normal faults that today form the horst structures and that were overprinted later on by SW-NE trending normal faults. The younger ones are presently active (see e.g. discussion in Perissoratis, 1995). Selected major branches of these faults are plotted in Figure 10 and allow identifying that the Santorini-Amorgos zone represents the SW-NE trending younger fault systems.

We conclude that the Santorini-Amorgos area is a zone of crustal weakness in an overall right-lateral transtensional regime. It represents a major structural boundary in the HVA which is required by independent observations from different disciplines. This results in a subdivision of the volcanic arc. The western part is characterized by considerably lower seismic activity (as also identified by Papanikolaou, 1981, based on a much sparser hypocenter catalog) and decreasing volcanic activity (Aegina, Milos) within the last 40 ka. In contrast, the eastern HVA is characterized by generally higher seismic and volcanic activity focused on the Santorini-Amorgos area and the Nisyros/Kos area as central part of the Dodecanese island group.

8.6. Conclusions

We presented results from a low magnitude detection threshold seismic monitoring experiment in the central Hellenic Volcanic Arc (HVA). Strong seismic activity that is clustered in space and time was identified in regions considered to be aseismic from catalogs containing earthquakes of $M>3$. Microseismic activity is linked to the occurrence of islands that represent horst structures or concentrated in the Santorini-Amorgos zone that also hosted the two largest earthquakes in the entire south Aegean region within the last century. We

identified four different types of spatiotemporal behaviour of microseismic activity. Cluster analysis revealed that more than fifty percent of events can be associated with cluster activity and relative relocation partly allows resolving their internal structure. The most prominent feature is the submarine Columbo volcano NE of Santorini with dominant activity concentrated in the uppermost 5-8 km. This activity is interpreted to be linked to the accumulation of magma below the volcano. Distinct activity spots around Anidros further to the NE are likely locations for future volcanic activity in this zone of crustal weakness or may indicate fluid pathways.

The Santorini-Amorgos zone developed in a right-lateral transtensional regime and is interpreted to mark a major structural boundary of the volcanic arc subdividing the HVA into a seismically and volcanically quiet western and an active eastern part. This model is supported by the GPS-derived horizontal velocity field, the distribution of historical earthquakes and by the occurrence of major faults in this region. The results emphasize that appropriate temporary seismic networks are an adequate tool to develop comprehensive regional seismotectonic models in selected regions.

8.7. Acknowledgements

We are grateful to J. Baskoutas, B. Klotz, L. Kühne and G. Michaletos for their support during installation and maintenance of the seismic stations on the islands under partly difficult conditions. This program was funded by the German Research Foundation (DFG) within the Collaborative Research Centre 526 entitled 'Rheology of the Earth – from the Upper Crust to the Subduction Zone'. We thank the GeoForschungsZentrum Potsdam for supplying seismic acquisition systems from the Geophysical Instrument Pool.

8.8. References

- Ambraseys, N.N., 1960. The seismic sea wave of July 9, 1956 in the Greek Archipelago. *J. Geophys. Res.*, **65**, 1257-1265.
- Avigad, D., Garfunkel, Z., 1989. Low-angle faults above and below a blueshist belt-Tinos Island, Cyclades, Greece. *Terra Nova*, **1**, 182-187.
- Avigad, D., Ziv, A., Garfunkel, Z., 2001. Ductile and brittle shortening, extension-parallel folds and maintenance of crustal thickness in the central Aegean (Cyclades, Greece). *Tectonics*, **20/2**, 277-287.
- Bohnhoff, M., Rische, M., Meier, T., Endrun, B., Harjes, H.-P., Stavrakakis, G., 2004. A temporary Seismic Network on the Cyclades (Aegean Sea, Greece). *Seismol. Res., Lett.*, **75/3**, 352-357.
- Brancato, A., Gresta, S., 2003. High-precision relocation of microearthquakes at Mt. Etna (1991-1993 eruption onset): a tool for better understanding the volcano seismicity. *J. Volc. Geotherm. Res.*, **124**, 219-239.
- Dominey-Howes, D., 2004. A re-analysis of the Late Bronze Age eruption and tsunamis of Santorini, Greece, and the implications for the volcano-tsunami hazard, *J. Volcanol. Geotherm. Res.*, **130**, 107-132.
- Dominey-Howes, D., Minos-Minopoulos, D., 2004. Perceptions of hazard and risk on Santorini. *J. Volc. Geotherm. Res.*, **137**, 285-310.
- Druitt, T.H., Edwards, L., Mellors, R.M., Pyle, D.M., Sparks, R.S.J., Lamphere, M., Davies, M., Barreiro, B., 1999. Santorini Volcano. *Geological Society, London, Memoirs*, **19**, 165pp.
- Engdahl, E.R., Van Der Hilst, R., Buland, R., 1998. Global teleseismic earthquake relocation with improved travel times and procedures for depth determination, *Bull. Seismol. Soc. Am.*, **88**, 722-743.
- Friedrich, W., 2000. Fire in the Sea. The Santorini volcano: Natural history and the legend of Atlantis, *Cambridge University Press*, 257pp.
- Galanopoulos, A.G., 1963. On mapping of seismic activity in Greece, *Ann. Geofis.*, **16**, 37-100.
- Gautier, P., Brun, J.P., 1994. Crustal-scale geometry and kinematics of late-orogenic extension in the central Aegean (Cyclades and Evvia Island). *Tectonophysics*, **238**, 399-424.
- Gautier, P., Brun, J.P., Jolivet, L., 1993. Structure and kinematics of Upper Cenozoic extensional detachment on Naxos and Paros (Cyclades islands, Greece). *Tectonics*, **12**, 1180-1194.

- Gautier, P., Brun, J.P., Moriceau, R., Sokoutis, D., Martinod, J., Jolivet, L., 1999. Timing, kinematics and cause of Aegean extension: a scenario based on comparison with simple analogue experiments. *Tectonophysics*, **315**, 31-72.
- Got, L., Frechet, M.J., Klein, F.W., 1994. Deep fault plane geometry inferred from multiplet relative location beneath the south flank of Kilauea. *J. Geophys. Res.*, **99**, 15375-15386.
- Hanka, W., Kind, R., 1994. The GEOFON Program, *Ann. Geofis.*, **37**, 1060-1065.
- Hatzfeld, D., Besnard, M., Makropoulos, K., Hatzidimitriou, 1993. Microearthquake seismicity and fault-plane solutions in the southern Aegean and its geodynamic implications. *Geophys. J. Int.*, **115**, 799-818.
- Hayashi, H., Morita, Y., 2003. An image of a magma intrusion process inferred from precise hypocentral migrations of the earthquake swarm east of the Izu Peninsula. *Geophys. J. Int.*, **153**, 159-174
- Jackson, J., 1994. Active tectonics of the Aegean region, *Annu. Rev. Earth Planet. Sci.*, **22**, 239-271.
- Jackson, J., McKenzie, D.P., 1988. The relationship between plate motion and seismic moment tensors, and the rates of active deformation in the Mediterranean and Middle East, *Geophys. J.*, **93**, 45-73.
- Keller, J., Rehren, Th., Stadlbauer, E., 1990. Explosive volcanism in the Hellenic arc: A summary and review. Proceedings of the third International Congress, *Thera and the Aegean World III*, **Vol. 2**, 13-26.
- Lee, W.H.K., Lahr, J.C., 1972. HYPO71: A computer program for determining hypocenter, magnitude, and first motion pattern of local earthquakes. *U.S. Geological Survey Open-File Report*.
- Lee, W.H.K., Lahr, J.C., 1975. HYPO71 (revised): A computer program for determining hypocenter, magnitude, and first motion pattern of local earthquakes. *U.S. Geological Survey Open-File Report*.
- Le Pichon, X., Angelier, J., 1979. The Hellenic arc and trench system: a key to the neotectonic evolution of the Eastern Mediterranean area, *Tectonophysics*, **60**, 1-42.
- Le Pichon, X., Chamot-Rooke, N., Lallemand, S., 1995. Geodetic determination of the kinematics of central Greece with respect to Europe: Implications for eastern Mediterranean tectonics, *J. Geophys. Res.*, **100**, 12675-12690.
- Lister, G.S., Banga, G., Feenstra, A., 1984. Metamorphic core complexes of Cordilleran type in the Cyclades, Aegean Sea, Greece. *Geology*, **12**, 221-225.
- Makris, J., Chonia, T., 1999. Active and passive seismic studies of Nisyros Volcano – East Aegean Sea, Proceedings of the 1999 CCSS Workshop, Communications of the Dublin Institute for advanced studies, A.W.B. Jacob, C.J. Bean, S.T.F. Jacob (eds.), Series D, *Geophysical Bulletin*, **49**, 9-12.
- Makropoulos, K.C., Burton, P.W., 1981. A catalogue of seismicity in Greece and adjacent areas, *Geophys. J.R. astron. Soc.*, **65**, 741-762.
- McKenzie, D.P., 1970. Plate tectonics of the Mediterranean region, *Nature*, **226**, 239-243.
- McClusky, S. et al., 2000. Global Positioning System constraints on plate kinematics and dynamics in the eastern Mediterranean and Caucasus, *J. Geophys. Res.*, **105**, 5695-5719.
- Meier, T., Dietrich, K., Stöckhert, B., Harjes, H.-P., 2004. One-dimensional models of shear wave velocity for the eastern Mediterranean obtained from the inversion of Rayleigh wave phase velocities and tectonic implications. *Geophys. J. Int.*, **156**, 45-58.
- Ochmann, N., Hollnack, D., Wohlenberg, J., 1989. Seismological exploration of the Milos geothermal reservoir, Greece, *Geothermics*, **18(4)**, 563-577.
- Panagiotopoulos, D.G., Stavrakakis, G., Makropoulos, K., Papanastasiou, D., Papazachos, C., Savvidis, A., Karagianni, A., 1996. Seismic monitoring at the Santorini volcano, The European laboratory volcanoes, *Proceedings of the second workshop Santorini, Greece*, 311-324.
- Papadopoulos, G.A., Pavlides, S.B., 1992. The large 1956 earthquake in the South Aegean: Macroseismic field configuration, faulting and neotectonics of Amorgos island, *Earth and Planet. Sci. Lett.*, **113**, 383-396.
- Papadopoulos, G.A., Kondopoulou, D.P., Leventakis, G.A., Pavlides, S.B., 1986. Seismotectonics of the Aegean region, *Tectonophysics*, **124**, 67-84.
- Papadopoulos, G., Sachpazi, M., Panopoulou, G., Stavrakakis, G., 1998. The volcanoseismic crisis of 1996-1997 in Nisyros, SE Aegean Sea, Greece. *Terra Nova*, **10**, 151-154.
- Papazachos, B.C., 1973. Distribution of seismic foci in the Mediterranean and surrounding area and its tectonic implications, *Geophys. J.R. astron. Soc.*, **33**, 421-430.
- Papazachos, B.C., Karakostas, V.G., Papazachos, C.B., Scordilis, E.M., 2000. The geometry of the Wadati-Benioff zone and lithospheric kinematics in the Hellenic arc, *Tectonophysics*, **319**, 275-300.
- Perissoratis, C., 1995. The Santorini volcanic complex and its relation to the stratigraphy and structure of the Aegean arc, Greece. *Mar. Geol.*, **128**, 37-58.
- Perissoratis, C., Papadopoulos, G., 1999. Sediment instability and slumping in the southern Aegean Sea and the case history of the 1956 tsunami. *Mar. Geol.*, **161**, 287-305.
- Rinaldi, M., Campos Vinuti, M., 2003. The submarine eruption of the Bombarda volcano, Milos island, Cyclades, Greece. *Bull. Volcanol.*, **65**, 282-293.
- Sachpazi, M., Kontoes, Ch., Voulgaris, N., Laigle, M., Vougioukalakis, G., Sikioti, O., Stavrakakis, G., Baskoutas, J., Kalogeras, J., Lepine, J.Cl., 2002. Seismological and SAR signature of unrest at Nisyros caldera, Greece. *J. Volcan. Geotherm. Res.*, **116**, 19-33.

- Spicak, A., Horalek, J., 2001. Possible role of fluids in the process of earthquake swarm generation in the West Bohemia/Vogtland seismoactive region. *Tectonophysics*, **336**, 151-161.
- Tirel, C., Gueydan, F., Tiberi, C., Brun, J.P., 2004. Aegean crustal thickness inferred from gravity inversion. Geodynamical implications. *Earth Planet. Sci. Lett.*, **228**, 267-280.
- Trotet, F., Jolivet, L., Vidal, O., 2001. Tectono-metamorphic evolution of Syros and Sifnos islands (Cyclades, Greece). *Tectonophysics*, **338**, 179-206.
- Tsapanos, T.M., Galanopoulos, D., Burton, P.W., 1994. Seismicity in the Hellenic Volcanic Arc: relation between seismic parameters and the geophysical fields in the region. *Geophys. J. Int.*, **117**, 677-694.
- Ukawa M., Tsukahara, H., 1996. Earthquake swarms and dike intrusions off the east coast of Izu Peninsula, central Japan. *Tectonophysics*, **253**, 285-303.
- Vougioukalakis, G. et al., 1994. The submarine volcanic centre of Kolumbo, Santorini, Greece. *Bull. Geol. Soc. Gr.*, **XXX/3**, 351-360.
- Walcott, C.R., White, S.H., 1998. Constraints on the kinematics of post-orogenic extension imposed by stretching lineations in the Aegean region. *Tectonophysics*, **298**, 155-175.
- Waldhauser, F., Ellsworth, W.L., 2000. A double difference earthquake location algorithm: Method and application to the northern Hayward fault. *Bull. Seis. Soc. Am.*, **90**, 1353-1368.
- Zobin, V.M., Gonzales Amezcuca, M., Reyes Davila, G.A., Dominguez, T., Cerda, Chacon, J.C., Chavez Alvarez, J.M., 2002. Comparative characteristics of the 1997-1998 seismic swarms preceding the November 1998 eruption of Volcan de Colima, Mexico. *J. Volcan. Geotherm. Res.*, **117**, 47-60.

9. Indications for a balanced state of the upper plate in the central magmatic arc, Greece, from spatial distribution of microseismic activity

This chapter has been prepared for submission. The reference is

Bohnhoff, M., Rische, M., Harjes, H.-P. (2005). Indications for a balanced state of the upper plate in the central magmatic arc, Greece, from spatial distribution of microseismicity. *Geophys. Res. Lett.* (to be submitted).

9.1. Abstract

The upper plate of the central Hellenic Volcanic Arc (HVA), Greece, was classified as an almost aseismic domain at its north-western part based on hypocenter catalogs from permanent regional networks. Recordings from a local seismic network deployed in the area since 2002 show a remarkable seismic activity for $M \leq 2$ that does not occur randomly distributed but shows distinct spatiotemporal patterns. A large portion of this activity occurs in the vicinity of islands representing horst structures at the periphery of the Cyclades metamorphic core complex. Most of the island-related seismicity is located within the uppermost 6 km. Taking into consideration the lateral extension of the islands with respect to the median regional elevation this correlates with the depth where maximum shear stress induced by the gravitational load of the islands is expected. The peak-magnitude of the load-induced shear stress at this depth is ~ 3 MPa and thus sufficient to reactivate pre-existing faults. We conclude that load-induced shear-stress caused by elevated crustal blocks in the HVA is one possible triggering mechanism for microseismic activity indicating that the upper plate is in a balanced state along the rim of the metamorphic core complex.

9.2. Introduction

Induced seismicity is a well-known phenomenon for more than half a century (e.g. Talwani, 1997). The largest magnitude example of a triggered earthquake was the $M=6.5$ event at Koyna reservoir, India, causing 200 deaths and severe damage to the nearby town (Gupta and Rastogi, 1976; Gupta, 2002). There is general agreement that either increased shear stress or reduced effective normal stress caused by increased pore pressure on pre-existing faults is the triggering mechanism responsible for induced earthquakes (see review by Simpson, 1986). Lateral variations in density, topography, and bathymetry are responsible for most of the shear stress within the Earth (Ruff, 2002). Additional gravitational load e.g. caused by local maxima in topography or man-made water dams adds to the tectonic shear stress by enlarging the radius of the Mohr circle through increasing the maximum principal stress (e.g. Jaeger and Cook, 1971). As a consequence increased vertical stress has the largest impact in normal faulting regimes where the vertical stress is the maximum (Snow, 1972; Simpson, 1976). Earthquakes then would be triggered once the induced stresses are large enough to produce failure. Examples from various sites in different tectonic environments consistently identified that even minor stress perturbations in the order of 0.1-4 MPa may cause shear failure on pre-existing faults (e.g. Beck, 1976; Zoback and Harjes, 1997; Pandey and Chadha, 2003). This indicates that brittle-failure equilibrium of the upper part of the Earth's crust is probably a general phenomenon.

In this paper, we focus on microseismicity in the central magmatic arc of the Hellenic subduction zone (Hellenic Volcanic Arc, referred to as HVA in the following) where intense extension occurred in two major phases since Oligocene times and volcanic activity started 4.3 million years ago (Keller et al., 1990). Spatiotemporal behaviour of small-scale ($M \leq 2$) seismic activity showed a high and constant level of activity in the vicinity of islands compared to surrounding offshore regions. We investigate the relation between local variations in topography and seismic activity pattern and relate the results to existing models of weight-induced shear stress anomalies.

9.3. Seismicity in the central HVA

Seismic activity in the Hellenic Subduction Zone is concentrated in the forearc region and predominantly follows the curved plate boundary. Considerable less activity is observed in the backarc region including the HVA (Engdahl et al., 1998; Papazachos et al.; 2000). The distribution of hypocenters in the HVA is monitored by the permanent Greek network of the National Observatory of Athens (catalog complete down to $M \sim 3$) and exhibits an increasing activity from west to east at moderate to small background level. A local maximum of the seismic activity is observed in the Santorini-Amorgos area whereas a diffuse distribution of hypocenters is recognized for the remaining area. With the aim to monitor the local seismicity with an improved resolution at lower magnitude detection threshold, the CYClades seismic NETWORK (CYCNET) was installed in the central HVA in 2002. CYCNET consists of up to 22 stations distributed on 17 islands (Bohnhoff et al., 2004). Some 2175 local earthquakes were recorded during the first 20 months of operation. More than 80% of the events occurred within the uppermost 10 km and are dominantly of $M \leq 2$.

Apart from several activity spots that are related to the Santorini-Amorgos zone of crustal weakness and volcanic centres it was found that a significant portion of this activity occurs in the vicinity of islands (Bohnhoff et al., 2005) (Figure 1). Most of these islands are related to horst structures that are associated with the two major extensional and intersecting compressional phases within the south Aegean in Oligocene and Late Miocene times (Gautier and Brun, 1994; Tirel et al., 2004). To a large extent, they form the outer rim of the Cyclades

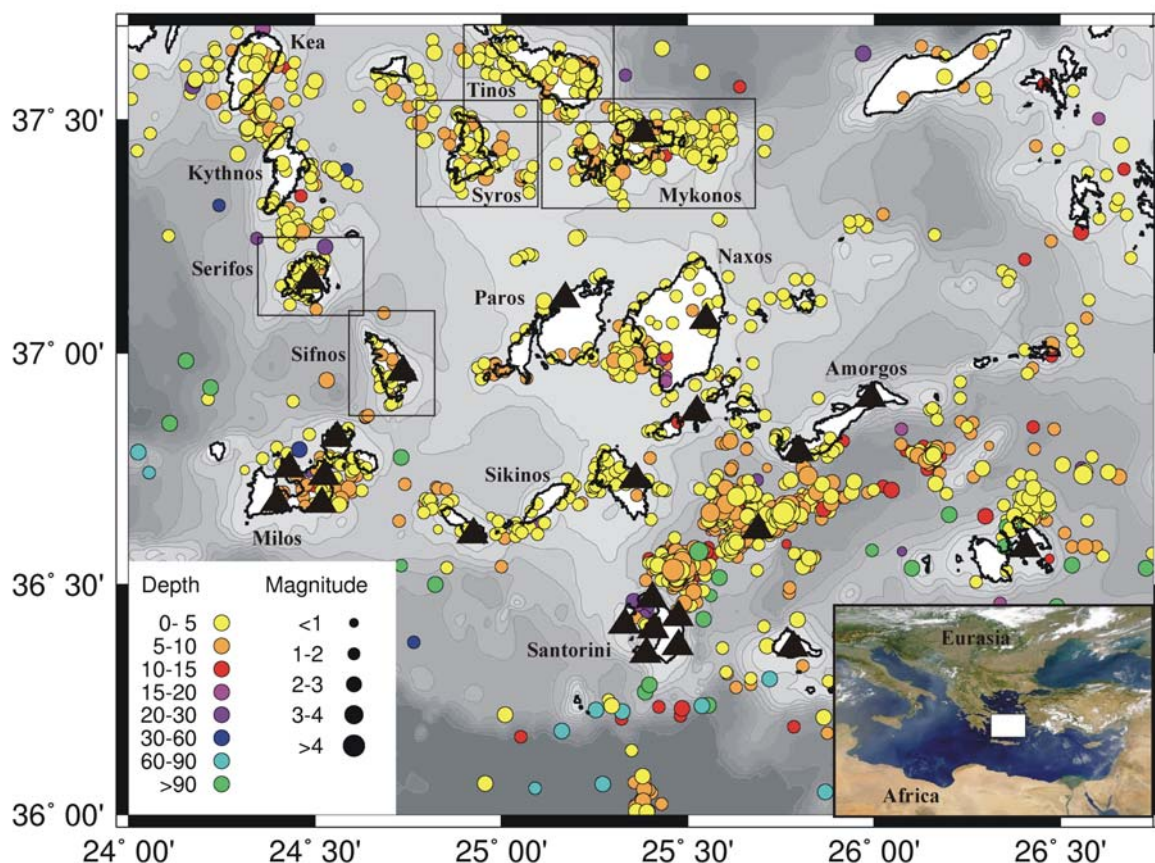


Figure 1: Seismic activity in the central Hellenic Volcanic Arc as recorded by the CYClades seismic NETWORK during a 20-month period starting in Sep2002. Earthquakes are colour-encoded and scaled with magnitude. Black triangles mark seismic stations. Islands marked by the black rectangle show remarkable activity spots and are discussed in the text and enlarged in Figure 2. Waterdepth is given by 100 m-isolines. In the location map at the lower right the area of investigation is marked by the white rectangle.

metamorphic core complex (Lister et al., 1984; Trotet et al., 2001) that exhibits considerable less activity at its centre around the islands of Naxos and Paros where a single activity spot was identified. This spot is dominated by swarm-like cluster activity. In contrast, the spatiotemporal behaviour of seismicity spots near or below islands reflects constant activity without significant variations during the recording period and occurs down to 6-8 km depth (Bohnhoff et al., 2005). The island-related seismicity is not an artefact of CYCNET's station distribution as it is observed also for islands where no seismic station was operated (e.g. islands of Syros and Sikinos) and even on islands outside the network (e.g. Kythnos, Kea, Tinos) (see Figure 1). Most offshore regions within CYCNET do not contain a single event which is remarkable considering that the magnitude detection threshold is uniform within the network.

9.4. Characteristics of island-related seismicity and island elevation

In the previous section we observed a correlation between seismic activity and elevated crustal blocks in the central HVA. In order to investigate the underlying physical mechanisms we focus on the islands of Serifos, Sifnos and Syros (all with a lateral extension in the order of 15x20 km) as well as on Mykonos and Tinos (~20x30 km) as these islands exhibit the most pronounced seismic activity. We proceed with considering all hypocenters within the marked

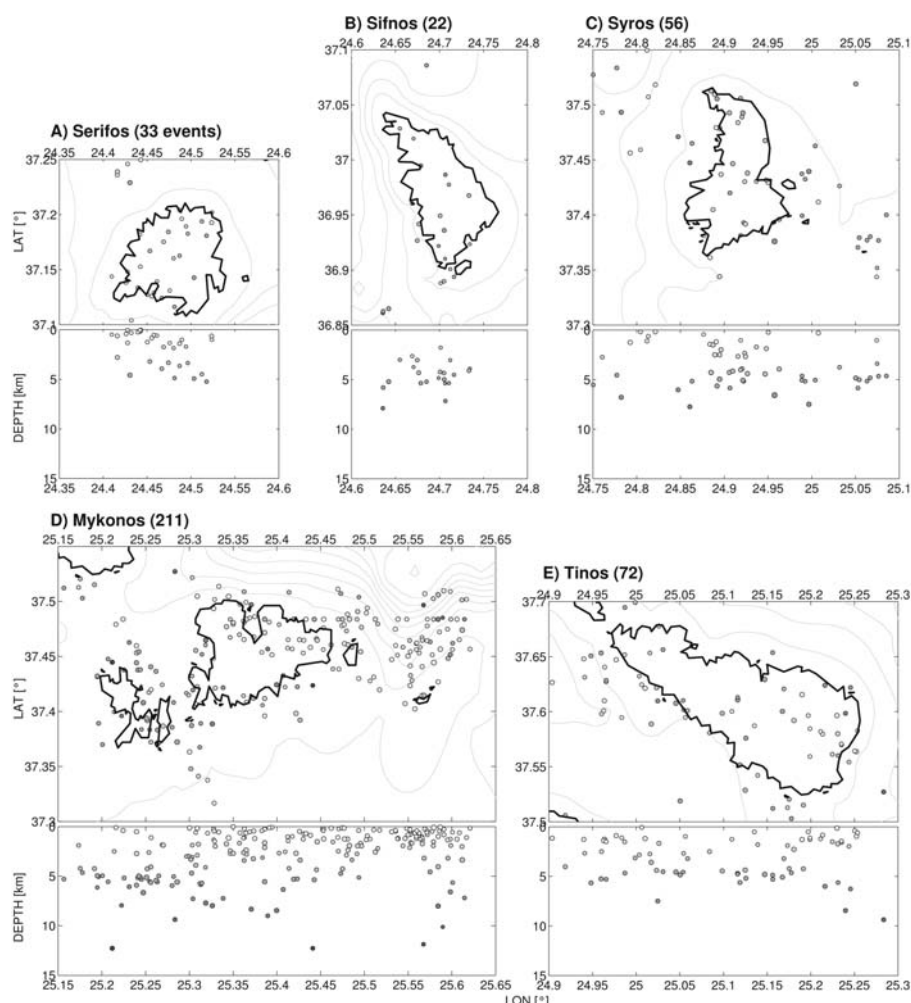


Figure 2: Map view and EW-depth section for the five islands (Serifos, Sifnos, Syros, Mykonos and Tinos in subfigures a-e, respectively) where associated shallow seismicity. All subfigures are uniformly scaled. The number of events below each island is given in brackets. Hypocentral distribution stresses a dominant activity within the uppermost 5-6 km for all islands. Individual events occur down to 13 km.

regions (Figure 1) down to a depth of 15 km resulting in a total of 394 events. In Figure 2 each of the selected blocks is shown in map view and as EW-depth section. The majority of hypocenters is located down to approximately 6 km and individual events reach down to 13 km (Figure 2).

The accuracy in depth determination for shallow events within CYCNET is in the order of 2 km. This depth control was achieved by increasingly weighting the s-p times for stations on islands with associated seismicity. However, the depth-distribution around islands where no seismic station was operated is similar (e.g. Syros, Tinos) indicating that hypocentral depth is reliable within a few kilometers. Only events based on at least eight (including at least two S) picks and a RMS value $<0.7s$ were considered for the CYCNET catalog. Hypocenters shown in Figures 1 and 2 are absolute locations. To verify the hypocentral distribution within local activity spots below the islands we applied a relative relocation technique for individual islands with associated seismicity using the hypoDD code by Waldhauser and Ellsworth (2000). No remarkable differences of the shape of seismic clouds were observed and we therefore decided to rely on the absolute locations.

The mean elevation of the islands reaches 300 m above sea level. Island topography is triangular-shaped in a first order approximation for Serifos, Sifnos and Syros. A similar shape with a slightly smaller slope is observed for the islands of Mykonos and Tinos (Figure 3). Both islands exhibit local maxima in elevation at their eastern part. Interestingly, this results in an increased shallow (depth: 0-3 km) seismicity in either case. One possible triggering mechanism for the island-related seismicity might be a load-induced shear-stress increase caused by the island's weight. To further investigate this we relate the island's elevation to the regional topographic/bathymetric median (390 m below sea level). The mean peak elevation of the five islands considered here is then in the order 600 m with no significant variation between islands of different size.

9.5. Jeffreys model and its application to the central HVA

Jeffreys (1970) presented a model describing the pressure at the bottom of a load located on the Earth surface. Here, we briefly describe the essence of this model based on more detailed discussions by McNutt (1980) and Ruff (2002). Given a load of known size, shape and density it is possible to calculate the additional shear stress with depth. Assuming a triangular shape of the topographic profile of the load this will result in a maximum of additional shear stress below the center of the load. Jeffreys (1970) showed that if this load is applied to an elastic half-space, then the peak shear stress is reached at a depth that is about one-quarter of the load's width. In order to apply this model to our observation of island-related seismicity we proceed in two steps. First, we focus on the depth distribution of hypocenters. The widths of the elevated blocks with the islands at their center are in the order of 25-30 km on average. Following Jeffreys' model we then would expect the maximum load-induced shear stress at a depth of 6-7 km. Shifting all 394 hypocenters related to the five islands shown in Figure 2 towards a reference frame based on the center of the islands along a EW direction we calculated a density matrix of earthquakes with depth (Figure 3). The lower boundary of dominant seismic activity is observed at 5-6 km depth which is in accordance with the depth of maximum shear stress as calculated from Jeffreys' model.

In a second step we focus on the magnitude of the load-induced shear stress. According to Jeffreys (1970) this magnitude can be calculated by

$$\tau_{\text{peak}} = (0.512) * (\rho * g * H) / 2 \quad (\text{equation 1})$$

where ρ is density, g is gravitational acceleration and H is the height of the rock column. In the case of the central HVA we assume $\rho=2.5 \text{ g/cm}^3$, $g=10 \text{ m/s}^2$ and $H=600 \text{ m}$ for the islands. Taking into consideration the reduced density contrast below the water surface (1.5 g/cm^3) for 75% of the rock column we calculate the maximum additional shear stress to 2.7 MPa below the islands at $\sim 6 \text{ km}$ depth.

Estimations for stress perturbations induced by water reservoirs (Pandey and Chadha, 2003) or fluid injection (Zoback and Harjes, 1997) that are responsible for triggering seismicity are in the order of 0.1-1 MPa at 6-9 km depth. As a consequence, the $\sim 3 \text{ MPa}$ we find for load-induced increase of shear stress below the elevated crustal blocks in the central HVA are sufficient to reactivate pre-existing faults below the islands.

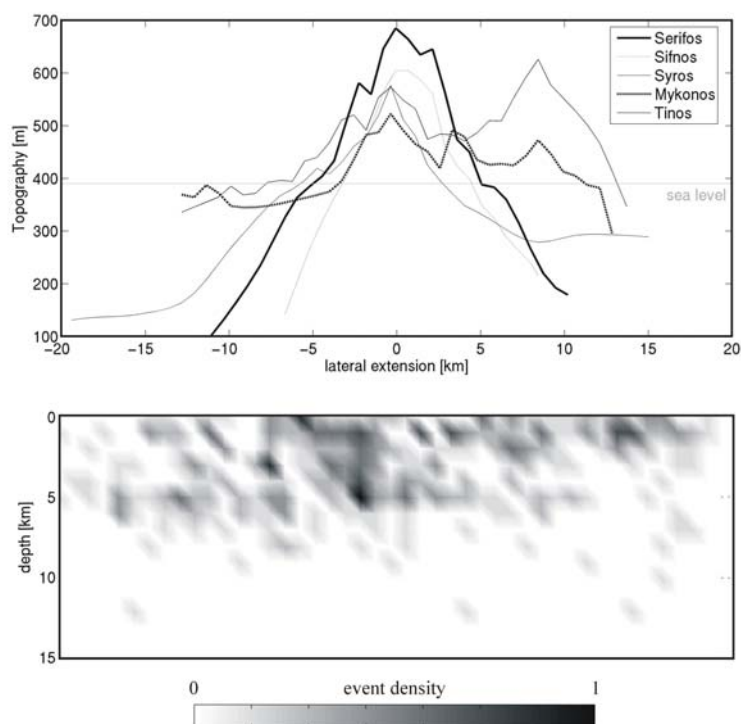


Figure 3: Topography of the five islands where dominant shallow seismicity was observed. Elevation is plotted with respect to the regional medium of 390 m below sea level. Peak elevation is mostly observed around the centre of the islands and reaches 600 m on average. The lower plot show the density matrix of all 394 events that occurred below the five islands. Dominant activity is observed within the uppermost 6 km and only sparse activity occurs at greater depth.

9.6. Discussion and conclusions

The here presented data base of microseismic activity in the central HVA reflects significant activity maxima in the vicinity of a number of islands. These islands are located along the outer rim of the Cyclades metamorphic core complex and related to horst structures that formed during two major extensional and intersecting short-term compressional phases since Oligocene. We investigate the hypocentral distribution of events with respect to the shape and size of the elevated crustal blocks and find that a large portion of the island-related seismicity occurs at 5-6 km depth where the maximum load-induced additional shear stress is expected. Estimating its magnitude we find 3 MPa as an average value for the five selected islands which is sufficient to reactivate pre-existing faults at depth following earlier results from dam and fluid-injection induced seismicity (e.g. Pandey and Chadha, 2003; Zoback and Harjes, 1997). The depth distribution of hypocenters as well as the 3 MPa additional shear stress

correlate with a model presented by Jeffreys (1970) describing shear-stress increase induced by gravitational loads as a general phenomenon. We conclude that shear-stress increase caused by the island's weight is a possible triggering mechanism for the observed island-related seismicity. If so, this would indicate that the crust is in a balanced state along the outer rim of the Cyclades metamorphic core complex. One should, however, keep in mind that existing studies focussing on water-dam or fluid-injection induced brittle failure analyze pressure pulses with short wavelengths (up to weeks). In our case, the additional pressure results from the existence of islands that evolved during tectonic time scales.

The effect of island-related seismicity is not observed at the center of the core complex where the highest elevation within the central HVA is observed (~1100 m on Naxos) and seismicity is limited to one spot with swarm-like cluster activity between Naxos and Paros. Fluid movements related to a not yet completed uplift of the centre of the core complex might account for this cluster activity while its periphery might have already reached isostatic equilibrium. Assuming the load of the islands to be responsible for triggering seismicity, one presumption is a normal faulting regime in the area of interest as discussed above. Internal deformation within the backarc of the Hellenic subduction zone is reported to be ~0.5 cm/a (McClusky et al., 2000) during the last ~two decades. This supports that regional extension has slowed-down recently. Focal mechanisms for larger earthquakes of the region (Papadopoulos and Pavlides, 1992; Hatzfeld et al., 1993) indicate a right-lateral transtensional environment. In conclusion, we find that gravitational load in the central HVA might account for triggering local spots of microseismicity activity in an otherwise almost aseismic environment. This activity is limited to small ($M \leq 2$) magnitudes that could not be detected by permanent networks emphasizing that the deployment of appropriate dense local networks is an adequate tool to improve our understanding on triggering mechanisms for seismicity on different scales.

9.7. Acknowledgements

We thank the German Research Foundation (DFG) for funding within the Collaborative Research Centre 526 'Rheology of the Earth – from the Upper Crust to the Subduction Zone'. We benefited from fruitful discussions with T. Meier, G. Dresen, E. Rybacki, A. Zang and O. Stephansson and are grateful to the GeoForschungsZentrum Potsdam for supplying seismic acquisition systems from the Geophysical Instrument Pool. We acknowledge support by B. Klotz, L. Kühne, D. Becker and G. Michaletos in installation and maintenance of the seismic stations.

9.8. References

- Beck, J.L. (1976), Weight-induced stresses and the recent seismicity at Lake Oroville, California, *Bull. Seism. Soc. Am.*, **66** (4), 1121-1131.
- Bohnhoff, M., M. Rische, T. Meier, B. Endrun, H.-P. Harjes and G. Stavrakakis (2004), A temporary Seismic Network on the Cyclades (Aegean Sea, Greece), *Seismol. Res., Lett.*, **75/3**, 352-357.
- Bohnhoff, M., M. Rische, T. Meier, D. Becker, G. Stavrakakis and H.-P. Harjes (2005), Microseismic activity in the Hellenic Volcanic Arc, Greece, with emphasis on the seismotectonic setting of the Santorini-Amorgos zone, *submitted to Tectonophysics*.
- Engdahl, E.R., R. Van Der Hilst and R. Buland (1998), Global teleseismic earthquake relocation with improved travel times and procedures for depth determination, *Bull. Seism. Soc. Am.*, **88**, 722-743.
- Gautier, P. and J.P. Brun (1994), Crustal-scale geometry and kinematics of late-orogenic extension in the central Aegean (Cyclades and Evvia Island), *Tectonophysics*, **238**, 399-424.
- Gupta, H.K. (2002), A review of recent studies of triggered earthquakes by artificial water reservoirs with special emphasis on earthquakes in Koyna, India, *Earth. Sci. Rev.*, **58**, 279-310.
- Gupta, H.K. and B.K. Rastogi (1976), Dams and Earthquakes, *Amsterdam: Elsevier*, 299pp.
- Hatzfeld, D., M. Besnard, K. Makropoulos, K., Hatzidimitriou (1993), Microearthquake seismicity and fault-plane solutions in the southern Aegean and its geodynamic implications, *Geophys. J. Int.*, **115**, 799-818.

- Jaeger, J.C. and N.G.W. Cook (1971), *Fundamental of Rock Mechanics*, London: Chapman & Hall, 515pp.
- Jeffreys, H. (1970), *The Earth*, Cambridge University Press, New York.
- Keller, J., T. Rehren and E. Stadlbauer (1990), Explosive volcanism in the Hellenic arc: A summary and review, Proceedings of the third International Congress, *Thera and the Aegean World III*, Vol. 2, 13-26.
- Lister, G.S., G. Banga and A. Feenstra (1984), Metamorphic core complexes of Cordilleran type in the Cyclades, Aegean Sea, Greece, *Geology*, **12**, 221-225.
- Mc Clusky, S. et al. (2000), Global Positioning System constraints on plate kinematics and dynamics in the eastern Mediterranean and Caucasus, *J. Geophys. Res.*, **105**, 5695-5719.
- McNutt, M. (1980), Implications of Regional Gravity for State of Stress in the Earth's Crust and Upper Mantle, *J. Geophys. Res.*, **85**, B11, 6377-6396.
- Pandey, A.P. and R.K. Chadha (2003), Surface loading and triggered earthquakes in the Koyna-Warna region, western India, *Phys. Earth. Planet. Int.*, **139**, 207-223.
- Papadopoulos, G.A. and S.B. Pavlides (1992), The large 1956 earthquake in the South Aegean: Macroseismic field configuration, faulting and neotectonics of Amorgos island, *Earth and Planet. Sci. Lett.*, **113**, 383-396.
- Papazachos, B.C., V.G. Karakostas, C.B. Papazachos and E.M. Scordilis (2000), The geometry of the Wadati-Benioff zone and lithospheric kinematics in the Hellenic arc, *Tectonophysics*, **319**, 275-300.
- Ruff, L.J. (2002), State of Stress Within the Earth, *Int. Handbook of Earthquake and Engineering Seismology*, vol. 81A, Int. Assoc. Seismol. and Phys. Earth's Int., Committee on Education, 539-557.
- Simpson, D.W. (1976), Seismicity changes associated with reservoir impounding, *Eng. Geol.*, **10**, 371-385.
- Simpson, D.W. (1986), Triggered Earthquakes, *Ann. Rev. Earth Planet. Sci.*, **14**, 21-42.
- Snow, D.T. (1972), Geodynamics of seismic reservoirs, *Proc. Symp. Percolation Through Fissured Rocks, T2-J*, Stuttgart, Ges. Erd- und Grundbau, 1-19.
- Talwani, P. (1997), On the Nature of Reservoir-induced Seismicity, *PAGEOPH*, **150**, 473-492.
- Tirel, C., F. Gueydan, C. Tiberi and J.P. Brun (2004), Aegean crustal thickness inferred from gravity inversion and Geodynamical implications, *Earth Planet. Sci. Lett.*, **228**, 267-280.
- Trotet, F., L. Jolivet and O. Vidal (2001), Tectono-metamorphic evolution of Syros and Sifnos islands (Cyclades, Greece), *Tectonophysics*, **338**, 179-206.
- Waldhauser, F. and W.L. Ellsworth (2000), A double difference earthquake location algorithm: Method and application to the northern Hayward fault, *Bull. Seis. Soc. Am.*, **90**, 1353-1368.
- Zoback, M.D. and H.-P. Harjes (1997), Injection-induced earthquakes and crustal stress at 9 km depth at the KTB deep drilling site, Germany, *J. Geophys. Res.*, **102**, 18477-18491.

Acknowledgements

I am much obliged to Prof. Dr. Hans-Peter Harjes for scientific guidance, providing excellent working conditions and putting me on the right track whenever I turned in turbulences.

Likewise I am grateful to Prof. Dr. Georg Dresen for offering an exceptional interdisciplinary scientific environment, for stimulating discussions and for introducing me into the world of rock mechanics.

For substancial and fruitful discussions I thank Prof. Dr. Bernhard Stöckhert, Prof. Dr. Jörg Renner and Dr. Stefan Baisch.

I thank Prof. Dr. Jannis Makris for a comprehensive education in the field of Applied Geophysics.

I indeed thank my family for supporting and pushing me during the different phases of this work, my parents Peter and Marion for a warm childhood and for providing the base for an education free of choice and Marc for real friendship.

Support of variable kind from the members of the Seismology group at Ruhr University Bochum, namely PD Dr. Thomas Meier, Martina Rische, Dirk Becker, Brigitte Endrun, Dr. Kasper Fischer, Norbert Schnieders, Mareike Messar and Jenny Lenhardt is greatly acknowledged.

The German Research Foundation (Deutsche Forschungs Gemeinschaft –DFG) is thanked for funding the projects B1 and C4 within the Collaborative Research Centre (SFB) 526 ‘Rheology of the Earth’ at Ruhr University Bochum.

I thank the GeoForschungsZentrum Potsdam for supplying data acquisition systems for a large number of the field campaigns described in the different chapters and for providing an excellent scientific working environment.

This work is dedicated to Roxana, Sophia and Patricia with whom I share the by far most exciting moments of my life.